

**Flexible Assistenztechnik für MRT-gesteuerte Interventionen  
in verschiedenen Körperregionen**

Von der Medizinischen Fakultät

der Universität Leipzig

genehmigte

HABILITATIONSSCHRIFT

zur Erlangung des akademischen Grades

Doctor rerum naturalium habilitatus

(Dr. rer. nat. habil.)

vorgelegt

von Dr. rer. nat. Harald Busse

geboren am 10.11.1965 in Bonn

Tag der Verleihung 28.02.2017

## **Bibliografische Beschreibung:**

Busse, Harald

## **Flexible Assistenztechnik für MRT-gesteuerte Interventionen in verschiedenen Körperregionen**

Universität Leipzig, Habilitation

116 Seiten inklusive 7 Originalarbeiten, 101 Literaturstellen, 11 Abbildungen

## **Referat:**

Bildgesteuerte, perkutane Interventionen stellen bei vielen diagnostischen und therapeutischen Fragestellungen eine Alternative zum chirurgischen Vorgehen dar. Hierbei kommen bevorzugt die Sonographie und die Computertomographie (CT) zum Einsatz. Zu den Indikationen für eine gezielte Nutzung der Magnetresonanztomographie (MRT) zählen Befunde, die sich mit anderen Modalitäten nicht ausreichend darstellen lassen, die fehlende Strahlenexposition (CT) sowie Alleinstellungsmerkmale wie der hervorragende native Weichteilkontrast oder die Möglichkeiten zur Darstellung von Temperaturen oder Diffusionsprozessen. Zu den Nachteilen zählen die langen Messzeiten, das starke Magnetfeld sowie die räumliche Enge in den meist röhrenförmigen Geräten, die ein interventionelles Vorgehen oft erschweren.

Stereotaktische Führungs- und Navigationshilfen sind kein notwendiger Bestandteil der interventionellen Ausrüstung, ermöglichen jedoch oft eine gezieltere Planung, bessere Visualisierung oder vereinfachte Durchführung, insbesondere gegenüber einer rein kognitiven Einbeziehung der MRT-Informationen. Assistenzsysteme für geschlossene MRT-Geräte sind meist *rahmenbasiert* und beschränken sich auf bestimmte Regionen, z. B. die Mamma, die Prostata oder das muskuloskeletale System. Diese Arbeit beschreibt hingegen eine leistungsstarke *rahmenlose* Assistenztechnik (Navigation), die sich praktisch in beliebigen Körperregionen einsetzen lässt. Der Operateur orientiert sich dabei anhand von hochwertigen MRT-Ansichten, die gemäß der *in Echtzeit* erfassten Nadellage aus einem kurz zuvor erhobenen Referenzdatensatz reformatiert werden.

Ausgehend von der Implementierung an einem speziellen offenen MRT-System (0,5 T) werden interventionelle Komponenten und Methoden beschrieben, die erfolgreich auf ein herkömmliches MRT-System (1,5 T) übertragen wurden. Die Einschränkungen des geschlossenen Systems führten dabei zu einer speziellen Registrierungstechnik mit Hilfe einer kompakten, frei positionierbaren Referenzplatte mit resonanten Miniatur-Hochfrequenzspulen (*semiaktiv*) als MR-Positionsmarker. Im Vordergrund stand die systematische Prüfung der Marker hinsichtlich Signalverhalten und Sicherheit sowie die Zuverlässigkeit und Genauigkeit einer vollautomatischen, bildbasierten 3D-Lokalisation unter experimentellen und klinischen Randbedingungen. Gegenüber herkömmlichen, *passiven* (Kontrastmittel-) Markern zeichnet sich die semiaktive Technik dadurch aus, dass sie *gleichzeitig*, auch mehrere, *beliebig* über das *gesamte* Messvolumen verteilte Marker, praktisch *unabhängig* von sämtlichen anatomischen Strukturen lokalisieren kann.

Sowohl die Festlegung einer Position (ein Marker) oder einer Ebene (drei Marker) wie auch die navigierte Platzierung einer Nadel zeigten im Experiment ausreichend hohe Genauigkeiten. Auf Basis einer zeitlich optimierten (Subsekunden-) Markerbildgebung konnte experimentell eine robotisch geführte Nadel direkt *im* MRT bildgebend verfolgt werden, was weitere Anwendungen der Lokalisationstechnik in Aussicht stellt. Navigierte Biopsien an einem Gewebephantom zeigten nach ausschließlich stereotaktischer Positionierung – ohne Kontrollbildgebung – unabhängig vom Erfahrungsgrad der medizinischen Anwender ausreichend hohe Trefferquoten. Gleichzeitig lieferte die Studie wertvolle, auch anwenderspezifische Erkenntnisse über die Bedienbarkeit sowie den Zeitbedarf für einzelne Interventionsschritte. Im Vergleich mit anderen prototypischen oder kommerziellen Systemen zeigte sich die vorgestellte Assistenztechnik – am Beispiel muskuloskelettaler Interventionen – als klinisch flexibel einsetzbar.

# Inhaltsverzeichnis

---

<b>1. Einführung in die Thematik</b>	<b>1</b>
<b>1.1 Bildgestützte Interventionen</b>	<b>1</b>
<b>1.2 Interventionelle Assistenzsysteme</b>	<b>2</b>
<b>1.3 Platzierung von Instrumenten mit Hilfe der MRT</b>	<b>3</b>
1.3.1 Kognitives Vorgehen	4
1.3.2 Bildgebende Steuerung	4
1.3.3 Stereotaktische Führung	6
<b>1.4 Registrierung stereotaktischer Systeme</b>	<b>7</b>
<b>1.5 Interventionelle Eignung verschiedener MRT-Systeme</b>	<b>8</b>
1.5.1 Geschlossene MRT-Systeme	8
1.5.2 Limitationen geschlossener MRT-Systeme	9
1.5.3 Offene MRT-Systeme	9
1.5.4 Intraoperatives MRT-System	10
1.5.5 Spezielle Limitationen	11
<b>1.6 Bereitstellung einer Echtzeit-Navigation</b>	<b>12</b>
1.6.1 Funktionsmerkmale	12
1.6.2 Technische Anforderungen	15
<b>2. Zusammenfassende Darstellung</b>	<b>16</b>
<b>3. Originalarbeiten</b>	<b>20</b>
<b>3.1 Implementation einer Echtzeit-Navigation an einem offenen MRT</b>	<b>20</b>
<b>3.2 Vollautomatisches Verfahren zur 3D-Lokalisation von MR-Positionsmarkern</b>	<b>34</b>
<b>3.3 Eignung von semiaktiven MR-Positionsmarkern für interventionelle Zwecke</b>	<b>46</b>
<b>3.4 Bereitstellung einer Echtzeit-Navigation an einem geschlossenen MRT</b>	<b>57</b>
<b>3.5 Machbarkeit einer Echtzeit-Verfolgung von semiaktiven MR-Positionsmarkern</b>	<b>66</b>
<b>3.6 Studie zur Anwenderabhängigkeit einer Echtzeit-Navigation</b>	<b>79</b>
<b>3.7 Vergleich verschiedener Navigationsverfahren unter praktischen Aspekten</b>	<b>93</b>
<b>4. Ausblick</b>	<b>105</b>
<b>Literaturverzeichnis</b>	<b>108</b>
<b>Danksagung</b>	<b>115</b>
<b>Erklärung</b>	<b>116</b>

## Abkürzungsverzeichnis

---

2D, 3D	zweidimensional, dreidimensional
BOLD	<i>blood oxygen level dependent</i> , abhängig vom Sauerstoffgehalt des Bluts
b-SSFP	<i>balanced steady state with free precession</i> (MRT-Pulssequenz)
CPU	<i>central processing unit</i> , Hauptprozessor
CT	Computertomographie
DSA	Digitale Subtraktionsangiographie
FLASH	<i>fast low-angle shot</i>
<sup>18</sup> F-FDG	radioaktiv ( <sup>18</sup> F) markierte Fluordesoxyglucose (PET-Tracer)
fMRT	funktionelle MRT, hier speziell auf Basis des BOLD-Effekts (s. o.)
fps	<i>frames per second</i> , Einheit der Bildwiederholrate: Bilder pro Sekunde
GMD	Gesellschaft für Mathematik und Datenverarbeitung
HASTE	<i>half Fourier acquisition single-shot turbo spin echo</i> (MRT-Pulssequenz)
HF	Hochfrequenz
HNO	Hals-Nasen-Ohren
LCD	<i>liquid crystal display</i> , Flüssigkristallanzeige
LED	<i>light-emitting diode</i> , Licht-emittierende Diode
math.	mathematisch
MRT	Magnetresonanztomographie
NDI	<i>Northern Digital Incorporated</i>
OP	Operation (medizinisch)
PC	<i>personal computer</i>
PET	Positronen-Emissionstomographie
T <sub>1</sub> , T <sub>2</sub>	longitudinale bzw. transversale Relaxationszeit
TrueFISP	<i>true fast imaging with steady precession</i> (MRT-Pulssequenz)
US	Ultraschall (Bildgebung)
VIBE	<i>volumetric interpolated breathhold examination</i>

# 1. Einführung in die Thematik

---

## 1.1 Bildgestützte Interventionen

Radiologische Bildinformationen werden bereits seit vielen Jahren zur Planung, Kontrolle und Steuerung von diagnostischen und therapeutischen Eingriffen herangezogen. Zu den Anwendungsbeispielen zählen die Drainage von Körperflüssigkeiten [1–3], die Biopsie suspekter Befunde [4–6] oder die thermische Koagulation eines Tumors über perkutan eingebrachte Applikatoren [7, 8]. Zur Bildgebung werden primär der Ultraschall (US) oder die Computertomographie (CT) eingesetzt, da diese breit verfügbar und leicht durchführbar sind. Grundsätzlich lassen sich perkutane (nicht-vaskuläre) und vaskuläre Interventionen unterscheiden. Die meisten perkutanen Eingriffe finden unter US- oder CT-Kontrolle statt [9]. Bei vaskulären Interventionen ist eine selektive Gefäßdarstellung mit der digitalen Subtraktionsangiographie (DSA) gebräuchlich [10, 11].

Die klinisch in den 1980er Jahren eingeführte Magnetresonanztomographie (MRT) zeichnet sich vor allem durch ihren exzellenten Weichteilkontrast mit und ohne Kontrastmittel (KM) aus. Aufgrund der fehlenden Strahlenbelastung, der zeitlich längeren KM-Darstellung, der freien Schichtauswahl bei der Aufnahme sowie der möglichen Temperaturüberwachung [12–14] bietet sich die MRT auch für interventionelle Zwecke an. Eine eingehende Darstellung der technischen Grundlagen und klinischen Einsatzmöglichkeiten der interventionellen MRT findet sich z. B. bei [15]. Als wesentliche Nachteile sind die relativ langen Bildgebungszeiten, das starke Magnetfeld, die elektromagnetischen Hochfrequenzfelder und die eingeschränkten Platzverhältnisse in den meist röhrenförmigen, geschlossenen Geräten zu nennen, die ein interventionelles Vorgehen meist erschweren.

Zu den Indikationen für ein gezieltes Vorgehen unter MRT-Kontrolle [16, 17] zählen vor allem Befunde, die schwer zugänglich und mit anderen Bildgebungsverfahren gar nicht oder nur unzureichend darstellbar sind (**Abb. 1**) sowie Patienten mit einer Kontraindikation für die Untersuchung, z. B. im Falle der CT bei einer Allergie gegenüber jodhaltigen Kontrastmitteln oder bestehender Schwangerschaft. Vielen perkutanen Eingriffen ist gemeinsam, dass ein spezielles Instrument in einer Zielregion platziert werden muss, welche zuvor auf MRT-Aufnahmen identifiziert wurde. Dieses Instrument kann z. B. ein Biopsiesystem für eine

Probenentnahme, ein Drahtkatheter für eine prächirurgische Markierung oder ein Applikator für eine Thermoablation sein. Die Einbringung erfolgt in der Regel über eine Koaxialnadel.

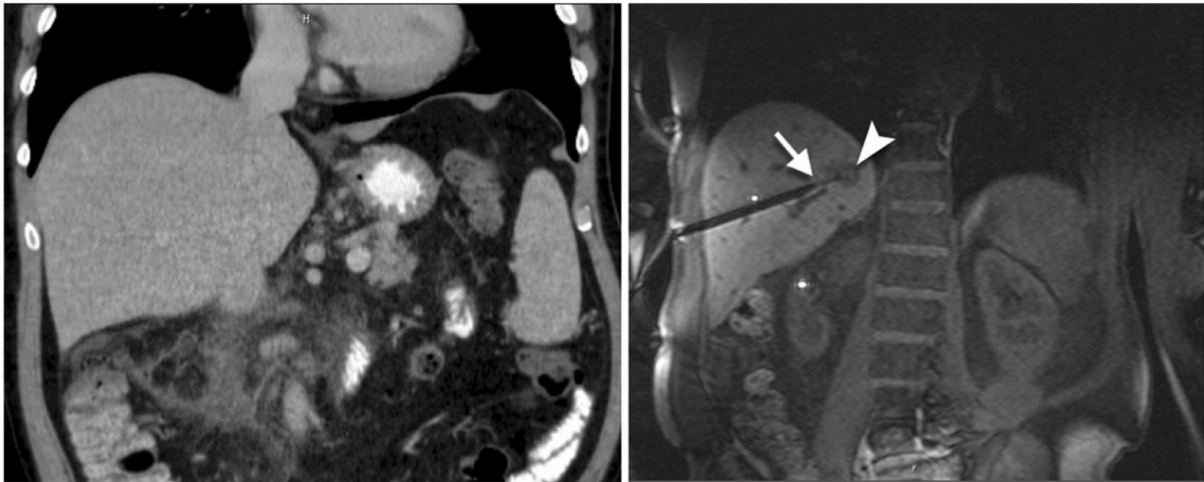


**Abb. 1** 63-jähriger Patient mit einer rund 130 mm tiefen Leberläsion in Segment VII. **Links:** Koronare CT-Schicht in der betreffenden Region ohne erkennbare Läsion. **Rechts:** Schräge MRT-Aufnahme ohne Kontrastmittel (schnelles  $T_1$ -gewichtetes Gradientenecho, *VIBE*) mit Artefakten der Koaxialnadel sowie des Biopsiesystems (Pfeil) am Rand der gut sichtbaren Läsion (Pfeilkopf). Reproduziert aus [18] gemäß *Creative Commons License* ([creativecommons.org/licenses/by-nc/4.0/](https://creativecommons.org/licenses/by-nc/4.0/)).

## 1.2 Interventionelle Assistenzsysteme

Ohne technische Unterstützung hängen Arbeitsschritte und Zeitbedarf eines bildgestützten Eingriffs relativ stark von der Komplexität des Falls sowie der interventionellen Erfahrung des Arztes ab [19, 20]. Führungs- und Navigationshilfen sind kein notwendiger Bestandteil der interventionellen Ausrüstung, bilden jedoch eine sinnvolle Erweiterung [21, 22], mit deren Hilfe sich Arbeitsschritte optimieren und vereinheitlichen lassen. Oft ermöglichen sie auch eine gezieltere Planung, eine bessere Visualisierung oder eine leichtere Steuerung [23].

Die Assistenzsysteme für die MRT reichen von einfachen Komponenten zur Halterung bzw. Einführung von Nadeln [24, 25] über Manipulatoren zur Einstellung einer geplanten Trajektorie [26] bis hin zu dedizierten Navigationssystemen, bei denen die genaue räumliche Lage eines Instruments in nahezu Echtzeit erfasst wird (**Abb. 2**). Diese Tracking-Systeme ermöglichen in der Regel eine genaue Lokalisierung und Kontrolle der Bewegung eines Instruments am und im Körper des Patienten. Im Gegensatz zu sonographischen oder röntgenbasierten Interventionen müssen die im MRT verwendeten Bauteile jedoch aus nicht-magnetischen Materialien gefertigt sein, die robust und sicher einsetzbar sind und die Bildgebung nicht beeinträchtigen [27, 28].

So erfolgt z. B. das Tracking im MRT-Raum oft über eine optische Signalübertragung im Infrarotbereich [29, 30]. Die für andere Modalitäten gebräuchliche elektromagnetische Sensortechnik [31] ist in einer MRT-Umgebung nicht einsetzbar. Die optischen Marker senden entweder selbst ein Signal aus (aktiv) oder reflektieren es lediglich (passiv). Dabei arbeiten die aktiven Marker tendenziell etwas genauer [32] während sich die passiven aufgrund der fehlenden elektrischen Anschlüsse flexibler und unbedenklicher einsetzen lassen. Seit langem ist im Bereich Tracking eine Auswahl kommerzieller Systeme mit entsprechender Ansteuerung und Datenschnittstelle vorhanden [32, 33].



**Abb. 2** Beispiele für stereotaktische Führungshilfen in der MRT. **Links:** Rastervorrichtung zur Einführung eines Biopsiesystems in der Mamma (*Sentinelle*, Invivo, Gainesville, USA). **Mitte:** Passives Assistenzsystem zur Ausrichtung einer Führungshülse bei der transrektalen Prostatabiopsie (*DynaTrim*, Invivo), zur Illustration mit eingeführtem, vollautomatischem Biopsiesystem. **Rechts:** Einsatz eines optischen Trackingsystems (*Polaris Spectra*, NDI, Waterloo, Kanada) auf einem Rollstativ für eine navigierte Leberbiopsie.

### 1.3 Platzierung von Instrumenten mit Hilfe der MRT

Grundsätzlich lassen sich Instrumente bzw. Koaxialnadeln auf drei verschiedene Arten in eine Zielregion bringen, und zwar in der Reihenfolge des technischen Aufwands: durch kognitive Übertragung der MR-Informationen auf die Verhältnisse am Patienten (kurz: *kognitiv*), mit Hilfe eines rahmenbasierten oder rahmenlosen Zielsystems (*stereotaktisch*) oder unter fortlaufender MRT-Bildgebung (*bildgebend*) [34].

Das einfache kognitive Verfahren ist universell anwendbar, zeigt jedoch oft eine Variabilität im Arbeitsablauf bzw. Zeitbedarf – abhängig von der Komplexität des Eingriffs und der interventionellen Erfahrung des Operateurs. Die bildgebende Steuerung bietet prinzipiell die besten Kontrollmöglichkeiten, ist jedoch technisch anspruchsvoll und an den meisten diagnostischen Systemen nicht praktikabel. Demgegenüber stellt das stereotaktische

Vorgehen einen angemessenen Kompromiss aus Aufwand und Nutzen dar und lässt sich praktisch an beliebigen Geräten implementieren.

### 1.3.1 Kognitives Vorgehen

Das kognitive Vorgehen findet an herkömmlichen MRT-Systemen breite Anwendung und kommt ohne größere Vorbereitungen bzw. Hilfsmittel aus. Die Intervention wird in der Regel *iterativ* geführt [34]. Dabei wird der MR-Tisch nach Aufnahme der initialen Planungsbilder wieder aus dem Magneten gefahren, um den Eingriff direkt am Patienten durchzuführen. Abhängig von den anatomischen Verhältnissen – Lage des Befundes, Zugangsweg und mögliche Risikostrukturen – wird dann die Nadel unterschiedlich weit vorgeschoben. Die bildgebende Kontrolle findet wieder im Gerät statt. Solange sich die Nadel noch nicht in der Zielregion befindet, erfolgt eine weitere *Iteration*.

Die auf den MR-Bildern erkennbaren Strukturen und deren Lage werden lediglich kognitiv auf die räumlichen Verhältnisse am Patienten übertragen. Zur genaueren Festlegung eines Nadeleintrittspunkts wird häufig noch ein MR-sichtbares Objekt auf der Haut befestigt [35], z. B. eine wasser- bzw. ölhaltige Weichkapsel oder ein kommerzieller MR-Marker. Nach Wahl eines möglichen Nadelwegs auf den Planungsbildern lässt sich dann der Hautmarker entsprechend positionieren. Die räumliche Ausrichtung der Nadel entlang des geplanten Zugangswegs erfolgt dann wieder kognitiv.

### 1.3.2 Bildgebende Steuerung

Bei der bildgebenden Steuerung erfolgt die Manipulation der Nadel unter fortlaufender MRT-Bildgebung *im Magneten*, d. h. der Patient muss nicht unbedingt bewegt werden (**Abb. 3**). Gleichzeitig bietet dieses Verfahren die besten Kontrollmöglichkeiten [36–38]. Aus zeitlichen Gründen werden jedoch oft nur einzelne Schichten akquiriert. Abhängig von der Art der Überlappung stellt sich die Nadel auf den dynamischen Bildern als punktförmiges oder längliches MR-Artefakt dar [39]. Mehrere MRT-Hersteller bieten graphisch orientierte Softwareschnittstellen an [40–44], welche den Nutzer bei der interaktiven Festlegung der jeweiligen Schichtebene unterstützen. Aufgrund der fortlaufenden Bildgebung wird das Verfahren vereinfachend auch als *MR-Fluoroskopie* bezeichnet, wobei die Bildfrequenzen deutlich niedriger als bei der namensgebenden *Röntgen-Fluoroskopie* sind.





**Abb. 3** Beispiele für MRT-gestützte Interventionen mit einer interaktiven, bildgebenden Steuerung **Links:** Operateur bei einer Leberintervention in einem seitlich offenen MRT-System (*Panorama 1.0T HFO*, Philips Healthcare, Best, Niederlande). Bild freundlicherweise zur Verfügung gestellt von Philips Healthcare und der Klinik für Radiologie des Universitätsklinikums Magdeburg. **Rechts:** Nadelvorschub in der Leber mit ausgestrecktem Arm des Operators an einem sehr kurzen (125 cm), geschlossenen *wide-bore* (70 cm) MRT. Reproduziert aus [37] mit Erlaubnis von *John Wiley and Sons*.

Neben der direkten bildgebenden Kontrolle des Nadelvorschubs ermöglicht die MR-Fluoroskopie auch die Berücksichtigung mechanischer oder physiologischer Gewebeverschiebungen. Dadurch eignet sie sich besonders für Eingriffe in bewegten Organen wie z. B. der Leber (**Abb. 3**). Wird dann noch die jeweilige räumliche Nadelposition automatisch über ein vorhandenes Tracking-System erfasst, so bräuchte die geometrische Ebene der MR-Aufnahmen – z. B. senkrecht oder entlang der Nadelrichtung – nicht mehr manuell nachgeführt werden [29, 43, 45]. Funktionell ähnelt eine solche MR-Variante dann einer Ultraschall-Bildgebung mit hohem Weichteilkontrast aber deutlich geringer Bildwiederholfrequenz.

Ein wesentlicher Nachteil der MR-Fluoroskopie ist die Bedingung, dass die Nadel innerhalb des MRT-Bildgebungsvolumens geführt werden muss, welches sich vom geometrischen Mittelpunkt des Magneten (Isozentrum) aus über einen Radius von etwa 25 cm erstreckt. Für Interventionen kommen daher praktisch nur sehr kurze röhrenförmige Systeme [37, 46, 47] oder offene Magneten mit einem seitlichen Zugang in Frage (**Abb. 3**). Ferner geht die notwendige Kürze der Datenakquisition häufig mit einer verminderten Bildqualität einher. Als Kompromiss wird oft eine größere Schichtdicke gewählt, die ihrerseits eine schlechtere räumliche Zuordnung mit sich bringt.

### 1.3.3 Stereotaktische Führung

Die Stereotaxie ist ein etabliertes Konzept in der computer-assistierten Chirurgie [48] mit Schwerpunkten im Bereich des Kopfes (Gehirn, Schädelbasis) [49] und der Wirbelsäule [50]. Bei der Konfiguration der Komponenten für eine MRT-Umgebung müssen Wechselwirkungen mit dem statischen Magnetfeld oder den gepulsten Hochfrequenzfeldern jedoch ausgeschlossen werden. Stereotaktische Führungssysteme sind an geschlossenen Systemen weit verbreitet und ermöglichen dort ein gezielteres Vorgehen im Vergleich mit einer rein kognitiven Übertragung. Die Intervention erfolgt ebenfalls auf *iterative* Weise, d. h. mit Nadelmanipulation *außerhalb des Magneten*. Dafür lassen sich stereotaktische Systeme prinzipiell an beliebigen MRT-Geräten – auch offenen – implementieren.

Wie bei konventionellen Operationen lassen sich *rahmenbasierte* und *rahmenlose* Stereotaxie unterscheiden. Bei der ersten Variante gibt ein Rahmen bzw. allgemein ein Führungssystem die möglichen Eintrittspunkte und Einstellungen des Instruments vor. Bei Mamma-Interventionen kommt z. B. ein rechteckiges Raster (engl. *grid*) zum Einsatz während bei transrektalen Prostata-Interventionen ein passives Führungssystem die genaue Positionierung bzw. Ausrichtung einer Führungshülse ermöglicht (**Abb. 2**). Die tatsächliche Position der eingeführten Nadel wird dann anhand einer MRT-Aufnahme kontrolliert. Bei der rahmenlosen Stereotaxie wird das Instrument selbst geortet, z. B. durch ein optisches Trackingsystem. Dies bietet dann die Möglichkeit, aus einem zuvor erhobenen 3D-Datensatz die entsprechende MR-Schicht zu reformatieren und so zur Ausrichtung und Führung des Instruments zu nutzen. In der Neurochirurgie wird dieses Prinzip seit vielen Jahren im Rahmen der sogenannten *Neuronavigation* eingesetzt [51]. Naturgemäß sollten bei allen stereotaktischen Verfahren die betreffende Organregion und die Referenzpunkte möglichst unbewegt bleiben.

## 1.4 Registrierung stereotaktischer Systeme

Im Gegensatz zur kognitiven Übertragung kann bei einem stereotaktischen System die Planung bzw. Orientierung auf den MR-Bildern selbst erfolgen. Dies erfordert eine möglichst genaue Kenntnis der Umrechnungsvorschrift (*math.*: Transformationsmatrix) zwischen MR-Bildkoordinaten einerseits und den realen Koordinaten bzw. Einstellungen am jeweiligen Führungssystem andererseits. Die Bestimmung dieser Transformation nennt sich Registrierung.

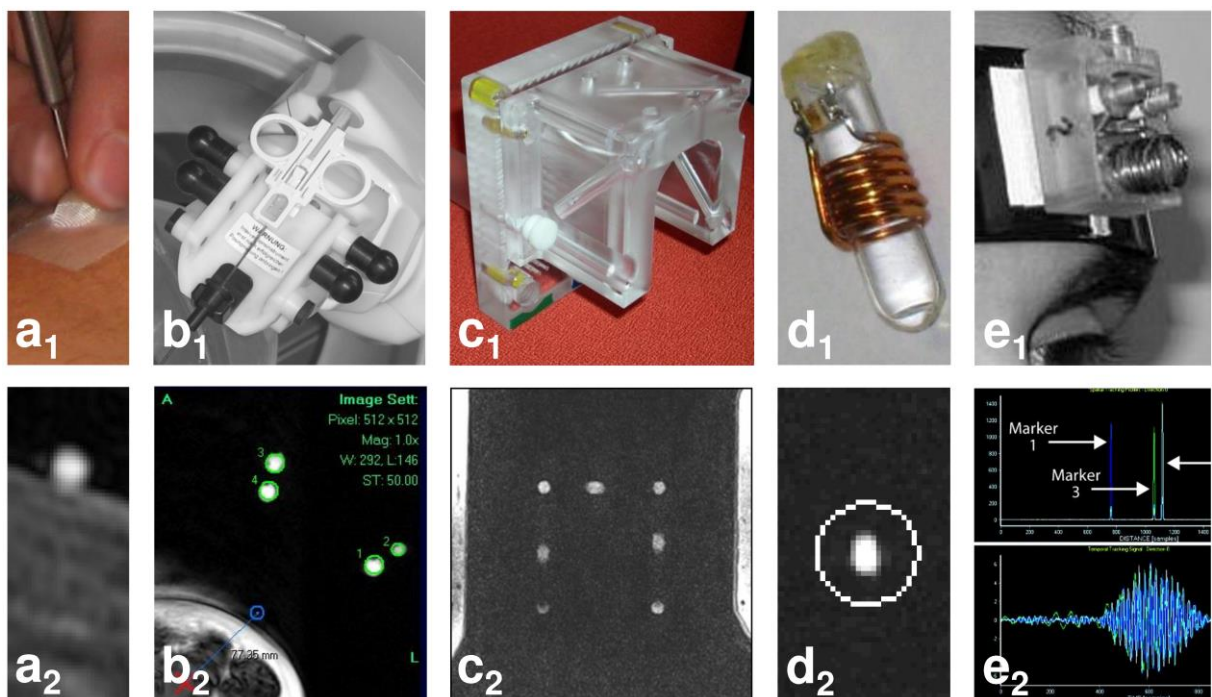


**Abb. 4** Beispiele unterschiedlicher MR-Marker ( $a_1$ – $e_1$ ) sowie deren MR-Darstellung ( $a_2$ – $e_2$ ). **a:** Herkömmliche Nitroglycerin-Weichkapsel und  $T_1$ -gewichtete Aufnahme. **b:** Mit Kontrastmittel (KM) gefüllte Kugelmarker eines robotischen Assistenzsystems (*Innomotion*, Innomedic GmbH, Karlsruhe) und Detektion auf manuell positionierter MRT-Aufnahme. **c:** 3D-Anordnung von sieben KM-gefüllten Glasröhren und räumliche Lokalisation auf Basis der geometrischen Anschnitte im MR-Bild (z-frame [52], Bilder freundlicherweise bereit gestellt von Nobuhiko Hata, Harvard Medical School, Boston, USA). **d:** Resonante Miniatur-HF-Spule mit signalgebendem Medium und Darstellung auf MR-Projektionsaufnahme mit sehr kleinem Flipwinkel. **e:** Prototyp und gemessene MR-Signale von drei *aktiven* Markern. Bei aktiver Technik stellen die langen, elektrischen Anschlüsse ein grundsätzliches Sicherheitsrisiko dar [53]. Reproduziert aus [54] mit Erlaubnis von *John Wiley and Sons*.

Zur Registrierung werden in der Regel MR-Referenzobjekte (allgemein: Marker) verwendet, die fest mit dem jeweiligen Führungssystem, z. B. einem Rahmen, verbunden sind. Die 3D-Koordinaten dieser Marker müssen sowohl im *MR-Bildraum* als auch im wirklichen Raum (*Ortsraum*) bestimmt werden. **Abbildung 4** zeigt eine Auswahl unterschiedlicher MR-Markerkonzepte. Im einfachsten Fall werden sogenannte *passive* MR-Marker mit einer

signalgebenden Substanz eingesetzt, die meist eine kurze  $T_1$ -Relaxationszeit aufweist. Solche Marker sind sowohl kommerziell erhältlich wie auch selbst herstellbar, kostengünstig, leicht zu handhaben, unempfindlich und relativ sicher. Im *MR-Bildraum* können sie auf den MR-Bildern markiert (manuell) oder durch eine bildbasierte Analyse der Signalintensitäten (automatisch) lokalisiert werden. Speziell bei der automatischen Variante müssen die MR-Schichten oft so platziert werden, dass sich die Signalprofile der Marker zuverlässig darstellen und nicht durch anatomische MR-Signale beeinträchtigt werden. Dies erfordert in der Regel ein Kenntnis von Anzahl, Form und ungefähre Lage der Marker. Im *Ortsraum* kann die Messung durch ein (optisches) Trackingsystem erfolgen. Eine Möglichkeit besteht darin, die MR-Referenzpunkte manuell mit einem optischen Zeiginstrument (*Tracker*) anzufahren und die dazugehörigen räumlichen Positionen zu erfassen [55]. Alternativ können optische Referenzmarker in fester Geometrie zu den MR-Markern angebracht werden, sodass das Trackingsystem die räumliche Lage des Instruments stets relativ zu dieser Referenz erfasst.

## 1.5 Interventionelle Eignung verschiedener MRT-Systeme

Die grundlegenden interventionellen Möglichkeiten an offenen und geschlossenen MRT-Systemen sollen nun kurz am Beispiel der tatsächlich eingesetzten Systeme beschrieben und verglichen werden, konkret für ein spezielles, offenes 0,5-T MRT sowie ein herkömmliches, geschlossenes 1,5-T-System.

### 1.5.1 Geschlossenes MRT-System

Die überwiegende Mehrheit der vorhandenen MRT-Geräte besitzt eine geschlossene, röhrenartige Bauform mit einem Innendurchmesser von entweder 60 cm (*engl.: standard bore*) oder 70 cm (*engl.: wide bore*). Die längliche Bauform resultiert aus der Notwendigkeit, im Inneren einer zylinderförmigen Spulenordnung ein äußerst homogenes Magnetfeld für eine hochwertige MRT-Bildgebung zu erzeugen. Das Bildgebungsvolumen der derzeitigen Geräte erreicht hierbei Durchmesser bis zu 55 cm. Geschlossene Geräte weisen hohe Feldstärken auf – praktisch meist 1,5 T oder 3 T – und stellen den De-facto-Standard für die bildmorphologische und funktionelle MRT-Diagnostik dar. Sämtliche Entwicklungen für eine geschlossene MRT-Umgebung erfolgten hier an einem herkömmlichen 1,5-T-System mit

einem Standard-Durchmesser von 60 cm (*Magnetom Symphony*, Siemens Healthcare, Erlangen).

### 1.5.2 Limitationen geschlossener MRT-Systeme

Für interventionelle Zwecke ist die längliche Bauform eher hinderlich. Bis auf einige wenige Systeme mit sehr kurzen Magnetlängen (*engl.: short bore*) im Bereich von 125 – 150 cm (**Abb. 3 rechts**) ist der Weg von der Geräteabdeckung bis zur Messregion zu lang, um dort ein Instrument am ausgestreckten Arm zu führen. An herkömmlichen Systemen werden Interventionen daher meist *iterativ* durchgeführt. Dabei muss der MR-Tisch für jede Kontrollbildgebung in den Magneten und für die weitere Intervention wieder aus dem Magneten heraus gefahren werden, was ein nahtloses Arbeiten erschwert. Insbesondere bei langen oder diffizilen Nadelwegen kann es außerdem erforderlich werden, die Nadelposition öfters zu kontrollieren [56]. Physiologische Gewebewebewegungen, eine Nadelverbiegung oder eine Gewebeverdrängung können während des Nadelvorschubs nicht unmittelbar berücksichtigt werden. Ferner muss darauf geachtet werden, dass Patient, Interventionswerkzeug und weitere Geräte sicher in den Magneten passen (**Abb . 5**).



**Abb. 5** Illustration der Platzverhältnisse in einem geschlossenen MRT-System mit einem Innendurchmesser von 60 cm. Erkennbar sind der seitlich am Tisch befestigte Gelenkarm mit dem Modul zur Ausrichtung und Halterung eines Interventionswerkzeugs. Mit Hilfe eines Navigationssystems wurde hier bereits perkutan eine Koaxialnadel eingeführt.

### 1.5.3 Offene MRT-Systeme

Die meisten offenen MRT-Systeme besitzen eine biplanare Magnetkonfiguration und sind seitlich mehr oder weniger offen [36, 57–61]. Diese Geräte bieten allgemein einen größeren Patientenkomfort und lassen sich auch gezielt für Untersuchungen in speziellen Körper- oder Gelenkpositionen [62, 63] sowie bei klaustrophobischen [64, 65] Patienten einsetzen. Bei

Interventionen kann sich der Operateur in den schmalen, horizontalen Spalt zwischen den Polschuhen begeben und so seitlich an den Patienten gelangen (**Abb. 3, links**). Moderne offene Systeme weisen Feldstärken im Hochfeldbereich auf, z. B. 1,0 T oder 1,2 T, tendenziell sind die diagnostischen Möglichkeiten jedoch eingeschränkt und die anfallenden Kosten relativ hoch.

#### 1.5.4 Intraoperatives MRT-System

Mitte der 1990er Jahre wurde ein spezielles, vertikal offenes System vorgestellt (*Signa SP/i*, GE Healthcare, Waukesha, USA), an dem erstmalig ein aufrechtes Arbeiten am Patienten möglich war [66]. Aufgrund der Möglichkeiten wurde dieses System auch als *intraoperatives MRT* bezeichnet. Das erste Gerät dieses 0,5-T-Systems wurde 1994 in Boston (USA) aufgestellt [67], 1996 erfolgte eine Inbetriebnahme in Leipzig [68] und weltweit kam es zu fast 20 Installationen. Hauptgründe für die Einstellung dieser Bauart waren der überdurchschnittliche technische Aufwand sowie die hohen Gesamtkosten für eine derartige Installation. Dennoch verfügte dieses System bereits über wesentliche Elemente moderner interventioneller Assistenzsysteme.

Das intraoperative System bestand aus zwei vertikalen Magnetelementen, die horizontal versetzt entlang der zylindrischen Symmetrieachse angeordnet waren (**Abb. 6**). Diese Bauform wurde umgangssprachlich auch als *double donut* bezeichnet. Das Bildgebungsvolumen befand sich dadurch im offenen Raum zwischen den Magnetelementen. Der effektiv 58-cm breite Bereich ermöglichte den Ärzten von zwei Seiten aus im Stehen ein weitgehend ungehindertes Arbeiten am Patienten. Das Gerät wurde für minimal-invasive diagnostische, therapeutische und operative Eingriffe von Interventionsradiologen und Chirurgen verschiedener Fachgebiete genutzt [45, 69–73].

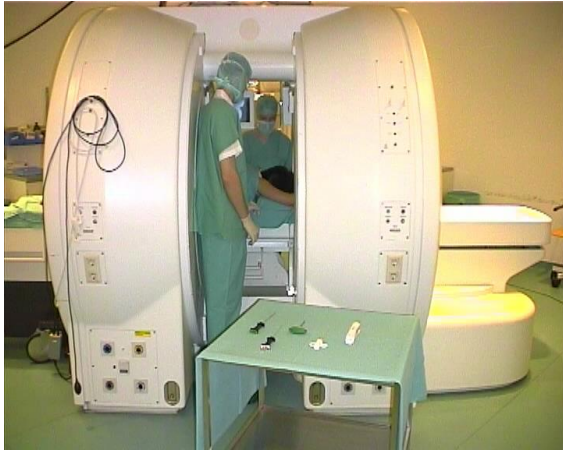


**Abb. 6** Intraoperatives 0,5-T-MRT-System (*Signa SP/i*, GE Healthcare) mit zwei separaten, Magnetelementen. Illustration der speziellen Konfiguration und der räumlichen Verhältnisse im 58-cm breiten Spalt zwischen den Elementen. Etwa auf Augenhöhe befanden sich zwei verstellbare *In-bore*-Monitore (10 Zoll). Die Infrarot-Sensoren eines aktiven Trackingssystems (*FlashPoint*, Image Guided Technologies) waren fest in die obere Verbindung eingebaut worden.

Im Gegensatz zum *iterativen* Vorgehen musste der Patient während der Intervention nicht bewegt werden, da Eingriff und Bildgebung in der gleichen Position stattfanden. Das MRT-Gerät verfügte bereits ab Werk über ein System zur Echtzeitverfolgung des Operationsinstruments (*FlashPoint*, Image Guided Technologies, Boulder, USA). In einem speziellen Scan-Modus konnten fortlaufend MR-Bilder aufgenommen werden, deren Schichtgeometrie automatisch dem Instrument folgte und die auf einem der zwei Monitore angezeigt wurden, die an Gelenkarmen zwischen den Magnethälften (*in bore*) angebracht waren. Auf diesen Bildern stellte sich das Instrument als Artefakt dar, wahlweise über die gesamte Länge oder orthogonal im Anschnitt (**Abb. 7 links**). Diese automatisch nachgeführte MR-Fluoroskopie erlaubte eine unmittelbare und unkomplizierte Kontrolle des Interventionsverlaufs.

### 1.5.5 Spezielle Limitationen

Aufgrund der offenen Bauform und der mittleren Feldstärke waren die Bildgebungsmöglichkeiten des Systems eingeschränkt. Des Weiteren erlaubte die dazugehörige MRT- und Computertechnik noch keine dynamische Bildgebung nach heutigen Maßstäben. So lag die Bildperiodendauer bei etwa 4 s – dies entspricht einer Bildwiederholrate von 0,25 fps (*frames per second*) – und die Bildanzeige erfolgte mit einer Latenzzeit von rund 7 s. Im sogenannten *Real-time*-Modus (MR-Fluoroskopie) war eine Schichtdicke von 10 mm gebräuchlich. Dementsprechend erreichten die *Real-time*-Bilder nicht die Bildqualität bzw. räumliche Auflösung der gewohnten diagnostischen Aufnahmen.

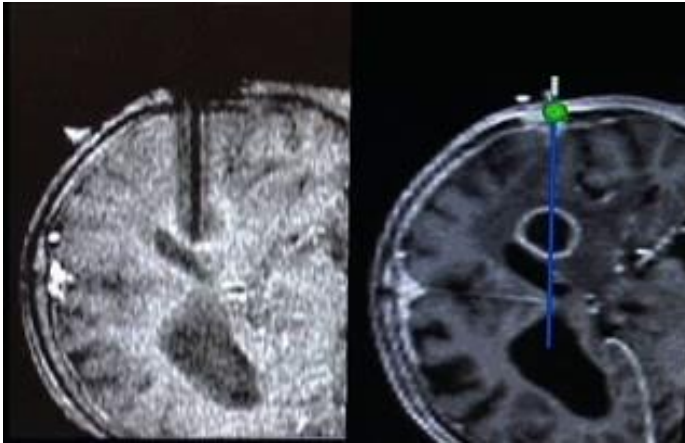


**Abb. 7** Vergleich zweier Navigationsverfahren bei der Biopsie einer Hirnmetastase in einem offenen 0,5-T-MRT. **links:** Einzelbild einer dynamischen Akquisition (etwa alle 4 s, Schichtdicke 10 mm) entlang der kontinuierlich erfassten Nadelrichtung. Gut erkennbar sind das randständige Kontrastmittel-Enhancement sowie das Nadelartefakt. **rechts:** reformatiertes MR-Bild aus dünnem (2 mm) 3D-Datensatz (engl.: *roadmap*) mit Überlagerung der virtuellen Nadeltrajektorie. Aus [74] mit Erlaubnis von *John Wiley and Sons*.

## 1.6 Bereitstellung einer Echtzeit-Navigation

### 1.6.1 Funktionsmerkmale

Eine rahmenlose, stereotaktische Hilfe stellt eine Lösung für die Limitationen beider Systeme bereit. Durch eine Echtzeit-Rekonstruktion aus einem zuvor aufgenommenen MRT-Datensatz könnten am offenen System Qualität, Details und Geschwindigkeit der Bilddarstellung verbessert werden. An einem geschlossenen System wäre eine MRT-basierte Zielführung möglich, die zur Vereinheitlichung und Sicherheit der Maßnahmen beitragen könnte. Diese Navigation ist vom Prinzip her der Neuronavigation ähnlich und wird im Folgenden auch als *Echtzeit-Navigation* bezeichnet, um sie von der fortlaufenden, *bildgebenden* Steuerung (MR-Fluoroskopie) zu unterscheiden.

Bei dieser Navigation orientiert sich der Operateur anhand von reformatierten MRT-Bildern, deren Geometrie sich fortlaufend an die räumliche Lage der Nadel anpasst (**Abb. 7 rechts**). Die Visualisierung kann sich wahlweise an der Nadelachse (parallel oder senkrecht) oder den radiologischen Standardebenen (koronal, sagittal oder axial) orientieren. Der als Referenz dienende, statische MRT-Datensatz (engl.: *roadmap*) sollte möglichst kurz zuvor erhoben worden sein und ausreichend Bildinformationen über anatomische Zielregion, Zugangsweg und mögliche Risikostrukturen beinhalten. Vor und während der Punktion kann der Radiologe die Nadelspitze samt virtueller Verlängerung auf einem Bildschirm im MRT-Raum verfolgen. Hierfür kommen z. B. ein Projektionssystem mit einer MR-kompatiblen Leinwand oder ein entsprechender Monitor in Frage.



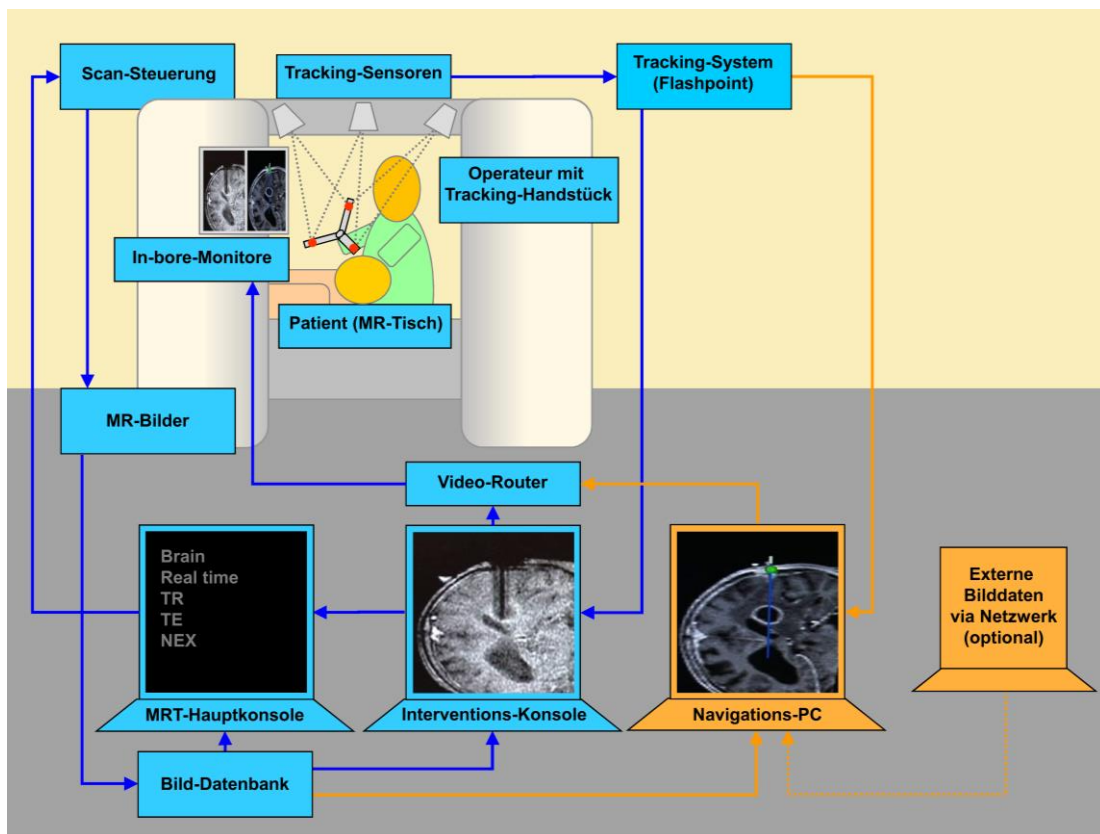


**Abb. 8** Schematische Übersicht der Navigationsmöglichkeiten an einem offenen 0,5-T-MRT-System (*Signa SP/i*, GE Healthcare): werkseigene bildgebende Navigation (blau, GE Healthcare) und zusätzlich implementierte Echtzeit-Navigation (orange, *iMRI Navigator*, Localite GmbH, St. Augustin). Modifiziert aus [79] mit Erlaubnis von *John Wiley and Sons*.

Eine schematische Übersicht der Navigationsmöglichkeiten am *offenen* 0,5-T-MRT ist in **Abb. 8** dargestellt. **Abbildung 9** illustriert beispielhaft das interventionelle Vorgehen am *geschlossenen* 1,5-T-MRT. Der Screenshot einer navigierten Biopsie ist in **Abb. 10** dargestellt.

Wie bei allen stereotaktischen Verfahren besteht auch hier die Limitation, dass sich die anatomischen Verhältnisse seit der Referenzaufnahme geändert haben können, z. B. bei Gewebeverschiebungen durch Nadelvorschub, Organmotilität oder Patientenbewegung. Um derartige Fehlerquellen zu minimieren, sollte der Patient entsprechend aufgeklärt und die Zielregion gegebenenfalls immobilisiert werden.

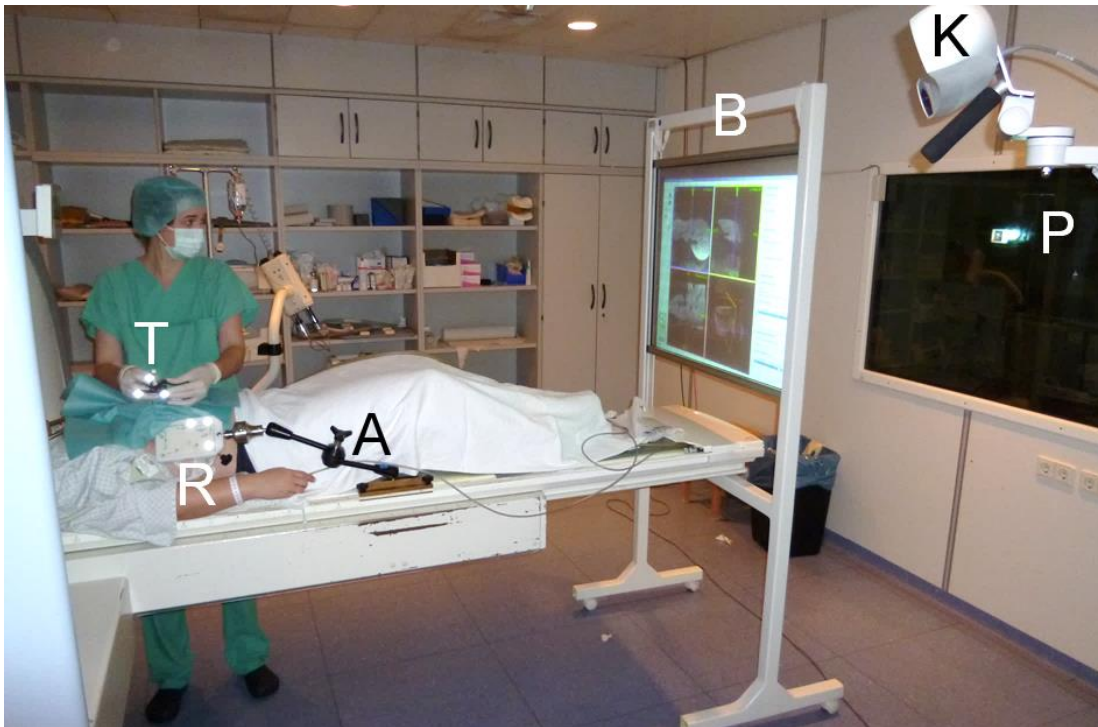


**Abb. 9** Echtzeit-Navigation einer Leberbiopsie an einem geschlossenen 1,5-T-MRT. T: Tracker (für Nadel), R: Referenzplatte, A: Gelenkarm, B: Bildschirm, K: Kamera (Tracking) und P: LCD-Projektor (hinter Glasscheibe)

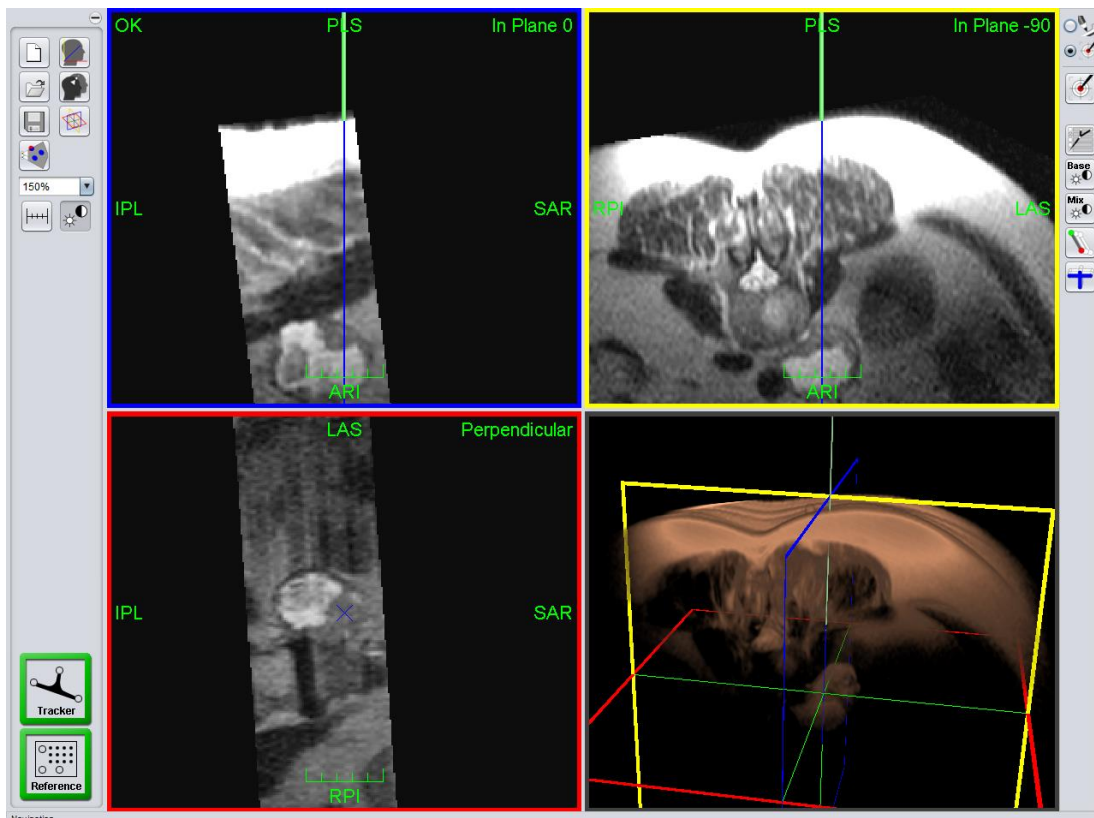


**Abb. 10** Screenshot einer navigierten Biopsie mit drei orthogonalen, reformatierten MR-Ansichten (schnelle T2-gewichtete Sequenz) entlang der optisch in Echtzeit verfolgten Nadellänge (*In Plane 0 und -90*) bzw. senkrecht dazu (*perpendicular*). Das Ziel war in diesem Beispiel der solide Anteil einer para-aortalen, infrarenalen Lymphknotenschwellung. Aus [75] mit Erlaubnis von *Wolters Kluwer Health, Inc.*

## 1.6.2 Technische Anforderungen

Generell ist für eine Echtzeit-Navigation das Zusammenspiel dreier Subsysteme erforderlich, die hier verkürzt mit *Tracking*, *Registrierung* und *Steuerung* bezeichnet werden sollen. Das *Tracking* dient der Echtzeit-Verfolgung der räumlichen Lage des Instruments (3D-Position und Ausrichtung), die *Registrierung* ist für die akkurate Umrechnung der räumlichen Koordinaten auf die MR-Bilder erforderlich und die *Steuerung* steht für die zentrale Bedieneinheit, die eine gezielte Planung auf MRT-Bildern erlaubt und während der eigentlichen Navigation aus den eingehenden Tracking-Informationen die registrierten MR-Schichten rekonstruiert und im MRT-Raum darstellt.

## 2. Zusammenfassende Darstellung

---

Übergeordnete Zielsetzung war die Bereitstellung einer Echtzeit-Navigationstechnik für MRT-gesteuerte, minimal-invasive Eingriffe. Die dazugehörige Technik sollte modular aufgebaut sein, sich nahtlos in eine vorhandene MRT-Umgebung integrieren lassen und flexibel einsetzbar sein. Die Entwicklungen umfassen vollwertige Installationen in zwei unterschiedlichen MRT-Umgebungen mit spezifischen Vor- und Nachteilen.

Die erste Umgebung war ein spezielles, offenes MRT-System, bei dem die intraoperative Navigation – auf Basis einer automatisch nachgeführten MR-Fluoroskopie – ein zentrales Element des interventionellen bzw. chirurgischen Vorgehens darstellte. Die dafür erforderliche Hard- und Software waren bereits Bestandteile des Systems (**Abb. 8**). Das *Tracking* basierte auf einem aktiven optischen Verfahren mit fest oberhalb des Operationsbereichs angebrachten Infrarot-Detektoren (*FlashPoint-System*). Die starre Messgeometrie kam daher einer universellen *Registrierung* gleich, sodass ein entscheidender, sonst aufwändiger, patientenspezifischer Arbeitsschritt entfiel. Die *Steuerung* erfolgte über eine Software des Herstellers an einer Satellitenkonsole (UNIX-*Workstation*) des MRT-Systems.

In diese Umgebung wurde nun *zusätzlich* die Echtzeit-Navigation implementiert, um dem Nutzer eine Navigationsoption anzubieten, die nicht die Nachteile der vorhandenen intraoperativen Navigation – geringe Bildwiederholrate, Latenz sowie moderate Qualität – aufweist (**Arbeit 1**). Zur Echtzeit-Verfolgung konnte das vorhandene *Tracking-System* genutzt werden, welches die Instrumentenkoordinaten bereits in *registrierter* Form bereitstellte. Als Workstation kam ein separater PC mit einer eigens erstellten Anwendungssoftware zum Einsatz, der über Schnittstellen mit dem MRT-System verbunden war. Diese Navigationsplattform (*iMRI Navigator*, Localite GmbH, St. Augustin) entstand in einer Zusammenarbeit von Entwicklern und Anwendern aus verschiedenen Einrichtungen (Localite, GMD-Forschungszentrum Informationstechnik St. Augustin, Klinikum Krefeld, Universitätsklinikum Leipzig).

Nach erfolgreicher technischer Umsetzung sowie den wertvollen praktischen Erfahrungen mit dieser speziellen Installation war es naheliegend, die Echtzeit-Navigation auch für ein herkömmliches diagnostisches MRT-System verfügbar zu machen. Dieses Navigationssystem sollte den folgenden Anforderungen genügen:

- Umsetzung an röhrenförmigem MRT-System mit minimalem Durchmesser von 60 cm
- MRT wird primär diagnostisch betrieben und bei Bedarf für Interventionen umgerüstet
- Anwendung für perkutane Interventionen in praktisch allen Körperbereichen

Aus technischer Sicht musste zunächst ein geeignetes *Tracking*-System für ein herkömmliches MRT-System gefunden werden – die Wahl fiel hierbei auf ein kommerzielles optisches System mit passiven, reflektierenden Markern (*Polaris Spectra*, NDI, Waterloo, Kanada, **Abb. 2 rechts**) und erweitertem Messvolumen (Entfernung bis 3 m). Zur *Steuerung* diente ein PC mit passenden Schnittstellen zum *Tracking*- und zum MRT-System. Die dazugehörige Software war eine Weiterentwicklung der vorhandenen *Localite*-Module aus der Installation am offenen System. Diese Anpassungen profitierten dabei auch vom stetigen Fortschritt der Computertechnik.

Für die Registrierung stereotaktischer Systeme sind *passive* MR-Marker weit verbreitet. Für eine 3D-Lokalisation müssen die MR-Schichten jedoch oft so platziert werden, dass sich die Signalprofile zuverlässig ohne größere anatomische Überlagerungen darstellen. Dies ist durchaus vertretbar, wenn die Marker in einem grob definierten Bereich liegen wie z. B. bei Mamma- oder Prostata-Interventionen. Für eine Anwendung in praktisch beliebigen Körperbereichen ergäbe sich jedoch ein merklicher Mehraufwand. Daher wurde eine äußerst flexible, vollautomatische Marker-Technik entwickelt (**Arbeit 2**), die nur wenig Platz einnimmt. Dabei wird ein bekanntes Prinzip zur MR-Signalerzeugung [76, 77] mit einer eigens entwickelten Methode zur 3D-Lokalisierung kombiniert. Die dazugehörigen Positionsmarker werden auch als *semiaktiv* bezeichnet (**Abb. 4d**). Das vereinfachte Attribut *flexibel* für diese Lokalisationstechnik umfasst die folgenden Leistungsmerkmale:

- *weiträumiger* Nachweis über großes Messvolumen, z. B. Würfel mit 30 cm Kantenlänge,
- *selektiver* Nachweis, unabhängig von anatomischen Strukturen im Messvolumen,
- *uneingeschränkter* Nachweis, unabhängig von den genauen Markerpositionen sowie
- *paralleler* Nachweis von mehreren Markern.

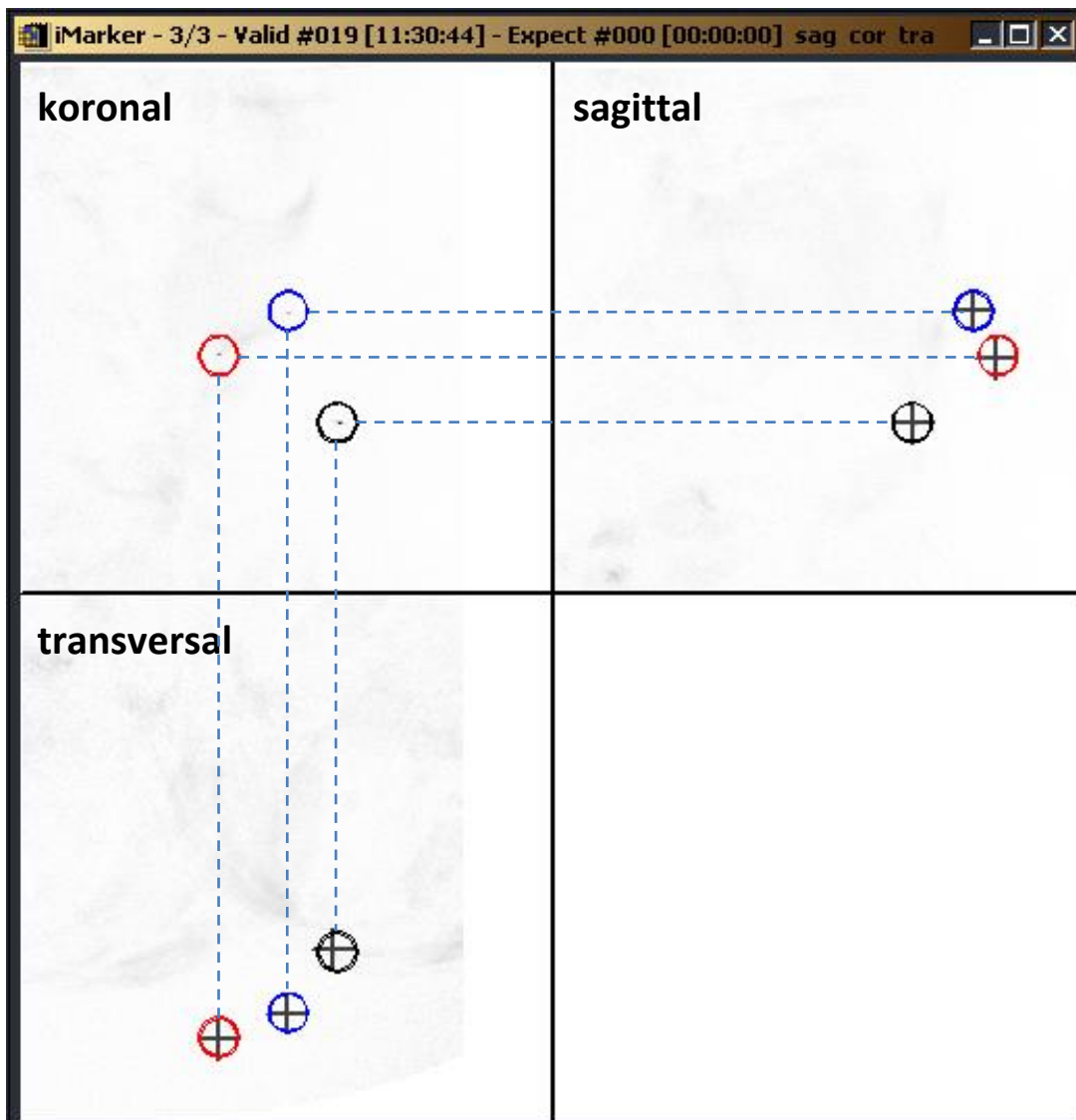


**Abb. 11** Screenshot einer erfolgreichen Lokalisation von drei *semiaktiven* Markern (Registrierung) unter klinischen Bedingungen (Absolute Koordinaten des Marker-Schwerpunkts waren links=146 mm, posterior=179 mm, superior=20 mm). Aufgrund der lokalen Verstärkung der Amplitude der HF-Anregung lassen sich die Marker bei sehr kleinen Flipwinkeln (hier  $1,0^\circ$ ) selektiv über schwachen anatomischen Hintergrundsignalen darstellen (negative Darstellung für bessere Sichtbarkeit). Kreuze zeigen die 2D-Peakpositionen potenzieller Marker in der jeweiligen 2D-Ansicht an und wurden in der koronalen Ansicht zur Darstellung der reinen Markersignale weggelassen. Kreise sind Ergebnisse der Koordinatenanpassung in 3D. Gestrichelte Linien veranschaulichen die Entsprechung der Koordinaten aus unabhängigen Projektionen. Reproduziert aus [78] mit Erlaubnis von *John Wiley and Sons*.

Demnach sind die *semiaktiven* Marker den *passiven* in sämtlichen Merkmalen überlegen. Für einen praktischen Einsatz war es jedoch auch erforderlich, das Signalverhalten der resonanten Marker systematisch unter verschiedenen, klinisch möglichen Bedingungen zu überprüfen (**Arbeit 3**). Die Zuverlässigkeit und Genauigkeit dieser Markerregistrierung, d. h. der parallelen Lokalisation von *drei* Markern (**Abb. 11**), wird unter klinischen Bedingungen sowie am Beispiel einer navigierten Intervention gezeigt (**Arbeit 4**).

Die automatisierte Registrierung, d. h. Bestimmung der Transformation zwischen MR-Bild- und Patientenkoordinaten, erfolgt im Idealfall nur einmal – vor der eigentlichen Navigation – und stellt effektiv eine statische Anwendung der *flexiblen* Marker-Lokalisierung dar. Diese Funktionalität trägt entscheidend zur Genauigkeit der Echtzeit-Navigation wie auch zu einer einheitlichen und nahtlosen Vorgehensweise bei.

Darüber hinaus wird gezeigt (**Arbeit 5**), inwiefern sich die Marker-Technologie auch für eine fortlaufende MR-Lokalisation (*MR-Tracking*) eignet. Perspektivisch könnte dies z. B. zur automatischen Positionsverfolgung bzw. Schichtauswahl bei Interventionen oder zur Bewegungskorrektur bei der diagnostischen Bildgebung genutzt werden. Im Gegensatz zur *flexiblen* Registrierung für die Echtzeit-Navigation sind die vorgestellten Ergebnisse zum dynamischen MR-Tracking experimenteller Natur.

Ein navigiertes Vorgehen stellt in der Regel eine Abweichung von einer einfachen kognitiven Übertragung dar und erfordert zusätzliche Arbeitsschritte, die trainiert werden sollten. In einer umfangreichen experimentellen Studie wurde daher untersucht, inwiefern sich Trefferquoten, Interventionszeiten und subjektive Bewertung zwischen unterschiedlich erfahrenen Anwendern unterscheiden (**Arbeit 6**). Hierbei zeigten sich zwar signifikante Unterschiede in den Interventionszeiten, nicht jedoch in den Trefferquoten.

Abschließend werden verschiedene Navigationstechniken für einen konkreten Anwendungsbereich – muskuloskelettale Interventionen – miteinander verglichen (**Arbeit 7**). Trotz der Besonderheiten eines stereotaktischen Verfahrens, dem Fehlen einer echten bildgebenden Führung und damit der Anfälligkeit für Bewegungen, spricht die universelle Einsetzbarkeit für eine weitere Verbreitung dieser Technologie.

Neben der technischen und klinischen Genauigkeit sowie der Sicherheit solcher Navigationskonzepte liegen wesentliche Herausforderungen für eine breitere Anwendung in der nahtlosen Integration, der einfachen Bedienung, dem Kosten-Nutzen-Faktor und der entsprechenden klinischen Validierung. In diesem Sinne liefert die vorliegende Arbeit eine umfassende Charakterisierung und Bewertung einer vielversprechenden Technologie für MRT-gestützte Interventionen in nahezu beliebigen Körperregionen.

## Originalarbeiten

---

### Arbeit 1 – Implementation einer Echtzeit-Navigation an einem offenen MRT

Die einleitende Arbeit [79] beschreibt die Implementation einer Echtzeit-Navigation an einem speziellen, offenen MRT-System. Zunächst werden der grundlegende Aufbau und die systemeigene Navigation auf Basis einer intraoperativen Bildgebung vorgestellt. Hierbei passte sich die Geometrie der fortlaufenden MR-Bilder automatisch der vom Tracking-System erfassten Instrumentenlage an. Zu den Nachteilen dieses Navigationsverfahren zählten die niedrige Bildqualität, geringe Wiederholrate (0,25 fps) und merkliche Latenz (7 s).

Der Lösungsansatz bestand darin, die höherwertigen Bildinformationen eines dünnenschichtigen diagnostischen Datensatzes für eine erweiterte (*engl.: advanced*) Navigation zu nutzen. Dieser sollte wahlweise vom intraoperativen MRT selbst oder aus einer präoperativen, diagnostischen MRT-Untersuchung – in der Regel bei 1,5 T – stammen [80]. Für die externe Zuspiegelung musste das Navigationssystem vorab eine Registrierung der präoperativen auf die intraoperativen Bilder erlauben. Damit ließen sich optional auch weitere präoperative Daten, z. B. aus funktionellen BOLD (*blood oxygen level dependent*)-Untersuchungen in die Navigation einbinden.

Im Hauptteil der Arbeit werden die Einbindung der neuen Komponenten in die vorhandene Hardware sowie der Arbeitsablauf der erweiterten Navigation (*iMRI Navigator*, Localite GmbH, St. Augustin) beschrieben. Die erfolgreiche CE-Kennzeichnung erleichterte den interventionellen Einsatz des Systems. Im Echtzeit-Modus nutzte das PC-basierte System die anfallenden *Tracking*-Daten zur Reformatierung der interaktiven MRT-Ansichten, die auf einem der *In-bore*-Monitore, auch parallel zu den dynamischen MR-Bildern, angezeigt werden konnten. Das neue System machte sich die vorhandene *Tracking*-Technik zu Nutze, insbesondere die Instrumenten-Handstücke mit den aktiven Infrarot-LEDs, die Infrarot-Detektoren (stereoskopische Kamera) sowie die dazugehörige Digitalisier-Software. Im Ergebnis erlaubte erst die Echtzeit-Navigation eine interventionelle Auge-Hand-Koordination mit hoher Wiederholrate (4 fps) und ohne Latenz.



Nach der technisch-methodischen Beschreibung werden im zweiten Teil retrospektiv MRT-navigierte Eingriffe im Gehirn ausgewertet. Über einen Zeitraum von dreieinhalb Jahren konnten hierfür fast 100 Fälle – 64 Tumorresektionen und 31 Biopsien – eingeschlossen werden, die von drei Neurochirurgen mit beiden Verfahren navigiert wurden. Hierbei lieferte die Echtzeit-Navigation qualitativ hochwertigere Bilder, erlaubte eine komfortable Auge-Hand-Koordination und ermöglichte ferner die Integration wertvoller präoperativer Bildinformationen. Im Vergleich mit der rein bildgebenden Navigation schien die Echtzeit-Navigation sogar etwas bessere klinische Ergebnisse zu zeigen (chirurgische Radikalität, Biopsiegenauigkeit sowie neurologisches Outcome nach fMRT-Überlagerung), insbesondere für den primären Operateur, statistisch waren die Unterschiede jedoch nicht signifikant. Dieser Sachverhalt ist für sehr spezielle Eingriffe mit heterogenen Befunden und geringen Fallzahlen nicht unüblich.

## Original Research

# Advanced Approach for Intraoperative MRI Guidance and Potential Benefit for Neurosurgical Applications

Harald Busse, PhD,<sup>1\*</sup> Arno Schmitgen, MIS,<sup>2</sup> Christos Trantakis, MD,<sup>3</sup> Ralf Schober, MD,<sup>4</sup> Thomas Kahn, MD,<sup>1</sup> and Michael Moche, MD<sup>1</sup>

**Purpose:** To present an advanced approach for intraoperative image guidance in an open 0.5 T MRI and to evaluate its effectiveness for neurosurgical interventions by comparison with a dynamic scan-guided localization technique.

**Materials and Methods:** The built-in scan guidance mode relied on successive interactive MRI scans. The additional advanced mode provided real-time navigation based on reformatted high-quality, intraoperatively acquired MR reference data, allowed multimodal image fusion, and used the successive scans of the built-in mode for quick verification of the position only. Analysis involved tumor resections and biopsies in either scan guidance ( $N = 36$ ) or advanced mode ( $N = 59$ ) by the same three neurosurgeons. Technical, surgical, and workflow aspects were compared.

**Results:** The image quality and hand-eye coordination of the advanced approach were improved. While the average extent of resection, neurologic outcome after functional MRI (fMRI) integration, and diagnostic yield appeared to be slightly better under advanced guidance, particularly for the main surgeon, statistical analysis revealed no significant differences. Resection times were comparable, while biopsies took around 30 minutes longer.

**Conclusion:** The presented approach is safe and provides more detailed images and higher navigation speed at the expense of actuality. The surgical outcome achieved with

advanced guidance is (at least) as good as that obtained with dynamic scan guidance.

**Key Words:** intraoperative MRI; image guidance; brain tumor; biopsy; navigation; image fusion

**J. Magn. Reson. Imaging 2006;24:140–151.**

© 2006 Wiley-Liss, Inc.

IMAGE GUIDANCE is becoming increasingly important to improve the effectiveness and safety of surgical interventions. The main advantage of MRI over other modalities is that it combines excellent contrast, multiplanar capabilities, and the absence of ionizing radiation. Various MR-guided approaches involving minimal patient transfer have been pursued successfully, predominantly in the neurosurgical domain (1–18). In a moderate departure from a conventional setting, an interventional MRI (iMRI) environment was built in line with a diagnostic 1.5 T scanner (5), which kept both functional (i.e., functional MRI (fMRI) and perfusion- and diffusion-weighted imaging) and spectroscopic imaging options open. Trajectories can be aligned by a technique called prospective stereotaxy (6). Various sites have worked with an open low-field 0.2 T MR scanner (7–11). One of these sites had explored different layouts of microscope navigation outside and inside the MR room before the open scanner was replaced with a closed high-field unit and a rotating surgical MRI table. Navigation is currently based on an in-room microscope and a ceiling-mounted commercial system (12). The only concept that is truly moving the operating environment into the imaging unit is an open mid-field 0.5 T MR scanner that was designed specifically for image-guided interventions without the need for patient transfer (13,14). In contrast to the more conventional neuronavigation schemes described above, the patient does not have to be registered, because an instrument tracking subsystem allows the MR scan planes to be selected directly at the patient.

In a previous study Schneider et al (18) evaluated the effectiveness of the system's intraoperative MRI guidance for achieving gross-total resection of low-grade gliomas. They found that at the point where the neuro-

<sup>1</sup>Department of Diagnostic and Interventional Radiology, Leipzig University Hospital, Leipzig, Germany.

<sup>2</sup>Fraunhofer Institute of Applied Information Technology, St. Augustin, Germany.

<sup>3</sup>Department of Neurosurgery, Leipzig University Hospital, Leipzig, Germany.

<sup>4</sup>Department of Neuropathology, Leipzig University Hospital, Leipzig, Germany.

Arno Schmitgen was a full-time employee of the Fraunhofer Institute of Applied Information Technology until 2004, when he became Executive Director of IT Development of Localite GmbH, a Fraunhofer spin-off.

Presented in part at the 2002 and 2005 Annual Meetings of ISMRM in Honolulu, HI, and Miami Beach, FL, USA, respectively.

\*Address reprint requests to: H.B., Department of Diagnostic Radiology, Leipzig University Hospital, Liebigstr. 20, 04103 Leipzig, Germany. E-mail: busse@medizin.uni-leipzig.de

Received April 11, 2005; Accepted March 21, 2006.

DOI 10.1002/jmri.20597

Published online 31 May 2006 in Wiley InterScience (www.interscience.wiley.com).

surgeon considered the procedure complete by visual inspection alone, eight of 12 patients showed massive residual tumor (i.e., more than 10% of the original tumor volume). It was discussed that intraoperative MRI guidance eliminates some problems caused by the use of preoperative data in frame-based or frameless neuronavigation systems. As a key benefit, all anatomic changes occurring under surgery, in particular brain shift (19), may be detected and corrected for in the same procedure. For some phases of the resection, the built-in "near real-time" scan guidance was considered indispensable.

Although the preliminary results were encouraging, we believe that image guidance during tumor resections may be further improved in two areas: 1) The anatomic mapping of the tumor is not always sufficient to avoid neurologic damage, because the tumor mass may have displaced the eloquent areas. Although fMRI is inferior to intraoperative localization techniques for measuring cortical activity, it is still an improvement over the traditional procedure, is largely accepted, and is also a common feature of conventional neuronavigation systems. 2) In the continuous scanning mode used for navigation, there is a trade-off between spatial and temporal resolution due to the inferior specifications of an open design. This compromises both accurate identification of small and diffuse tumor masses, and hand-eye coordination during navigation. Also, image annotations, such as surgical entry and target points, should be available to the physicians in the MR room.

The purpose of this work was to present an advanced approach to intraoperative guidance in an open MR scanner, discuss its clinical compatibility, and evaluate its performance by a retrospective analysis of neurosurgical applications. Data were analyzed with respect to surgical effectiveness (i.e., extent of resection and diagnostic yield of biopsies), total imaging time requirements, procedural safety, and potential benefit of using supplementary information from fMRI.

## MATERIALS AND METHODS

### *Intraoperative MRI Environment*

Our intraoperative MRI environment featured an open 0.5 T MR scanner (Signa SP/i; GE Healthcare, Milwaukee, WI, USA) and a nonmagnetic, free-floating microscope (SMED-3.1; Studer Medical Engineering, Neuhäusen, Switzerland). Anesthesia was induced in a preparation room adjacent to the MR room. There the patient was also placed on the MRI table with the head tilted to allow optimum access to the brain tumor and imaging near the isocenter. The patient's head was fixed with a carbon-fiber three-pin Mayfield headholder to restrict movement during MRI. Further preparatory steps included the attachment of a flexible transmit-receive imaging coil ( $27 \times 24 \text{ cm}^2$ , Flex 3; GE Healthcare) and sterile draping.

Intraoperative image guidance was based on either a series of two-dimensional MRI scans (a mode included with every Signa SP/i installation, and referred to as "scan guidance") or the real-time display of reformatted high-quality reference data acquired at the time of the

procedure (a mode called "advanced navigation," which requires the add-on of a dedicated navigation system (Localite GmbH, Bonn, Germany)). After the new system had been installed both modes were available at any time during the procedure. After initial testing, though, the surgeons involved in the work preferred to use the advanced approach exclusively because they subjectively considered it to be more convenient and effective for navigation. Nevertheless, navigation steps were still verified by quick serial 2D MRI scans provided by the original mode. Figure 1 schematically shows the main components of our interventional MR scanner and illustrates the operating principle for both image guidance modes.

### *Scan Guidance*

Scan guidance was based on successive MR scans (2D multiplanar fast spoiled gradient-recalled (FSPGR) technique, repetition/echo time (TR/TE) = 30/8 msec, slice thickness = 10.0 mm, FOV =  $24 \times 24 \text{ cm}^2$ , matrix =  $256 \times 256$ , signal average = 1, acquisition time (TA) = 4 seconds) whose planes were interactively selected by the current location and orientation of a handpiece. Three in-bore cameras mounted above the surgical area detected the optical signals from light-emitting diodes on the handpiece.

A subsystem (Flashpoint computer; Image Guided Technologies, Boulder, CO, USA) calculated the 3D position and trajectory vector of the handpiece, and, taking into account the exact geometry with respect to the instrument, communicated the values in magnet coordinates to the interactive workstation. At the workstation the image display and MR acquisition parameters, such as the slice geometry, number of experiments, pointer type, and needle offset, could be changed interactively.

The images were displayed at 0.25 frames per second (fps) and were annotated with the position of the scan plane pointer relative to the anatomy within the FOV. The needle and trajectory were displayed as long-dashed and dotted lines, respectively. Unlike frame-based approaches, this design required no additional image registration because both MR image and tracking data were specified in magnet coordinates. Video output from various displays in the control room could be routed to the in-bore monitors.

### *Advanced Navigation*

Advanced navigation was operated from a PC-based supplementary system (Localite). The application software was programmed in Java on a 32-bit Windows platform. The system had received the CE mark of approval (the European equivalent of FDA approval in the United States) and was thus certified as a medical product. The Localite PC was connected to the Flashpoint computer of the tracking system. The geometric vectors for scan plane control were also continuously fed to the PC. In navigation mode, the three-dimensional reference volume acquired at the time of the procedure was reformatted on the fly. Image annotation was similar to the built-in mode, but also included a display of the

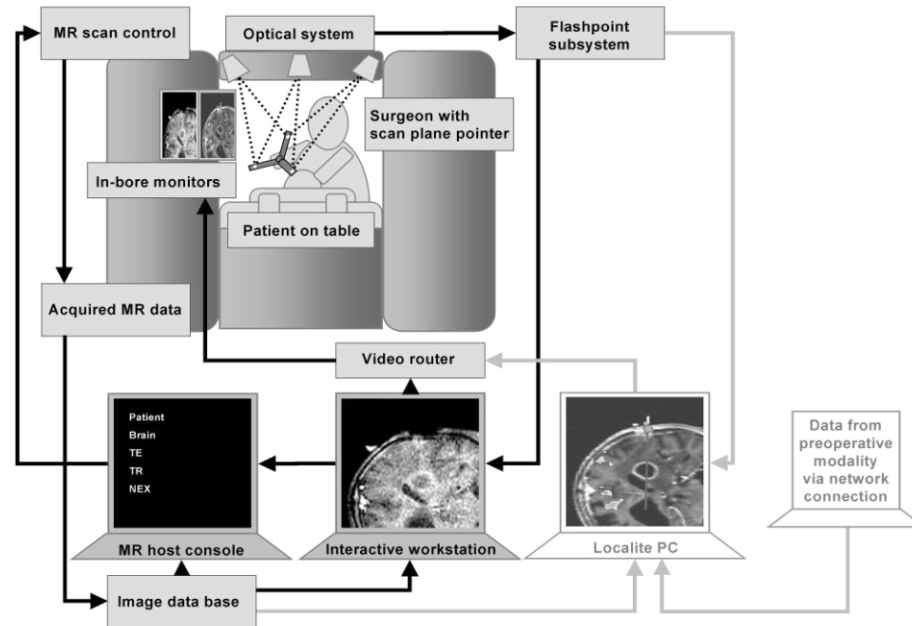


**Figure 1.** Schematic overview of the two interactive guidance modes available on our intraoperative MRI suite. 1) Scan guidance (black arrows): scan plane selection with Flashpoint device at the patient, continuous MR data acquisition, and display of respective MR images on the in-bore monitors. 2) Advanced navigation (gray arrows): reference volume acquisition at the time of the procedure, data transfer to the Localite PC along with optional preoperative data from other modalities (e.g., high-field MRI, fMRI, and CT for image fusion), image registration and planning on the PC, and on-the-fly MR image reconstruction with interactive plane information from the Flashpoint device and real-time display on the in-bore monitor.

time elapsed since reference volume acquisition and whether the scan pointer was in line of sight with the cameras.

The factor that limited the effective display rate to about 4 fps was the relatively slow communication between the optical system and the PC—not the reconstruction algorithm. A command-line tool on the MR host computer was invoked over an Ethernet connection to extract the acquired MR reference data from the host database. This procedure provided safe access to the MR data because it did not interfere with the operation of the host computer; however, it was time-consuming and limited much more by image extraction than by network transfer.

Only one cable to the video router and an additional entry in the control software running on the interactive workstation were needed to display the Localite screen on one of the in-bore monitors. The first reference scan for advanced navigation, typically with T1 weighting (3D FSPGR, TR/TE = 13.3/2.7 msec, 60 slices, thickness/spacing = 2.0/0.0 mm, FOV = 24 × 24 cm<sup>2</sup>, matrix = 256 × 128, signal average = 3, TA = 5:28 min), was acquired to plan the craniotomy or the biopsy trajectory. These data were loaded onto the PC workstation, where they were either directly used for planning or were first fused with selected preoperative image information.

### Image Fusion

If the tumor was located in or near eloquent brain areas, an fMRI investigation was performed to identify the

specific sites of activation. The Localite PC had network access to the export directory at the respective modality. Functional studies were typically conducted one to two days prior to surgery. Unlike morphological data, however, the T2\*-weighted EPI blood oxygen level-dependent (BOLD) data cannot be used reliably for registration due to the lack of anatomical information (20). Therefore, an additional T1-weighted data set was acquired with the patient in exactly the same position. We confirmed the correct co-alignment of T2\*- and T1-weighted volumes visually by inspecting the transition at an adjustable line between functional and morphological image portions of the overlay display. On the day of the intervention, registration involved only the preoperative T1-weighted reference volume and the intraoperatively acquired mid-field MRI data. The resulting transformation parameters were then taken to map the actual BOLD data to the intraoperative MRI data. The fMRI data could not be validated intraoperatively because an MR-compatible stimulator was not available.

Image registration was performed in two ways: In manual mode the user had to identify the position of at least three fiducial markers or anatomical landmarks in both modalities. Rigid transformation parameters were derived from a least-squares error minimization. In semiautomatic mode, the result of a crude manual pre-registration was used as an initial configuration for an automatic minimization algorithm based on mutual information.

In manual mode the software reported the mean difference between the corresponding positions after registration. Such a measurement, however, is of limited value

Table 1  
Summary of Resections Guided by Advanced Navigation

Patient	Sex <sup>b</sup>	Age (years)	Surgeon	Location	Histology (WHO grade)	Volume (mL)	Extent of resection	Time (hours:minute)
01	M	49	A	Left parietal	Glioblastoma (IV)	86.4	Partial	7:55
02	M	46	A	Left frontal	Astrocytoma (II)	15.9	Partial	5:16
03 <sup>a</sup>	F	28	A	Left temporal	Astrocytoma (II), recurrent	82.4	Partial	6:24
04	M	61	A	Right temporal	Glioblastoma (IV)	41.2	Subtotal	3:48
05 <sup>a</sup>	M	24	A	Left frontal	Astrocytoma (I)	2.1	Subtotal	4:47
06 <sup>a</sup>	F	35	A	Left temporal	Glioblastoma (IV), recurrent	58.6	Subtotal	6:23
07	M	49	A	Right parietal	Glioblastoma (IV)	20.1	Subtotal	4:44
08	F	68	A	Right temporal	Glioblastoma (IV)	27.7	Subtotal	5:41
09 <sup>a</sup>	M	64	A	Right parietal	Glioblastoma (IV), recurrent	34.8	Subtotal	4:53
10	F	28	A	Left parietal	Astrocytoma (II)	22.0	Subtotal	5:16
11	M	66	B	Left temporal	Astrocytoma (II)	67.7	Partial	4:59
12	M	43	B	Right temporal	Astrocytoma (III)	222.9	Partial	6:28
13	F	49	B	Right frontal	Gliosarcoma (IV)	86.4	Subtotal	4:11
14	F	69	B	Right frontal	Glioblastoma (IV)	33.0	Subtotal	3:39
15 <sup>a</sup>	M	68	B	Left parietal	Metastasis	23.6	Subtotal	3:43
16	M	69	B	Right temporal	Glioblastoma (IV), recurrent	9.6	Subtotal	3:20
17	M	59	B	Left temporal	Glioblastoma (IV)	51.3	Subtotal	6:15
18	M	32	B	Left frontal	Reactive changes	7.9	Subtotal	3:47
19	M	54	B	Left frontal	Astrocytoma (II)	46.1	Subtotal	4:24
20	F	48	B	Right frontal	Astrocytoma (II)	15.7	Subtotal	5:08
21	M	53	B	Right parietal	Metastasis	0.5	Total	2:47
22 <sup>a</sup>	M	16	B	Left parietal	Meningeoma (II)	5.2	Total	3:14
23 <sup>a</sup>	M	36	B	Left parietal	Astrocytoma (II)	24.7	Total	3:32
24	M	62	B	Left temporal	Glioblastoma (IV), recurrent	25.1	Total	4:05
25 <sup>a</sup>	F	55	B	Left temporal	Necrosis	30.8	Total	6:55
26	F	57	B	Left parietal	Metastasis	15.7	Total	2:48
27 <sup>a</sup>	M	40	B	Right frontal	Astrocytoma (III)	43.2	Total	5:01
28	M	67	B	Right temporal	Metastasis	2.7	Total	3:58
29	M	33	B	Right frontal	Astrocytoma (III), recurrent	8.1	Total	3:50
30 <sup>a</sup>	M	54	B	Right frontal	Metastasis	10.3	Total	4:24
31	F	27	B	Right frontal	Astrocytoma (III)	11.8	Total	5:06
32	M	59	C	Left temporal	Glioblastoma (IV)	20.2	Partial	3:41
33	F	57	C	Left frontal	Glioblastoma (IV)	59.6	Subtotal	5:36
34	F	66	C	Left frontal	Glioblastoma (IV)	10.9	Subtotal	4:57
35	M	56	C	Left frontal	Glioblastoma (IV)	15.7	Subtotal	4:35
36 <sup>a</sup>	M	26	C	Left parietal	Astrocytoma (II)	3.7	Subtotal	5:34
37 <sup>a</sup>	F	45	C	Left temporal	Metastasis	25.7	Subtotal	5:13
38 <sup>a</sup>	M	66	C	Right occipital	Metastasis	32.3	Total	4:25
39 <sup>a</sup>	F	36	C	Right frontal	Astrocytoma (II)	0.5	Total	3:12
40 <sup>a</sup>	M	31	C	Left temporal	Astrocytoma (I)	5.7	Total	4:35
41 <sup>a</sup>	M	75	C	Right frontal	Lymphoma	4.4	Total	2:37
		<b>53</b>				<b>22.0</b>		<b>4:35</b>

\*Bold values for age, tumor volume, and time requirement are the respective medians.

<sup>a</sup>Additional image fusion.

<sup>b</sup>Female = 14 patients; male = 28 patients.

<sup>c</sup>Patient underwent surgical treatment because clinical and imaging findings suggested a glial tumor.

because it is sometimes difficult to identify marker positions or landmarks, and skin markers are subject to shifts. Ultimately, the numerical registration result had to be validated by visual inspection for both modes. For that purpose, a “magic lens” with a view of the preoperative image portion was dragged across the corresponding intraoperative image. As a matter of course, this procedure had to be repeated for various slice positions and orientations.

### Patients

All interventions were approved by the local ethics committee and were performed with the patients’ informed consent. A total of 110 neurosurgical cases from a pe-

riod of about 3.5 years were available. To better compare the effectiveness of scan guidance and advanced navigation, we included only 95 cases from three neurosurgeons who had worked with both modes and performed at least 10 interventions. Patient data for both modes are given in Tables 1–3. The extent of resection was assessed by consensus between the neurosurgeon and radiologist with the help of contrast-enhanced MR control images, and was rated as either total, subtotal, or partial. Subtotal resections were differentiated from partial resections according to whether evidence of residual tumor was equivocal or not. Sixteen of 41 resections were performed with supplementary preoperative information, predominantly BOLD fMRI data.

Table 2  
Summary of Resections Under Scan Guidance\*

Patients	Sex <sup>a</sup>	Age (years)	Surgeon	Location	Histology (WHO grade)	Volume (mL)	Extent of resection	Time (hours:minute)
01	F	61	A	Right temporal	Glioblastoma (IV)	84.9	Subtotal	5:40
02	F	43	A	Left frontal	Astrocytoma (II), recurrent	3.0	Subtotal	5:25
03	F	27	A	Left frontal	Vascular malformation	5.2	Total	3:36
04	F	28	A	Left parietal	Vascular malformation	2.1	Total	4:40
05	M	36	B	Right fronto-parietal	Ependymoma (III)	64.3	Partial	4:55
06	M	74	B	Left occipito-temporal	Abscess	37.7	Partial	2:38
07	M	65	B	Right parieto-occipital	Glioblastoma (IV)	44.5	Partial	3:55
08	M	44	B	Right frontal	Astrocytoma (III)	11.0	Subtotal	5:35
09	F	21	B	Right frontal	Meningeoma (II)	14.1	Subtotal	4:22
10	F	56	B	Right paramedian	Glioblastoma (IV)	4.2	Subtotal	3:37
11	M	30	B	Left temporal	Astrocytoma (II)	6.3	Subtotal	5:30
12	M	61	B	Right parietal	Glioblastoma (IV)	15.9	Subtotal	5:09
13	M	47	B	Left temporal	Glioblastoma (IV), recurrent	41.6	Subtotal	3:55
14	M	59	B	Left frontal	Metastasis	0.5	Subtotal	3:12
15	M	24	B	Right fronto-parietal	Metastasis	1.6	Total	2:35
16	M	45	B	Left temporal	Glioblastoma (IV)	36.7	Total	4:39
17	M	45	B	Left frontal	Glioblastoma (IV)	26.9	Total	4:38
18	M	39	B	Left frontal	Metastasis	1.2	Total	2:27
19	M	45	C	Right temporal	Gliosarcoma (IV), recurrent	13.9	Partial	4:09
20	M	38	C	Left frontal	Astrocytoma (III)	13.7	Subtotal	5:41
21	F	61	C	Left parieto-occipital	Metastasis	8.2	Total	4:17
22	M	72	C	Left frontal	Metastasis	15.7	Total	4:23
23	F	48	C	Right frontal	Glioblastoma (IV)	6.3	Total	3:00
		<b>45</b>				<b>13.7</b>		<b>4:22</b>

\*Bold values for age, tumor volume, and time requirement are the respective medians.

<sup>a</sup>Female = 8 patients; Male = 15 patients.

Generally, data from three surgeons were included to determine the average surgical outcome for both guidance modes. In addition, we analyzed the results of a single surgeon to avoid operator bias. We selected the surgeon with the highest number of cases (surgeon B in Tables 1–3; also called the “main surgeon” in the following) to minimize the impacts of reduced statistical power and individual learning curves, respectively. To analyze the potential benefit of functional information for advanced navigation, we compared 14 cases with supplementary BOLD information with 22 cases under scan guidance. At the time of discharge from the hospital, postoperative neurologic outcome and deficits were rated as worse, the same, or better compared to the preoperative status.

### Statistical Analysis

A Mann-Whitney test was performed to confirm that there were no significant differences in age or tumor volume between corresponding groups. The same test was used to assess possible changes in surgical effectiveness and postoperative neurologic outcome. All proportions are given with the standard error, i.e., the square root of  $p(1-p)/n$ , with proportion  $p$  and sample size  $n$ . Differences in time exposures between both guidance modes were also analyzed with a Mann-Whit-

ney test. The observed times were rounded to the full minute and are given as the median and range. Non-parametric tests were used because of the relatively small samples. All significance levels were set to 0.05 (SPSS Inc., Chicago, IL, USA).

## RESULTS

### Advanced Navigation

For the brain interventions presented here, image fusion involved preoperative data (generally BOLD fMRI data) from a 1.5 T high-field MR scanner only (Siemens Magnetom Vision, Erlangen, Germany). Usually a silent word-generation task (21,22) was performed for critical temporal locations, and a sensorimotor finger-tapping task was performed for frontoparietal tumor locations close to the precentral region. For two low-grade astrocytomas, we also used preoperative high-field T2-weighted data because the respective tumors were relatively small and could not be delineated well with the intraoperative images alone.

In five of the early cases reported, manual image registration was performed with no deterioration in postoperative neurologic status. This method was not very computation-intensive but required an accurate identification of the positions in both data sets. Also,

Table 3  
Summary of Biopsies Under Advanced Navigation (Patients 1–18, n = 18) and Under Scan Guidance (Patients 19–31, n = 13)\*

Patient #	Sex <sup>b</sup>	Age (years)	Surgeon	Location	Histology (WHO grade)	Volume (mL)	Histologic evaluation	Time (hours: minute)
Advanced navigation								
01	M	60	A	Left occipital	PML	29.3	+	2:00
02 <sup>a</sup>	F	25	B	Left temporal	Astrocytoma (I)	51.7	+	4:23
03	F	57	B	Left parietal	Astrocytoma (II)	59.6	+	1:25
04	F	82	B	Left parietal	Glioblastoma (IV)	44.0	+	1:21
05	M	66	B	Left parietal	Glioblastoma (IV)	47.1	+	3:16
06	F	46	B	Bilateral parietal	Glioblastoma (IV)	19.2	+	1:34
07	M	64	B	Left temporal	Metastasis	— <sup>c</sup>	+	2:02
08	F	60	B	Bilateral parietal	Metastasis	4.1	+	2:43
09	M	67	B	Right frontal	Metastasis	1.6	+	1:32
10	M	70	B	Left parietal	Oligodendroglioma (II)	11.8	+	2:05
11	F	70	C	Left temporal	Astrocytoma (I)	16.5	+	1:38
12	F	36	C	Median temporal	Astrocytoma (I)	42.7	+	2:15
13	F	57	C	Right basal ganglia	Astrocytoma (III)	31.8	+	1:34
14	M	55	C	Right basal ganglia	Astrocytoma (III)	0.5	+	2:19
15	M	28	C	Left temporal	Ganglioglioma	0.5	+	2:41
16	F	80	C	Left frontal	Glioblastoma (IV)	18.8	+	2:52
17	F	70	C	Left temporal	Necrosis	25.1	–	2:45
18	M	63	C	Left temporal	No tumor	— <sup>c</sup>	–	4:30
		<b>61.5</b>				<b>22.2</b>		<b>2:10</b>
Scan guidance								
19	M	44	B	Right temporal	Astrocytoma (II)	8.4	+	2:09
20	F	43	B	Right corpus callosum	Astrocytoma (II)	88.0	+	1:32
21	M	41	B	Left frontal	Astrocytoma (II)	22.9	+	2:28
22	M	75	B	Right temporal	Glioblastoma (IV)	1.8	+	1:37
23	M	67	B	Right temporal	Glioblastoma (IV)	91.6	+	1:20
24	F	56	B	Right temporal	Glioblastoma (IV)	3.6	+	1:43
25	M	58	B	Bilateral frontal	Glioblastoma (IV)	36.8	+	1:46
26	F	69	B	Left parieto-occipital	Glioblastoma (IV)	89.7	+	1:36
27	F	34	B	Right temporal	Metastasis	1.6	+	1:38
28	M	54	B	Corpus callosum	Necrosis	31.4	–	1:31
29	F	63	C	Corpus callosum	Glioblastoma (IV)	36.5	+	1:47
30	M	41	C	Left occipital	Necrosis	4.2	–	1:14
31	F	72	C	Right temporal	No tumor	16.5	–	2:04
		<b>56</b>				<b>22.9</b>		<b>1:38</b>

\*Bold values for age, tumor volume, and time requirement are the respective medians for both guidance modes.

<sup>a</sup>Additional image fusion.

<sup>b</sup>Under advanced navigation: Female = 10 patients; Male = 8 patients. Under scan guidance: Female = 6 patients; Male = 7 patients.

<sup>c</sup>Diffuse tumor appearance.

PML = progressive multifocal leucoencephalopathy, + = diagnostic biopsy, – = nondiagnostic biopsy.

the fiducial markers had to be visible in both imaging modalities and had to stick firmly to the head, which was a potential source of error. In contrast, the numerical approach based on mutual information required only a crude identification of anatomical landmarks, but depended largely on computing power. After a hardware upgrade was made, the numerical approach was stable and fast enough, and became the standard for image registration.

The registration result had to be visually inspected because an iterative algorithm does not necessarily converge to the global minimum. In addition, certain structures (e.g., the scalp, neck, and auricles) were subject to shifts, especially between intraoperative scans in a lateral head position and preoperative scans in a supine position. Because of the nonlinear nature of such shifts, the degree of alignment after rigid registration was not necessarily uniform. In such a case, registration was still accepted if devia-

tions occurred only in brain areas that were not affected by surgery.

Figure 2 shows an illustrative case of an fMRI-assisted craniotomy planning for the resection of a glioblastoma multiforme (WHO grade IV) in a 55-year-old female patient. After microsurgical tumor resection, the intraoperative MRI control revealed residual tumor (Fig. 3). After an intraoperative update of the reference data, the residual tumor was successfully targeted and completely resected in advanced mode.

In two cases (a resection under advanced guidance, and a resection under scan guidance) an acute epidural hemorrhage occurred. Both complications were treated surgically the same day. Upon discharge from the hospital, one patient had no additional neurologic deficits, and the condition of the other patient had slightly improved. In cases in which the navigation images did not correspond to the control images, the mismatch was due to an unintentional shift of the patient's head and

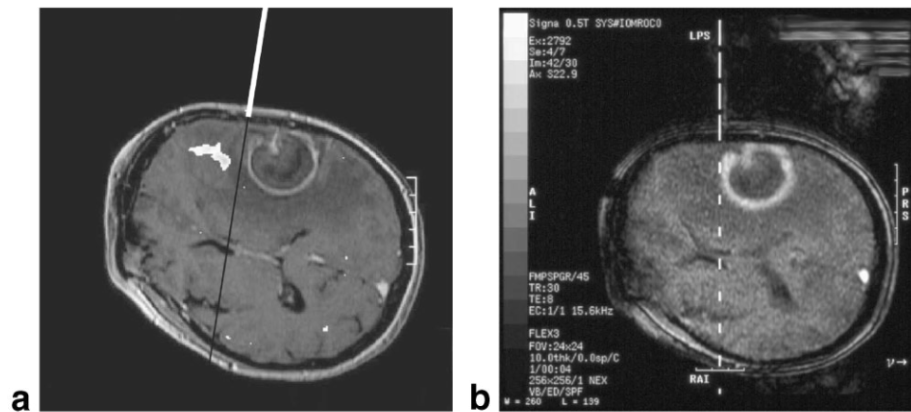


**Figure 2.** Craniotomy planning for the MRI-guided resection of a glioblastoma multiforme (WHO grade IV) in a 55-year-old female patient. The tumor was about 31 mL in size and was located in the temporal lobe of the left hemisphere. **a:** Snapshot during real-time (4 fps) definition of the frontal craniotomy boundary using advanced navigation and overlaid fMRI data (white region) to avoid damage to language functions (slice thickness = 2 mm). **b:** For comparison, an MR image obtained in scan guidance mode is shown. The validity of the virtual planning can be checked in this mode, but three-dimensional information on the eloquent cortex is missing (slice thickness = 10 mm).

required an update of the reference data. Table 4 summarizes the working principles of both guidance modes and their specific pros and cons.

Operation of the Localite system required the intraoperative reference data to be physically loaded onto the PC. Under advanced guidance, this image transfer took around seven minutes for 60 slices, and four minutes for fewer slices (28 or less). The associated average frequencies were 2.1 (60 slices) and 1.2 ( $\leq 28$  slices) for the resections, and 1.2 (60 slices) and 0.6 ( $\leq 28$  slices) for the biopsies. These transfers accounted for almost 20 minutes of the resection time and more than 10 minutes of the biopsy time, and introduced a bias for the comparison of both modes. Therefore, we also calculated “effective” imaging times given by subtracting the individual time delays from the raw time values. Although these effective times are theoretical in nature, they illustrate the potential of the advanced approach

with the original hardware if data-handling were optimized. In comparison with scan guidance, cases with multimodal navigation required extra time for image data fusion. We considered three minutes for the manual pre-registration and 10 minutes for the automatic optimization to be average times, with actual values for the latter ranging from seven to 13 minutes.

### Technical Failures

With the initial PC configuration, a system halt occurred in two cases during the semiautomatic image registration of fMRI data. We believe this complication was due to a critical use of the available PC resources (in particular the limited working memory) because the image registration was completed successfully in both cases after a simple system reboot. A similar cause is suspected for transient reductions of the image display

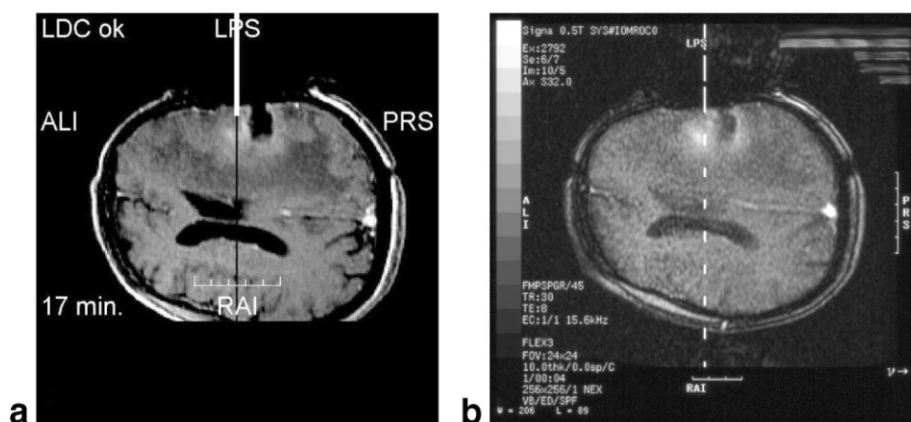


**Figure 3.** Planning of a residual tumor resection in the same patient as in Fig. 2. **a:** Snapshot of the advanced navigation scene. The underlying reference data had to be updated because brain tissue had shifted as a result of the initial resection. Acquisition and transfer of the new reference data took about 12 minutes. Preoperative fMRI data could not be used because it no longer corresponded to the surgical situation. Targeting of the residual tumor was resumed and the mass was completely resected. **b:** Corresponding MR image in scan guidance mode.



Table 4  
Summary and Comparison of Image Guidance Schemes Available in the Open MRI Environment

Mode	Pros	Cons	Equipment
<b>Scan guidance</b> Based on fast successive MR scans	Up-to-date representation of current surgical situation simultaneous display of inserted instruments/artifacts	Trade-off between temporal and spatial resolution slow frame rate (0.25 frames/second), only near real time cumbersome hand-eye coordination delayed image display (7 seconds)	Base system (General Electric); MR scanner (Signa SP/i) with device tracking system (Flashpoint)
<b>Advanced navigation</b> Based on real-time reformatted high resolution MR images	High image quality of 3D reference data fast refresh rate (real time) good hand-eye coordination	Images may reflect outdated surgical situation no display of inserted instruments requires extra time	Navigation PC (Localite) with interfaces to Flashpoint computer, image data base of MR host and video routing system
<b>Optional image fusion</b> Based on real-time virtual fused images	Augmented image information, supported modalities include MRI, fMRI, CT, PET, SPECT	requires extra time	Image fusion module (Localite) with import filter for preoperative modality, registration algorithm, and tool to inspect the result

rate in navigation mode. Since we upgraded the hardware and changed the memory-management software, the system has worked without a technical failure. Because the system was not used for investigational purposes only, product approval required compliance with safety regulations, thorough testing, and maintenance of records, which greatly assisted in ensuring reliable system operation.

### Tumor Resections

With advanced navigation, 15 total (36.6%  $\pm$  7.5%), 20 subtotal (48.8%  $\pm$  7.8%), and six partial (14.6%  $\pm$  5.5%) resections were achieved by all three surgeons. In the reference group with scan guidance, resections were classified as nine total (39.1%  $\pm$  10.2%), 10 subtotal (43.5%  $\pm$  10.3%), and four partial (17.4%  $\pm$  7.9%). This corresponds to an increase by about 5% in subtotal and a decrease by 2.8% in partial and 2.5% in total resections, respectively. These average differences are insignificant ( $P = 0.976$ ), as already suggested by the relatively large standard errors. In the analysis of data from one surgeon only, we found that total resections with advanced navigation were increased (52.4% vs. 28.6%) while both subtotal (38.1% vs. 50.0%) and partial resections (9.5% vs. 21.4%) were decreased (Fig. 4). Although these intraindividual differences appear to be relatively large, they fail to reach statistical significance ( $P = 0.142$ ).

The median time (range) between first and last surgical MR scans under advanced guidance for three neurosurgeons was 4:35 (2:37–7:55) hours, which is 13 minutes longer than that for the scan-guided procedures at 4:22 (2:27–5:41) hours ( $P = 0.351$ , Fig. 5a). For illustration, the distribution of the effective times was also added. At an estimated 4:08 (2:10–7:44) hours, the potential median time associated with the advanced

mode would be 14 minutes less than under scan guidance.

If only data from the main surgeon were included for analysis, the corresponding procedures would require 4:05 (2:47–6:55) hours under advanced and 4:08 (2:27–5:35) hours under scan guidance (Fig. 5b). The potential value of 3:37 (2:15–6:28) illustrates that the novel approach may be very time-effective.

For interventions guided by additional preoperative fMRI information, the postoperative neurologic status improved in 21.4%, was unchanged in 57.1%, and deteriorated in 21.4% of the cases. In comparison with cases guided by morphological data only, the neurologic status was found to be better in 13.6%, the same in 54.5%, and worse in 31.8% of the cases, respectively. A test for differences in neurologic outcome between both groups yielded  $P = 0.426$ .

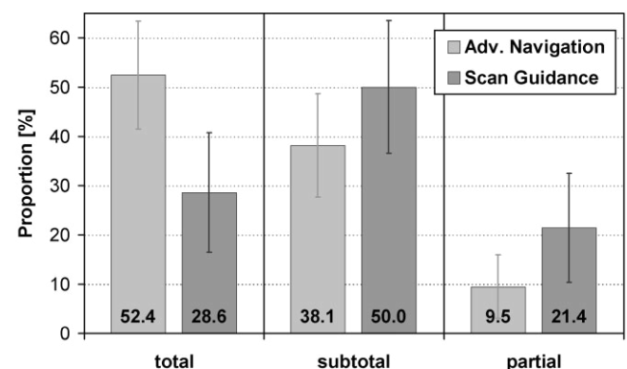


**Figure 4.** Comparison of the extent of resection observed for the main surgeon. Analysis of 21 cases with advanced navigation and 14 cases under scan guidance. Proportions are given along with standard errors.

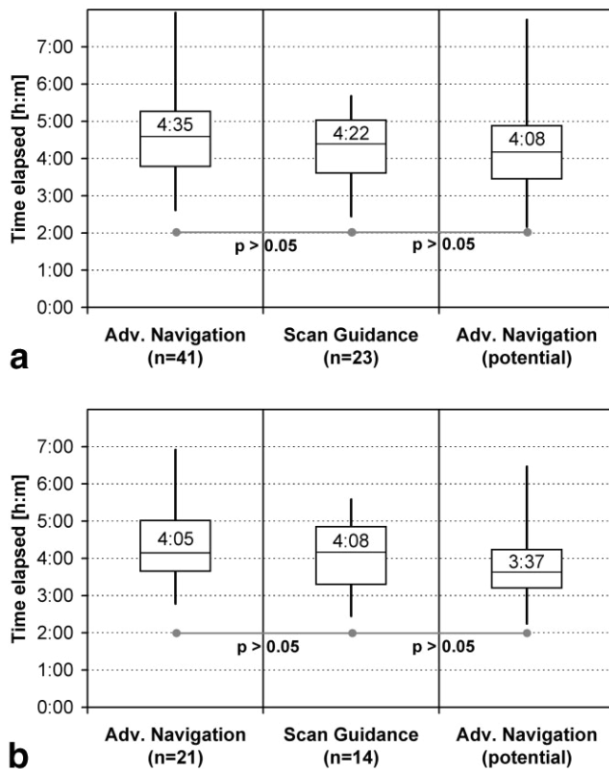


**Figure 5.** Comparison of imaging times recorded for resections performed by (a) three neurosurgeons and (b) only the main surgeon. Whiskers indicate extreme times, and boxes represent upper and lower quartiles, respectively. Potential values were corrected for the time consumed by the constrained data processing.

### Tumor Biopsies

With the advanced approach, 16 out of 18 biopsies (88.9%) were diagnostic; one biopsy yielded necrotic tissue only, another no tumor tissue. With the use of scan guidance, 10 out of 13 biopsies (76.9%) were successful (Fig. 6a). The remaining three revealed no tumor or necrotic tissue only. Despite a higher fraction of diagnostic biopsies with advanced navigation, this difference is not significant ( $P = 0.379$ ), which is also reflected by the size of the standard error bars. Intra-individually, the main surgeon had nine out of 10 diagnostic biopsies under scan guidance (90%) and nine successful biopsies with the advanced approach (100%,  $P = 0.343$ ). Functional MRI data fusion was applied in one case. The comparison of the recorded times between initial and final scans showed that the biopsies with the new approach took 32 minutes longer (2:10 (1:21–4:30) hours vs. 1:38 (1:14–2:28) hours), which was found to be significant (Fig. 6b). After the data-handling times were subtracted, the effective time requirement for the advanced approach was 1:58 (1:14–4:12) hours, an insignificant 20 minutes longer than under scan guidance.

### DISCUSSION

The key to more effective and safer image-guided procedures is to routinely provide the surgeon with the

most adequate and reliable image information readily available. This involves an intuitive planning option, a fast display of high-contrast images during navigation, and a user-friendly way to integrate image information from other modalities or functional studies. We present an approach whereby the quality of the guiding MR images is determined by a 3D acquisition with a relatively high SNR and little partial volume averaging. Although the MR image quality of a 0.5 T mid-field scanner cannot match that of a diagnostic high-field scanner, we considered it sufficient for successful guidance. In particular, the image display was fast enough (4 fps) to permit direct hand-eye coordination during dynamic targeting, which could not be done with the image quality, display rate (0.25 fps), and display delay (about seven seconds) of the provided 2D MRI scans. The intraoperative in-bore display of previously selected marker points was considered to improve surgical orientation. Image fusion with various modalities was stable, user-friendly, and added an average of 13 minutes to the procedure. It is important to note that tests on a recent standard PC showed typical computation times for fMRI registration of less than 90 seconds. Generally, brain shift after tumor resection or

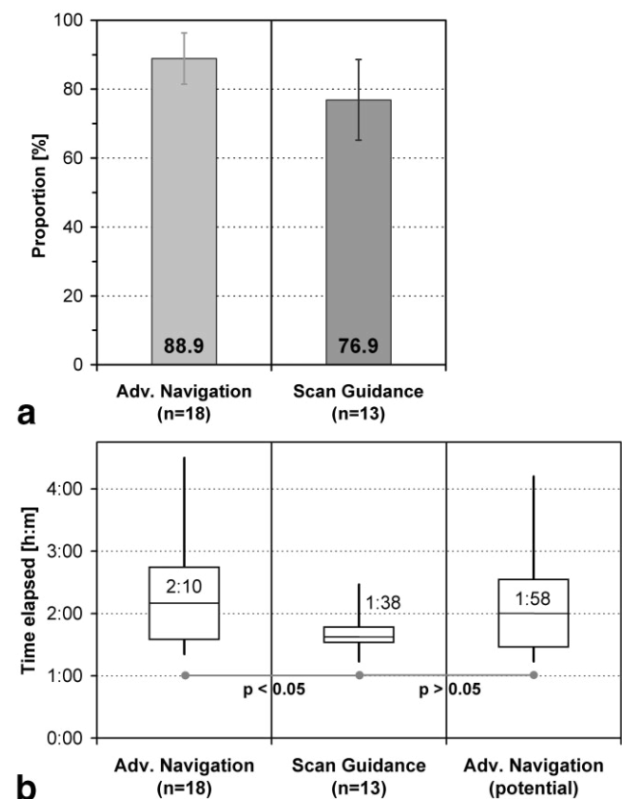


**Figure 6. a:** Comparison of the diagnostic yield of biopsies achieved by three neurosurgeons (18 with advanced navigation and 13 under scan guidance). Proportions are given along with standard errors. **b:** Comparison of associated imaging times observed for the biopsies. Whiskers indicate extreme times, and boxes represent upper and lower quartiles, respectively. Potential values were corrected for the time consumed by the constrained data processing.

drainage of cerebrospinal fluid is so massive that preoperative data may no longer be reliably used for rigid image registration. As a safety measure fMRI data fusion strictly for craniotomy planning only of the cortical surface was observed in almost every case (23).

Over the past few years, various navigation solutions and image fusion modules have been developed for both research and clinical applications. The 3D Slicer is an example of a powerful medical visualization and processing software that was adapted to an open MR scanner. It was reported to be a feasible guidance approach for brain interventions using multimodal image fusion with rigid registration in less than five minutes (24), and for microwave coagulation of liver tumors (25). Current developments of the software include the difficult task of implementing a non-rigid registration that is compatible with intraoperative decision-making and remains sufficiently accurate (26). In contrast to our platform, however, the 3D Slicer is not a fully tested and validated medical product, and therefore is not intended for general clinical use. While the integration of the 3D Slicer into the clinical workflow has generally been described as good, important aspects, such as the extra effort and associated time required for preprocessing and data transfer, have not been discussed in detail (24–26).

On the other hand, guidance solutions with image fusion options from major medical manufacturers, especially those closely integrated with the MRI application, are often proprietary, which means that upgrades or data import/export may be more restrictive. The presented stand-alone system is generally based on off-the-shelf hardware and modular software written in an open programming language (Java). Such a design allows relatively easy and cost-effective upgrades of both hard- and software to be made, and is also open to platform migration.

In contrast to more research-oriented solutions, the development of the Localite system could not be driven by performance issues alone because, as a certified medical product, it also had to meet the safety requirements of an interventional MRI suite. One of our goals was to be able to fall back on the existing scan guidance scheme if the new system failed. Therefore, system installation and connection involved only little modifications to the existing hard- and software (Fig. 1). While this did not affect the fast readout of vector information from the tracking computer and the immediate routing of the navigation screen to an in-bore monitor, access to the intraoperative reference data on the MR host was very slow.

In general, operation of the Localite PC was considered easy, reliable, and safe by all users. They also appreciated that only the basic functionality following established cognitive skills of a physician was supplied instead of overloading the screen with operating elements perceived by only a technical expert. As a consequence, changes in the clinical workflow were generally moderate, except for the relatively long procedure times required for reference volume acquisitions, image transfers, and image fusion.

The presented clinical results were derived from analyses of brain interventions by three neurosurgeons. A

comparison of average surgical-effectiveness values revealed that the novel approach is as effective as scan guidance only. The 24% increase in total resections and 12% decrease in both partial and subtotal resections for the main surgeon appear to suggest improved performance under advanced guidance, but this hypothesis was not confirmed statistically. It should be recalled, however, that the 96% average extent of resection that was reported in an earlier study of 12 selected low-grade glioma patients using scan guidance was already quite high (18). To derive the significance of a potential improvement with respect to such a figure might require patient numbers that are difficult to achieve. For example, a simple calculation for a proportion of 96% shows that a sample size of  $N = 369$  is required to achieve a 95% confidence interval of 94–98% ( $96\% \pm 2\%$ ).

One limitation of our study is the heterogeneity of the patient groups, which were selected according to simple procedure-oriented rather than neuropathological criteria. Therefore, the comparison of resection and postoperative neurologic outcomes is of limited clinical value, given the differences in nature, biological behavior, imaging, and surgical characteristics of lesions such as meningiomas, intraaxial tumors, and vascular malformations. On the other hand, the realities of MR-guided operations in a complex environment like the open 0.5 T scanner make a rigorous comparison with large patient numbers problematic. Another limitation lies in the fact that the needs of the patients and surgeons had to take precedence over the scientific need to compare one approach with another.

Analysis of the biopsies showed that the slightly higher fractions of diagnostic biopsies under advanced guidance for all three surgeons (89% vs. 77%), as well as the main surgeon only (100% vs. 90%), were not significant.

The second aspect of the clinical analysis was to assess the time required to complete the reported cases. This is important because risk of complications and convalescence time increase with the length of time spent under general anesthesia. In addition, longer procedure times are associated with higher costs, especially personnel costs, and also have a negative impact on the clinical workflow. Generally, image extraction and transfer are integral components of an image-guided procedure, and the associated times cannot be simply subtracted from the total procedure time. In our case, however, the available extraction mechanism, which was implemented in the mid 1990s, was probably not intended to be used for time-critical purposes. Because effective extraction rates were considerably slower than even the slowest Ethernet speeds (0.02 vs. 1 MB/s), it seems justifiable to also report the subtracted times to illustrate the potential impact of using an optimized data-access mechanism. On average, resections with advanced navigation did not require significantly more time and potentially may be performed even faster than those with scan guidance. Very little differences in the median procedure time were observed for the main surgeon, which suggests that trained surgeons might use the system in a more effective way. In contrast, biopsies guided by the new approach were 32

minutes and an insignificant 20 minutes longer without and with correction of the image extraction delay, respectively.

An earlier study (27) found that craniotomies under scan guidance in an open MR scanner took more than one hour (1:20 hours) longer than in a conventional operating room ( $5:03 \pm 1:22$  hours vs.  $3:43 \pm 0:58$  hours). Likewise, pituitary surgery took more than 1.5 hours longer ( $3:23 \pm 0:53$  hours vs.  $1:44 \pm 0:17$  hours), almost twice as long. Although these times are not exactly comparable to ours, they may serve as reference values. In the present study, operation times under image guidance were not only generally reduced (probably due to a learning effect), but also reached the benchmark values of the conventional operating environment despite the extra time spent for intraoperative imaging.

For systematic investigations of complex interventions like these, it remains difficult to collect data from a large number of patients within reasonable observation periods. Our evaluation study was not designed to assess the long-term outcome of the patients. The impact of spectroscopic and functional information (28), as well as diffusion tensor imaging (29,30), on patient outcome still needs to be defined. It has been argued that to date no study has demonstrated that imaging guidance improves the outcome for any group of neurosurgical patients (31), and that a truly user-friendly system that preserves adequate image quality has not yet been developed. We expect, however, that image information of high quality will be increasingly available given the progress in scanner hardware, imaging sequences, and data processing. We believe that, besides the technical presentation, our work provides valuable insight into the clinical practicability of two distinct concepts for intraoperative MRI guidance. The two approaches are mutually beneficial because they combine aspects of "true" reality, such as intraoperative detection of brain shift and head motion, with those of virtual reality, such as high speed, high image quality, and overlay of additional information.

In conclusion, we believe the presented approach is safe and effective in combining aspects of functional neuronavigation with intraoperative MRI guidance. The clinical results clearly show that even though certain aspects of true reality were sacrificed for image detail and navigation speed, the surgical outcomes achieved under advanced guidance were (at least) as good as those obtained with the established intraoperative scanning scheme. Despite the additional procedure steps that are inherent to any advanced guidance approach, and the time-consuming data access that is particular to our approach, the resection times were not prolonged. Though differences in postoperative neurologic status with additional fMRI information were not significant, our initial experience, especially with respect to user friendliness and clinical practicability, is encouraging. More clinical studies with larger patient numbers will be required to firmly establish the possible advantages of functional image integration.

## ACKNOWLEDGMENTS

We thank Sascha Prothmann and Claudia Dannenberg for their fMRI measurements, and Jens-Peter Schneider, Matthias Seiwerts, and Cathrin Vörkel for their valuable assistance. Thanks are also due to Wolfgang Heinke from the Department of Anesthesiology and Intensive Care Medicine, and to Dirk Winkler and Wolfgang Krupp from the Department of Neurosurgery. Hans-Joachim Schwarzmaier and Martin Bublat are acknowledged for many helpful discussions and support.

## REFERENCES

- Rubino GJ, Farahani K, McGill D, Van De Wiele B, Villablanca JP, Wang-Mathieson A. Magnetic resonance imaging-guided neurosurgery in the magnetic fringe fields: the next step in neuronavigation. *Neurosurgery* 2000;46:643-654.
- Seifert V, Zimmermann M, Trantakis C, et al. Open MRI-guided neurosurgery. *Acta Neurochir (Wien)* 1999;141:455-464.
- Sutherland GR, Kaibara T, Louw D, Hoult DI, Tomanek B, Saunders J. A mobile high-field magnetic resonance system for neurosurgery. *J Neurosurg* 1999;91:804-813.
- Jolesz FA. Future perspectives in intraoperative imaging. *Acta Neurochir Suppl* 2003;85:7-13.
- Hall WA, Liu H, Martin AJ, Pozza CH, Maxwell RE, Truwit CL. Safety, efficacy, and functionality of high-field strength interventional magnetic resonance imaging for neurosurgery. *Neurosurgery* 2000;46:632-641.
- Truwit CL, Liu H. Prospective stereotaxy: a novel method of trajectory alignment using real-time image guidance. *J Magn Reson Imaging*. 2001;13:452-457.
- Tronnier VM, Wirtz CR, Knauth M, et al. Intraoperative diagnostic and interventional magnetic resonance imaging in neurosurgery. *Neurosurgery* 1997;40:891-900.
- Wirtz CR, Tronnier VM, Bonsanto MM, et al. Image-guided neurosurgery with intraoperative MRI: update of frameless stereotaxy and radicality control. *Stereotact Funct Neurosurg* 1997;68:39-43.
- Steinmeier R, Fahlbusch R, Ganslandt O, et al. Intraoperative magnetic resonance imaging with the Magnetom open scanner: concepts, neurosurgical indications, and procedures: a preliminary report. *Neurosurgery* 1998;43:739-747.
- Nimsky C, Ganslandt O, Kober H, Buchfelder M, Fahlbusch R. Intraoperative magnetic resonance imaging combined with neuronavigation: a new concept. *Neurosurgery* 2001;48:1082-1089.
- Metzger AK, Lewin JS. Optimizing brain tumor resection. Low-field interventional MR imaging. *Neuroimaging Clin N Am* 2001;11:651-657.
- Nimsky C, Fujita A, Ganslandt O, Von Keller B, Fahlbusch R. Volumetric assessment of glioma removal by intraoperative high-field magnetic resonance imaging. *Neurosurgery* 2004;55:358-370.
- Schenck JF, Jolesz FA, Roemer PB, et al. Superconducting open-configuration MR imaging system for image-guided therapy. *Radiology* 1995;195:805-814.
- Silverman SG, Jolesz FA, Newman RW, et al. Design and implementation of an interventional MR imaging suite. *AJR Am J Roentgenol* 1997;168:1465-1471.
- Black PM, Alexander III E, Martin C, et al. Craniotomy for tumor treatment in an intraoperative magnetic resonance imaging unit. *Neurosurgery* 1999;45:423-431.
- Black PM, Moriarty T, Alexander III E, et al. Development and implementation of intraoperative magnetic resonance imaging and its neurosurgical applications. *Neurosurgery* 1997;41:831-842.
- Alexander III E, Moriarty TM, Kikinis R, Black P, Jolesz FM. The present and future role of intraoperative MRI in neurosurgical procedures. *Stereotact Funct Neurosurg* 1997;68:10-17.
- Schneider JP, Schulz T, Schmidt F, et al. Gross-total surgery of supratentorial low-grade gliomas under intraoperative MR guidance. *AJNR Am J Neuroradiol* 2001;22:89-98.

19. Nabavi A, Black PM, Gering DT, et al. Serial intraoperative magnetic resonance imaging of brain shift. *Neurosurgery* 2001;48:787-797.
20. Hennig J, Speck O, Koch MA, Weiller C. Functional magnetic resonance imaging: a review of methodological aspects and clinical applications. *J Magn Reson Imaging* 2003;18:1-15.
21. Yetkin FZ, Hammeke TA, Swanson SJ, et al. A comparison of functional MR activation patterns during silent and audible language tasks. *AJNR Am J Neuroradiol* 1995;16:1087-1092.
22. Friedman L, Kenny JT, Wise AL, et al. Brain activation during silent word generation evaluated with functional MRI. *Brain Lang* 1998;64:231-256.
23. Nabavi A, Black PM, Gering DT, et al. Serial intraoperative magnetic resonance imaging of brain shift. *Neurosurgery* 2001;48:787-797.
24. Gering DT, Nabavi A, Kikinis R, et al. An integrated visualization system for surgical planning and guidance using image fusion and an open MR. *J Magn Reson Imaging* 2001;13:967-975.
25. Morikawa S, Inubushi T, Kurumi Y, et al. New assistive devices for MR-guided microwave thermocoagulation of liver tumors. *Acad Radiol* 2003;10:180-188.
26. Warfield SK, Haker SJ, Talos IF, et al. Capturing intraoperative deformations: research experience at Brigham and Women's Hospital. *Med Image Anal* 2005;9:145-62.
27. Laufer M, Schaffranietz L, Rudolph C, Schneider JP, Schulz T. Anesthesiologic technical problems in procedures with open MRI. Results following 104 anesthetics. *Anaesthetist* 1999;48:51-56.
28. Oh J, Henry RG, Pirzkall A, et al. Survival analysis in patients with glioblastoma multiforme: predictive value of choline-to-n-acetylaspartate index, apparent diffusion coefficient, and relative cerebral blood volume. *J Magn Reson Imaging* 2004;19:546-554.
29. Dong Q, Welsh RC, Chenevert TL, et al. Clinical applications of diffusion tensor imaging. *J Magn Reson Imaging* 2004;19:6-18.
30. Nimsy C, Ganslandt O, Hastreiter P, et al. Preoperative and intraoperative diffusion tensor imaging-based fiber tracking in glioma surgery. *Neurosurgery* 2005;56:130-137.
31. Laws Jr ER. Comment to: Nimsy C, Ganslandt O, Hofmann B, Fahlbusch R. Limited benefit of intraoperative low-field magnetic resonance imaging in craniopharyngioma surgery. *Neurosurgery* 2003;53:72-80.

## Arbeit 2 – Vollautomatisches Verfahren zur 3D-Lokalisation von MR-Positionsmarkern

Die überwiegende Mehrzahl der heutigen MRT-Systeme ist nicht offen sondern röhrenförmig. Eine Navigation könnte gerade an diesen Geräten wertvolle Hilfe leisten, da eine kognitive Übertragung ungenau und eine bildgebende Führung oft nicht möglich sein kann. Die nachfolgenden Arbeiten beschäftigen sich daher mit der technisch-methodischen Entwicklung einer Echtzeit-Navigation für ein herkömmliches MRT-System. Grundsätzlich fehlen diesen Geräten sowohl Tracking-System, Registrierungstechnik wie auch eine Steuerungskonsole.

Beim Tracking fiel die Wahl auf ein kommerzielles optisches System, das auch für konventionelle Anwendungen gebräuchlich ist. Hard- und Software für die Steuerung der Navigation konnten hingegen auf den Entwicklungen für das offene MRT aufbauen. Ein wesentlicher Teil der Arbeiten galt daher der Bereitstellung einer zuverlässigen Registrierungsmethode bei geringem Platzangebot und Einsatzmöglichkeiten in verschiedenen Körperregionen. Die Basis hierfür bildete eine flexible (*semiaktive*) Marker-Technologie, die resonante, induktiv gekoppelte HF-Spulen zur MR-Signalgebung verwendet.

Die folgende Arbeit [81] beschäftigt sich eingehend mit einer vollautomatischen Lokalisation dieser Miniatur-HF-Spulen im *gesamten* MRT-Messvolumen. Im Gegensatz zu herkömmlichen, passiven Markern lassen sich *semiaktive* Marker unabhängig von deren genauen Anzahl, Lage und Anordnung lokalisieren. Jede HF-Spule umfasst ein Plastikröhrchen (Durchmesser 3 mm) mit einer signalgebenden Flüssigkeit und wurde auf die Resonanzfrequenz des 1,5-T-MRT-Systems abgestimmt (rund 64 MHz). Die induktive Kopplung dieser Spulen mit den normalen, bildgebenden Spulen führt dazu, dass der magnetische Fluss und damit der effektive Anregungswinkel in der Miniaturspule um ein Vielfaches – etwa 30- bis 100-fach – erhöht werden. Wird nun im Messprotokoll ein sehr kleiner nominaler Flipwinkel von nur wenigen Grad gewählt, so ergeben sich an der HF-Spule praktisch übliche Anregungswinkel mit herkömmlichen Signalintensitäten während die MR-Signale im restlichen Messvolumen nur sehr gering ausfallen. Die resonanten HF-Spulen werden somit zu drahtlosen, signal-positiven MRT-Positionsmarkern.

Dieses Verfahren generierte selbst bei Summation aller MR-Signale über eine sehr große Schichtdicke (z. B. 300 mm) einen ausreichenden Bildkontrast zum umgebenden Gewebe. Dadurch entfällt ein aufwändiges Planen und Ausrichten der Schichten an der ungefähren Position der Marker so wie es bei herkömmlichen, kontrastmittelgefüllten Strukturen notwendig ist. Stattdessen projizieren sich die Signale aller Marker im Bildgebungsvolumen auf ein MR-Bild. Bei einem quadratischen Messfeld mit einer Basisdimension von ebenfalls 300 mm werden so z. B. sämtliche Marker in einem Volumen von insgesamt 27 Litern erfasst. Die unbekannte dritte Koordinate senkrecht zur MR-Bildebene lässt sich durch MR-Aufnahmen in orthogonaler Projektion bestimmen. Das hier implementierte Verfahren nutzt die Informationen aus allen drei Projektionsrichtungen (axial, koronal und sagittal) um die Zuverlässigkeit und Genauigkeit der Bestimmung zu erhöhen.

Zentrales Element der Bildanalyse war das Auffinden lokaler Signalerhöhungen (*Peaks*) im Einklang mit dem Signalprofil der Miniatur-Spulen. Mathematisch wurde hierbei versucht, eine zweidimensionale (2D) Gaussfunktion numerisch anzupassen (*engl.: fit*). Zur Differenzierung der Marker von Artefakten oder zufälligen Strukturen wurden sowohl die Intensitäten wie auch das geometrische Profil (Symmetrie und Ausdehnung) der MR-Signale berücksichtigt. Geeignete Schwellwerte ergaben sich durch die Auswertung einer größeren Anzahl von Messungen unter verschiedenen Bedingungen. Aus der großen Vielzahl der numerisch gefundenen 2D-Gaussprofile ergab sich dadurch eine überschaubare Anzahl wahrscheinlicher Markersignale für jede Projektionsrichtung. Ein abschließendes Kriterium zur Differenzierung von Markersignalen war die enge Übereinstimmung der korrespondierenden Koordinaten aus den unabhängigen Projektionsmessungen.

Die folgende Arbeit enthält eine detaillierte Beschreibung der Bildverarbeitung und liefert wertvolle Ergebnisse zur Präzision und Genauigkeit des Lokalisationsverfahrens. Der 3D-Positionsfehler eines einzelnen Markers wächst mit dem Abstand ( $r_M$ ) zum Isozentrum, was sich am ehesten mit der Nichtlinearität der Gradientenfelder erklären lässt. Die Fehler sind generell tolerabel, selbst bei  $r_M = 175$  mm beträgt die mittlere 3D-Abweichung nur etwa 1,5 mm. Minimal lassen sich nun drei solcher Marker einsetzen, um die räumliche Ausrichtung einer Ebene zu definieren. Eine entsprechende Abschätzung ergab akzeptable Winkelfehler (maximal  $0,44^\circ$ ) für mittlere Markerabstände bis zu 170 mm vom Isozentrum.

## Original Research

# Method for Automatic Localization of MR-Visible Markers using Morphological Image Processing and Conventional Pulse Sequences: Feasibility for Image-Guided Procedures

Harald Busse, PhD,<sup>1\*</sup> Robert Trampel, PhD,<sup>1</sup> Wilfried Gründer, PhD,<sup>2</sup> Michael Moche, MD,<sup>1</sup> and Thomas Kahn, MD<sup>1</sup>

**Purpose:** To evaluate the feasibility and accuracy of an automated method to determine the 3D position of MR-visible markers.

**Materials and Methods:** Inductively coupled RF coils were imaged in a whole-body 1.5T scanner using the body coil and two conventional gradient echo sequences (FLASH and TrueFISP) and large imaging volumes up to (300 mm<sup>3</sup>). To minimize background signals, a flip angle of  $\approx 1^\circ$  was used. Morphological 2D image processing in orthogonal scan planes was used to determine the 3D positions of a configuration of three fiducial markers (FMC). The accuracies of the marker positions and of the orientation of the plane defined by the FMC were evaluated at various distances  $r_M$  from the isocenter.

**Results:** Fiducial marker detection with conventional equipment (pulse sequences, imaging coils) was very reliable and highly reproducible over a wide range of experimental conditions. For  $r_M \leq 100$  mm, the estimated maximum errors in 3D position and angular orientation were 1.7 mm and 0.33°, respectively. For  $r_M \leq 175$  mm, the respective values were 2.9 mm and 0.44°.

**Conclusions:** Detection and localization of MR-visible markers by morphological image processing is feasible, simple, and very accurate. In combination with safe wireless markers, the method is found to be useful for image-guided procedures.

**Key Words:** interventional MRI; MRI guidance; percutaneous biopsies; MR-visible markers; marker detection

**J. Magn. Reson. Imaging 2007;26:1087–1096.**

© 2007 Wiley-Liss, Inc.

MAGNETIC RESONANCE (MR) imaging has gained considerable interest as a guidance modality for percutaneous biopsies and other minimally invasive interventions (1,2). Successful applications include, but are not limited to, bone and soft tissue biopsies of lesions in the musculoskeletal system (3,4), breast (5,6), liver (7,8), and the prostate (9,10). Open-configuration MR scanners have advanced the development of MR-guided techniques and eliminated the need for patient transfer between imaging and actual intervention. These scanners are well suited for brain interventions (11–13) and have been applied for MR-guided biopsies in various regions of the body (3,14,15). Despite a number of challenges including limited access to the patient, closed-bore scanners continue to be used as interventional platforms (8,9,16), mainly because of their superior imaging capabilities, wide availability, and lower cost of operation. With the advent of powerful computer hardware, interventional MR scanners are also increasingly used in combination with frameless stereotactic devices or navigation systems (10–13,17). These systems allow the interventionalist to easily switch between the patient anatomy and MRI representation according to the patient's and interventional needs. The exact transformation between both representations is called co-registration and requires adequate reference points for both coordinate frames.

Outside the bore a medical instrument such as a biopsy needle can be easily localized by using active or passive optical elements mounted on an instrument holder and detecting the light emitted or reflected from them, respectively. Inside the scanner the choice of commercial MR-visible markers and devices is still limited, but the research interest in this area is large (18,19). For MR-visible markers the difference between active and passive techniques is fundamental. Active markers are small receive coils which are hardwired to the regular receiver channels of the MR system and allow an electronic readout and processing of the marker signals (20–23). Such markers may be selected independently and can be localized easily and accurately by a dedicated pulse sequence using a one-dimensional projection technique. However, active mark-

<sup>1</sup>Department of Diagnostic and Interventional Radiology, Leipzig University Hospital, Leipzig, Germany.

<sup>2</sup>Department of Medical Physics and Biophysics, Leipzig University, Leipzig, Germany.

Parts of this work were presented at the 2007 Joint Annual Meeting ISMRM-ESMRMB in Berlin, Germany.

\*Address reprint requests to: Harald Busse, Department of Diagnostic and Interventional Radiology, Leipzig University Hospital, Liebigstr. 20, 04103 Leipzig, Germany.

E-mail: harald.busse@medizin.uni-leipzig.de

Received December 21, 2006; Accepted July 13, 2007.

DOI 10.1002/jmri.21129

Published online in Wiley InterScience (www.interscience.wiley.com).



ers pose a safety hazard due to the coupling of the exciting RF wave with the connecting wires (24–26). Although some sophisticated approaches to suppress these resonances in the transmission line have been proposed (27,28), the respective designs are rather complex and may not be adequate for clinical use. In contrast, passive markers produce a special contrast that is visible on a standard MR image. A negative contrast may be generated by locally altering the magnetic susceptibility of a tissue region but, therefore, will not work outside the patient. A positive contrast is created by a signal source, for example, a contrast solution (6,29,30), and may be further amplified by inductively coupled RF coils wound around the signal source (31–33). For that purpose, a miniature RF coil needs to be tuned to the Larmor frequency of the scanner. Inductive signal coupling between RF coils will lead to locally increased effective flip angles inside and immediately around the coil. Excitation at low flip angles will then brightly depict the signal source but give only little signal from the background, which results in a high contrast between fiducial marker and background.

The goal of this work was to evaluate the feasibility and accuracy of a new method to localize MR-visible fiducial markers based on morphological image processing of conventional 2D MR images. To avoid potential hazards due to RF heating and to facilitate clinical application, a passive technique was chosen. Basic background suppression was achieved by using self-developed inductively coupled RF coils in combination with low flip-angle excitation. In addition, an image preprocessing was implemented to suppress remaining background contributions.

Although this work is rather early and describes the basic setup, various clinical applications are conceivable. Besides promoting navigation concepts for percutaneous interventions in a closed-bore MR scanner, the marker technology may, for instance, be adapted to stereotactic breast biopsy systems, used in the field of MR-guided neurosurgery, or provide reference points for more advanced assistance devices operating inside (18) or outside (19) the magnet bore. The selective contrast also offers great potential for intracorporal use of the markers, although the current implementation is not yet suited for applications such as the tracking of endovascular devices. In general, the presented technology may potentially facilitate the workflow of MRI-guided procedures but also improve their reliability or precision.

## MATERIALS AND METHODS

### Fiducial Markers

The inductively coupled RF coils were tuned to the resonance frequency of our whole-body 1.5T MR scanner (63.8 MHz, Magnetom Symphony, Siemens Medical Solutions, Erlangen, Germany) and wound around a plastic tube (diameter  $\approx 3$  mm) containing a glyceroltrinitrate liquid (Nitranjin Isis 0.8 mg, Alparma-Isis, Langenfeld, Germany) with a short T1 relaxation time. To allow a flexible and accurate positioning of the coils they were mounted on  $2 \times 2$  ( $15.8 \times 15.8$  mm<sup>2</sup>) Lego

bricks and could be attached to a  $32 \times 32$  ( $256 \times 256$  mm<sup>2</sup>) base plate (Fig. 1a). The machining accuracy of the parts is estimated to be on the order of 0.05 mm but all reported fit results were rounded to the tenth of a millimeter.

### Pulse Sequences

The fiducial marker configuration (FMC) was imaged with the integrated body coil unless stated otherwise using conventional pulse sequences in 2D projection technique. For both the field of view (FOV) and slice thickness (SL) larger values in the 200–300 mm range were used to assure that the markers were captured after only a rough definition of the imaging volume and irrespective of the exact position of the markers.

The initial experiments were performed with a gradient-recalled echo fast low angle shot (FLASH) sequence (echo time TE = 6.9 msec, repetition time TR = 14 msec, FOV =  $300 \times 300$  mm<sup>2</sup>, matrix  $512 \times 512$ , SL = 300 mm). An occasional ghost peak along the phase-encoding direction could be effectively suppressed by choosing a slightly higher TR (20 msec). We then used this value routinely because here the choice of TR was not critical. This corresponds to a total acquisition time for three fully reconstructed  $512 \times 512$  MR images in all standard views of  $\approx 22/31$  seconds. The observed background-subtracted signals in a coronal view were maximal for flip angles in the range of  $0.5$ – $1.4^\circ$  (between 31.3 and 36.9 arbitrary units, a.u.) steadily dropping to lower values for both smaller (eg, 15.6 a.u. at  $0.2^\circ$ ) and higher flip angles (FA; eg, 12.8 a.u. at  $3^\circ$ ). Furthermore, a true fast imaging with steady-state precession (TrueFISP) pulse sequence (TE = 2.85 msec, TR = 3651 msec, FOV =  $300 \times 300$  mm<sup>2</sup>, matrix  $512 \times 512$ , SL = 200 mm, FA =  $1^\circ$ ) with a total acquisition time of  $\approx 11$  seconds for three orthogonal views was also used. In

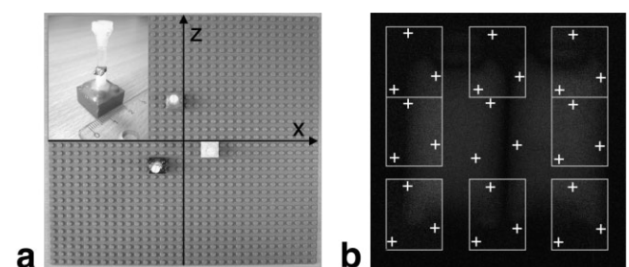


**Figure 1. a:** Experimental setup. The shown configuration of three fiducial markers was realized at different well-defined positions on a baseplate (stud spacing 8 mm). The inset shows the inductively coupled RF coil (four turns of 0.3-mm-diameter copper wire, length  $\approx 2$  mm, outer diameter  $\approx 4$  mm) wound around a plastic tube. **b:** 2D localization of fiducial marker configuration (FMC) in different positions on the plate. Markers were imaged with a spoiled gradient-recalled echo sequence (FLASH, FA =  $0.7^\circ$ , SL = 200 mm, NSA = 2). Relevant regions of coronal MR images (gray frames) with FMC in eight extreme positions overlaid on background image with FMC in neutral position, ie, close to the magnet isocenter. White crosses denote the peak positions of the fitted 2D-GF. Due to the low flip angle, signal contributions from the two bottles filled with doped water are very faint.

contrast to the FLASH sequence, the FA of the TrueFISP sequence could only be varied in steps of  $1^\circ$ . The background-subtracted signals were maximal for  $1^\circ$  and  $2^\circ$  (87.2 and 92.4 a.u.) and rapidly reached lower values for  $3^\circ$  and  $4^\circ$  (57.9 and only 11.2 a.u.).

### 2D Localization Algorithm

A three-stage method to determine the 2D coordinates of  $n_{mrk}$  fiducial markers in a fully reconstructed 2D projection image was developed with IDL (Interactive Data Language, RSI, Boulder, CO). Figure 2 shows a flow chart for  $n_{mrk} = 3$ . Each stage of the algorithm is described in detail below. It should be noted that all mentioned parameters were refined simply as more marker data were collected rather than in a well-designed manner involving particular training data.

#### Stage 1: Preprocessing and Segmentation

In the case of inductively coupled coils, most background signals may be suppressed by choosing a low FA. With steady-state free precession (SSFP) pulse sequences, however, off-resonance effects can lead to the well-described banding artifacts that have high signal intensities for low FAs (34,35). Therefore, the original image was preprocessed to allow a better discrimina-

tion of the fiducial marker signals. A median filter was applied to the image to remove pixel noise and preserve sharp edges, in particular around the marker signals. A subsequent convolution with a custom-made normalized kernel was then used for moderate enhancement of the edges. The mean and standard deviation of the resulting image was then calculated. The segmentation then simply involved thresholding at a multiple number of standard deviations above that mean intensity. The effect of preprocessing is illustrated in Fig. 3 for a TrueFISP image with background signals from a volunteer's abdomen.

#### Stage 2: Peak Fitting Algorithm

In this stage we assumed that the 2D signal distributions from the fiducial markers can be fitted by a 2D Gaussian function (2D-GF) given by:

$$g(x,y) = a \cdot \exp\left[-\frac{1}{2}\left(\frac{x - \mu_x}{\sigma_x}\right)^2\right] \cdot \exp\left[-\frac{1}{2}\left(\frac{y - \mu_y}{\sigma_y}\right)^2\right] + b \quad (1)$$

where  $x$  and  $y$  are the 2D spatial coordinates of the image,  $\mu_x$  and  $\mu_y$  are the centroid coordinates,  $\sigma_x$  and  $\sigma_y$

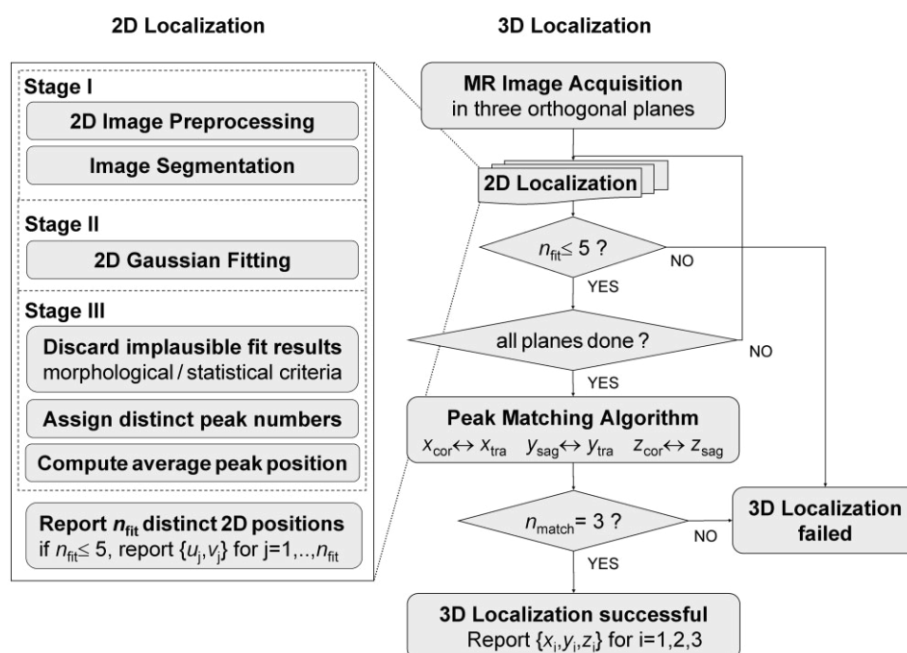


**Figure 2.** Flow chart of the algorithm used for 3D localization of three markers. 2D Localization (left part): In stage one the fully reconstructed 2D image is preprocessed to suppress background contributions. A simple thresholding is then used to compute a binary segmentation image. In stage two the bounding box of the segmented image is used as a target region to scan for signal distributions in the median-filtered original image that may be locally fitted by a 2D-GF. This produces a list of numerically successful fits. Stage three seeks to identify those fit results that agree with the geometry and MRI appearance of the fiducial markers and results in a distinct set of up to five likely 2D positions for the fiducial markers. 3D Localization (right): The 2D localization is performed for three orthogonal scan planes. A peak matching algorithm tries to correlate the coordinates from independent views. Signals from nonmarkers should have no correspondence in other views, unless by coincidence, and will be ignored. If the marker signals appear in at least two views and are sufficiently close to each other, the 3D positions of the three markers will be reported. The 3D localization fails if the coordinate sets are only consistent with more or less than three marker signals or if too many ( $>5$ ) potential marker signals were identified in one of the three planes.

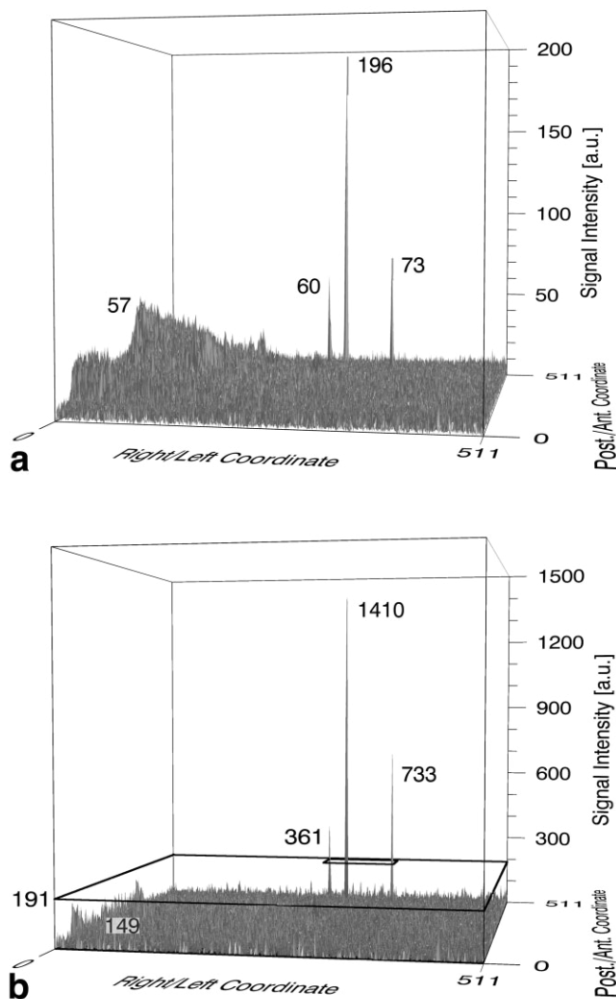


**Figure 3.** Image preprocessing for 2D localization. **a:** 3D surface plot of the original transverse TrueFISP image (matrix =  $512 \times 512$ ) of three fiducial markers placed over a volunteer's abdomen (see also Fig. 4). Signal intensities (arbitrary units, a.u.) of the markers differ as indicated by the maximum values of respective regions. Segmentation of that image would be compromised by similar intensities of background and markers, respectively. **b:** Image after median filtering and convolution with a self-designed kernel. The background was largely reduced with respect to the marker signals, which improves segmentation. The thick rectangles indicate the actual threshold level ( $\approx 200$  a.u.) and the smaller one is the actual bounding box of the segmented structures (peaks).

are the widths of the distribution,  $a$  is the amplitude of the peak, and  $b$  is the background level. The bounding box is the smallest rectangular 2D region that completely contains all segmented structures. Within the bounding box of the segmented image the marker image was sampled at regularly spaced anchor points using a 2D local data region (2D-LDR) with a dimension slightly larger than that of the signal source. To reduce the computational burden, peak fitting was only attempted at those positions where the number of segmented data points within the 2D-LDR was larger than a predefined value, typically between 1 and 10. Peak fitting was car-

ried out via an implementation of the Levenberg–Marquardt algorithm, an iterative method that has become the standard of nonlinear least-squares routines and works very well in practice (36). As conditions for stopping, iterations were performed until the  $\chi^2$  decreased by a specified but negligible amount that was considered a numerically successful fit, or until a preselected maximum number of iterations were performed and the fit was considered a failure. An initial guess for the set of fit parameters ( $\mu_x$ ,  $\mu_y$ ,  $\sigma_x$ ,  $\sigma_y$ ,  $a$ ,  $b$ ) was also required. For the signal distributions of actual markers, we observed that the stopping condition of the LM algorithm was reached within 10 iterations. This criterion was therefore used to suppress further time-consuming iterations into less likely results. The resulting fit parameters of all numerically successful attempts were stored in a list that was analyzed in the following stage.

### Stage 3: Identification of Plausible Fit Results

The number of successful fits,  $n_{succ}$ , was typically larger than the number of fiducial markers,  $n_{mrk}$ , for two main reasons: 1) Because the local data regions were slightly overlapping, the same peak could be fitted multiple times; 2) Artifacts or other background signals with intensities above the segmentation threshold could happen to have a 2D distribution that can be fitted with a 2D-GF. Therefore, a discrimination strategy was implemented that first discards implausible results. The actual implementation featured morphological and 'statistical' criteria summarized in Table 1. The remaining results were scanned for multiple findings. A first inspection of the list of plausible fit results assigned consecutive peak numbers to each set of fit parameters. If the centroid of the current set was within 0.5 mm of that of an existing peak, the same peak number was assigned. Also, the number of segmented points,  $n_{seg}$ , within the corresponding 2D-LDR was stored. For a given peak number the peak position was then estimated by weighted ( $1/n_{seg}$ ) averaging over the individual centroid positions. This resulted in a list of  $n_{fit}$  distinct centroid positions of fitted peaks that all met the discrimination criteria of Table 1.

### Determination of 3D Coordinates using Orthogonal Scan Planes

Finally, the 3D locations of the markers were determined by acquiring 2D data from three orthogonal scan planes (coronal, transverse, and sagittal). The 2D localization algorithm was then applied to determine the  $xy$ ,  $yz$ , and  $zx$  coordinate pairs of the fiducial markers. To obtain the 3D coordinates of a detected fiducial marker an automatic algorithm tried to correlate the  $x$  (left–right),  $y$  (anterior–posterior), and  $z$  (head–feet) coordinates from different scan planes. Irrespective of the true number of detected peaks,  $n_{fit}$  in each view that was allowed to be any number between zero and five, we generated a list of five coordinate pairs for all views:  $\{z_c, x_c\}$ ,  $\{x_t, y_t\}$ , and  $\{y_s, z_s\}$  for the coronal ( $c = \{1, 2, \dots, 5\}$ ), transverse ( $t = \{1, 2, \dots, 5\}$ ), and sagittal ( $s = \{1, 2, \dots, 5\}$ ) views, respectively. To allow a uniform processing missing peaks were given numerical but dummy values outside the normal coordinate range to avoid random peak matches.

Table 1  
Criteria to Distinguish Marker from Nonmarker Signal Profiles

Criterion	Assume marker if . . .	Rationale
Morphological		
min. peak width $\sigma_{min}$	$\sigma_{x/y} > \sigma_{min}$	Irrespective of the actual signal intensity, the MR signal profile of a fiducial marker, characterized by the peak widths $\sigma_x$ and $\sigma_y$ , should be consistent with the geometrical dimensions of the signal source.
max. peak width $\sigma_{max}$	$\sigma_{x/y} < \sigma_{max}$	
min. peak area $A_{min}$	$\sigma_x \cdot \sigma_y > A_{min}$	
max. peak area $A_{max}$	$\sigma_x \cdot \sigma_y < A_{max}$	
max. peak asymmetry $r_{max}$	$1 \leq \sigma_1 / \sigma_2 < r_{max}$ where $\sigma_1 > \sigma_2$	
Statistical (SNR)		
min. amplitude $a_{min}$	$a < a_{min}$	Both the absolute as well as the relative fitted peak amplitude with respect to the background level $b$ should not be too small.
min. contrast $c_{min}$	$a / b < c_{min}$	

SNR, signal-to-noise ratio.

The matching algorithm itself consisted of two phases. In phase one it cross-compared all  $x$  coordinates between coronal and transverse views. If the  $x$  values of two pairs (identified by the indices  $c'$  and  $t'$ ) agreed within a predefined margin of error ( $x_{c'} \approx x_{t'}$ ), eg, 1.0 mm, the algorithm looked for a peak in the sagittal view (identified by the index  $s'$ ), where both the  $y$  and  $z$  coordinates agreed with the corresponding values of the identified pairs in the coronal and transverse views, respectively ( $y_{s'} \approx y_{t'}$  and  $z_{s'} \approx z_{c'}$ ). If this search was successful the 3D coordinates of the fiducial marker were estimated by the average of the two values determined in the respective views. This phase worked successfully if all three markers were detected in all views. If one or more markers, however, only appeared in two of the three views, these markers could still be localized in the following phase.

Phase two operated with simple agreements between coordinates. The first of three consecutive evaluation loops again cross-compared all  $x$  coordinates between coronal and transverse views. If the  $x$  values of two pairs matched up ( $x_{c'} \approx x_{t'}$ ), the 3D coordinates of the marker were directly estimated by  $((x_{c'} + x_{t'})/2, y_{t'}, z_{c'})$ . The remaining loops evaluated the simple agreement between either the  $y$  values ( $y_{t'} \approx y_{s'}$ ) or the  $z$  values ( $z_{s'} \approx z_{c'}$ ) and computed the corresponding estimates for the 3D coordinates,  $(x_{t'}, (y_{t'} + y_{s'})/2, z_{s'})$  and  $(x_{c'}, y_{s'}, (z_{s'} + z_{c'})/2)$ , respectively. Whenever 3D coordinates were assigned in a step, the corresponding entries in the coordinate list were reset to the dummy values described above, which meant that the peak was not available for further comparisons. This measure should also prevent false assignments if different markers happened to line up closely in a particular view. In principle, an additional false peak could be erroneously reported if one of its coordinates happens to match with that of an existing peak (unlikely) or another false peak (very unlikely) in another view. If, however, false peaks may not be matched (likely) in other views their existence will not interfere with the correct matching of the true marker peaks.

To investigate critical scenarios for the localization and peak matching algorithm, we deliberately reduced the segmentation threshold in 10 steps down to 1/10 of the optimized value, which somehow simulates a corresponding decrease in the signal-to-noise ratio (SNR) of the marker signals.

### Precision and Accuracy of the Localization Algorithm

To evaluate the signal characteristics of the RF coils a fixed configuration of three markers was realized at different positions on the base plate (Fig. 1a) and, hence, at different distances  $r_M$  from the magnet isocenter. The plate was placed above two plastic bottles ( $\emptyset$  12 cm) filled with doped water that acted as background signal.

The stability and reproducibility of the 2D localization algorithm was analyzed in a series of 30 phantom images (FLASH) acquired at 10 flip angles (FA = 0.5, 0.6, ... 1.4°) and three number of signal averages (NSA = 1, 2, and 4) for each flip angle with the FMC in a neutral position, ie, close to the magnet isocenter. As an independent check of reproducibility for marker positions further away from the isocenter, we placed the FMC near the four corners of the plate (see Fig. 1b) and compared the three marker positions between MR images in both phase encode directions using FA = 0.7° and NSA = 2 ( $n = 12$  total). To estimate the accuracy of the 2D localization algorithm we moved the FMC in discrete step widths (16 mm) between the extreme  $\pm x$  as well as the extreme  $\pm z$  positions on the baseplate. Again, the position measurements at the four corner locations of the FMC (see Fig. 1b) were included for analysis to also estimate the accuracy at larger  $r_M$  values. By aligning our setup with the crosshair of the laser we tried to minimize errors due to a rotation of our setup within the  $xz$  plane, ie, around the  $y$  axis. We then calculated the differences in  $x$  and  $z$  coordinates, respectively, between the localized and the expected position according to the plate geometry. Due to the principal symmetry of the  $x$  and  $y$  axes, we did not measure the  $y$  position separately in this series and also assumed the position errors for the  $x$  and  $y$  coordinates to be the same. Possible deviations in the  $x$  and  $z$  coordinates resulting from a slight tilt of the base plate were neglected because they scale with the cosine of the tilting angle. An exemplary calculation shows that a tilt of  $\pm 2.5^\circ$  would yield a maximum offset of only  $-0.2$  mm at a distance of 200 mm.

To estimate the angular accuracy of our localization method we performed a series of 10 measurements at different distances  $r_M$  from the isocenter and used the  $x$  and  $z$  coordinates of the coronal and the  $y$  coordinate of

Table 2

Detection Characteristics of a Marker Image Set (see Figs. 3 and 4) as the Segmentation Threshold Is Deliberately Reduced from the Optimized Original Value (=100%)

512 x 512 Matrix	Relative Segmentation Threshold									
	1/1 100%	1/2 50%	1/3 ~ 33%	1/4 25%	1/5 20%	1/6 ~ 17%	1/7 ~ 14%	1/8 12.5%	1/9 ~ 11%	1/10 10%
<b>TrueFISP Sequence</b>										
$n_{\text{peaks}}$ sagittal	3	3	3	4	4	4	4	4	5	5
$n_{\text{peaks}}$ coronal	3	3	3	3	4	4	4	4	5	5
$n_{\text{peaks}}$ transverse	3	3	3	3	4	5	5	6	7	7
Peak matching?	yes	yes	yes	yes	yes	yes	yes	no	no	no
Fitting time per view [sec]	~ 0.15	~ 0.28	~ 0.81	~ 2.9	~ 7.0	~ 12	~ 16	~ 19	~ 21	~ 22
<b>FLASH Sequence</b>										
$n_{\text{peaks}}$ sagittal	2	2	3	3	4	7	7	9	9	9
$n_{\text{peaks}}$ coronal	3	3	3	4	5	6	6	6	6	6
$n_{\text{peaks}}$ transverse	3	3	3	4	9	13	13	15	15	15
Peak matching?	yes	yes	yes	yes	no	no	no	no	no	no
Fitting time per view [sec]	~ 0.20	~ 0.29	~ 1.1	~ 7.6	~ 23	~ 34	~ 43	~ 44	~ 44	~ 45

Fitting time estimated on a 1.7 GHz single-core Pentium IV with 1 GB RAM.

the sagittal view. For each position we calculated the normal vectors of the planes defined by the 3D positions of the three markers. To demonstrate the feasibility of marker localization involving anatomical structures, two healthy human volunteers were examined. Both gave informed written consent.

## RESULTS

### Pulse Sequences, Fiducial Markers, and Localization Algorithm

The FLASH and TrueFISP sequences successfully acquired the fiducial marker signals for flip angles around 1–2° (data provided in Materials and Methods). Due to the low flip angle, all images showed distinct fiducial marker peaks and a minimal signal amplitude of the water phantom. The 2D-GF fitting required around 170 msec for the detection of all markers in a coronal FLASH image of the FMC shown in Fig. 1a on a standard PC (1.7 GHz single-core Pentium IV CPU, 1 GB RAM). The time was estimated (upper limit) by the difference between subsequent calls of the system time. The fitting time slightly depended on the size of the bounding box or, equivalently, on the number of anchor points to be considered. If, for example, a TrueFISP artifact was segmented in a region away from the true marker signals, 2D-GF fitting took up to 500 msec. If, on the other hand, the fiducial markers happened to line up closely and almost horizontally or vertically in an image, fitting required around 130 msec only. The main dependence, however, was on the number of segmented structures within the bounding box, because 2D-GF fitting is attempted in all segmented regions. Irrespective of the type of pulse sequence, median filtering amounted another 200 msec and convolution took around 80 msec. The times required for computation of the segmentation image, peak sorting/discrimination, and peak matching were negligible on that scale.

Table 2 illustrates the detection characteristics for a marker image set under simulated critical conditions.

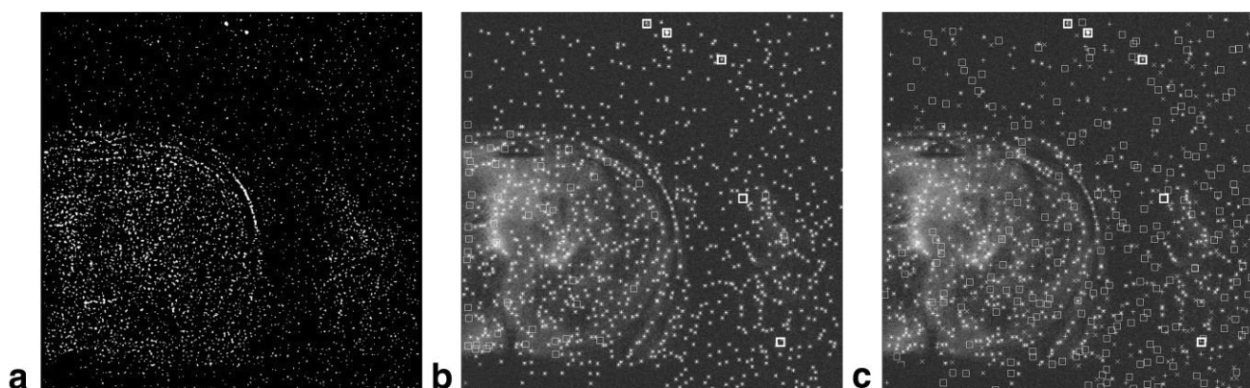
For each of the 10 deliberately reduced segmentation thresholds, the number of detected peaks per view, the corresponding fitting time, and the result of the peak matching is given. As the threshold was reduced, more and more signals from the background became segmented and had to be considered for 2D-GF fitting, which also increased the corresponding time. Despite missing or additional peaks in one or more of the views, however, peak matching was still successful down to a relative threshold of only  $\approx 14\%$  for the TrueFISP and of 25% for the FLASH sequence, respectively.

Figure 4 illustrates the role of statistical and morphological discrimination criteria for the transverse TrueFISP image segmented at only  $\approx 14\%$  of the optimized original threshold. It should be noted that such a scenario serves to evaluate the discrimination power of our algorithm and report the corresponding (hypothetical) increase in computation time. Unlike in Fig. 4a, the segmentation pattern of marker images obtained with the original 100% threshold will only feature a moderate number of structures because the background intensities are typically much lower than the marker intensities (see also Figs. 3, 8).

### Precision and Accuracy of the Localization Algorithm

The feasibility of the 2D localization approach for a range of FMC positions within the field of view is illustrated in Fig. 1b. Figure 5 illustrates the reproducibility of the fitted 2D-GF positions in the experimental series. The analysis of the 2D distances from that position yields (rounded) maximum values of 0.2, 0.1, and 0.1 mm for NSA = 1, 2, and 4, respectively. The independent check with the markers near the corners of the baseplate (see Fig. 1b) yielded an average, ie, mean  $\pm$  SD (extreme) 2D displacement of  $0.2 \pm 0.2$  (0.6) mm.

The results of the accuracy measurement are given in Fig. 6. The plot shows the calculated 3D difference between the measured and the expected position as a function of marker distance from the isocenter. The



**Figure 4.** Marker discrimination under simulated critical conditions using a transverse TrueFISP image of a volunteer's abdomen (see also Fig. 3). The segmentation threshold has been deliberately reduced to only  $\approx 14\%$  ( $1/7$ ) of the optimized original value. **a:** Segmented image. The threshold is so low that not only background signal intensities in the abdomen but also noise outside the body was segmented. This resulted in 2353 successful 2D-GF fitting attempts yielding 1021 unique peak positions. **b:** Successful fits meeting ( $n = 55$ , squares) or violating (asterisks,  $n = 966$ ) the local contrast criterion ( $a/b > c_{min}$ , see Table 1). **c:** Successful fits meeting ( $n = 208$ , squares) or violating ( $n = 808$ ) the maximum (fitted) peak width criterion ( $\sigma_{x/y} < \sigma_{max}$ , see Table 1); X signs indicate violations in  $x$  only, plus (+) signs in  $y$  only, and asterisks in both  $x$  and  $y$  directions. Only five fit results met both local contrast and maximum peak width criteria (thick squares). Despite two nonmarker peaks in an inconspicuous area, peak matching was still successful (see Table 2).

results of the angular accuracy of our localization method are summarized in Fig. 7.

The feasibility of 3D localization is illustrated in Fig. 8. The surface rendering in Fig. 8d gives an overview of the volunteer's anatomy (here, right knee) relative to the FMC, which was fixed above the knee. The corresponding projection MR images in three orthogonal planes are shown in Fig. 8a-c. Figure 8 also illustrates that the exact amplitude of the marker signals varied between

individual markers and between orthogonal views of the same marker.

## DISCUSSION

Marker localization by morphological analysis of the signal distributions in a fully reconstructed 2D image is feasible and offers a number of benefits over 1D projection measurements. Most of all, standard imaging protocols may be used that remove the need for implement-

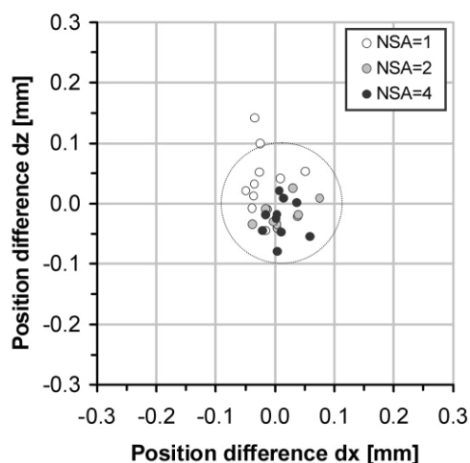


**Figure 5.** Reproducibility of 2D localization algorithm for 10 flip angles (FA) in the  $0.5^\circ$ - $1.4^\circ$  range for which the background-subtracted marker signals were maximal. For each FA, FLASH images were acquired with three NSAs. Plot shows difference in 2D position ( $x,z$ ) of one fiducial marker with respect to the average position of all 30 values. That marker was located relatively close (at a 45-mm distance) to the isocenter. Circle indicates 95% confidence interval for all values assuming a normal distribution of the 2D differences. Displayed plot range approximately corresponds to pixel dimension.

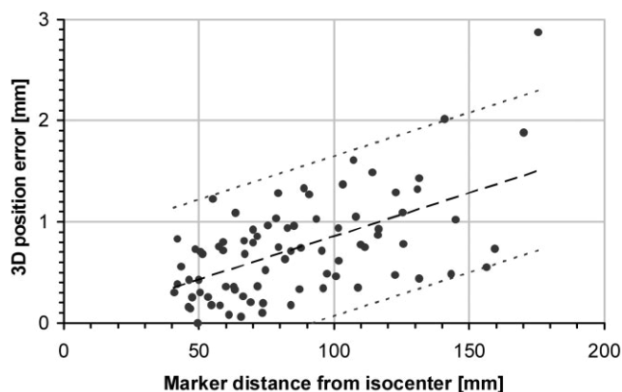


**Figure 6.** Calculated error in 3D position of the fiducial markers. In the entire range of marker distances  $r_M$  from the isocenter, the data may be fitted by a simple line (long dashes) that coincidentally intercepts near zero so that the average 3D error may be approximated by  $d_{3D} = 0.0086 \cdot r_M$ . The actual values are scattered more or less uniformly around that line, apparently independent of the marker distance. Assuming an approximate normal distribution of the differences between actual and average 3D position error, the standard deviation of these differences (0.40 mm) may be used to estimate the variation in that series. The short dashed lines indicate the corresponding 95% confidence interval.

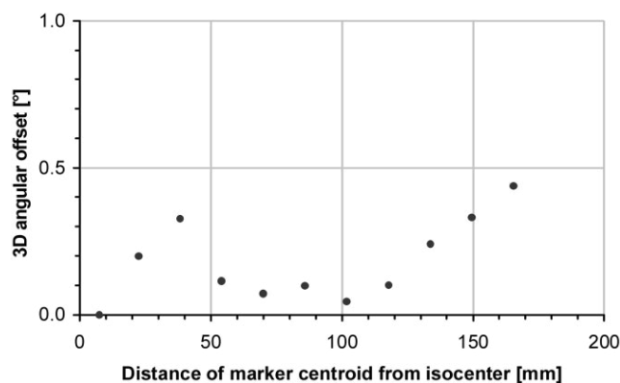


**Figure 7.** Calculated offset in angular orientation of the FMC realized at different distances from the isocenter. At each position the 3D centroid and the normal vector of the plane defined by these markers were calculated. The neutral position of the FMC (Fig. 1) was chosen as reference and had a minimal distance to the isocenter (7.4 mm). The plot shows the angular offsets of the normal vectors with respect to that of the reference FMC as a function of the distance between FMC centroid and isocenter.

ing vendor- and hardware-specific pulse sequences. Such an approach is also very flexible. The detection algorithm may be tuned to different pulse sequences and, most important, to different imaging conditions (coil selection and geometry, imaging region) without having to modify the pulse sequence. It is worth noting that all results presented here were obtained with the same set of analysis parameters. The deviation between repeated measurements near the isocenter was negligible, which demonstrates the high reproducibility of the method. Even at larger distances and between different phase-encode directions variations were very small. While a simple consideration of the maximum signal value would only yield discrete locations as position estimates, a 2D-GF fitting allows a subpixel localization of the centroid. The high reproducibility also suggests that the acquisition might be sped up by reducing the base resolution of the images.

The key to a successful implementation was a thorough implementation of the localization algorithm. To obtain numerical convergence, we used the particular position of the maximum signal within the 2D-LDR and a common value close to the diameter of the signal source as initial values for  $(\mu_x, \mu_y)$  and  $(\sigma_x, \sigma_y)$ , respectively. In contrast, convergence was relatively insensitive to the exact choice of  $a$  and  $b$ . We consider it very unlikely to miss a true peak with such an initial selection, because the numerical fitting was highly successful even in random background regions.

In the subsequent phase of the localization, suitable morphological parameters had to be defined to identify more plausible results. The absolute signal amplitudes between otherwise identical markers, however, showed larger variations that may be explained by experimental factors like the resonant tuning of the markers or their position and orientation within the receiver coil. Therefore, the fitted peak amplitude alone might not be the best choice for marker identification. In addition, we

used the peak widths  $\sigma_x$  and  $\sigma_y$  for morphological analysis, which turned out to be a powerful criterion to differentiate between marker and nonmarker signals. A possible explanation involves the above-mentioned experimental factors. If they do not necessarily induce large intramarker variations of the 2D signal distribution, then the peak width should not change the way that the amplitude does. The range of acceptable peak widths was optimized by observing the values obtained for true marker signals under different experimental conditions. Likewise, the peak asymmetry, defined as the ratio between the larger and the smaller width, helped to rule out successful fits of nonmarker signals, for example, in the phase dispersion regions of TrueFISP images.

Unlike other algorithms that only use two orthogonal scan planes for the determination of 3D coordinates, we acquired the third scan plane as well. Although this adds 50% to the scan time, it provides more reliability and flexibility for the determination. For example, our version allows correct 3D localization also for cases where more or less than three markers were identified in a 2D image. We actually allowed having a range of

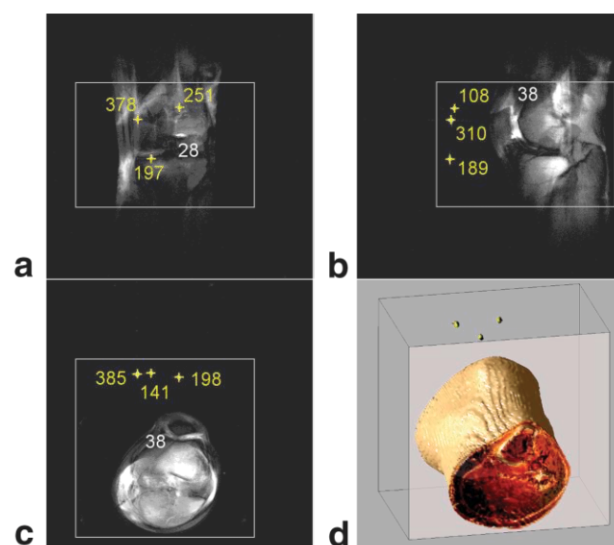


**Figure 8.** Illustration of fiducial marker localization in three dimensions. The FMC was placed above a volunteer's right knee and imaged with the knee coil. Coronal (a), sagittal (b), and (c) transverse marker images using a TrueFISP pulse sequence (FOV =  $300 \times 300$  mm<sup>2</sup>, SL = 200 mm) and a low flip angle (FA = 1°). Yellow crosses indicate the positions of the detected markers. Window settings (width and level) were adjusted to enhance the low-intensity anatomical signal remaining at such a low flip angle. Numbers indicate maximum intensities of anatomical background (white) and marker signals (yellow). If signal intensities are displayed at full scale (auto window) the anatomical background is not discernible and only the marker signals are visible (not shown here). **d:** Illustration of the 3D geometry using a surface-rendered view of the knee and markers with a semitransparent overlay of a transverse MR image in pseudocolor (TrueFISP, FOV =  $200 \times 200$  mm<sup>2</sup>, matrix =  $128 \times 128$ , SL = 3.5 mm, 64 slices, FA = 10°). Note that the imaging volume (also indicated in a–c as gray frames) is smaller than that of the marker detection sequence.

zero to five potential marker peaks in any of the three images. This is only possible due to the additional coordinate information from the third scan plane, which may also resolve potential conflicts arising from coordinates that happen to lie close to each other. In addition, the average of two coordinates should also be a better estimator for the true position.

An implementation of a localization algorithm based on 1D projections and intended for the fast 3D tracking of markers was reported by Flask et al (32). They designed a fast imaging with steady-state precession (FISP) pulse sequence with radial  $k$ -space sampling and limited projection reconstruction (LPR). With such a technique, however, discrimination of the marker from the noise signals may be challenging due to the limited number of samples. Therefore, they applied an extra dephasing gradient perpendicular to the imaging plane to further suppress or eliminate the global background signals from the 1D projections. Their work describes nicely how the SNR will depend on both the flip angle as well as the amplitude of the dephasing gradient but also illustrates the various efforts that have to be made to balance spatial accuracy and acquisition time.

In contrast to their work, our goal was the design of a marker localization that supplies high accuracy for MR-guided interventions but does not need to run in real time. The main purpose is an automated and immediate co-registration between patient positions inside and outside the magnet that is required for a potential navigation concept in a closed-bore MR scanner. A different application is the immediate control of an instrument position that was realized outside the scanner, either manually or with the help of a navigation system. Mounting the fiducial markers in a fixed geometry to an instrument holder that is either manually attached to the patient table or part of a robotic arm will then allow the immediate acquisition of MR control images in scan planes that are exactly defined by the marker geometry. For all these applications, marker localization should be relatively fast, but does not need to be in the sub-second range. Also, we have not yet explored potential acceleration schemes like half Fourier techniques, radial  $k$ -space sampling—especially with limited projection reconstruction—or simply matrix sizes less than  $512 \times 512$  because our focus was on positional and angular accuracy. For example, an angular offset of  $2$  ( $3$ ) $^\circ$  alone will result in a position displacement of  $3.5$  ( $5.2$ ) mm at the end of a 10-cm-long instrument. The clinical experience with robotic devices for closed-bore scanners has already been described for biopsies of the breast and prostate, respectively (37,38).

In its current implementation, computation of the marker positions took 1–2 seconds, which compares well with the 12–25 seconds reported for a commercial product, although processing times will vary between hardware platforms (30). While the commercial solution required the optimization of an absolute threshold that was also reported to depend on the slice thickness, our algorithm uses dynamic thresholds derived from the signal characteristics of an individual image and does not depend on slice thickness. Therefore, we believe that our approach is very flexible, which is also sup-

ported by the fact that the presented results were obtained with the same set of analysis parameters.

Silverman et al (14) investigated the accuracy of an optical stereotactic localization system built into an open 0.5T scanner. They found that the system was most accurate near the isocenter, with a maximum measured error of 3.1 mm within a sphere of radius 25 mm about the isocenter. They also reported maximum errors of 3.9, 5.7, and 7.5 mm for points within a radius of 100, 150, and 200 mm, respectively. Flask et al used commercial oil-filled markers that were tuned to the resonance frequency of a 0.2T MR scanner (82.5 Hz). They determined maximum errors of 3 mm and less than  $3^\circ$  for markers located within 80 mm of the isocenter. Therefore, our maximum position errors of 1.5 mm and 1.7 mm (within 80 and 100 mm, respectively, and estimated at the upper limit of the 95% confidence interval) are 1.5–2.2 mm more accurate than the reference values reported for localization using inductively coupled markers and an optical device, respectively. Flask et al also made attempts with 2D morphological image processing but reported that they could not reproduce the level of precision achieved with their analytic approach based on an LPR-FISP sequence (39).

The 1.7-mm accuracy in 3D position derived here provides an excellent safety margin for interventional procedures within a 100-mm sphere. For even an average-sized patient in standard position on the table, however, an 80- or 100-mm sphere around the isocenter will lie largely if not completely inside the body. Instead, entry points for percutaneous procedures on the skin are likely to be at larger distances from the isocenter, in particular, for a lateral access to the lesion. In addition, the markers will be placed above rather than on the skin or will be mounted on a device (eg, holder or localizing wand), which will further increase the typical distance from the isocenter.

Therefore, we believe that is important to provide values for the positional and angular accuracy beyond 100 mm because they are more relevant in practice. In our case this could happen by providing the plot of Fig. 7 or by simply stating that the maximum position error was less than 3 mm at a 175-mm distance. In addition, the maximum angular offset in the investigated range was  $0.44^\circ$ , which would correspond to a maximum displacement of only 0.8 mm at the tip of a 10-cm-long instrument. These results demonstrate that our method is very accurate in a restricted range (up to 100 mm) but is also suited for distances up to around 200 mm. It should be noted that the accuracy might be improved by using more than three markers for the FMC, as reported for a configuration with four markers (29).

The main reason for increasing deviations at larger distances from the isocenter are the nonlinearities of the gradient fields, which affects other active and passive localization techniques as well. Although that effect may be quantified by a spherical harmonic expansion in three directions (40), a possible correction for nonlinear gradients was beyond the scope of this feasibility study, but is expected to yield more accurate results.

In conclusion, we believe that 2D morphological image processing based on 2D Gaussian functions is a



reliable and accurate method to determine the 3D localization of MR-visible markers. The presented algorithm requires no prior knowledge of the exact number nor the absolute or relative position of the markers. The localization method is simple and flexible because no dedicated imaging coils and pulse sequences are needed. It also appears effective and safe for clinical use due to the lack of connecting wires. The approach, however, is currently not suited for tracking applications due to the time required for acquisition and full 2D reconstruction of the MR images.

## REFERENCES

- Nour SG, Lewin JS. Percutaneous biopsy from blinded to MR guided: an update on current techniques and applications. *Magn Reson Imaging Clin N Am* 2005;13:441-464.
- Gedroyc WM. Magnetic resonance guidance of thermal ablation. *Top Magn Reson Imaging* 2005;16:339-353.
- Koenig CW, Duda SH, Truelsenbach J, et al. MR-guided biopsy of musculoskeletal lesions in a low-field system. *J Magn Reson Imaging* 2001;13:761-768.
- Adam G, Bucker A, Nolte-Ernsting C, Tacke J, Gunther RW. Interventional MR imaging: percutaneous abdominal and skeletal biopsies and drainages of the abdomen. *Eur Radiol* 1999;9:1471-1478.
- Causar PA, Piron CA, Jong RA, et al. MR imaging-guided breast localization system with medial or lateral access. *Radiology* 2006;240:369-379.
- deSouza NM, Coutts GA, Puni RK, Young IR. Magnetic resonance imaging guided breast biopsy using a frameless stereotactic technique. *Clin Radiol* 1996;51:425-428.
- Konig CW, Truelsenbach J, Fritz J, Lauer UM, Claussen CD, Pereira PL. Contrast enhanced MR-guided biopsy of hepatocellular carcinoma. *Abdom Imaging* 2004;29:71-76.
- Rofsky NM, Yang BM, Schlossberg P, Goldenberg A, Teperman LW, Weinreb JC. MR-guided needle aspiration biopsies of hepatic masses using a closed bore magnet. *J Comput Assist Tomogr* 1998;22:633-637.
- Beyersdorff D, Winkel A, Hamm B, Lenk S, Loening SA, Taupitz M. MR imaging-guided prostate biopsy with a closed MR unit at 1.5 T: initial results. *Radiology* 2005;234:576-581.
- Hata N, Jinzaki M, Kacher D, et al. MR imaging-guided prostate biopsy with surgical navigation software: device validation and feasibility. *Radiology* 2001;220:263-268.
- Steinmeier R, Fahlbusch R, Ganslandt O, et al. Intraoperative magnetic resonance imaging with the magnetom open scanner: concepts, neurosurgical indications, and procedures: a preliminary report. *Neurosurgery* 1998;43:739-747.
- Gering DT, Nabavi A, Kikinis R, et al. An integrated visualization system for surgical planning and guidance using image fusion and an open MR. *J Magn Reson Imaging* 2001;13:967-975.
- Maciunas RJ, Dean D, Lewin J, Selman WR, Ratcheson RA. Integration of neurosurgical image guidance and an intraoperative magnetic resonance scanner. The University Hospitals of Cleveland experience. *Stereotact Funct Neurosurg* 2003;80:136-139.
- Silverman SG, Collick BD, Figueira MR, et al. Interactive MR-guided biopsy in an open-configuration MR imaging system. *Radiology* 1995;197:175-181.
- Genant JW, Vandevenne JE, Bergman AG, et al. Interventional musculoskeletal procedures performed by using MR imaging guidance with a vertically open MR unit: assessment of techniques and applicability. *Radiology* 2002;223:127-136.
- Salomonowitz EK, Cejna M, Dewey C. Simple and effective technique of guided biopsy in a closed MRI system. *Abdom Imaging* 2000;25:638-642.
- Busse H, Schmitgen A, Trantakis C, Schober R, Kahn T, Moche M. Advanced approach for intraoperative MRI guidance and potential benefit for neurosurgical applications. *J Magn Reson Imaging* 2006;24:140-151.
- Zimmermann H, Muller S, Gutmann B, et al. Targeted-HASTE imaging with automated device tracking for MR-guided needle interventions in closed-bore MR systems. *Magn Reson Med* 2006;56:481-488.
- Wacker FK, Vogt S, Khamene A, et al. An augmented reality system for MR image-guided needle biopsy: initial results in a swine model. *Radiology* 2006;238:497-504.
- Dumoulin CL, Souza SP, Darrow RD. Real-time position monitoring of invasive devices using magnetic resonance. *Magn Reson Med* 1993;29:411-415.
- Coutts GA, Gilderdale DJ, Chui M, Kasuboski L, DeSouza NM. Integrated and interactive position tracking and imaging of interventional tools and internal devices using small fiducial receiver coils. *Magn Reson Med* 1998;40:908-913.
- Bock M, Volz S, Zuhlsdorff S, et al. MR-guided intravascular procedures: real-time parameter control and automated slice positioning with active tracking coils. *J Magn Reson Imaging* 2004;19:580-589.
- Werner R, Krueger S, Winkel A, et al. MR-guided breast biopsy using an active marker: a phantom study. *J Magn Reson Imaging* 2006;24:235-241.
- Wildermuth S, Dumoulin CL, Pfammatter T, Maier SE, Hofmann E, Debatin JF. MR-guided percutaneous angioplasty: assessment of tracking safety, catheter handling and functionality. *Cardiovasc Intervent Radiol* 1998;21:404-410.
- Nitz WR, Oppelt A, Renz W, Manke C, Lenhart M, Link J. On the heating of linear conductive structures as guide wires and catheters in interventional MRI. *J Magn Reson Imaging* 2001;13:105-114.
- Kugel H, Bremer C, Puschel M, et al. Hazardous situation in the MR bore: induction in ECG leads causes fire. *Eur Radiol* 2003;13:690-694.
- Ladd ME, Quick HH. Reduction of resonant RF heating in intravascular catheters using coaxial chokes. *Magn Reson Med* 2000;43:615-619.
- Weiss S, Vernickel P, Schaeffter T, Schulz V, Gleich B. Transmission line for improved RF safety of interventional devices. *Magn Reson Med* 2005;54:182-189.
- Kremser C, Plangger C, Bosecke R, Pallua A, Aichner F, Felber SR. Image registration of MR and CT images using a frameless fiducial marker system. *Magn Reson Imaging* 1997;15:579-585.
- Krishnan R, Hermann E, Wolff R, Zimmermann M, Seifert V, Raabe A. Automated fiducial marker detection for patient registration in image-guided neurosurgery. *Comput Aided Surg* 2003;8:17-23.
- Burl M, Coutts GA, Young IR. Tuned fiducial markers to identify body locations with minimal perturbation of tissue magnetization. *Magn Reson Med* 1996;36:491-493.
- Flask C, Elgort D, Wong E, et al. A method for fast 3D tracking using tuned fiducial markers and a limited projection reconstruction FISP (LPR-FISP) sequence. *J Magn Reson Imaging* 2001;14:617-627.
- Quick HH, Zenge MO, Kuehl H, et al. Interventional magnetic resonance angiography with no strings attached: wireless active catheter visualization. *Magn Reson Med* 2005;53:446-455.
- Scheffler K, Lehnardt S. Principles and applications of balanced SSFP techniques. *Eur Radiol* 2003;13:2409-2418.
- Mekle R, Hofmann E, Scheffler K, Bilecen D. A polymer-based MR-compatible guidewire: a study to explore new prospects for interventional peripheral magnetic resonance angiography (ip-MRA). *J Magn Reson Imaging* 2006;23:145-155.
- Press WH, Teukolsky SA, Vetterling WT, Flannery BP. *Numerical recipes in C: the art of scientific computing*, 2nd ed. New York: Cambridge University Press; 1992.
- Pfleiderer SO, Reichenbach JR, Azhari T, et al. A manipulator system for 14-gauge large core breast biopsies inside a high-field whole-body MR scanner. *J Magn Reson Imaging* 2003;17:493-498.
- Zangos S, Herzog C, Eichler K, et al. MR-compatible assistance system for puncture in a high-field system: device and feasibility of transgluteal biopsies of the prostate gland. *Eur Radiol* 2007;17:1118-1124.
- Wong EY, Zhang Q, Lee K, Lewin JS, Duerk JL, Wendt M. A novel fiducial marker design with enhanced SNR and extended usable range for wireless localization. In: *Proceedings of the Radiological Society of North America (RSNA), 86th Scientific Meeting and Exhibition*; 2000:166-166.
- Yu H, Fahrigr R, Pelc NJ. Co-registration of x-ray and MR fields of view in a hybrid XMR system. *J Magn Reson Imaging* 2005;22:291-301.

### Arbeit 3 – Eignung von semiaktiven MR-Positionsmarkern für interventionelle Zwecke

Nach dem Nachweis der Machbarkeit einer neuartigen, bildgestützten Markerlokalisierung wurden die Miniatur-HF-Spulen in der folgenden Arbeit [82] einer umfassenden Überprüfung unter klinischen Randbedingungen unterzogen. Die Anforderungen übertrafen insofern das übliche Maß, als dass die Marker nicht allein für den medizinischen Anwender *sichtbar* sondern mit der entwickelten Methode auch automatisch *lokalisierbar* sein sollten. Hierzu wurden die MRT-Signalintensitäten in Abhängigkeit verschiedener Fertigungs- bzw. Messparameter bestimmt. Als signalgebende Medien wurden Leitungswasser, destilliertes Wasser und Kontrastmittellösung betrachtet. Die Bildgebung erfolgte über einen breiten Flipwinkelbereich von  $0,1^\circ$  bis  $90^\circ$  mit zwei schnellen Pulssequenzen – einem  $T_1$ -gewichteten *gespoilten* Gradientenecho (Eigenname: *FLASH*) sowie einer  $T_1/T_2$ -gewichteten *balanced steady-state free precession* b-SSFP-Sequenz (Eigenname: *TrueFISP*).

Für die Bewertung waren insbesondere die Lokalisierbarkeit im gesamten Messvolumen sowie bei variabler Spulenausrichtung bedeutsam. Als Parameter wurde der Winkel  $\theta_{\text{TRA}}$  zwischen Spulenachse und transversaler Ebene gewählt. Die Marker zeigten mit der *TrueFISP*-Sequenz generell höhere Kontrastverhältnisse als mit der *FLASH*-Sequenz. Als Referenz diente hierbei das *summierte* Hintergrundsignal eines MR-Phantoms des Herstellers. Im Gegensatz zur *FLASH*-Sequenz ergaben sich mit der *TrueFISP*-Sequenz zudem keine nennenswerten Kontrastunterschiede zwischen den drei Signalträgern. Insgesamt generierten die Marker nahezu über das gesamte untersuchte Messfeld ( $\pm 215$  mm) sowie für bis zu 82% aller theoretisch möglichen Spulenausrichtungen ausreichend Kontrast für einen erfolgreichen Nachweis in allen drei Bildebenen. Für den Einsatz als statische, extrakorporale Referenzmarker sollte es praktisch immer möglich sein, die HF-Spulen dementsprechend zu positionieren ( $|\theta_{\text{TRA}}| \leq 55^\circ$ ). Für dynamische Anwendungen ließe sich das Problem z. B. durch zusätzliche orthogonale HF-Spulen lösen, die wechselseitig zur optimalen Darstellung kämen.

Zur Beurteilung der thermischen Sicherheit wurde die HF-Erwärmung während der Bildgebung untersucht, beispielhaft mit einer b-SSFP-Sequenz (*TrueFISP*), einem schnellen *single-shot* Spinecho (*HASTE*) sowie einem *gespoilten* 3D-Gradientenecho (*VIBE*). Nach 10-minütiger Dauereinwirkung wurden *in der Flüssigkeit* maximale Temperaturerhöhungen von 5,1°C (*HASTE* und *TrueFISP*) bzw. 1,3°C (*VIBE*) beobachtet, die bei extrakorporaler Anwendung der Marker unbedenklich sein sollten. Des Weiteren haben diese Sequenzen üblicherweise kürzere Akquisitionszeiten bzw. werden durch Messpausen unterbrochen, in denen die Temperatur – wie auch hier beobachtet – relativ rasch abfällt. Durch eine spezielle elektrische bzw. thermische Isolation der Marker ließe sich das Risiko einer Gefährdung weiter reduzieren.

Abschließend wurde noch eine Anordnung von drei Markern auf ihre praktische Eignung zur Festlegung einer MRT-Bildebene geprüft. Hierzu wurden die Marker koplanar mit einem ringförmigen, wassergefüllten Schlauch auf einer Platte angeordnet und dann willkürlich in 20 verschiedene räumliche Lagen gebracht. Als Signalträger wurde Leitungswasser verwendet. Die aus den Markerbildern (*TrueFISP*) bestimmten 3D-Positionen dienten dann der geometrischen Festlegung einer nachfolgenden Kontrollbildgebung. In 65% der Fälle (13 von 20) war der Ring optimal angeschnitten, in den verbleibenden Fällen ließ sich aus den leichten Ungenauigkeiten eine mittlere bzw. maximale Winkelabweichung von fast 0,6° bzw. 3,4° abschätzen. Auf MRT-Bildern mit einer gebräuchlichen Schichtdicke (hier 2,8 mm) war der Ring praktisch immer durchgehend sichtbar und wies allein bei den ungenauen Fällen eine leichte Signalvariation entlang des Durchmessers auf.

Insgesamt zeigten die kompakten, induktiv gekoppelten HF-Spulen in der *balanced SSFP*-Bildgebung mit sehr kleinem Flipwinkel (hier 0,3°) ausgezeichnete Signaleigenschaften und bieten sich damit als zuverlässige und relativ sichere MR-Positionsmarker für klinische Anwendungen an.

# Suitability of miniature inductively coupled RF coils as MR-visible markers for clinical purposes

Nikita Garnov and Gregor Thörmer

*Department of Diagnostic and Interventional Radiology, Leipzig University Hospital, Leipzig D-04103, Germany*

Robert Trampel

*Max Planck Institute for Human Cognitive and Brain Sciences, Leipzig D-04103, Germany*

Wilfried Gründer

*Department of Medical Physics and Biophysics, Leipzig University, Leipzig D-04107, Germany*

Thomas Kahn, Michael Moche, and Harald Busse<sup>a)</sup>

*Department of Diagnostic and Interventional Radiology, Leipzig University Hospital, Leipzig D-04103, Germany*

(Received 9 May 2011; revised 12 August 2011; accepted for publication 28 September 2011; published 31 October 2011)

**Purpose:** MR-visible markers have already been used for various purposes such as image registration, motion detection, and device tracking. Inductively coupled RF (ICRF) coils, in particular, provide a high contrast and do not require connecting wires to the scanner, which makes their application highly flexible and safe. This work aims to thoroughly characterize the MR signals of such ICRF markers under various conditions with a special emphasis on fully automatic detection.

**Methods:** The small markers consisted of a solenoid coil that was wound around a glass tube containing the MR signal source and tuned to the resonance frequency of a 1.5 T MRI. Marker imaging was performed with a spoiled gradient echo sequence (FLASH) and a balanced steady-state free precession (SSFP) sequence (TrueFISP) in three standard projections. The signal intensities of the markers were recorded for both pulse sequences, three source materials (tap water, distilled water, and contrast agent solution), different flip angles and coil alignments with respect to the  $B_0$  direction as well as for different marker positions in the entire imaging volume (field of view, FOV). Heating of the ICRF coils was measured during 10-min RF expositions to three conventional pulse sequences. Clinical utility of the markers was assessed from their performance in computer-aided detection and in defining double oblique scan planes.

**Results:** For almost the entire FOV ( $\pm 215$  mm) and an estimated 82% of all possible RF coil alignments with respect to  $B_0$ , the ICRF markers generated clearly visible MR signals and could be reliably localized over a large range of flip angles, in particular with the TrueFISP sequence ( $0.3^\circ$ – $4.0^\circ$ ). Generally, TrueFISP provided a higher marker contrast than FLASH. RF exposition caused a moderate heating ( $\leq 5^\circ\text{C}$ ) of the ICRF coils only.

**Conclusions:** Small ICRF coils, imaged at low flip angles with a balanced SSFP sequence showed an excellent performance under a variety of experimental conditions and therefore make for a reliable, compact, flexible, and relatively safe marker for clinical use. © 2011 American Association of Physicists in Medicine. [DOI: 10.1118/1.3655027]

Key words: MR markers, detection, image guidance, interventional MRI, point-based registration

## I. INTRODUCTION

MR-visible markers are used for various referencing purposes and are usually categorized with respect to their design and method of detection. Passive markers have no electric components and basically rely on the magnetic properties of a particular material. A positive MR image contrast can be achieved with paramagnetic agents like gadolinium compounds, which reduce the proton T1 relaxation time of neighboring (water) molecules. Corresponding markers are commercially available in various forms that can be directly attached to the skin, for example, to define areas of interest or plan percutaneous interventions.<sup>1</sup> In order to obtain sig-

nals of a particular intensity, size or shape, paramagnetic markers can also be custom-built by filling a solution with defined relaxation properties into spheres, tubes or other matching structures. Diamagnetic materials produce a susceptibility artifact (negative contrast) and commercial gold markers, for example, are used as fiducials for brachytherapy. Other applications of passive markers include the registration of frameless guidance and navigation systems<sup>2,3</sup> as well as the accurate fusion of MR images with data from other modalities, for example X-ray,<sup>4</sup> computed tomography,<sup>5</sup> positron emission tomography,<sup>6,7</sup> or single photon emission computed tomography.<sup>8</sup> In a feasibility study, capsules filled with Gd-DTPA solution have even been

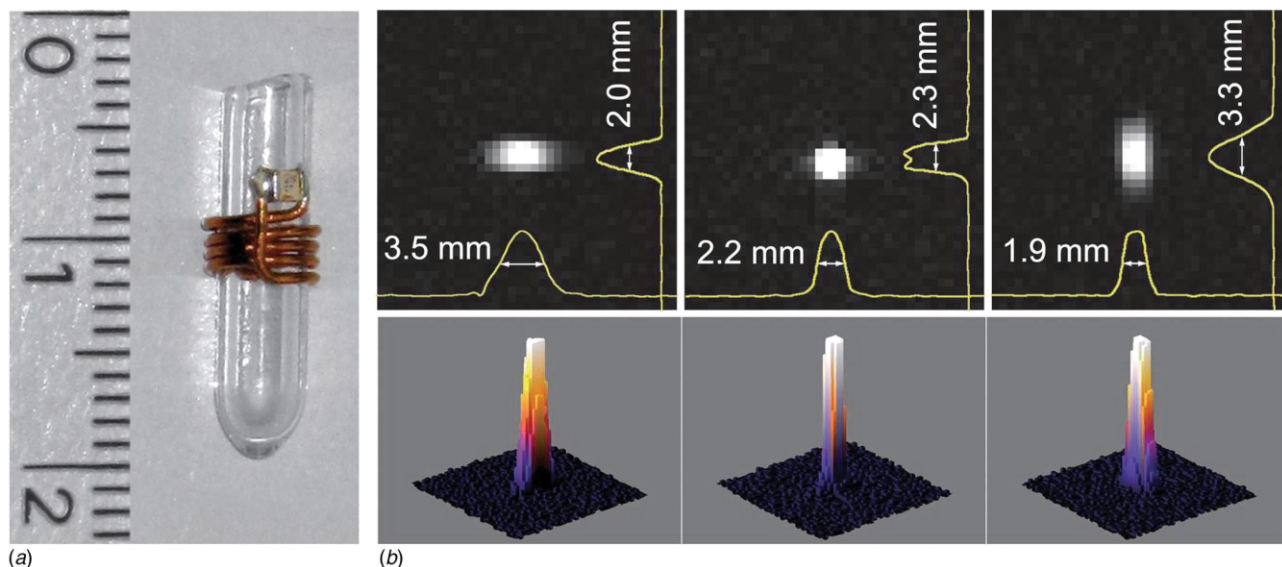


Fig. 1. (a) Resonant RF coil as MR marker (numbers are centimeters). (b) Details ( $40 \times 40$  pixels) of marker MR images (TrueFISP sequence, flip angle of  $0.3^\circ$ , spatial resolution  $0.586$  mm/pixel) in standard views (sagittal, coronal, transverse) and respective intensity profiles. Millimeter values represent full width at half maximum of the 1D projections of the marker signals onto the respective axes.

swallowed and then imaged to assess the colonic transit time.<sup>9</sup> Irrespective of the particular design, the depiction of passive markers usually involves two-dimensional image reconstruction, which is rather time consuming.

Active MR markers are resonant pick-up RF coils that are connected to a separate receiver channel of the MRI scanner. They have been used for the detection of unwanted patient motion<sup>10</sup> and the tracking of interventional instruments like biopsy needles<sup>11</sup> or catheters.<sup>12</sup> Active markers can be quickly localized by a dedicated pulse sequence that uses orthogonal one-dimensional (1D) projections of the marker signal to determine the marker position in three dimensions (3D). One drawback of this design is that inductive coupling between the imaging coils and long conducting structures (connecting wires) poses a safety hazard.<sup>13</sup>

Semiactive markers based on inductively coupled RF (ICRF) coils are resonant circuits laid out in a compact closed loop (wireless with respect to the scanner), which makes them relatively simple and safe to use.<sup>3</sup> They will also be detected in fully reconstructed MR images. Unlike passive ones, however, the contrast of ICRF markers with respect to the anatomical background can be largely increased by simply imaging them at small flip angles (FA),<sup>14,15</sup> which also provides more flexible and robust options for automatic localization.<sup>14,16,17</sup>

Although active markers have some inherent advantages over ICRF coils, the most prominent one being fast localization, they have not yet found their way into clinical practice, which is mainly attributed to remaining safety issues and technical effort.<sup>13,18</sup> Semiactive markers, in contrast, are easier to set up and operate<sup>14,16,17</sup> and reports on more routine applications for automatic patient-to-image registration of a clinical navigation solution can be found in the literature.<sup>19,20</sup>

## II. METHODS

### II.A. Marker design

The miniature markers consisted of a solenoid coil with four turns of insulated copper wire ( $0.5$  mm thickness) wound around a glass tube ( $2.2$  mm inner and  $4.0$  mm outer diameter) and an MR-compatible ceramic chip capacitor ( $100$  pF, American Technical Ceramics, NY). The tube was filled with tap water (TW), distilled water (DW), or contrast agent (CA) solution (Dotarem,  $0.5$  mmol/l, Guerbet, Roissy, France, 1:300 dilution in distilled water), which served as source material. The overall dimensions of the marker were  $5 \times 5 \times 6$  mm<sup>3</sup> [Fig. 1(a)]. The circuit was tuned to the frequency of  $63.7$  MHz by slightly adjusting the wire configuration. The inductance of the coil was calculated as  $0.06$   $\mu$ H. The quality factor of the loaded circuit was determined to be  $\approx 110$  by measuring the resulting amplitude of the resonant circuit at different generator frequencies.

### II.B. MRI measurements

Marker imaging was performed in a  $1.5$  T whole-body scanner (Magnetom Symphony, Siemens, Erlangen, Germany) using the built-in body coil. Plastic bottles filled with NiSO<sub>4</sub> solution (Siemens) served as background phantom. A spoiled gradient echo sequence (FLASH, matrix size  $MX = 512 \times 512$ , field of view  $FOV = 300 \times 300$  mm<sup>2</sup>, slice thickness  $ST = 300$  mm, repetition time/echo time  $TR/TE = 12/5.8$  ms, bandwidth  $BW = 220$  Hz/pixel) and a balanced SSFP sequence (TrueFISP,  $MX = 512 \times 512$ ,  $FOV = 300 \times 300$  mm<sup>2</sup>,  $ST = 300$  mm,  $TR/TE = 6.8/2.8$  ms,  $BW = 220$  Hz/pixel) were used to image the markers in three standard projections (sagittal, coronal, transverse). The contrast-to-background ratio (CBR) was calculated as

$$CBR = \frac{S_M - S_B}{S_B} \quad (1)$$

with  $S_M$  and  $S_B$  as average signal intensities calculated in a  $3 \times 3$ -pixel region of interest (ROI) over the marker and a  $40 \times 40$ -pixel ROI over the phantom bottle, respectively. In the coronal projection images,  $S_M$  was corrected for the overlapping signal from the bottle  $S_B$  by subtracting the average intensity of a ROI placed around the marker but excluding the marker region [Figs. 2(a) and 2(b)]. In a clinical setting,

$S_B$  will correspond to the signal from the anatomical background tissue which happens to project around the marker.

Suitability of the markers for automatic detection of the signals was investigated by using a previously described localization algorithm. That approach attempts to fit 2D Gaussian functions to the signal distributions in fully reconstructed MR images. The 3D position of the marker is then

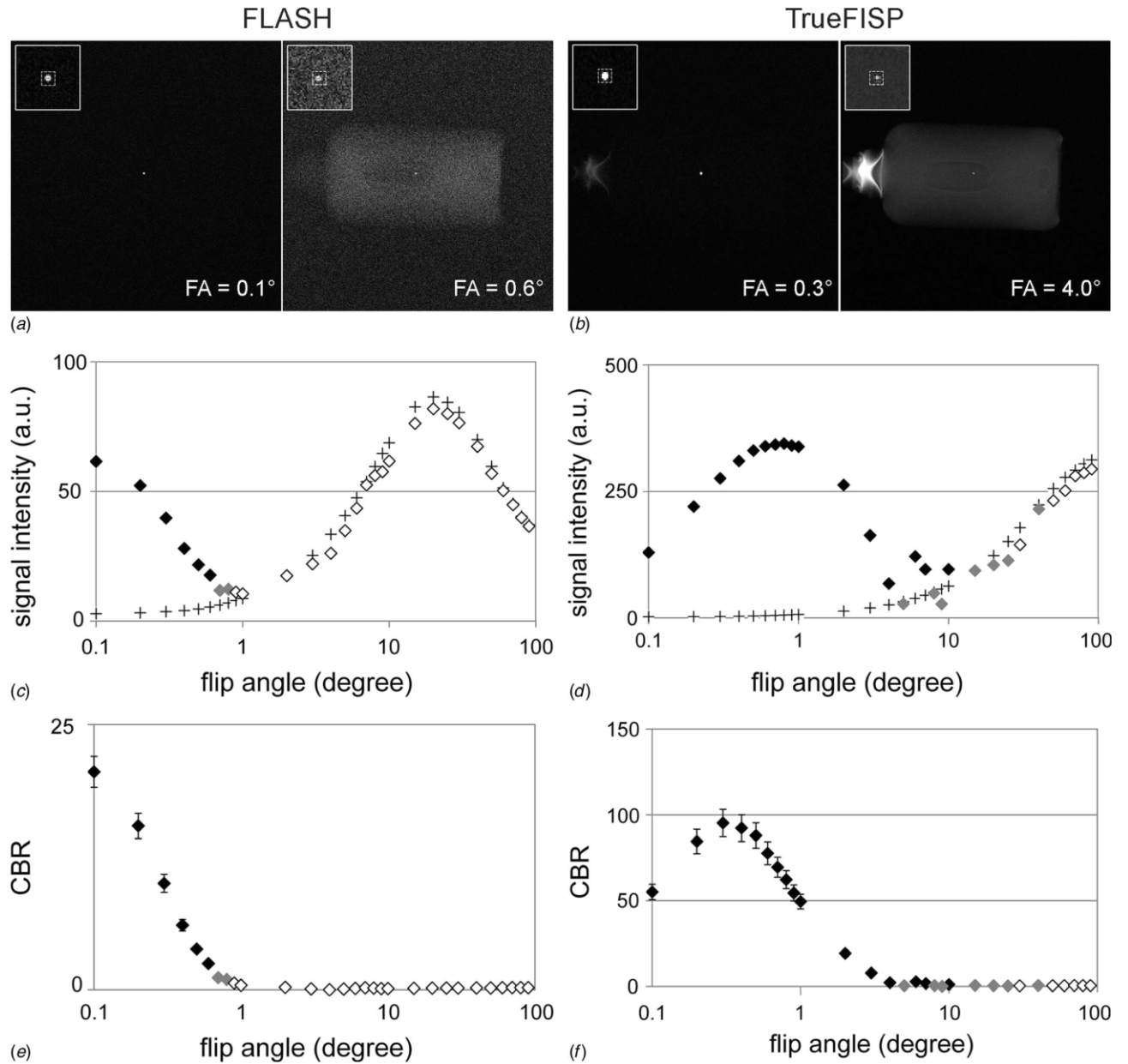


Fig. 2. (a) Sample coronal FLASH images at a flip angle of  $0.1^\circ$  (optimum) and  $0.6^\circ$  (highest possible value for automatic detection) with the tap water (TW) markers projecting over the phantom bottle. Insets denote background (solid line) and marker (dashed line) ROIs used for CBR calculation. (b) Corresponding coronal MR images obtained with a TrueFISP sequence. [(c) and (d)] Variation of marker  $S_M$  and background  $S_B$  signals with flip angle (logarithmic scale) on coronal images for FLASH and TrueFISP, respectively. Plots show the marker signal intensity  $S_M$  (diamonds) and average intensity of the background signal  $S_B$  (plus signs, +). [(e) and (f)] Corresponding plots of CBR values on a logarithmic scale. Filled diamonds ( $\blacklozenge$ ) in black and gray correspond to automatic marker detection in three and two views, respectively, and indicate successful marker localization in 3D. An open diamond symbol ( $\lozenge$ ) means that the marker was detected in less than two views and could therefore not be automatically localized in 3D. In the case of smaller errors, the corresponding bars are obscured by the larger plot symbols.

determined by mutually matching the coordinates of the fitted 2D peaks in three orthogonal projection images.<sup>14</sup>

### II.C. Flip angle dependence

The signal intensities of the markers were assessed for both pulse sequences (TrueFISP and FLASH, see Sec. II B), 29 different flip angles in the 0.1°–90° range, and for three different source materials (see Sec. II A). All flip angles referred to in the following are the nominal flip angles reported by the scanner.

### II.D. Orientation and position dependence

The dependence of the signal intensity on the coil orientation with respect to the direction of the static magnetic field  $B_0$  was investigated by placing the marker horizontally on a custom-made MR-compatible rotary mount. A goniometric scale allowed an accurate setting of the tilt angle  $\theta_{\text{TRA}}$  between solenoid axis and transverse plane.

Visibility of the markers was also investigated at different positions within the maximum measurement range (50 cm diameter spherical volume) of the scanner. One marker mounted on a brick was translated up to  $\pm 240$  mm (step width 24.0 mm) with respect to the isocenter along the  $x$  (left-right) and  $z$  (head-feet) directions on a standard grid phantom. Translation along the  $y$  direction was not considered due to the symmetry of the  $x$  and  $y$  gradients. The center position of the field of view was shifted in parallel with the marker.

Measurements were performed for both pulse sequences and all source materials (TW, DW, CA, see Sec. II A and Sec. II B) using the flip angle that corresponded to the highest CBR value on the coronal marker images [see Sec. III B and Table I].

### II.E. Marker heating

In order to evaluate the thermal safety of the markers, the inductive heating of the RF coils during MR imaging was measured in an experimental setup. The temperature evolution was recorded over 21 min (1 min baseline, 10 min RF exposition, 10 min cool down) with a four-channel fiber optical thermometer (Fluoroptic 790, Luxtron, Santa Clara, CA) for four

different pulse sequences three of them are routinely used for abdominal imaging: half-Fourier single shot turbo spin echo (HASTE, TR/TE = 1090/121 ms, FA = 150°, whole-body specific absorption rate SAR = 1.93 W/kg as reported by the scanner), volume-interpolated breath-hold examination (VIBE, TR/TE = 3.8/1.4 ms, FA = 15°, SAR = 0.49 W/kg), standard TrueFISP (TR/TE = 4.3/2.2 ms, FA = 72°, SAR = 1.95 W/kg) and the marker sequence [TrueFISP, see Sec. II B] with a low flip angle (TR/TE = 9.7/4.2 ms, FA = 2°, SAR < 0.001 W/kg). One temperature probe was taped on the coil wire and a second one was placed inside the glass tube (signal source: TW) near the center of the solenoid. All measurements were performed at an ambient temperature of  $\approx 24$  °C without air circulation inside the scanner. The temperature evolution with time  $t$  during RF exposition was fitted with an exponential saturation function of the form

$$\Delta T = \Delta T_{\text{max}} \cdot \left(1 - e^{-t/\tau}\right) \quad (2)$$

to estimate the maximum heating  $\Delta T_{\text{max}}$  from the data over the limited exposure time. The time constant  $\tau$  depends on the effectiveness of RF heating and cooling around the temperature probes.

### II.F. Sample application

Practical utility of our MR markers was demonstrated in a sample application where the automatic localization of three ICRF coils was used to track an MR-visible object (circular water-filled tube). Markers and tube were attached to a custom-made board in a coplanar manner [Fig. 6(a)]. This assembly was attached to a flexible MR-compatible holder (Invivo, Schwerin, Germany) and scanned in 20 arbitrary positions and orientations. The localization tool mentioned in Sec. II B<sup>14</sup> was slightly modified such that the coordinates of the detected markers were supplied in the appropriate format for scan plane definition on the MR host. Both a single MR image with a 2.8 mm-thick slice (HASTE, TR/TE = 2440/196 ms, FA = 90°, MX = 512 × 512, FOV = 400 × 400 mm<sup>2</sup>) as well as a 3D block with 10 thinner slices (HASTE, TR/TE = 2440/204 ms, FA = 90°, MX = 512 × 512, FOV = 400 × 400 mm<sup>2</sup>, ST = 1 mm, GAP = 0 mm) were acquired using a large 19 cm-diameter loop coil (Siemens) for signal reception.

TABLE I. Marker performance as a function of flip angle for different source materials and pulse sequences.

		Source material		
		Tap water	Distilled water	Contrast agent
FLASH	FA with highest CBR <sup>a</sup>	0.1°/0.1°/0.1°	0.1°/0.1°/0.1°	0.3°/0.2°/0.3°
	Maximum CBR <sup>a</sup>	20/13/15	21/13/14	69/29/47
	FA with CBR > 70 <sup>a</sup>	—	—	—
	FA with successful localization <sup>b</sup>	0.1°–0.6° (0.7°–0.8°)	0.1°–0.5° (0.6°)	0.1°–2.0° (0.3°–40°)
TrueFISP	FA with highest CBR <sup>a</sup>	0.3°/0.2°/0.3°	0.2°/0.2°/0.2°	0.2°/0.1°/0.2°
	Maximum CBR <sup>a</sup>	95/74/94	125/88/108	88/95/131
	FA with CBR > 70 <sup>a</sup>	0.2°–0.6°/0.2°/0.2°–0.5°	0.1°–0.7°/0.1°–0.3°/0.1°–0.5°	0.1°–0.5°/0.1°–0.2°/0.1°–0.6°
	FA with successful localization <sup>b</sup>	0.1°–4.0° (5.0°–25°)	0.1°–4.0° (5.0°–10°)	0.1°–6.0° (7.0°–20°)

<sup>a</sup>Three values (ranges) correspond to coronal/sagittal/transverse views.

<sup>b</sup>Based on all three (only two) views.

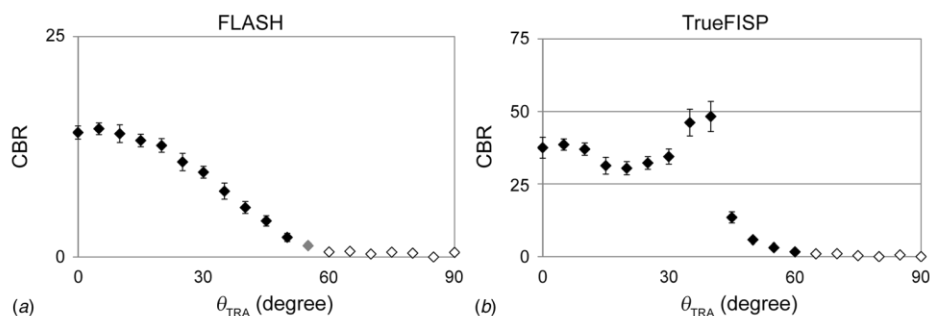


FIG. 3. (a) Variation of CBR with tilt angle  $\theta_{TRA}$  of coil axis for FLASH images (coronal, TW, logarithmic scale). (b) Corresponding CBR values for TrueFISP images. See Fig. 2 for a legend of symbols.

### III. RESULTS

#### III.A. MRI measurements

The markers typically imposed as hyperintense round objects ( $\varnothing = 2.2 \pm 0.1$  mm) in the coronal and as oval objects ( $2.0 \pm 0.1$  mm  $\times$   $3.1 \pm 0.4$  mm) in the sagittal and transverse MR images. The dimensions were measured as full widths at half maximum of the intensity profiles of ten randomly selected TrueFISP images of the marker (signal source: TW) acquired with a flip angle of  $0.3^\circ$  [Fig. 1(b)].

#### III.B. Dependence on flip angle, pulse sequence, and source material

Figure 2 shows the dependence of the marker signal and contrast on the flip angle in coronal images for both pulse sequences. With TrueFISP, the flip angle dependence of both noncontrast (TW and DW) and contrast-filled (CA) markers were comparable. In FLASH images, contrast agent solution provided a higher contrast than the TW and DW samples, which were similar to each other. Overall, all mean CBR values in TrueFISP images were higher than the corresponding values in the FLASH images (Table I). In particular, the TW marker yielded a higher CBR in the TrueFISP image than the contrast-filled CA marker (with the highest CBR) in the FLASH image.

Tap water and distilled water markers (TW, DW) could be best localized with the TrueFISP sequence, in particular for flip angles up to  $4.0^\circ$  and  $10^\circ$  in three and two views, respectively. Contrast-filled markers (CA) could be localized over the  $0.1^\circ$ – $40^\circ$  flip angle range with the FLASH sequence, but marker coordinates from three views were available up to  $2.0^\circ$  only. Irrespective of the underlying pulse sequence, all marker types could be successfully localized in the  $0.1^\circ$ – $0.5^\circ$  range of flip angles.

#### III.C. Orientation and position dependence

Figure 3 shows the orientation dependence of the CBR for a tap water marker (TW). With both pulse sequences, the marker could be automatically localized in 3D for tilt angles  $\theta_{TRA}$  up to  $55^\circ$ . Given the cylindrical symmetry around the  $B_0$  axis, the  $-55^\circ$  to  $+55^\circ$  angle range covers  $\approx 82\%$  of the area of a unit sphere. The contrast-filled (CA) and non-contrast TW markers could be localized up to  $\theta_{TRA} = 60^\circ$  (Table II) in FLASH and TrueFISP images, respectively. Above that tilt angle, automatic 3D localization failed independent of marker type and pulse sequence.

Figure 4 shows the variation of the marker signal as a function of position within the FOV of the scanner. Again, CBR values obtained with the TrueFISP sequence are higher than those with the FLASH sequence [Figs. 4(c) and 4(f)]. In the central region around the isocenter ( $\pm 120$  mm), defined

TABLE II. Marker performance as a function of coil alignment ( $\theta_{TRA}$ ) for different source materials and pulse sequences.

		Sample material		
		Tap water	Distilled water	Contrast agent
FLASH	$\theta_{TRA}$ with highest CBR <sup>a</sup>	$5^\circ/0^\circ/10^\circ$	$0^\circ/0^\circ/0^\circ$	$5^\circ/0^\circ/0^\circ$
	Maximum CBR <sup>a</sup>	14.4/18.2/13.3	13.0/16.2/12.1	43.2/30.6/37.0
	Minimum CBR for automatic detection <sup>a</sup>	1.9/1.2/1.4	3.6/1.2/1.3	2.0/0.7/1.2
	$\theta_{TRA}$ with successful localization <sup>b</sup>	$0^\circ$ – $50^\circ$ ( $55^\circ$ )	$0^\circ$ – $45^\circ$ ( $50^\circ$ – $55^\circ$ )	$0^\circ$ – $55^\circ$ ( $60^\circ$ )
TrueFISP	$\theta_{TRA}$ with highest CBR <sup>a</sup>	$40^\circ/35^\circ/30^\circ$	$40^\circ/35^\circ/35^\circ$	$35^\circ/35^\circ/35^\circ$
	Maximum CBR <sup>a</sup>	48.2/51.9/45.3	44.1/18.8/53.4	55.7/20.0/68.1
	Minimum CBR for automatic detection <sup>a</sup>	1.3/1.1/2.1	2.0/0.1/2.5	3.8/0.3/2.3
	$\theta_{TRA}$ with successful localization <sup>b</sup>	$0^\circ$ – $60^\circ$ (–)	$0^\circ$ – $55^\circ$ (–)	$0^\circ$ – $50^\circ$ ( $55^\circ$ )

<sup>a</sup>Three values (ranges) correspond to coronal/sagittal/transverse views.

<sup>b</sup>Based on all three (only two) views.



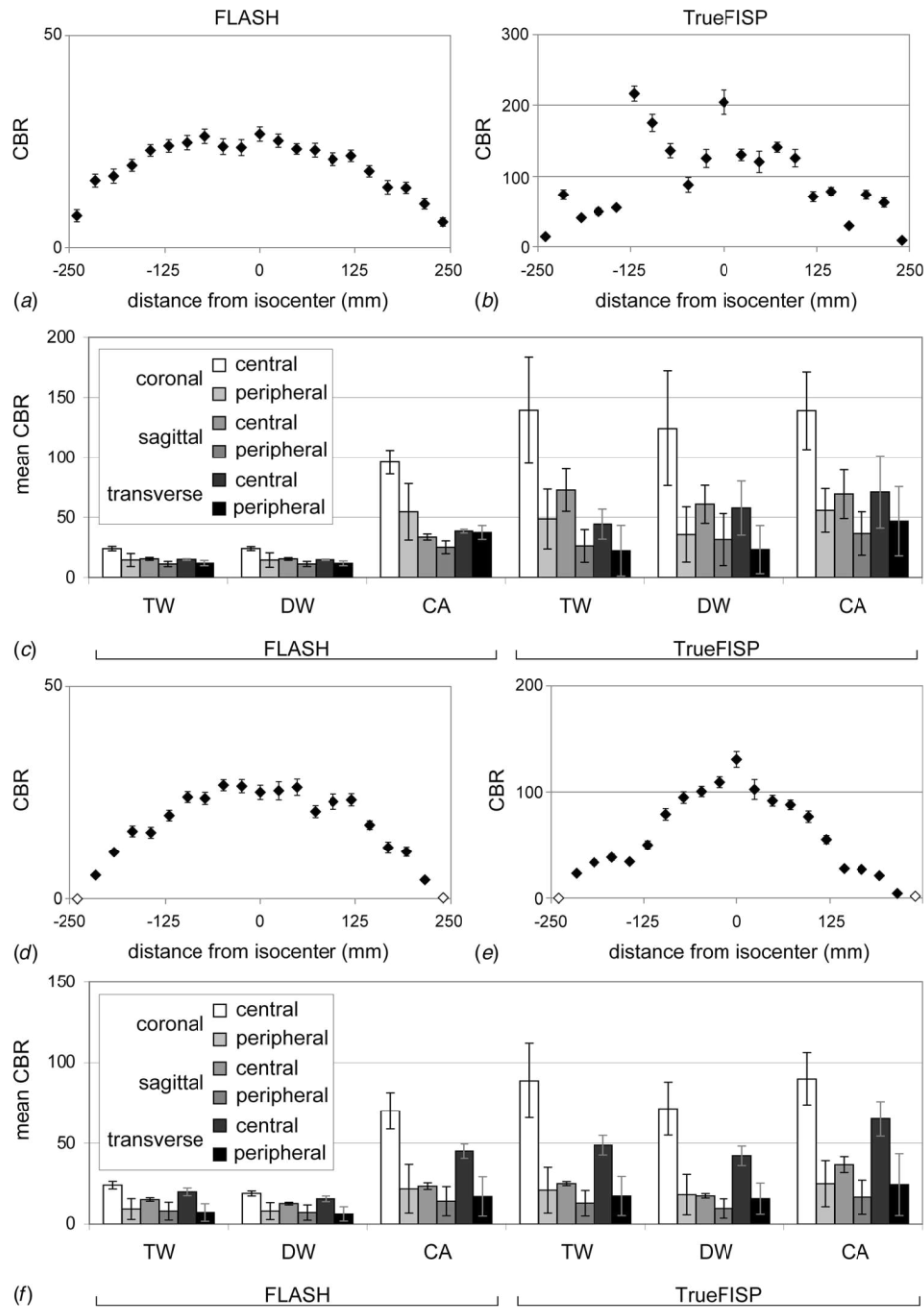


Fig. 4. [(a) and (b)] Variation of CBR with marker translation along the  $z$  axis for FLASH and TrueFISP images, respectively (coronal, TW, logarithmic scale). (c) Mean CBR values for different source materials, image projection planes, FOV regions (see Sec. III C), and pulse sequences for marker translation along the  $z$  axis. [(d) – (f)]: Corresponding CBR values [see Figs. 4(a)–4(c)] for marker translation along the  $x$  axis. See Fig. 2 for a legend of symbols.

as the inner half of the maximum range ( $\pm 240$  mm), CBR values were generally higher than those in the peripheral zone (outer half) [Fig. 4]. Automatic 3D localization was successful for all marker types, both sequences, and all  $x$  and  $z$  positions in the entire FOV but the extreme  $x$  coordinates at  $\pm 240$  mm [Figs. 4(d) and 4(e)].

### III.D. Marker heating

Figure 5 shows the results of the temperature measurements inside the signal source (TW). The corresponding

temperatures measured on the wire were systematically lower with a maximum difference of  $-1.1$  °C. A maximum heating of around  $5$  °C was observed after a 10-min RF exposition of the markers to both TrueFISP and HASTE sequences. The temperature increase for the VIBE sequence was  $<1.5$  °C whereas that of the marker (low flip angle TrueFISP) sequence was negligible. After termination of the sequences, the temperatures dropped rapidly and, 10 min later, reached the starting values for HASTE and VIBE. At this time point, a slightly elevated temperature of about  $0.5$  °C was still observed for the TrueFISP sequence. A

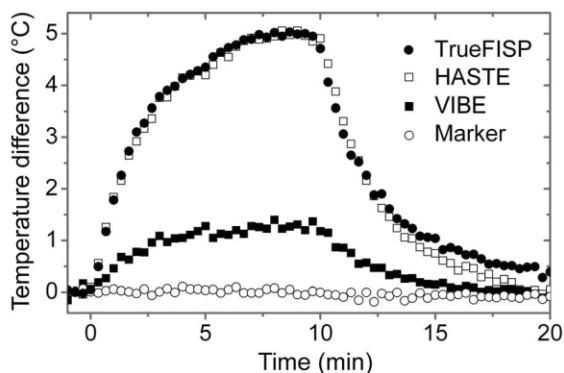


Fig. 5. Temporal evolution of the temperature in the source material (TW) for four different pulse sequences. Plots show temperature difference with respect to average temperature observed one minute before RF exposition (baseline). RF exposition occurred between  $t = 0$  and  $t = 10$  min and cooling was observed for 10 more minutes after sequence had stopped.

numerical fit of the data to a simple exponential model function [Eq. (2)] revealed  $\Delta T_{\max} = 5.1$  °C for HASTE and TrueFISP and  $\Delta T_{\max} = 1.3$  °C for VIBE which suggest that the temperatures have already reached a steady state after 10 min. These maximum values also correlated well with the SAR limits reported by the scanner software; the corresponding  $\Delta T_{\max}/\text{SAR}$  ratios [K per (W/kg)] of 2.6 (HASTE), 2.7 (VIBE), and 2.6 (TrueFISP) were nearly identical.

### III.E. Marker application

Optimal definition of the scan plane was given when the water in the circular tube [Fig. 6(a)] was evenly depicted on the four 1 mm-thick middle slices of the 3D data with the highest signal intensities on the two central ones. This was observed in 13/20 cases (65%). A slight misalignment of the derived plane was identified by a partially open ring on the central slices and an additional signal appearance on one or two of the neighboring slices. In 2 (10%) and 5 (25%) of the remaining cases, the ring was displayed on a total of five and six slices, respectively. From these data, a maximum angular error of 3° was derived. On the single, 2.8 mm-thick slices aligned with the measured geometry, the ring was always

properly seen, and in the case of slight misalignments, showed only minor signal variations around its perimeter [Figs. 6(b) and 6(c)].

## IV. DISCUSSION

### IV.A. Marker design

The presented inductively coupled miniature RF coils generated well-defined MR signal distributions under various experimental conditions. The full widths at half maximum of the signal profiles projected along and perpendicular to the coil axis were close to the effective length of the coil and the inner diameter of the glass tube, respectively. The marker components are easily available, low-priced, and inherently safe. A standard insulated copper wire was used as inductance because the coating appeared to have no adverse effect on image quality. A nonmagnetic capacitor was found to be essential to avoid larger field distortions and signal voids. The same marker set was used throughout our experimental series without having to readjust the resonance properties. While markers could be easily adapted to other field strengths by simply matching the capacitance, the majority of applications have been reported for 1.5 T. If these markers are already visible in other imaging modalities or made visible by adding a suitable contrast material, the same markers can be used for registration purposes.

### IV.B. Source materials for marker signals

Materials with a high proton density like oil,<sup>14,16</sup> a T1-shortening contrast medium<sup>21</sup> or a special vinyl plastisol material<sup>11,17</sup> have already been used as MR signal sources. Our results for the FLASH sequence indicate that adding contrast medium to the water yields a clear, about three-fold increase in CBR. In contrast, the TrueFISP sequence generated a consistently high CBR, independent of the respective signal source.

Such signal behavior is explained by the fact that the contrast of TrueFISP is given by the ratio of T2 and T1 whereas

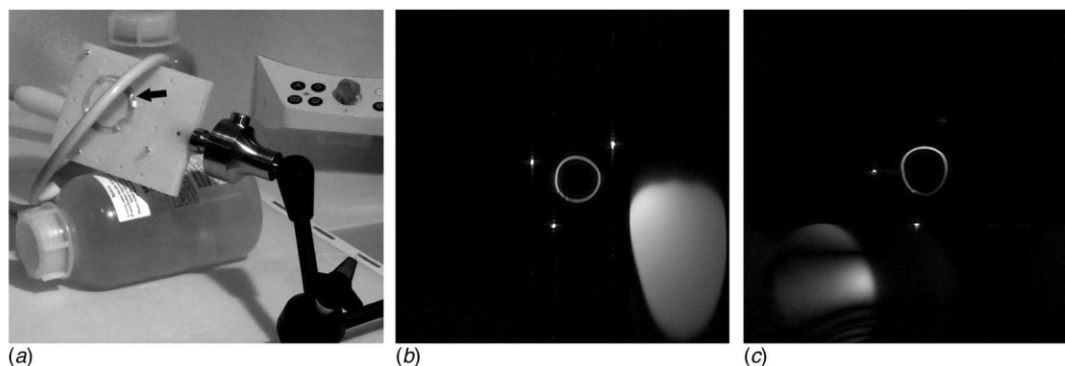


Fig. 6. Practical use of semiactive MR markers for the definition of a scan plane. (a) In an experimental setup, three identical markers were arranged as a triangle (base length  $\approx 10$  cm) on a custom-made plastic board. A circular (diameter  $\approx 5$  cm) water-filled tube (inner diameter  $\approx 3$  mm, arrow) was attached to a board with three markers in the same plane. MR images (slice thickness 2.8 mm) of the tube illustrating optimal (b) and suboptimal (c) definition of the double oblique scan plane by the automatically determined marker coordinates.

the FLASH sequence provides a clearly T1-weighted contrast.<sup>22</sup>

#### IV.C. Pulse sequence

Generally, balanced SSFP (TrueFISP) sequences yield higher signal-to-noise ratios per unit time than other sequences<sup>22</sup> and are therefore considered to be superior for marker imaging as well. This is confirmed in our experimental series where TrueFISP provided a higher marker contrast (CBR) than FLASH. The strong dependence of the signal amplitude on the local shim,<sup>22</sup> however, makes TrueFISP prone to intensity variations as a function of marker location [Figs. 4(b) and 4(e)].

In contrast, FLASH provided higher signal stability and is therefore recommended for applications that require the signal intensity to be less variable. At higher flip angles, however, FLASH required the use of contrast agent (Table I) while TrueFISP could successfully localize even noncontrast markers for flip angles between 0.1° and 25°. Most important, the addition of contrast agent did not provide a substantially higher CBR.

The pulse sequence had only a minor influence on the automatic detection of markers at higher tilt angles. The best performance in that respect was observed for contrast-filled and TW markers when using the FLASH and TrueFISP sequence, respectively (Table II). Localization efficiency for different marker positions was independent of the pulse sequence. It should be noted, however, that here, the total acquisition time for three orthogonal projections was substantially shorter for the TrueFISP than for the FLASH sequence (10 vs. 18 s).

#### IV.D. Flip angle dependence

The maximum CBR was obtained for flip angles less than 1° (Table I) where the sample volume of the ICRF coil is imaged with a highly amplified flip angle<sup>21</sup> while the background signals are very low. This also permits to automatically detect the markers in projection images, here with an arbitrary slice thickness of 300 mm, even in the presence of anatomical signals. In combination with a large FOV, there is no need to accurately position the volume of interest, which improves the workflow for marker imaging.<sup>14,19</sup> For flip angles of 1° and higher, the TrueFISP sequence will reliably work with all source materials (TW, DW, CA) while the FLASH sequence requires the addition of contrast agent for a sufficient marker contrast.

#### IV.E. Orientation and position dependence

Using a simple solenoid design, resonance coupling to the  $B_1$  field is strongly dependent on the coil orientation with respect to the  $B_0$  direction. An adverse orientation will cause a substantial signal loss [Fig. 3] such that the marker can no longer be detected automatically. Therefore, extreme tilt angles of the coil should generally be avoided. This inherent limitation can be overcome by using differ-

ent coil geometries, two orthogonal coils, or a gimbal mount.<sup>21,23,24</sup>

Near the isocenter, all marker types were clearly visible under various experimental conditions. At the edges, the signal intensity was consistently lower due to the inhomogeneity of the  $B_0$  field. In practice, however, the markers would be placed as close as possible to the isocenter to minimize the localization errors imposed by field inhomogeneities, shimming errors, and gradient nonlinearities.<sup>25</sup> For larger distances from the isocenter, Wang *et al.* have described a dedicated method to correct for image distortions.<sup>26</sup>

#### IV.F. Marker heating

The potential MR heating of electrical devices due to electromagnetic coupling is also an important issue for ICRF coils. We have therefore performed temperature measurements under continuous RF exposition where the SAR was reported close to the maximum allowed value (2 W/kg). However, the SAR reported by the scanner is an upper limit of the patient's whole-body SAR<sup>27</sup> only and is known to be unreliable for phantom experiments.<sup>28</sup> While some authors have suggested the measurement of  $B_{1\text{rms}}$  to estimate the RF-induced device heating<sup>27</sup> others have argued that the use of  $B_{1\text{rms}}$  has not yet been shown to yield better results than the scanner-reported SAR.<sup>29</sup> Our measurements should therefore be regarded as a crude estimate of the potential marker heating under the various experimental conditions. The maximum temperature rise of 5 °C seems to be acceptable for clinical application, in particular when considering that this temperature limit was estimated for very long exposition times [Eq. (2)]. In order to minimize potential hazards, however, we suggest insulating the marker thermally and electrically.

#### IV.G. Marker application

The experiment demonstrated that a double oblique scan plane with a typical slice thickness (2.8 mm) could be reliably defined by three identical ICRF coils. Usually, the scan plane can be defined by either manual entry of the parameters, interactive alignment on the screen, or by graphical selection of three landmarks on any of the displayed MR images. In our case, the scan plane parameters were determined numerically by an automatic localization tool, which is generally helpful to minimize user interaction and hence improve workflow, but will be essential for dynamic applications such as instrument or motion tracking.

### V. CONCLUSIONS

Our systematic study of inductively coupled RF coils at 1.5 T has shown that these miniature devices are well suited as MR-visible markers. The markers had a relatively simple design, provided a high contrast over almost the entire field of view, and worked for 82% of all possible coil orientations with respect to the  $B_0$  direction. Unlike other marker designs, the best contrast was obtained for very low flip angles, which allows for an easy detection in the presence of arbitrary body regions within the imaging volume. While tap water would

generally not be rated first choice, this work demonstrates that more common and better characterized source materials do not necessarily provide better results. Independent of the addition of contrast agent, the TrueFISP sequence provided higher contrast and was better suited for automatic localization of the markers.

<sup>a)</sup>Author to whom correspondence should be addressed. Electronic mail: harald.busse@medizin.uni-leipzig.de; Telephone: +49 (341) 97-17413; Fax: +49 (341) 97-17409.

<sup>1</sup>R. Lufkin, L. Teresi, L. Chiu, and W. Hanafee, "A technique for MR-guided needle placement," *Am. J. Roentgenol.* **151**, 193–106 (1988).

<sup>2</sup>J. Rächinger, B. von Keller, O. Ganslandt, R. Fahlbusch, and C. Nimsky, "Application accuracy of automatic registration in frameless stereotaxy," *Stereotact. Funct. Neurosurg.* **84**, 109–119 (2006).

<sup>3</sup>M. Moche, R. Trampel, T. Kahn, and H. Busse, "Navigation concepts for MR image-guided interventions," *J. Magn. Reson. Imaging* **27**, 276–291 (2008).

<sup>4</sup>A. K. George, M. Sonmez, R. J. Lederman, and A. Z. Faranesh, "Robust automatic rigid registration of MRI and X-ray using external fiducial markers for XFM-guided interventional procedures," *Med. Phys.* **38**, 125–141 (2011).

<sup>5</sup>C. C. Parker, A. Damyanovich, T. Haycocks, M. Haider, A. Bayley, and C. N. Catton, "Magnetic resonance imaging in the radiation treatment planning of localized prostate cancer using intra-prostatic fiducial markers for computed tomography co-registration," *Radiother. Oncol.* **66**, 217–224 (2003).

<sup>6</sup>K. Strobel, R. Bergmann, S. Meister, J. van den Hoff, and J. Pietzsch, "Improved multimodality imaging using alginate molding in xenograft tumor models," *J. Magn. Reson. Imaging* **31**, 747–752 (2010).

<sup>7</sup>M. Z. Unlu, A. Krol, A. Magri, J. A. Mandel, W. Lee, K. G. Baum, E. D. Lipson, I. L. Coman, and D. H. Feiglin, "Computerized method for non-rigid MR-to-PET breast-image registration," *Comput. Biol. Med.* **40**, 37–53 (2010).

<sup>8</sup>Y. E. Erdi, B. W. Wessels, R. DeJager, A. K. Erdi, L. Der, Y. Cheek, R. Shiri, E. Yorke, R. Altemus, V. Varma, L. E. Smith, and M. G. Hanna, "A new fiducial alignment system to overlay abdominal computed tomography or magnetic resonance anatomical images with radiolabeled antibody single-photon emission computed tomographic scans," *Cancer* **73**, 923–931 (1994).

<sup>9</sup>S. Buhmann, C. Kirchhoff, R. Ladurner, T. Mussack, M. F. Reiser, and A. Lienemann, "Assessment of colonic transit time using MRI: a feasibility study," *Eur. Radiol.* **17**, 669–674 (2007).

<sup>10</sup>M. B. Ooi, S. Krueger, W. J. Thomas, S. V. Swaminathan, and T. R. Brown, "Prospective real-time correction for arbitrary head motion using active markers," *Magn. Reson. Med.* **62**, 943–954 (2009).

<sup>11</sup>G. Coutts, D. Gilderdale, M. Chui, L. Kasuboski, and N. DeSouza, "Integrated and interactive position tracking and imaging of interventional tools and internal devices using small fiducial receiver coils," *Magn. Reson. Med.* **40**, 908–913 (1998).

<sup>12</sup>M. Bock, S. Volz, S. Zuhlsdorff, R. Umatham, C. Fink, P. Hallscheidt, and W. Semmler, "MR-guided intravascular procedures: real-time parameter control and automated slice positioning with active tracking coils," *J. Magn. Reson. Imaging* **19**, 580–589 (2004).

<sup>13</sup>M. K. Konings, L. W. Bartels, H. F. Smits, and C. J. Bakker, "Heating around intravascular guidewires by resonating RF waves," *J. Magn. Reson. Imaging* **12**, 79–85 (2000).

<sup>14</sup>H. Busse, R. Trampel, W. Gründer, M. Moche, and T. Kahn, "Method for automatic localization of MR-visible markers using morphological image processing and conventional pulse sequences: feasibility for image-guided procedures," *J. Magn. Reson. Imaging* **26**, 1087–1096 (2007).

<sup>15</sup>H.H. Quick, M.O. Zenge, H. Kuehl, G. Kaiser, S. Aker, S. Massing, S. Bosk, and M. E. Ladd, "Interventional magnetic resonance angiography with no strings attached: Wireless active catheter visualization," *Magn. Reson. Med.* **53**, 446–455 (2005).

<sup>16</sup>C. Flask, D. Elgort, E. Wong, A. Shankaranarayanan, J. S. Lewin, M. Wendt, and J. L. Duerk, "A method for fast 3D tracking using tuned fiducial markers and a limited projection reconstruction FISP (LPR-FISP) sequence," *J. Magn. Reson. Imaging* **14**, 617–627 (2001).

<sup>17</sup>M. Rea, D. McRobbie, H. Elhawary, Z. Tse, M. Lamperth, and I. Young, "Sub-pixel localisation of passive micro-coil fiducial markers in interventional MRI," *Magn. Reson. Mater. Phys.* **22**, 71–76 (2009).

<sup>18</sup>A. de Oliveira, J. Rauschenberg, D. Beyersdorff, W. Semmler, and M. Bock, "Automatic passive tracking of an endorectal prostate biopsy device using phase-only cross-correlation," *Magn. Reson. Med.* **59**, 1043–1050 (2008).

<sup>19</sup>H. Busse, N. Garnov, G. Thörmer, D. Zajonz, W. Gründer, T. Kahn, M. Moche, "Flexible add-on solution for MR image-guided interventions in a closed-bore scanner environment," *Magn. Reson. Med.* **64**, 922–928 (2010).

<sup>20</sup>M. Moche, G. Thörmer, N. Garnov, J. Fuchs, S. Heinig, T. Riedel, T. Kahn, and H. Busse, "Navigated liver biopsies in a closed-bore MR scanner: First clinical experience," Presented at the Joint Annual Meeting ISMRM-ESMRMB 2010, Stockholm, Sweden, May 1–7, 2010.

<sup>21</sup>M. Burl, G. A. Coutts, and I. R. Young, "Tuned fiducial markers to identify body locations with minimal perturbation of tissue magnetization," *Magn. Reson. Med.* **36**, 491–493 (1996).

<sup>22</sup>K. Scheffler and S. Lehnardt, "Principles and applications of balanced SSFP techniques," *Eur. Radiol.* **13**, 2409–2418 (2003).

<sup>23</sup>C. Bakker, "MR-guided endovascular interventions: susceptibility-based catheter and near-real-time imaging technique," *Radiology* **202**, 273–276 (1997).

<sup>24</sup>T. Kuehne, R. Fahrig, and K. Butts, "Pair of resonant fiducial markers for localization of endovascular catheters at all catheter orientations," *J. Magn. Reson. Imaging* **17**, 620–624 (2003).

<sup>25</sup>D. Wang, W. Strugnell, G. Cowin, D. M. Doddrell, and R. Slaughter, "Geometric distortion in clinical MRI systems. Part I: evaluation using a 3D phantom," *Magn. Reson. Imaging* **22**, 1211–1221 (2004).

<sup>26</sup>D. Wang, W. Strugnell, G. Cowin, D. M. Doddrell, and R. Slaughter, "Geometric distortion in clinical MRI systems. Part II: correction using a 3D phantom," *Magn. Reson. Imaging* **22**, 1223–1232 (2004).

<sup>27</sup>W. Kainz, "MR heating tests of MR critical implants," *J. Magn. Reson. Imaging* **26**, 450–451 (2007).

<sup>28</sup>H. Celik, A. Ulutürk, T. Tali, and E. Atalar, "A catheter tracking method using reverse polarization for MR-guided interventions," *Magn. Reson. Med.* **58**, 1224–1231 (2007).

<sup>29</sup>F. G. Shellock, "Comments on MR heating tests of critical implants," *J. Magn. Reson. Imaging* **26**, 1182–1185 (2007).

#### Arbeit 4 – Bereitstellung einer Echtzeit-Navigation an einem geschlossenen MRT

Nach erfolgreicher Prüfung der semiaktiven Marker sowie der bildbasierten 3D-Lokalisation wird diese Technik nun zur Registrierung in einer herkömmlichen MRT-Umgebung eingesetzt. Die folgende Arbeit [79] beschreibt zunächst die *add-on* Komponenten für die Echtzeit-Navigation. Der Begriff *add-on* soll verdeutlichen, dass diese Elemente nur bei Bedarf angebracht werden und nach Entfernung wieder eine normale diagnostische MRT-Umgebung vorliegt.

Erstmalig wurden Präzision und Genauigkeit der *Lokalisation* für die *klinisch* eingesetzte Referenzkonfiguration bestimmt. Wie in den Voruntersuchungen arbeitete die Lokalisation sehr zuverlässig. Für herkömmliche Ausrichtungswinkel ( $\theta_{\text{TRA}} = 2 - 46^\circ$ ) war die Reproduzierbarkeit bis auf zwei Ausreißer sehr genau (mittlere Abweichung  $< 0,05$  mm). In 89,4% der Fälle (143 von 160) wurden die drei Marker korrekt lokalisiert, in den verbleibenden Fällen ergaben sich *zusätzliche* Marker. Durch Beschränkung auf eine bestimmte Markergeometrie könnten zahlreiche *falsche* Marker dann durch die fehlende Übereinstimmung mit den vorgegebenen Markerabständen identifiziert werden. Auf solch ein Kriterium wurde hier jedoch bewusst verzichtet, um das Leistungsvermögen für den ungünstigsten Fall zu bestimmen.

Unter Einsatz der klinischen Komponenten wurde die resultierende *Punktionsgenauigkeit* an einem Phantom bestimmt. Je nachdem, ob die Referenzplatte näher oder ferner vom Isozentrum lag, betrug der Abstand zwischen Zielpunkt und Nadelachse im Mittel 2 mm oder 4 mm. Diese Abweichungen sind für die meisten perkutanen Anwendungen tolerabel und liegen auch im Bereich der Genauigkeiten anderer Zielhilfen. Ferner zeigten sich keine systematischen Abweichungen vom Zielpunkt.

Im Gegensatz zur Navigation am intraoperativen System weist diese Implementation keine CE-Kennzeichnung auf. Die klinische Anwendung erfolgte daher im Rahmen einer Studie zur Evaluation der klinischen Wertigkeit einer MR-geführten Zielhilfe für Biopsien unter entsprechenden Auflagen (Ethikkommission der Medizinischen Fakultät der Universität Leipzig, Nr. 344-2007).

Als klinisches Beispiel wird eine präoperative Drahtmarkierung im linken Schulterbereich beschrieben. Ziel war eine kleine (0,34 ml), T<sub>1</sub>-hyperintense Läsion unterhalb des Schulterblatts, die bereits im <sup>18</sup>F-FDG-PET eine erhöhte Traceraufnahme gezeigt hatte. Die Indikation zur Drahtmarkierung unter MRT-Kontrolle erfolgte aufgrund der schwierigen Lage und der guten MRT-Darstellung. Die mittlere Abweichung zwischen geometrischen und gemessenen Markerpositionen wurde als ungefähres Maß für die Genauigkeit der Registrierung herangezogen und war hier vergleichsweise klein (1,4 mm). Der Zeitaufwand zwischen Systemaufbau und finaler Nadelplatzierung betrug 52 min. Bei der MR-Intervention traten keinerlei Komplikationen auf. In der anschließenden Operation konnte das markierte Gewebe leicht aufgefunden und entfernt werden. Die pathologische Analyse des Präparats zeigte tumorfreie Ränder und ergab die Metastase eines malignen Melanoms.

Zusammenfassend zeigt diese Arbeit die erfolgreiche technische und klinische Bereitstellung der entwickelten Technologie und bildet somit die Basis für weitere Entwicklungen und klinische Anwendungen.

# Flexible Add-on Solution for MR Image-Guided Interventions in a Closed-Bore Scanner Environment

Harald Busse,<sup>1\*</sup> Nikita Garnov,<sup>1</sup> Gregor Thörmer,<sup>1</sup> Dirk Zajonz,<sup>1</sup> Wilfried Gründer,<sup>2</sup> Thomas Kahn,<sup>1</sup> and Michael Moche<sup>1</sup>

**MRI is of great clinical utility for the guidance of various diagnostic and therapeutic procedures. In a standard closed-bore scanner, the simplest approach is to manipulate the instrument outside the bore and move the patient into the bore for reference and control imaging only. Without navigational assistance, however, such an approach can be difficult, inaccurate, and time consuming. Therefore, an add-on navigation solution is described that addresses these limitations. Patient registration is established by an automatic, robust, and fast (<30 sec) localization of table-mounted MR reference markers and the instrument is tracked optically. Good hand-eye coordination is provided by following the virtual instrument on MR images that are reconstructed in real time from the reference data. Needle displacements of  $2.2 \pm 0.6$  mm and  $3.9 \pm 2.4$  mm were determined in a phantom ( $P < 0.05$ ), depending on whether the reference markers were placed at smaller (98–139 mm) or larger (147–188 mm) distances from the isocenter. Clinical functionality of the navigation concept is demonstrated by a double oblique, subscapular hook-wire insertion in a patient with a body mass index of  $30.1$  kg/m<sup>2</sup>. Ease of use, compactness, and flexibility of this technique suggest that it can be used for many other procedures in different body regions. More patient cases are needed to evaluate clinical performance and workflow. *Magn Reson Med* 64:922–928, 2010. © 2010 Wiley-Liss, Inc.**

**Key words:** interventional MRI; MRI guidance; navigation; biopsies; closed bore; target positioning error

The majority of image-guided interventions is routinely performed under ultrasound or CT guidance. Despite longer procedure times and the need for special instrumentation, MRI may be necessary in cases where the lesions are not or only poorly seen with ultrasound or CT; for example, in the breast, liver, and prostate. Additionally, MRI may be preferable because of well-known advantages such as the absence of ionizing radiation, multiplanar imaging options, and capabilities to monitor percutaneous therapies or assess postprocedural changes (1–3). Open MRI scanners provide sufficient space to manipulate an instrument inside the bore and an external tracking system can be used for navigation (2,4). On the downside, most open scanners operate at low or mid-

field strength and do not provide the adequate image quality, imaging speed, and advanced imaging options of high-field closed-bore systems (1). Although two high-field open scanner models have recently been introduced, their distribution is still limited.

High-field closed-bore scanners, on the other hand, are widely available, are less expensive to purchase and operate, and have also been used extensively for many different interventions (2,3,5–7). Inside the standard 60-cm bore, however, the remaining space is practically too small to handle the instrument. Special wide-bore (70 cm) scanners provide more space, usually at the expense of field homogeneity (8,9). Another option is to use an assisting device that takes over the guiding function inside the bore. Corresponding manipulators and robotic systems for single-body regions such as breast (10,11), liver (12), and prostate (13,14), as well as multiple ones (4,15,16), have already been presented.

A simpler approach for closed-bore scanners is to manipulate the instrument after the patient table has been moved out of the bore and to use the scanner for control scans only. One solution to then provide accurate guidance is to properly register the patient position outside the bore onto a previously acquired MRI data set (roadmap) and to continuously detect the instrument position with a dedicated tracking device.

Examples of such a navigation concept include an augmented-reality system for percutaneous procedures (17) and a commercial system for brain interventions in the fringe field of the magnet (18). The times reported for reference calibration of the former (12–15 min) and navigation updates with the latter system (5 min), however, were relatively long. Simpler assistance solutions for a standard MRI environment that may be used in different body regions are still rare.

The objectives of this work were to introduce a navigation layout outside the bore with automatic and fast patient registration in arbitrary table positions, to integrate this technique into a diagnostic closed-bore scanner environment, and to develop that system into a potential clinical solution for various MR-guided procedures that might benefit from accurate real-time guidance.

## MATERIALS AND METHODS

### Hardware Components

Two commercial holding arms (Invivo Germany GmbH, Schwerin, Germany) are attached to the side of the patient table and allow a very flexible positioning and fixation of

<sup>1</sup>Department of Diagnostic and Interventional Radiology, Leipzig University Hospital, Leipzig, Germany.

<sup>2</sup>Department of Medical Physics and Biophysics, Leipzig University, Leipzig, Germany.

Presented at the 2007 Joint Annual Meeting ISMRM-ESMRMB, Berlin, Germany.

\*Correspondence to: Harald Busse, Ph.D., Department of Diagnostic and Interventional Radiology, Leipzig University Hospital, Liebigstr. 20, 04103 Leipzig, Germany. E-mail: harald.busse@medizin.uni-leipzig.de

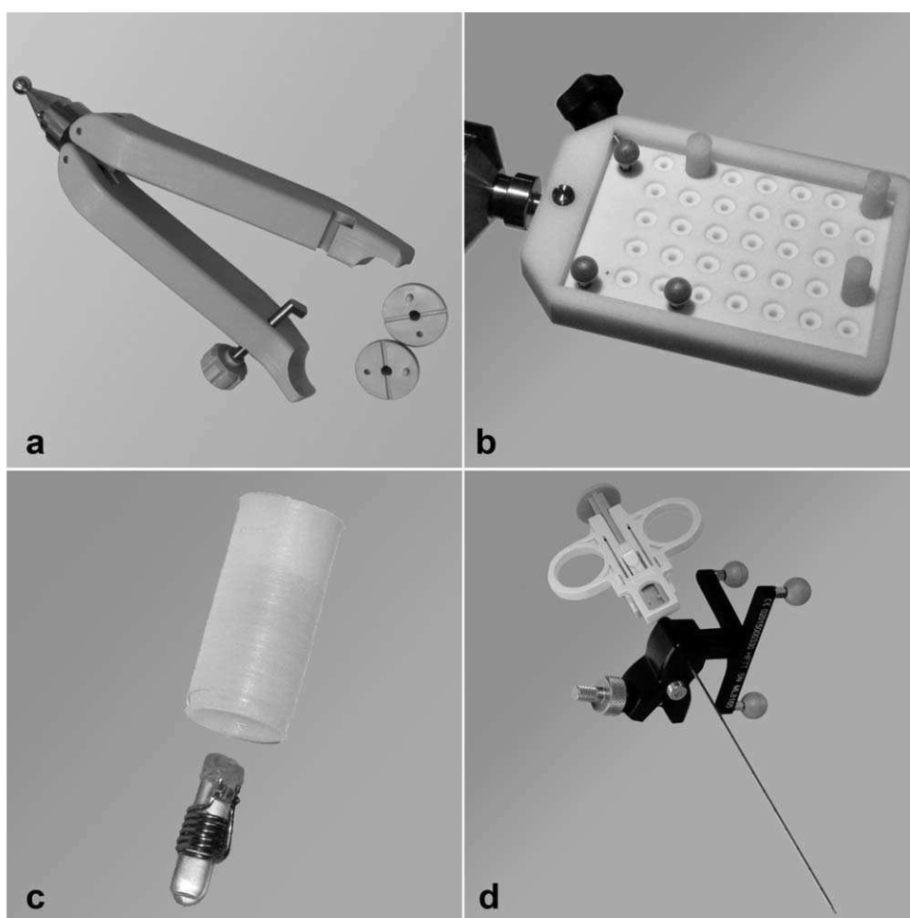
Received 6 October 2009; revised 25 February 2010; accepted 1 March 2010.

DOI 10.1002/mrm.22464

Published online 1 June 2010 in Wiley Online Library (wileyonlinelibrary.com).

© 2010 Wiley-Liss, Inc.

FIG. 1. Selected hardware components of the add-on navigation system. **a:** Autoclavable front-end module with gripping jaw and ball that holds and guides the instrument. The ball can be continuously tightened or loosened up to a point where it can be detached from the jaw. The ball consists of two matching half-spheres that can be split to use the instrument to full length. **b:** Custom-made reference marker board with a set of three reflective optical (spheres) and three MR markers (under cylindrical caps) in a known geometry. **c:** The custom-made MR markers (maximum diameter 3.4 mm) consist of an inducting coil tightly wrapped around a small water-filled glass tube (outer diameter 2.0 mm) and a capacitor. These miniature coils have no galvanic connection to the MR scanner and couple inductively with the MR coils used for imaging. **d:** Instrument tracker attached to biopsy gun. The three reflective optical markers define the exact geometry (position and orientation) of the instrument.



the instrument-supporting device (custom-made front-end module, Fig. 1a, codeveloped with Invivo Germany GmbH) and of the reference marker board (Fig. 1b) used for automatic patient registration. The reflective optical markers are provided by the manufacturer of the tracking system (NDI, Waterloo, Ontario, Canada). The custom-made MR markers (Fig. 1c) are resonant circuits that have been tuned to the resonance frequency (63.8 MHz) of our 1.5-T scanner. According to their mechanism of signal generation, they will be referred to as inductively coupled radiofrequency coils (19–21). Three-dimensional (3D) tracking is achieved by attaching an autoclavable tracker (Fig. 1d; Localite GmbH, St. Augustin, Germany) with three reflective optical markers (NDI) to the instrument.

An illustration of the MR environment with the main hardware components inside and outside the MR room is given in Fig. 2a. The stereoscopic tracking camera (Polaris Spectra; NDI) is mounted on an MR-compatible rollaway stand and was set to allow optical tracking at marker distances between 95 and 240 cm. The navigation scene is displayed on a 112-cm large rollaway screen in the MR room. The navigation workstation (Localite) is a medical personal computer with appropriate interfaces. Imaging was performed in a conventional 1.5-T MR scanner (Magnetom Symphony; Siemens Medical Solutions, Erlangen, Germany) with a 60-cm bore.

### Software Components

The custom-made software tool for 3D localization of MR-visible structures is a stand-alone IDL program (Interactive Data Language; ITT Visual Information Solutions, Boulder, CO) on the navigation workstation and requires no further interaction of the user. 3D marker localization is performed as independent two-dimensional (2D) localizations on three standard views and a subsequent matching of the 2D peak coordinates between the views. This technique is very flexible in the sense that each marker needs to correctly appear on any two views only (may be missing in one view) to be detected. As described elsewhere (19), the localization algorithm is also quite robust against the presence of false peaks in any of the views.

Automatic patient registration and continuous (real-time) reformatting of the 3D roadmap data into the 2D slices during navigation are accomplished with the commercial Java-based navigation application (Localite). After selecting the 3D roadmap file, the geometric marker positions will automatically be registered onto the latest corresponding marker data, using a least squares fitting algorithm. As a crude estimate for the quality of marker registration and as an independent check for the integrity of marker setup and localization, the software provides the residual 3D marker distances (individual and mean of all markers) after registration. If the user



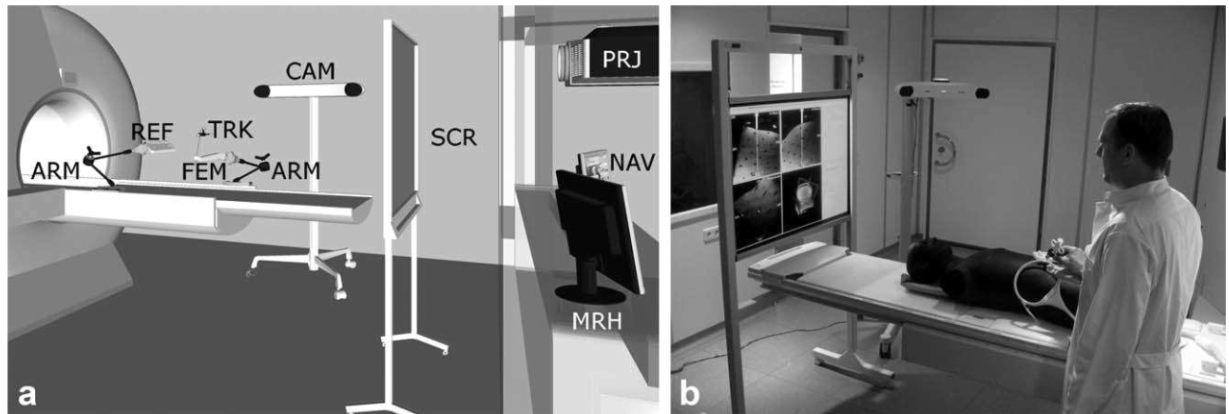


FIG. 2. **a:** Schematic drawing of the add-on navigation system for a standard closed-bore MR scanner. ARM: adjustable holding arm; REF: reference marker board; FEM: front-end module; TRK: instrument tracker; CAM: optical 3D tracking camera; SCR: projection screen in MR room; PRJ: LCD projector; NAV: navigation workstation; MRH: MR host computer. **b:** Illustration of navigation outside the bore in an experimental setup. As the instrument is moved at the “patient,” the virtual instrument can be followed with respect to the MR anatomy on the large in-room screen. The user may switch between radiologic standard (sagittal, coronal, transverse) and instrument-related views (in-plane 90°, in-plane 0°, perpendicular). A short text in the top left corner informs the user about the status of the tracking camera (see Fig. 4c). A green “OK” denotes proper line of sight with both instrument and reference markers, while red messages indicate missing data from the instrument (“Needle blocked”), reference (“Reference blocked”), or both (“All blocked”).

provides the exact length and diameter of the instrument, the tip position will be displayed correctly. The image rendering speed was set to 5 Hz. Figure 2b shows an experimental setup during navigation.

#### Marker Localization

Throughout this work, the three markers were imaged with the integrated body coil, using a true fast imaging with steady state precession sequence (matrix size =  $512 \times 512$ , field of view =  $300 \times 300 \text{ mm}^2$ , slice thickness = 300 mm, pulse repetition time/echo time = 6.78/2.82 ms, flip angle = 1°, bandwidth = 220 Hz/pixel, acquisition time = 10.4 sec, distortion correction enabled). The data are interactively sent to the navigation workstation, where the resulting assignment is quickly verified.

Marker localization was evaluated as a function of tilt angle because the inductive coupling between imaging and marker coils depends on the relative orientation between solenoid axis and direction of the static field. Therefore, the solenoid marker coils were scanned in 20 different board positions, with orientations between coronal (0°) and transverse (90°). At each position, the markers were scanned 10 times. Localization was considered correct if exactly three markers were found in 3D. The precision or reproducibility of localization was estimated by the mean 3D displacement between the individual positions of each true marker and their respective average position at each angle.

#### Target Positioning Error

The target positioning error was estimated by targeting a small glass capillary filled with contrast solution (Fig. 3a). The target volume was imaged with a large 19-cm-diameter loop coil (Loop Flex Coil, large; Siemens), using a  $T_1$ -weighted fast low-angle-shot sequence (pulse repetition time = 4.3 ms, echo time = 1.67 or 1.51 ms,

partial Fourier = 5/8, slice thickness = 1 mm, 30 transverse slices, no gap, five averages) with an in-plane resolution of  $1.0 \times 1.0 \text{ mm}^2$  or better.

After automatic registration, the operator relied on the navigation scene to reach the virtual target position displayed on the in-room screen. A possible offset between virtual and true position along the needle (length 137 mm) was corrected for by setting a needle offset (in full millimeters). The displacement in the horizontal  $xz$ -plane ( $x$ : left-right,  $z$ : head-feet) was directly read from the measurement grid. The tolerance of setting was estimated as  $\pm 1.0 \text{ mm}$  (display) and the reading accuracy was assumed as  $\pm 0.5 \text{ mm}$ .

Two different types of accuracy were assessed. In one series, the reference markers remained at a fixed location, with their centroid at a 3D distance of 116 mm from the magnet isocenter (radius  $r$ ) while the target was placed in 20 arbitrary positions (target radii between  $\approx 91$  and 140 mm). This allows study of the influence of target location for a given intervention. In the second series, the reference marker board was placed in 20 arbitrary positions (radii of the marker centroid between 98 and 188 mm) while the target remained stationary at  $r \approx 40 \text{ mm}$ , which allows study of the influence of reference board position. One-sample  $t$  tests were used to determine whether the mean coordinates along  $x$ ,  $z$ , and needle direction were significantly different from the target position. A potential influence of the marker radii on target positioning error was evaluated by a  $t$  test of two subsamples, dividing smaller and larger marker radii ( $n = 10$  each). All statistical analyses were performed with SPSS 15.0 (SPSS Inc., Chicago, IL).

## RESULTS

#### Marker Localization

The results of the marker performance at 20 different tilt angles in the 2-72° range are summarized in Table 1. For

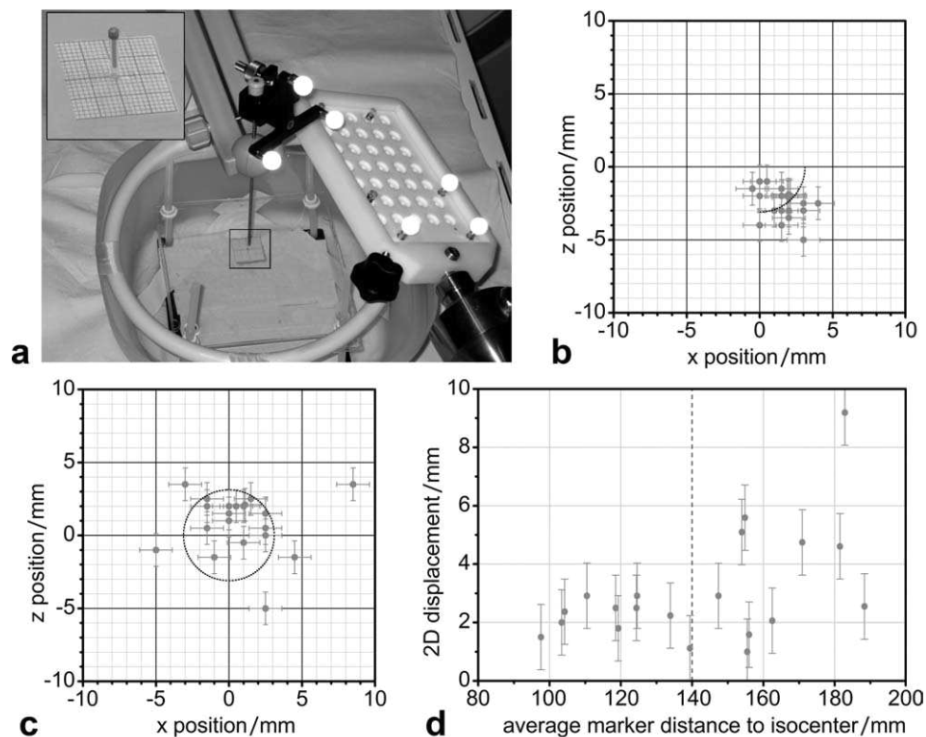


FIG. 3. Experimental estimation of target positioning error. **a:** A transparent plastic board with a small central hole for the target was supported by four plastic rods and could be adjusted to different heights. The whole assembly was placed inside a plastic container filled with tap water and aligned to  $x$  and  $z$ -axes of the scanner. Inset: A 2 mm-high column of a gadolinium-based contrast agent (Dotarem, 0.5 mmol/L; Guerbet, Roissy, France; 1:300 dilution in water) inside a capillary (0.8 mm inner diameter) was used as target. The needle displacement was read from a horizontal measurement grid (1 mm spacing). **b:** Plot of the needle positions (along  $x$  and  $z$ ) after correction of the needle offset for different target positions and constant reference board position. The origin corresponds to the true position of the target (capillary). The error bars reflect both tolerance of setting and reading accuracy. An arc with a 3.1 mm radius (mean displacement) has been overlaid for visual guidance. **c:** Corresponding plot of the needle positions for different reference board positions and constant target position. A circle with a 3.1 mm radius has been overlaid for visual guidance. **d:** Plot of 2D needle displacement as a function of the average marker distance from the isocenter. The dashed line separates the 10 smaller from the 10 larger marker radii.

16 tilt angles in the 2-46° subrange, 89.4% (143 of 160) of the localization trials revealed exactly three marker peaks (correct localization). If localization had relied on coordinate information from less than all three views, the rate for correct localization would have been smaller, for example, only 66.3% (106 of 160) for sagittal and transverse views only. In 10.6% (17 of 160) of the trials in the 2-46° subrange, false markers were detected in addition to the three true ones ( $m > 3$ ). If the mutual marker distances (48.0, 80.0, and 93.3 mm) had been provided to the algorithm, these extra markers could have been ruled out by geometric criteria and the corresponding localization rate would have been 100% in that subrange. In the 49-72° subrange, all but one of the 40 trials failed. For each case, marker scan, data transfer, and marker localization took less than 30 sec.

The precision of localization also depended on tilt angle. In cases with extra markers ( $m > 3$ ), the selected 3D positions of the true markers were included in the calculation of precision. In the 2-41° range ( $n = 13$ ), the precision was better than 0.05 mm. The corresponding statistical analysis revealed a mean precision of 0.02 mm and a 95% confidence interval of less than 0.01 mm. In

the 42-46° range ( $n = 3$ ), however, two deviations of 0.56 mm and 0.64 mm were observed.

#### Target Positioning Error

The results of the accuracy measurement at a fixed reference board position are shown in Fig. 3b. The needle position had a significant bias in both  $x$  and  $z$ -coordinates ( $P < 0.05$ ). The 2D deviation ranged between 1.0 and 5.8 mm and had a mean of 3.1 mm. The offset in needle depth ranged between +2 and +7 mm and had a mean value of +4.5 mm ( $P < 0.05$ ) and a median of +4.0 mm.

The corresponding plot of the actual needle positions for different reference board placements is shown in Fig. 3c. There was no significant bias in the  $x$  ( $P = 0.269$ ) and  $z$  ( $P = 0.069$ ) coordinates. The 2D deviation ranged between 1.0 and 9.2 mm and had a mean of 3.1 mm. The offset in needle depth ranged between -4 and +8 mm and had a mean value of +0.75 mm ( $P = 0.353$ ) and a median of +0.5 mm. The 2D deviation tends to be higher for larger marker distances (Fig. 3d). In particular, the five largest deviations (outside the mean 2D error

Table 1  
Performance of Marker Localization at Different Tilt Angles

Tilt angle (°)	True marker peaks in 2D			Cases with localization in 3D (out of 10 trials)			3D precision (mm)
	Coronal	Sagittal	Transverse	Correct ( $m=3$ )	Extra markers ( $m>3$ )	Failed ( $m<3$ )	
2	3	3	3	9	1	0	0.04
6	3	3	3	7	3	0	0.02
10	3	3	3	10	0	0	0.02
12	3	3	3	7	3	0	0.02
16	3	3	3	10	0	0	0.02
19	3	3	3	9	1	0	0.02
22	3	3	3	10	0	0	0.02
24	3	3	3	10	0	0	0.04
28	3	3	3	10	0	0	0.02
30	3	3	3	6	4	0	0.02
34	3	3	3	10	0	0	0.02
36	3	3	2	9	0	0	0.02
	3	3	1	0	1	0	n.a.
41	3	3	2	10	0	0	0.02
42	3	3	1	8	2	0	0.64
45	3	3	3	8	0	0	0.03
	3	3	2	0	2	0	n.a.
46	2	3	2	9	0	0	0.56
	2	3	2	1	0	0	n.a.
49	2	3	1	1	0	0	n.a.
	3	2	1	0	0	9	n.a.
51	2	2	1	0	0	10	n.a.
65	3	1	0	0	0	6	n.a.
	2	1	0	0	0	4	n.a.
72	2	1	0	0	0	2	n.a.
	1	1	0	0	0	8	n.a.

n.a., not applicable.

circle in Fig. 3c) were all observed for marker radii larger than  $\approx 154$  mm. The  $t$  test assumed unequal variances and revealed a significant ( $P < 0.05$ ) difference between smaller (98 to 139 mm) and larger (147 to 188 mm) marker radii. The corresponding 2D target errors (mean  $\pm$  SD) were  $2.2 \pm 0.6$  mm and  $3.9 \pm 2.4$  mm.

#### Clinical Procedure

Diagnostic imaging on a 43-year-old male patient with a body mass index of  $30.1 \text{ kg/m}^2$  had revealed a suspicious,  $12 \times 9 \times 6 \text{ mm}^3$  large lesion under the left scapula, which appeared hyperintense on native  $T_1$ -weighted MRI and had shown a high fluorodeoxyglucose uptake in positron emission tomography. A navigated hook-wire insertion was planned for the preoperative marking of the lesion due to its complex location. Clinical application of the guidance system had been approved by the institutional ethic committee and informed written consent of the patient had been obtained.

Technical setup and patient positioning took 5 and 10 min, respectively. The patient was moved inside the magnet to acquire marker (Fig. 4a) and roadmap images. The navigation software reported a mean 3D marker deviation of 1.4 mm after registration. These planning steps took 9 min. An overview of the subsequent clinical setting is shown in Fig. 4b. The skin had been disinfected and the area around the access site was covered with a sterile drape. A 20-gauge, 120 mm-long coaxial needle equipped with the sterile tracker was then inserted into the ball of the front-end module to define the needle trajectory (Fig.

4c). After tightening the ball, local anesthesia was administered (10 mL of a 1% lidocaine solution) along the established trajectory. The resulting quality of the reformatted MR images was not compromised by the attached hardware components. Patient preparation and access planning required 15 min.

The hook wire (MRI Duo System; Somatex GmbH, Teltow, Germany) was inserted through the coaxial needle. Figure 4d-f illustrates the course of the intervention until the final control image (13 min) was acquired. Neither minor nor major complications occurred. In the subsequent surgical procedure, the tumor could easily be located and resected because the anchor lay exactly within the lesion. The histopathological finding revealed the metastasis of a malignant melanoma with tumor-free margins (R0 resection).

#### DISCUSSION AND CONCLUSIONS

Good hand-eye coordination was provided by the real-time navigation scene. The implemented patient registration outside the bore is automatic and requires only minimal time. The referencing scheme is considered highly flexible because it allows nearly arbitrary patient table and camera positions. Both components may also be moved *during* navigation without any interruption of the real-time MR image display. If the patient table were detachable, navigation could be performed beyond the 5-gauss line or even outside the MR room. The table-mounted components (front-end module, reference board) were very flexible and had a small footprint only. Modifications to existing hardware and

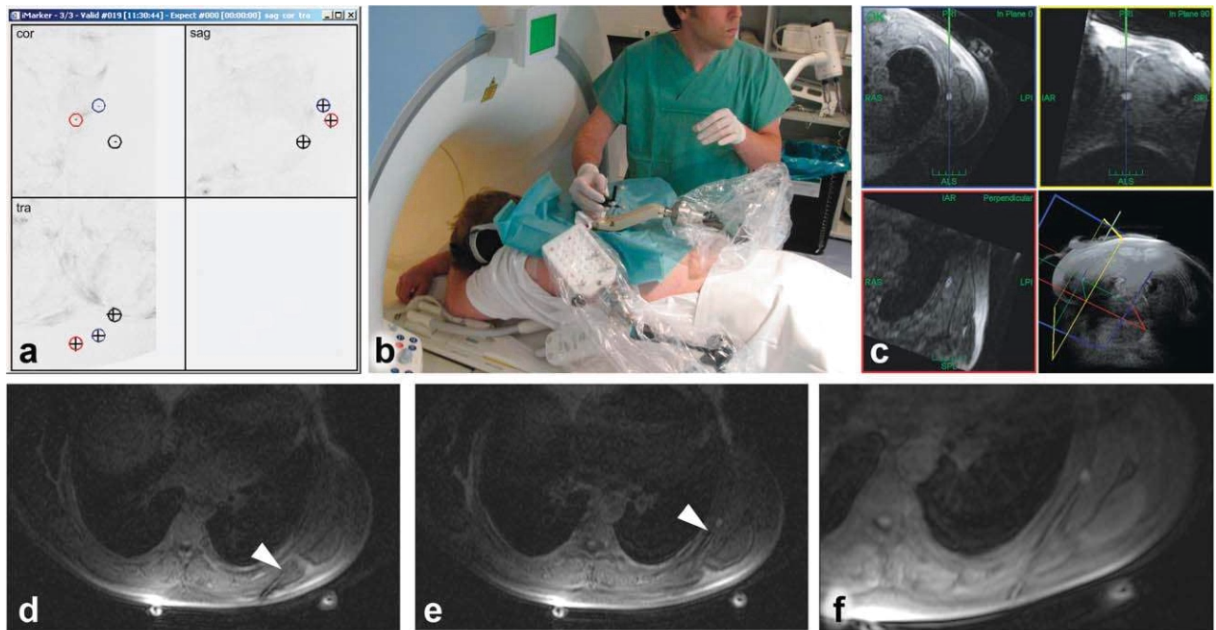


FIG. 4. **a**: Screenshot of successful marker localization under clinical conditions (marker centroid at left = 146 mm, posterior = 179 mm, superior = -20 mm). Due to the local amplification of the amplitude of radiofrequency field, the markers can be imaged at very small flip angles (here,  $1^\circ$ ), with excellent background suppression. Crosses denote the 2D peak positions of potential markers in each view and have been omitted in coronal view to clearly show the underlying marker signals. Circles indicate the 3D coordinates after peak matching. Images have been inverted to improve visibility. **b**: Clinical (sterile) setup during navigation. A large loop coil was used for signal reception (hidden under sterile drape) because it provides a good compromise between interventional access, image quality, and imaging depth. **c**: Screenshot of the navigation scene in instrument-related views (top-left: in-plane  $0^\circ$ , top-right: in-plane  $90^\circ$ , bottom-left: perpendicular, bottom-right: 3D volume rendering) showing the virtual position of the slightly inserted coax needle (green) and its extension (blue) into the subscapular region. Suspicious lesion is discernible as hyperintense area in the center of a native  $T_1$ -weighted volume-interpolated breath-hold examination (VIBE) image (matrix size =  $256 \times 125$ , field of view =  $400 \times 300$  mm<sup>2</sup>, pulse repetition time/echo time = 3.31/1.35 ms, 64 transverse slices, slice thickness = 3 mm). **d**: Transverse VIBE control image (same parameters) after needle insertion. The white arrowhead points to the tip of the needle artifact. **e**: Transverse VIBE image after needle repositioning. **f**: Oblique VIBE image (slice thickness = 5 mm) along final needle trajectory (double oblique between scapula and rib cage, insertion depth  $\approx 95$  mm).

software were only moderate, which potentially allows the solution to be adapted to different scanner models and environments.

The presented inductively coupled radiofrequency coil markers are easy to implement, can be detected with routine pulse sequences, and require no connection to the scanner, which makes them very convenient. In addition, tap water is safe to use as a signal source and generates no chemical shift artifact. The preferred marker board orientation for the clinical setup is anywhere between coronal and sagittal, where the solenoid axis will be perpendicular to direction of the static field and, hence, inductive coupling will be optimal. Our results even suggest that the board may be tilted up to  $40\text{--}45^\circ$  toward a transverse plane without any substantial loss in performance. In principle, localization could be accelerated by acquiring and analyzing two projection images only. For our purposes, however, we recommend a three-view localization because it appears to be more robust and takes only little extra time ( $<4$  sec here).

The magnitudes of registration and target positioning errors is largely determined by the error in measuring the MR-marker positions on MR images that are inherently distorted by nonlinear gradients, inhomogeneities of the static

field, and shimming errors. On a scanner with the same gradient system and distortion correction enabled, Wang and coworkers (22) have determined absolute positional deviations of 1.33 mm (mean) and 4.4 mm (maximum) on a cubic ( $\pm 120$  mm) grid phantom and observed an increasing distortion at the edges. Larger displacements may need to be assumed here because, in 75% of our cases, at least one of the markers was beyond these edges.

Therefore, the significant difference of the target positioning error between smaller and larger marker radii is most likely explained by image distortion. Although further errors are introduced by the machining tolerance of the reference elements (markers, board, and instrument tracker, estimated at  $\approx 0.3$  mm) and by the optical measurement (vendor-specified volumetric root-mean-square (RMS) accuracy of 0.25 mm), their weight is considered to be relatively small.

The small but significant bias in target position of the first experiment is attributed to the fact that the positions of the three MR markers are distorted according to their specific locations and radii rather than randomly which may result in a systematic reference error for a given (constant) board position. This error will be minimized by placing the marker board as close as possible to the isocenter, in particular, by aligning the marker centroid axially

near  $z = 0$  mm. The insignificant bias of the second experiment suggests that the individual bias averages out over different (random) board positions.

Generally, the magnitude of our target positioning error is in line with previous *in vitro* findings and considered small enough for most interventional purposes. A direct comparison, however, is difficult because other results were obtained under different conditions (scanner model, technical equipment, clinical purpose). In an open scanner, for example, spatial deviations in the 3.1–7.5 mm range (23) and of 3.0 mm (12) were reported for a built-in optical guidance tool and a custom-made manipulator, respectively. In closed-bore scanners, RMS positional errors of 2.6–4.8 mm (13) and a target accuracy of 3.2 mm (16) were determined for an open-source-based guidance system for robotic prostate interventions and a multipurpose manipulator.

A similar registration approach to ours revealed slightly smaller localization errors (1.0–3.1 mm) but relied on up to seven markers that are permanently attached to the head coil and can therefore not easily be adapted to body interventions (18). A table-mounted arch has been used as a reference outside the bore for body interventions with augmented reality guidance. A mean needle placement error of 9.6 mm was determined in an animal study and smaller errors in a phantom (17).

A fundamental limitation of any stereotactic reference solution is that patient motion must be avoided or at least carefully controlled. Recommended measures are to clearly instruct the patient not to move the specific body region after roadmap acquisition, to place the patient in a comfortable and stable position (with optional immobilization by a vacuum mattress or splint), and adequate sedation and analgesia. Likewise, the time between reference data acquisition and navigation should be minimized. A clear advantage of our setup is that the true instrument position can be quickly verified at any time. Whenever patient motion is detected, an updated roadmap needs to be acquired to continue with navigation. In addition, each intermediate 3D control scan may also serve as an updated roadmap for navigation.

Ease of use, compactness, and flexibility of the presented technique suggest that it can be used for many other interventions in different body regions. The procedure times are expected to decrease slightly with further applications (learning curve) and an optimized setup of the table-mounted components and the patient. More clinical cases are needed to properly assess technical, clinical, and workflow issues.

## ACKNOWLEDGMENTS

The authors thank the people at Localite GmbH and Invivo Germany GmbH, in particular Arno Schmitgen, Martin Bublat, Sven Arnold, and Axel Winkel, for their continuous support and valuable assistance at various stages of this interdisciplinary effort. Clinical support by Jochen Fuchs and Tim-Ole Petersen is also acknowledged.

## REFERENCES

1. Tatli S, Morrison PR, Tuncali K, Silverman SG. Interventional MRI for oncologic applications. *Tech Vasc Interv Radiol* 2007;10:159–170.
2. Weiss CR, Nour SG, Lewin JS. MR-guided biopsy: a review of current techniques and applications. *J Magn Reson Imaging* 2008;27:311–325.
3. Smith KA, Carrino J. MRI-guided interventions of the musculoskeletal system. *J Magn Reson Imaging* 2008;27:339–346.
4. Moche M, Trampel R, Kahn T, Busse H. Navigation concepts for MR image-guided interventions. *J Magn Reson Imaging* 2008;27:276–291.
5. Tempny C, Straus S, Hata N, Haker S. MR-guided prostate interventions. *J Magn Reson Imaging* 2008;27:356–367.
6. Salomonowitz E. MR imaging-guided biopsy and therapeutic intervention in a closed-configuration magnet: single-center series of 361 punctures. *AJR Am J Roentgenol* 2001;177:159–163.
7. Kuhl CK, Elevelt A, Leutner CC, Gieseke J, Pakos E, Schild HH. Interventional breast MR imaging: clinical use of a stereotactic localization and biopsy device. *Radiology* 1997;224:667–675.
8. Boss A, Remp H, Martirosian P, Clasen S, Schraml C, Stenzl A, Claussen CD, Schick F, Pereira PL. Wide-bore 1.5 tesla MR imagers for guidance and monitoring of radiofrequency ablation of renal cell carcinoma: initial experience on feasibility. *Eur Radiol* 2008;18:1449–1455.
9. Stattaus J, Maderwald S, Baba HA, Gerken G, Barkhausen J, Forsting M, Ladd ME. MR-guided liver biopsy within a short, wide-bore 1.5 tesla MR system. *Eur Radiol* 2008;18:2865–2873.
10. Pfeleiderer SO, Marx C, Vagner J, Franke RP, Reichenbach JR, Kaiser WA. Magnetic resonance-guided large-core breast biopsy inside a 1.5-T magnetic resonance scanner using an automatic system: *in vitro* experiments and preliminary clinical experience in four patients. *Invest Radiol* 2005;40:458–463.
11. Kaiser WA, Fischer H, Vagner J, Selig M. Robotic system for biopsy and therapy of breast lesions in a high-field whole-body magnetic resonance tomography unit. *Invest Radiol* 2000;35:513–519.
12. Hata N, Tokuda J, Hurwitz S, Morikawa S. MRI-compatible manipulator with remote-center-of-motion control. *J Magn Reson Imaging* 2008;27:1130–1138.
13. Tokuda J, Fischer GS, Csoma C, DiMaio SP, Gobbi DG, Fichtinger G, Tempny CM, Hata N. Software strategy for robotic transperineal prostate therapy in closed-bore MRI. *Med Image Comput Comput Assist Interv* 2008;11:701–709.
14. Susil RC, Camphausen K, Choyke P, McVeigh ER, Gustafson GS, Ning H, Miller RW, Atalar E, Coleman CN, Ménard C. System for prostate brachytherapy and biopsy in a standard 1.5 T MRI scanner. *Magn Reson Med* 2004;52:683–687.
15. Zangos S, Herzog C, Eichler K, Hammerstingl R, Lukoschek A, Guthmann S, Gutmann B, Schoepf UJ, Costello P, Vogl TJ. MR-compatible assistance system for function in a high-field system: device and feasibility of transgluteal biopsies of the prostate gland. *Eur Radiol* 2007;17:1118–1124.
16. Christoforou E, Akbudak E, Ozcan A, Karanikolas M, Tsekos NV. Performance of interventions with manipulator-driven real-time MR guidance: implementation and initial *in vitro* tests. *Magn Reson Imaging* 2007;25:69–77.
17. Wacker FK, Vogt S, Khamene A, Jesberger JA, Nour SG, Elgort DR, Sauer F, Duerk JL, Lewin JS. An augmented reality system for MR image-guided needle biopsy: initial results in a swine model. *Radiology* 2006;238:497–504.
18. Rachinger J, von Keller B, Ganslandt O, Fahlbusch R, Nimsky C. Application accuracy of automatic registration in frameless stereotaxy. *Stereotact Funct Neurosurg* 2006;84:109–117.
19. Busse H, Trampel R, Gründer W, Moche M, Kahn T. Method for automatic localization of MR-visible markers using morphological image processing and conventional pulse sequences: feasibility for image-guided procedures. *J Magn Reson Imaging* 2007;26:1087–1096.
20. Flask C, Elgort D, Wong E, Shankaranarayanan A, Lewin J, Wendt M, Duerk JL. A method for fast 3D tracking using tuned fiducial markers and a limited projection reconstruction FISP (LPR-FISP) sequence. *J Magn Reson Imaging* 2001;14:617–627.
21. Burl M, Coutts GA, Young IA. Tuned fiducial markers to identify body locations with minimal perturbation of tissue magnetization. *Magn Reson Med* 1996;36:491–493.
22. Wang D, Strugnell W, Cowin G, Doddrell DM, Slaughter R. Geometric distortion in clinical MRI systems, part I: evaluation using a 3D phantom. *Magn Reson Imaging* 2004;22:1211–1221.
23. Silverman SG, Collick BD, Figueira MR, Khorasani R, Adams DF, Newman RW, Topulos GP, Jolesz FA. Interactive MR-guided biopsy in an open-configuration MR imaging system. *Radiology* 1995;197:175–181.

## Arbeit 5 – Machbarkeit einer Echtzeit-Verfolgung von semiaktiven MR-Positionsmarkern

Ein Schlüsselmerkmal der flexiblen Lokalisationsmethode ist die parallele Erfassung aller Marker in einem großen Messvolumen, sodass weder deren Lage noch die damit erfassten anatomischen Bereiche beachtet werden müssen. Im zuvor beschriebenen klinischen Fall wurde die Lokalisation praktisch nur bei der initialen Registrierung genutzt. Die folgende Arbeit [83] beschäftigt sich daher mit einer kontinuierlichen Anwendung wie sie perspektivisch z. B. für eine Positionsverfolgung im MRT anwendbar wäre. Hierzu musste der mit Abstand zeitaufwändigste Arbeitsschritt – die Markerbildgebung – beschleunigt werden.

Die Umsetzung beruhte auf der gezielten Anpassung einiger Bildgebungsparameter: kleinere Basisauflösung, d. h. weniger Phasenkodierschritte, partielle k-Raum-Abtastung sowie größere Empfängerbandbreite, was eine kürzere Repetitionszeit erlaubte. Die zentrale Frage war, inwiefern sich der Informationsgehalt der 2D-Projektionsbilder reduzieren ließe, ohne zu sehr die Detektierbarkeit und Positionsgenauigkeit zu beeinträchtigen. Als Zielwert für die zeitliche Auflösung wurde eine Sekunde gewählt, was gegenwärtig in etwa der Bildperiodendauer einer fluoroskopischen Sequenz entspricht. Des Weiteren gewann ein Merkmal der entwickelten Bildanalyse nun an Bedeutung. Die 2D-Position eines Marker-*Peaks* wurde nicht einfach durch die Koordinaten des Pixels mit der höchsten Signalintensität definiert, sondern explizit durch eine numerische Anpassung auf einer Subpixelskala bestimmt. Dieses Vorgehen sollte im Mittel genauer sein, da hierbei die gesamte 2D-Signalverteilung und nicht nur isolierte Pixelwerte in die Bestimmung eingehen.

In der folgenden Arbeit wurde diese Arbeitshypothese sowohl an synthetischen wie auch gemessenen Markersignalen überprüft. Bei festem quadratischem FOV (Basislänge 300 mm) wurde die Matrixgröße (MX) von 512 bis 64 sukzessiv halbiert. In der niedrigsten Auflösung (MX = 64) ergab sich eine mittlere Lokalisationszeit von rund 350 ms (mit 2,6 GHz *Dual Core* CPU). Die experimentell bestimmte 3D-Genauigkeit verschlechterte sich im statistischen Mittel (220 Einzelmessungen) von rund 0,5 mm (MX = 512) auf lediglich 1,0 mm (MX = 64). Eine ähnlich moderate, relative Einbuße an Genauigkeit zeigte sich auch bei der Analyse synthetischer Markerbilder (Anzahl 40.000).

Sensitivität und Spezifität der beschleunigten Markerlokalisierung lagen selbst in der niedrigsten Auflösung ( $MX = 64$ ) noch bei 95 bzw. 96%. Eine solche Lokalisation würde demnach im Mittel nur an einem von insgesamt 20 Zeitpunkten fehlschlagen, was für viele dynamische Anwendungen akzeptabel zu sein scheint.

Die skizzierte Lösung erfüllt somit nicht nur die gewünschten Anforderungen einer hinreichend genauen, Subsekunden-Lokalisierung dreier Marker, sondern liefert zudem wertvolle Kenngrößen (Genauigkeit, Erfolgsrate, Winkeltoleranz der Spulen) für verschiedene Bildauflösungen. Für eine gegebene praktische Anforderung ließen sich so geeignete MR-Parameter finden.

Abschließend wurde die kontinuierliche Markerverfolgung noch praktisch getestet. Am Ende eines robotischen Arms [84, 85] wurden eine Koaxialnadel und eine dazu senkrechte Anordnung von drei Referenzmarkern befestigt. Auf einer willkürlichen, aber technisch wiederholbaren Trajektorie wurde die Koaxialnadel robotisch durch ein Wasserbad geführt (Dauer 24 s). Alle 300 ms wurden die Referenzmarker mit einer räumlichen Basisauflösung von 4,7 mm aufgenommen. Die anschließende Lokalisation war an 75 von insgesamt 80 Zeitpunkten (93,8%) erfolgreich. Dieser Wert ist in sehr gutem Einklang mit den Voruntersuchungen zur Sensitivität (94,8%). Anschließend wurden 20 MR-Kontrollaufnahmen (Schichtdicke 3 mm) synchronisiert entlang der jeweils lokalisierten Nadelrichtung geplant. Nach wiederholter robotischer Nadelbewegung zeigten *alle* Aufnahmen klar das ungefähr 6 mm breite Nadelartefakt. Dieses Experiment deutet eindrücklich die Praxistauglichkeit der entwickelten Technik an.



## Simultaneous 3D localization of multiple MR-visible markers in fully reconstructed MR images: proof-of-concept for subsecond position tracking

Gregor Thörmer<sup>a,b</sup>, Nikita Garnov<sup>a</sup>, Michael Moche<sup>a</sup>, Jürgen Haase<sup>b</sup>,  
Thomas Kahn<sup>a</sup>, Harald Busse<sup>a,\*</sup>

<sup>a</sup>Department of Diagnostic and Interventional Radiology, Leipzig University Hospital, Leipzig, Germany

<sup>b</sup>Department of Physics and Earth Sciences, University of Leipzig, Leipzig, Germany

Received 16 May 2011; revised 26 August 2011; accepted 21 October 2011

### Abstract

**Purpose:** To determine whether a greatly reduced spatial resolution of fully reconstructed projection MR images can be used for the simultaneous 3D localization of multiple MR-visible markers and to assess the feasibility of a subsecond position tracking for clinical purposes.

**Materials and Methods:** Miniature, inductively coupled RF coils were imaged in three orthogonal planes with a balanced steady-state free precession (SSFP) sequence and automatically localized using a two-dimensional template fitting and a subsequent three-dimensional (3D) matching of the coordinates. Precision, accuracy, speed and robustness of 3D localization were assessed for decreasing in-plane resolutions (0.6–4.7 mm). The feasibility of marker tracking was evaluated at the lowest resolution by following a robotically driven needle on a complex 3D trajectory.

**Results:** Average 3D precision and accuracy, sensitivity and specificity of localization ranged between 0.1 and 0.4 mm, 0.5 and 1.0 mm, 100% and 95%, and 100% and 96%, respectively. At the lowest resolution, imaging and localization took  $\approx 350$  ms and provided an accuracy of  $\approx 1.0$  mm. In the tracking experiment, the needle was clearly depicted on the oblique scan planes defined by the markers.

**Conclusion:** Image-based marker localization at a greatly reduced spatial resolution is considered a feasible approach to monitor reference points or rigid instruments at subsecond update rates.

© 2012 Elsevier Inc. All rights reserved.

**Keywords:** MR markers; Localization; Guidance; Navigation; Tracking; Interventional MRI

### 1. Introduction

Magnetic resonance imaging is not only one of the most powerful diagnostic tools but is also becoming more important as a modality to guide minimally invasive interventions. A key requirement for such procedures is the proper visualization of the specific instrument with respect to the MR anatomy of the patient. While earlier techniques had to rely on the intrinsic artifact of an instrument inside the body [1], current efforts are being made to generally improve

the MR visibility of instruments and develop concepts to accurately detect and track them. The rationale for adding this technology is to improve the guidance, safety and workflow of the interventional procedure, and corresponding examples can be found in the literature [2–7]. In addition, the detection and tracking of MR-visible objects also provide a potential solution to minimize artifacts caused by respiration [8], intestinal peristalsis [9], blood vessel pulsation [10], or by motion of the respective organ itself, for example, of the head [11].

Automatic position monitoring inside the scanner typically requires MR-visible objects that accurately define a reference position as well as an adequate technique to detect such markers in near real time. High accuracy and fast position updates are provided by active markers [2] which

\* Corresponding author. Department of Diagnostic and Interventional Radiology, Leipzig University Hospital, 04103 Leipzig, Germany. Tel.: +49 341 971 7413/7409; fax: +49 341 971 7413/7409.

E-mail address: [harald.busse@medizin.uni-leipzig.de](mailto:harald.busse@medizin.uni-leipzig.de) (H. Busse).



have already been used for various purposes [4,12–14]. These markers are resonant pick-up RF coils whose position can be directly measured by analyzing a limited number of projections of a simple imaging sequence. In order to localize multiple markers, each individual one needs to be connected to a separate receiver channel. Potential safety hazards [15], crosstalk between the connecting wires, and related design considerations [12], however, have so far limited the clinical application of active localization and tracking techniques.

Therefore, marker concepts based on passive contrast [6,7] or on semi-active, resonant RF micro coils [5,16], neither with connection to the scanner (wireless), are equally pursued. These markers offer increased flexibility and safety, but localization usually involves a more complex analysis of the image data, in particular because their signals need to be discriminated against the background and against each other. Corresponding algorithms have been described that either analyze the  $k$ -space data [6,17] or the reconstructed image information [18] to automatically determine the position of the markers. Such techniques are often used for accurate patient-to-image registration, which is required for the proper MRI guidance of interventional instruments or robotic devices. Clinical applications have been described for various target organs such as the brain [19,20], liver [21,22] and prostate [23].

So far, only a few efforts have been made to use passive and semi-active markers for tracking purposes, probably because of the need for a fast and robust localization concept. Flask et al. [5] have implemented a limited projection reconstruction in a fast imaging with steady-state precession (FISP) sequence to reliably detect the signals of semi-active markers. They conclude that their prototype marker positions can be acquired in approximately 200 ms and report a corresponding average three-dimensional (3D) accuracy of around 2 mm. Patil et al. [7] have developed a phase-only cross-correlation algorithm to track a passive (Gd-DTPA-filled) marker in near real time. Localization of multiple markers in fully reconstructed projection images has, to the best of our knowledge, not yet been considered for tracking purposes. This may be explained by the fact that image acquisition at a common in-plane resolution ( $\approx 1$  mm or less) will take several seconds alone [18–20]. On the other hand, it has been shown that a numerical fitting of the marker signals to a template function provides a means to reliably determine peak positions on the subpixel level [24,25].

Therefore, the hypothesis of the present work was that the accuracy of an image-based marker localization with a subsequent template fitting depends only moderately on the underlying image resolution. The time to acquire the marker data in two dimensions (2D) could then be reduced to an extent that would allow at least one update of a complete 3D MRI geometry (position and orientation) per second and, ultimately, device tracking in near real time with only moderate technical efforts. We therefore systematically investigated the effect of reduced spatial sampling on the

precision, accuracy and speed of an image-based localization of three semi-active markers. The analysis of scanned marker images was supplemented with coordinate measurements in a large number of computer-generated (synthetic) images to estimate the inherent accuracy of the processing algorithm without errors due to the processes of MR signal generation and imaging.

## 2. Methods

### 2.1. Fiducial marker and pulse sequence

Three miniature, solenoid coils were built by winding four turns of a thin (0.3 mm diameter), insulated copper wire around a glass tube (outer diameter of 4 mm). Tap water was filled into the tubes and served as signal source (Fig. 1A). These miniature coils were tuned (GSP-830 network analyzer, GW Instek, Taiwan) to the resonance frequency (63.8 MHz) of a whole-body 1.5-T MR scanner (Magnetom Symphony, Siemens Medical Solutions, Erlangen, Germany) by using ceramic chip capacitors (A-series, ATC, Huntington Station, NY, USA) with appropriate capacitance.

The integrated whole-body coil of the scanner was used for RF excitation and signal reception. The miniature coils generated distinct MR signals by inductive coupling with the imaging coil and are therefore referred to as inductively coupled radiofrequency (ICRF) coils. A high marker-to-background contrast is obtained at very low flip angles because the effective excitation angle inside the coil is increased [26].

A balanced steady-state free precession (b-SSFP) sequence was used for marker imaging, because it is relatively fast and provided a better signal-to-noise ratio (SNR) than a fast spoiled gradient-echo sequence in our experiments (data not shown here). A marker data set consisted of three standard (coronal, sagittal, transverse) 2D projections (slice thickness of 300  $\mu$ m) at a large field of view (FOV: 300 $\times$ 300 mm). With the scan geometry kept constant, acquisition matrix size (MX),  $k$ -space sampling [partial Fourier factor (PF)] and receiver bandwidth (BW) were varied to investigate different spatio-temporal resolutions (Table 1). A flip angle of 0.3° had been found to provide optimal marker contrast and was used throughout the series.

### 2.2. Three-dimensional marker localization

Automatic 3D marker localization was performed with a custom-made analysis tool, which has been previously described [24]. The tool was developed under IDL (ITT Visual Information Solutions, Boulder, CO, USA) and runs on a standard PC (here: 2.6 GHz dual-core CPU, 3.2 GB RAM) in a freely available environment (IDL Virtual Machine). The software identifies potential marker signals in three orthogonal 2D projection images and then tries to match the independently derived peak coordinates to a consistent 3D coordinate set. Marker detection is based on a



Fig. 1. (A) MR-visible marker consisting of a small solenoid RF coil (outer diameter 4.6 mm, length 4 mm) and a ceramic chip capacitor. (B) Setup for accuracy measurements showing marker board (12×12×2 cm) and phantom bottle (diameter 12 cm, length 25 cm). One ICRF marker (arrow) was scanned five times in each of the 44 accurately defined positions along the *x*- and *z*-direction. (C) Robotic manipulator (Innomotion) with six degrees of freedom mounted on the patient table. Different instruments can be attached to a so-called application module (AMO) at the end of the robotic arm. (D) Custom-made board [dotted frame in (C)] with three MR-visible markers (arrows) and model instrument (16G coaxial needle, 150 mm long; Invivo, Schwerin, Germany) attached to the AMO. The needle is inserted at the position of the marker centroid and aligned perpendicular to the board.

least squares 2D Gaussian template fitting of the signal profiles in segmented regions of the MR image. The fit results are then checked for plausibility by regarding signal intensity and shape parameters. Fit parameters and results are written to a log file for further analysis. Localization times were estimated (upper limit) by the difference between subsequent calls of the system time (see CPU configurations above).

### 2.3. Precision and accuracy

Precision and accuracy were determined by using a custom-made marker board, which was placed over a phantom bottle (Siemens) filled with NiSO<sub>4</sub> solution (Fig. 1B). The marker board (12×12×2 cm) consisted of an MR-compatible polyamide material and featured a pattern of 11×11 equally spaced (spacing 10 mm) holes (diameter 4.0 mm) drilled by a computer numerical control machine with an estimated accuracy of <0.1 mm (Fig. 1). One corner hole was placed at the isocenter (laser crosshair) position, while the board was properly aligned with the scanner axes. One marker was then translated along both ±*x* (left–right) and ±*z* (head–feet) axes to determine the precision and accuracy of marker localization at different spatial

resolutions of marker imaging. The markers were scanned five times in each of the 44 accurately defined positions along both axes resulting in 41 unique positions (three repeated measurements near the isocenter).

The precision of marker localization was calculated as the mean 3D deviation of each individual MR measurement from the corresponding mean value at the respective position. Three-dimensional errors between MR-determined marker locations and the corresponding actual positions ( $\Delta x$ ,  $\Delta y$ ,  $\Delta z$ ) on the board were calculated as the Euclidean distance

$$r = \sqrt{\Delta x^2 + \Delta y^2 + \Delta z^2}$$

for each of the 44 individual marker positions. The average 3D accuracy of marker localization was derived independently for each translation direction ( $r_x$  and  $r_z$ ) and for all of the obtained values ( $r$ ). The mean localization time was averaged over all marker positions and five repetitions ( $n=220$ ). The sensitivity and specificity of marker localization were determined by considering a 3D localization with only the true and hence no false marker as both true positive and true negative, without any marker as false negative, and with other markers than the true one as false positive.

### 2.4. Orientation dependence

The marker was mounted on a custom-made rotary holder, which was placed beside a phantom bottle (Siemens) and rotated in a horizontal plane (polar angle  $\theta$  with respect to  $B_1$ ) between  $\theta=0^\circ$  and  $65^\circ$  in steps of  $5^\circ$ . The marker was scanned five times in each position at different spatio-temporal resolutions. The dependence of the signal intensity on the coil orientation with respect to the direction of the static magnetic field  $B_0$  was investigated by measuring the average signal intensities in a 2×2-pixel region of interest (ROI) over the marker in coronal projection images. Reference ROIs with sizes of 80×80 pixels [MX=512,

Table 1  
Parameters of balanced SSFP sequence used for marker imaging

Matrix size (square)	Pixel size (mm)	Partial Fourier factor	Bandwidth (Hz/pixel)	TR (ms)	TE (ms)	TA (s)	TL=TA+TP (s)
512	0.59	1	220	6.78	2.82	10.41	11.10
256	1.17	1	220	6.02	2.60	4.62	5.18
128	2.34	0.54	765	2.87	1.20	0.59	0.68
64	4.69	0.75	1395	2.11	0.91	0.30	0.34

TR, repetition time; TE, echo time; TA, acquisition time = 3\*(TR\*matrix size\*partial Fourier factor); TL, localization time; TP, processing time.

pixel spacing (PS)=0.59 mm] and 10×10 pixels (MX=64, PS=4.69 mm) were drawn over the phantom bottle.

### 2.5. Synthetic marker images

A total of 40,000 synthetic marker images were computed by using a custom-made utility developed under Matlab (The MathWorks, Natick, MA, USA). In short, a simplified model [27] was used to calculate a 2D distribution of the magnetic field of our coil design (four turns, length and diameter 4.0 mm) which was then extended to three dimensions by assuming a cylindrical symmetry. This distribution was randomly rotated around its long and its short axis and centered at a random but known position. The synthetic marker images were generated by projecting the respective 3D raw data along a fixed viewing direction (sampled at 2048×2048 points over 300×300 mm), adding noise and resampling the data to (square) matrix sizes of 512, 256, 128 and 64. Corresponding projection images of a volunteer were superimposed to provide an anatomical background. The 3D estimate of the localization error was calculated from the mean 1D displacement between the measured and the known peak coordinates, assuming the 1D errors to be independent from each other.

### 2.6. Feasibility of near-real-time tracking

The feasibility of the presented localization technique for device tracking was evaluated in an experimental setup involving an MR-compatible robotic manipulator (Innomotion, Innomedic, Herxheim, Germany) that fits into a standard bore (Fig. 1C). The components and operating principles of the device have already been described elsewhere [28]. Different instruments can be attached to a

so-called application module (AMO) at the end of a robotic arm that is remotely driven by servo-pneumatic actuators.

A custom-made board attached to the AMO was used as a model instrument holder. Three fiducial markers served to define the location and orientation of a centrally inserted coaxial needle (Fig. 1D). The manipulator was then mounted on the MR table with the AMO placed over a large water-filled plastic container. A numerical control utility provided by the manufacturer allowed the AMO to reproducibly move from starting to target position with the tip of the needle remaining inside the water. During this approach, the board markers were dynamically scanned with the fastest marker sequence used here (MX=64; see Table 1). The marker positions were determined retrospectively and used to calculate the geometries of the scan planes that contain the needle axis at each localization time point. A b-SSFP sequence [flip angle (FA)=70°, TR/TE=4.3/2.14 ms, FOV=150×150 mm<sup>2</sup>, slice thickness=3 mm, MX=128×128, PF=4/8, BW=1085 Hz/pixel] was then used to capture the needle and surrounding structures during a repeated robotic motion of the needle along the same trajectory. These morphological images were acquired at every fourth localization time point ( $n=20$ ) because the standard sequence took an extra 900 ms for preparation and local shimming (actual imaging time was 300 ms only).

## 3. Results

### 3.1. Precision and accuracy

At a flip angle of 0.3°, the background in the marker images was very low and appeared unstructured. Fig. 2A

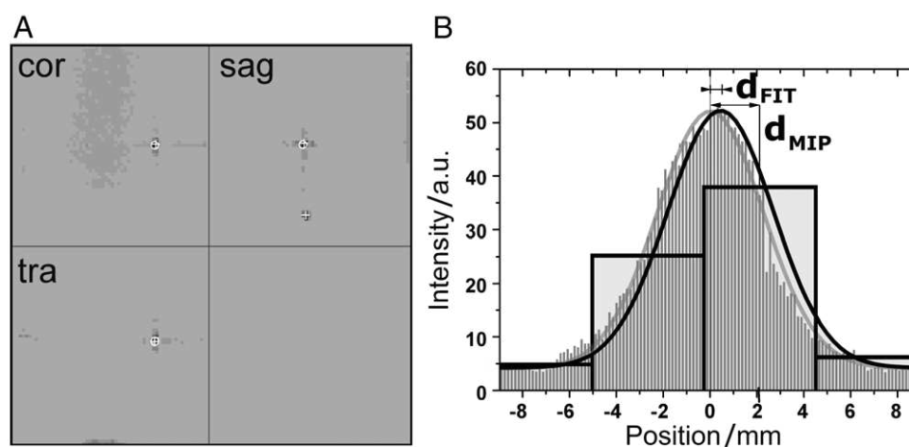


Fig. 2. (A) Screenshot of the localization tool with marker images [b-SSFP, MX=64×64, (square) FOV/slice thickness=300 mm] in three orthogonal scan planes (coronal, sagittal, transverse). Images have been inverted to improve visibility. Note the faint background signal from the phantom bottle at a FA of 0.3°. White crosses indicate peak positions of fitted 2D Gaussian profiles, and white circles properly matched marker positions in 3D. This case also illustrates that a false peak in one of the views (here: sagittal) does not necessarily lead to a false marker because there is no matching peak in the other views. (B) Original (thin gray bars, PS=0.15 mm) and resampled (wide transparent bars with black borders, PS=4.69 mm) 1D signal distributions of a synthetic marker. The maximum intensity pixel is shifted by 2.1 mm ( $d_{MIP}$ ) with respect to the true peak position (0 mm). In contrast, the peak of the fitted 1D Gaussian (black curve) is only shifted by 0.55 mm ( $d_{FIT}$ ). Note that the actual algorithm uses 2D Gaussians.

shows an example for a successful 3D detection at  $MX=64$ . The distributions of the measured coordinate deviations from the respective mean values for the highest ( $MX=512$ ,  $PS=0.59$  mm) and lowest ( $MX=64$ ,  $PS=4.69$  mm) spatial resolution investigated here are plotted in Fig. 3A and C. The distribution at low spatial resolution is wider than that at high resolution, which is also reflected by the respective mean values (0.39 and 0.09 mm). The corresponding results of the calculated 3D deviations as a function of marker distance from the isocenter are given in Fig. 3B and D. These plots indicate that the localization errors measured along the  $z$ -axis were larger than those measured along the  $x$ -axis. The maximum values and the statistical analysis of the absolute deviations for all spatial resolutions are summarized in Table 2.

### 3.2. Orientation dependence

Fig. 4 shows the orientation dependence of the marker signal with respect to the signal of the phantom bottle for the highest ( $MX=512$ ,  $PS=0.59$  mm) and the lowest ( $MX=64$ ,  $PS=4.69$  mm) resolution considered here. In a range of tilt angles below  $45^\circ$ , the true marker was localized in all trials for both resolutions (sensitivity 100%), and false (additional)

Table 2

Summary of 3D localization errors as a function of spatial resolution and direction ( $x, z$ ) of marker translation

Matrix size (square)	Pixel size (mm)	Type (direction)	Localization error		
			$\mu$ (mm)	$\sigma$ (mm)	Max (mm)
512	0.59	$r_x$	0.44	0.34	0.93
		$r_z$	0.58	0.35	1.01
		$r$	0.51	0.33	
256	1.17	$r_x$	0.45	0.36	1.19
		$r_z$	0.65	0.43	1.73
		$r$	0.55	0.37	
128	2.34	$r_x$	0.69	0.52	1.58
		$r_z$	0.82	0.49	1.52
		$r$	0.76	0.50	
64	4.69	$r_x$	0.94	0.58	1.53
		$r_z$	1.12	0.92	2.81
		$r$	1.03	0.57	

$\mu$ , Mean;  $\sigma$ , standard deviation.

markers were only observed for the lowest resolution in 2 of 50 trials at  $\theta=15^\circ$  and  $35^\circ$  (specificity 96%). Automatic 3D localization also succeeded between  $45^\circ$  and  $60^\circ/55^\circ$  (high/low resolution) but failed for angles above the latter values. The influence of marker orientation on precision is shown in Fig. 4B and D for both resolutions.

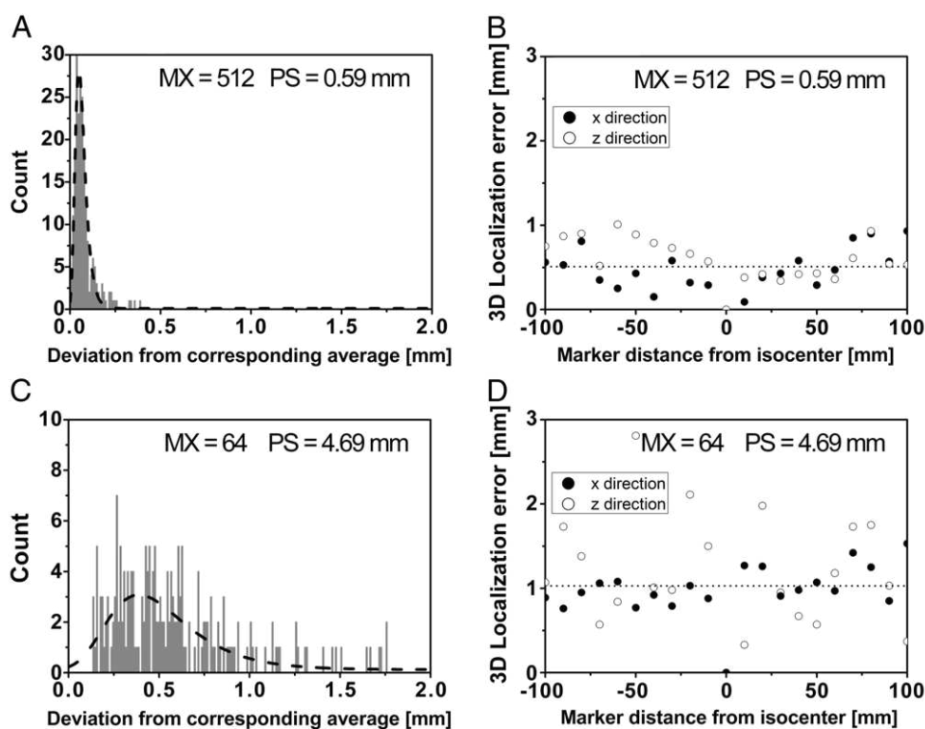


Fig. 3. Precision (A) and accuracy (B) of 3D localization for the *highest* spatial resolution ( $MX=512$ ,  $PS=0.59$  mm), as well as precision (C) and accuracy (D) for the *lowest* spatial resolution ( $MX=64$ ,  $PS=4.69$  mm) considered here. Precision (reproducibility) was calculated as the deviation of each MR measurement from its corresponding mean value. In (A) and (C), Lorentzian fits to the histogram data (dashed lines) were used to determine mean precisions of 0.09 and 0.39 mm, respectively. In (B) and (D), absolute localization errors were plotted against marker distance from the isocenter. For translations along  $z$ , 3D errors are slightly larger than those along  $x$ . Assuming  $x$ - and  $y$ -errors to be the same (symmetry of gradients), dotted lines denote the weighted average of individual 3D localization errors.

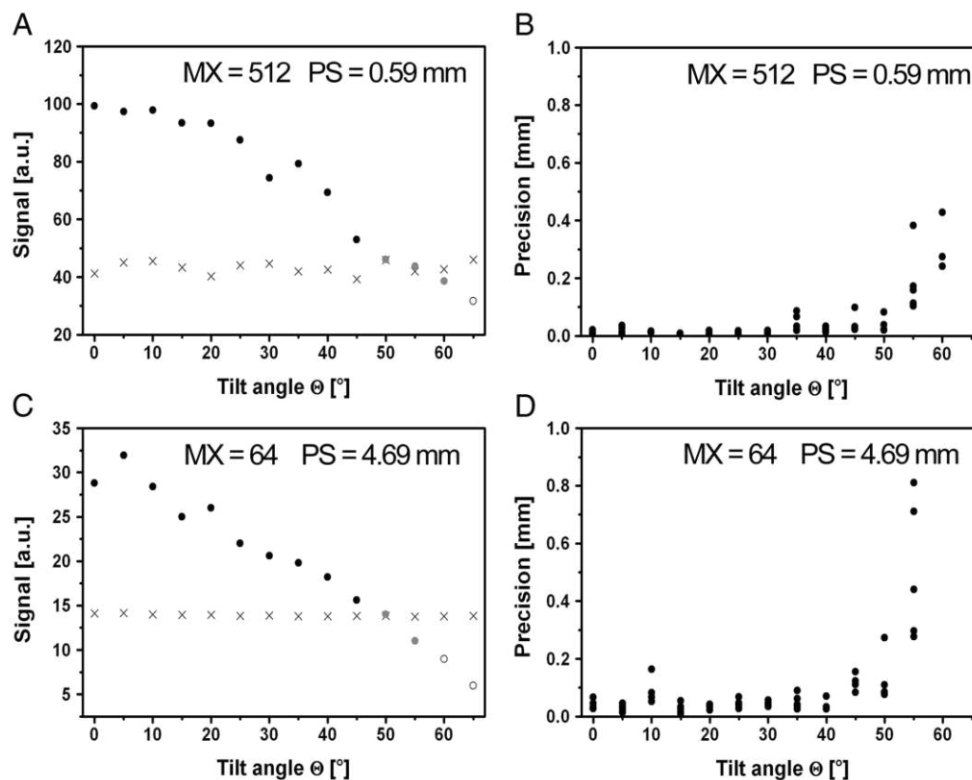


Fig. 4. Variation of average marker ( $\bullet$ ,  $\bullet$ ,  $\circ$ ) and background signals ( $\times$ ) with tilt angle  $\theta$  for the highest (A) and lowest (C) spatial resolution considered here. Solid circles correspond to automatic marker detection in three ( $\bullet$ ) and two ( $\bullet$ ) views, respectively, and mean successful marker localization in 3D. An open circle ( $\circ$ ) means that the marker was detected in less than two views and, therefore, 3D localization failed. The dependence of precision on tilt angle  $\theta$  is shown in (B) and (D) for the highest and for the lowest spatial resolution, respectively.

### 3.3. Synthetic marker images

Fig. 5 shows the synthetic marker images at different spatial resolutions derived from the same distribution of the input signal. Fig. 2B illustrates for a 1D example how different resolutions influence the accuracy of marker localization based on Gaussian fitting. A comparison with the experimental profiles shows that the mean 3D errors of the synthetic profiles,  $0.20 \pm 0.15$ ,  $0.27 \pm 0.21$ ,  $0.36 \pm 0.30$  and  $0.49 \pm 0.48$  mm for MX=512, MX=256, MX=128 and MX=64, respectively, were systematically lower than the measured ones (Fig. 6). The results on the statistical performance of our marker localization are summarized in Table 3.

### 3.4. Feasibility of near-real-time tracking

The time needed for the acquisition of three 2D marker images was substantially reduced by sparse spatial (large pixels) and partial  $k$ -space sampling (Fig. 6B). At MX=64, the time needed for automatic processing of the marker images was 31 ms, which results in an overall time of  $\approx 334$  ms for marker imaging and analysis.

Fig. 7 shows an overlay of selected photographs from two orthogonal views taken during a 24-s robotic needle motion. Localization images were acquired every  $\approx 300$  ms, and 3D

marker detection was successful in 75 ( $\approx 94\%$ ) of 80 cases. The needle artifact could be clearly depicted on all (20/20) “anatomical” control images, which suggests an accurate automatic definition of the scan plane geometry. Fig. 8 shows the actual double oblique MR scans in the AMO positions depicted in Fig. 7.

## 4. Discussion

### 4.1. Fiducial marker

The performance, flexibility and safety of MR-visible markers are essential for their technical and clinical application. In this work, inductively coupled RF coils have been used as markers. These markers can be easily visualized against the anatomical background if they are imaged at very low flip angles [21]. Typically, materials with a short  $T_1$  relaxation time are used as signal source and marker imaging often relies on fast spoiled gradient-echo sequences [6,26]. In this study, we deliberately chose tap water for a number of reasons: it is safe, readily available, generates no chemical shift artifact from lipid components, and represents an extreme sample material due to its long  $T_1$  time. The already high contrast observed here suggests that common signal sources with a much shorter  $T_1$  time are not

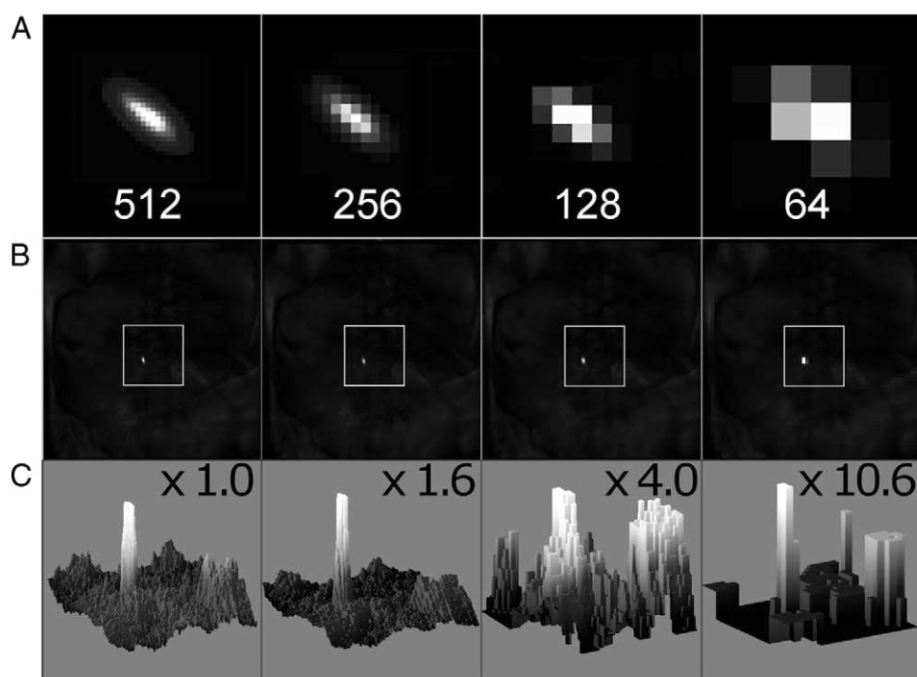


Fig. 5. Synthetic MR marker signals at different spatial resolutions. Numbers indicate (square) matrix size. (A) Two-dimensional distributions of simulated signal intensities with random noise after projection. (B) Simulated distributions superimposed on an anatomical background image. (C) Three-dimensional surface plots of marker images illustrating relative signal intensities [plot range corresponds to square ROIs in (b)]. Plots have been scaled by the given factors to allow better comparison of signal and background features.

necessarily required for this technique. In addition, good experience with water-filled markers in a clinical setting has already been reported [21]. The disadvantages of coil-based

markers are the signal loss for certain orientations (coil axis parallel to the  $B_0$  direction) [5] and the possible heating due to electromagnetic coupling [29]. The orientation dependence in the magnetic field may be reduced by specific coil designs [30], while device heating can be controlled by adjusting the quality factor [29]. Temperature measurements after 10 min of RF exposure (specific absorption rate 2.0 W/kg) revealed a 5°C heating of the coils used here, which appears to be safe enough for extracorporeal use [31]. For applications inside the body, for example in the vascular system [7] or in body cavities [9], passive markers are more adequate. It should be noted that our localization technique can also detect purely passive markers, if they appear with a high enough contrast against the background. Unlike other methods [6,7], our algorithm can be easily adapted to other sizes and shapes of the marker by simply adjusting the accepted range of the independently fitted half widths of the 2D Gaussians accordingly. Thus, it could also be used to detect elongated objects such as contrast-filled tubes.

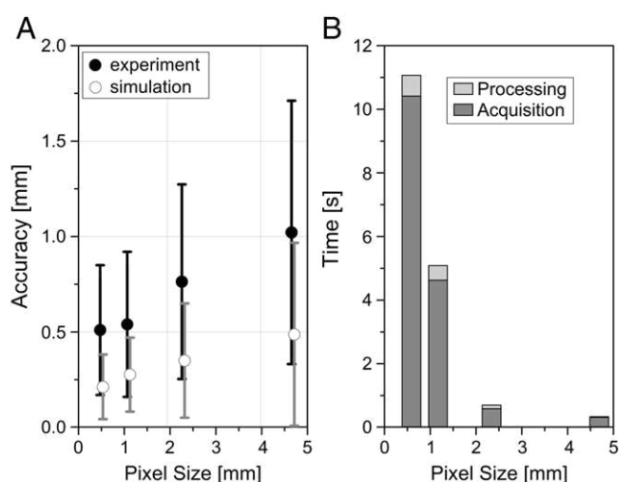


Fig. 6. (A) Three-dimensional localization errors and corresponding variations as a function of pixel size (spatial resolution). The individual data points represent averages over 220 experimental and 10,000 synthetic images for each image resolution. The different errors observed for experimental and synthetic marker images are attributed to the process of MR signal generation. (B) Contributions of image acquisition (dark gray) and processing times (light gray) to the overall localization time as a function of pixel size. The magnitude of the localization time is governed by the acquisition time of the images, in particular for larger pixel sizes.

Table 3  
Sensitivity and specificity of marker localization in scanned MR images of different spatial resolution

Matrix size (square)	Pixel size (mm)	Sensitivity	Specificity
512	0.59	100.0%	100.0%
256	1.17	99.1%	95.9%
128	2.34	99.5%	100.0%
64	4.69	94.8%	95.7%

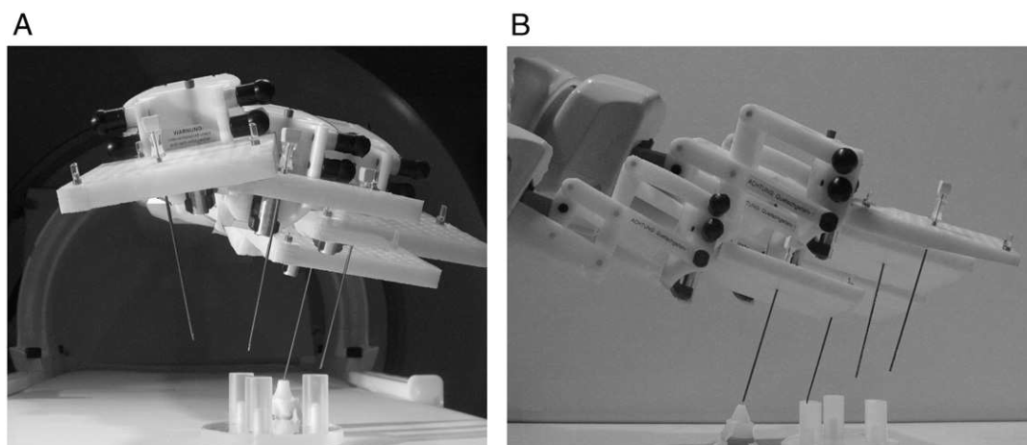


Fig. 7. Head-on (A) and lateral (B) views of the robotic arm with the attached needle at four selected time points during an experimental 24-s-long approach to a model target (plastic cone). The background water phantom has been removed to clearly depict the entire needle length.

This work evaluates the capability of an image-based marker localization at different spatio-temporal resolutions, in particular at low spatial resolution. With the same peak fitting and matching algorithm during image analysis, localization was sped up into the subsecond regime mainly by reducing the spatial and  $k$ -space sampling of a conventional b-SSFP sequence and then finding appropriate image processing and peak discrimination parameters [24]. Three performance criteria will be discussed in the following: (1) how well could the marker coordinates be reproduced? (2) how accurate did MR-calculated and actual marker positions match? and (3) how often did detection fail?

#### 4.2. Precision

The precision of determining the marker positions by MRI was generally very high. At the lowest spatial resolution (pixel size 4.7 mm), the average deviation was

0.4 mm only. This value is essentially caused by random signal fluctuations as well as by experimental factors during signal processing.

Precision of automated localization is nearly independent from marker orientation for tilt angles less than  $45^\circ$ . For more extreme positions, the inductive coupling is less effective and the signal-to-background contrast is reduced, which results in a lower precision. This limitation, however, could be resolved by using a different marker design [30]. Although passive markers do not exhibit such orientation dependence, they generally provide a lower signal-to-background contrast because they need to be imaged at higher flip angles where the contribution of background structures is much larger [16].

#### 4.3. Accuracy

Contributions of the machining tolerance (0.1 mm) and imperfect alignment of the marker board with the scanner

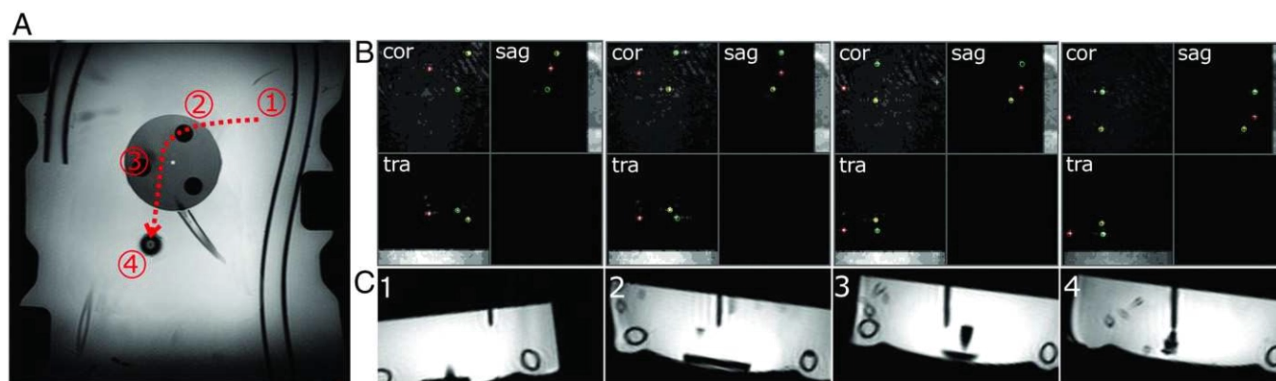


Fig. 8. (A) Coronal roadmap image with overlaid needle trajectory (dashed line) realized by robotic manipulator. (B) Marker positions (colored circles) are automatically overlaid onto each 2D view of the marker images. (C) The needle artifact (full width at half maximum of 6 mm) is clearly depicted in the “anatomical” control images (detail) acquired with a slice thickness of 3.0 mm. Numbers correspond to device positions on (A).

axis (estimated with  $0.1^\circ$  along the  $z$  direction) to the overall accuracy are assumed to be negligible. As expected, the absolute errors were in the subpixel range for all spatial resolutions. The accuracy of  $\approx 0.5$  mm observed for the highest spatial resolution (PS=0.59 mm) appears to be adequate, for example, for the registration of stereotactic systems in neurosurgical applications [19]. A doubling of the pixel size from 0.59 to 1.17 mm, however, led to a marginal loss of accuracy only. An eightfold increase in pixel sampling with respect to the highest resolution used here was associated with just a twofold increase in the average 3D error (0.5 mm to about 1.0 mm). This suggests that a higher spatial resolution does not necessarily generate a corresponding gain in accuracy. The most notable result, however, is that even at a pixel size of  $4.7 \times 4.7$  mm<sup>2</sup>, the MR-derived marker coordinates showed an average deviation of only 1.0 mm from the true ones.

This initially surprising result may be explained as follows: while a coarse spatial sampling does not reproduce the exact signal curve, the quantitative information about the 3D distribution is still included in the intensities of the projected signals. The calculation of the marker centroid should only be moderately affected by this redistribution of signal intensities into larger bins because the former is a linear operation on the input signals. The use of a large enough but otherwise arbitrary slice thickness of 300 mm for all spatial resolutions also made sure that no signal contributions were lost along the projection direction.

Further contributions to the observed error come from inherent image distortions caused by nonlinear gradients, a nonhomogeneous static field and shimming errors [32]. The accuracy was also determined on synthetic marker images to estimate the order of these contributions. The corresponding results suggest that image distortions will contribute considerably to the overall error, for example, 50% at the highest spatial resolution. For most practical purposes, however, the absolute accuracy will still be adequate. In special cases, a previously published numerical method can be used to correct for such image distortions [33].

#### 4.4. Reliability

The good reliability of our automatic marker detection is demonstrated by the high values of the sensitivity and specificity observed here. The sensitivity of marker localization was larger than 99% for pixel spacings as high as 2.34 mm. At a spacing of 4.7 mm, the sensitivity was still around 95%, which means that a true marker will be missed in only 1 of 20 localizations on average. The specificity of all marker localizations was larger than 95%, which means that the chance of detecting a false marker will be relatively low. For coil rotations up to  $55^\circ$ , our data indicate that neither sensitivity nor specificity of localization is affected. For tilt angles above  $55^\circ$ , however, localization failed. Acquisition of all three independent projections is considered to largely contribute to the high values for sensitivity and specificity. If

a single marker is missing or if a background structure is tagged as a marker in one of the views, these detection errors can still be resolved during the subsequent mutual matching of the 2D marker coordinates from all individual views [21]. At tilt angles of  $50^\circ$  and  $55^\circ$ , for example, the marker could be localized in 3D without coordinate information from the transverse view, where the marker signal was corrupted by signal contributions from the phantom bottle. Errors in more than one view, however, are likely to result in wrong or missing 3D coordinates. In a clinical setting, the coils should ideally be oriented with their axis perpendicular to  $B_0$  (tilt angle  $0^\circ$ ) such that inductive coupling is best. These results indicate that the axis can also be tilted up to  $40$ – $45^\circ$  without any substantial loss in performance.

Our results are of particular importance for MR-guided interventions. In our experiment with a robotically driven instrument, the entire needle path could be followed by MR imaging. Therefore, by using at least three attached markers and imaging them at a reduced spatial resolution, it should be possible to track the position and orientation of any rigid instrument, such as a biopsy needle, in near real time. If this information is used to align a scan plane with respect to the needle axis, the average (maximum) error of the marker position translates to an average (maximum) deviation of the centroid and angle of 1.0 mm (2.8 mm) and  $1.2^\circ$  ( $3.5^\circ$ ), respectively. These values agree with results that can be found in the literature for semi-active, optical and magnetic tracking [20,34]. Tracking techniques that are solely based on differential changes relative to the previous device position are very efficient but prone to sudden movements and twists of the instrument as reported by de Oliveira et al. [6]. In contrast, our tracking technique is referenceless and an occasional error in localization as observed in 6% of our cases (5/80) will mean a singular loss of tracking information but will not affect the subsequent measurement. Whereas active techniques typically provide accurate positions in tens of milliseconds, the main advantage of our technique is its flexibility. Our cordless markers do not require individual wires connecting to the scanner which minimizes potential safety hazards and also makes them easier to set up or readjust. With the algorithm applied here, localization is not limited either to a specific number and arrangement of the markers or to their specific size and shape because the localization algorithm will independently consider all signals from the projection images that meet predefined geometric marker criteria, especially of size and shape [24]. The technique is relatively simple to implement and may easily be adapted to different scanner models and environments.

In principle, a complete tracking application would require a custom-made imaging sequence that interleaves marker imaging and automatic detection with a geometrically updated anatomical imaging, which was beyond the scope of this work. Although this limitation practically prevents a direct comparison with the results of previously



reported tracking methods, the localization performance can still be evaluated. It is worth noting that most methods work with pixel sizes in the millimeter and submillimeter range, but do not necessarily achieve a much higher accuracy or precision. The present results provide a possible explanation for such a behavior, in particular if we note the marginal improvement in accuracy between the smallest two pixel sizes considered here.

Recently, Rea et al. [25] have investigated how well the position of a small ICRF marker ( $3 \times 3 \times 5 \text{ mm}^3$ ) can be measured with different signal processing methods. At a constant pixel size of  $1.1 \times 1.1 \text{ mm}^2$ , they have found that the mean absolute position error for a simple search of the maximum intensity pixel was three times larger than that observed when 2D Gaussians were fitted to the signal distribution. This could also explain the magnitude of 3D errors for the fast localization of a paramagnetic marker reported by Patil et al. [7]. With the use of a custom-made pulse sequence with 1D projections along all three axes, the marker position was defined at the pixel with maximum intensity. Although the spatial resolution was less than 1.2 mm, the measured and true 3D marker coordinates differed by an average of 4.0–4.6 mm. De Oliveira et al. [6] have used a similar resolution (1.0 mm isotropic) to localize a Gd-DTPA-filled marker and determined an accuracy of  $1.5 \pm 1.1 \text{ mm}$ . In comparison with the aforementioned work, they have extended a simple pixel search with a subsequent centroid correction. In another work, Flask et al. [5] have reported a maximum error of 3 mm, a mean accuracy of  $\approx 2 \text{ mm}$  and reproducibility measures of 0.2–0.3 mm for a field strength of 0.2 T. Using a limited projection reconstruction technique with a base resolution of 0.8 mm, they achieved update rates of around 200 ms. The authors themselves note that such a feature is more prone to errors because it becomes difficult to differentiate between marker and background signals. The reliability of their limited projection method is expected to be higher at 1.5 T due to the increased SNR.

## 5. Conclusion

Image-based detection of MR-visible markers at a greatly reduced spatial resolution is considered a feasible approach to automatically monitor reference points or rigid instruments inside the scanner at subsecond update rates. For an inline device tracking, the presented 3D marker localization (marker imaging and analysis) needs to be integrated into a custom-made real-time pulse sequence and followed by a corresponding anatomical scan. More general, our results imply that marker signals do not necessarily have to be sampled at submillimeter resolution to achieve a 3D localization accuracy on the order of 1 mm, which is considered typical for the majority of purposes discussed here. The shorter imaging time could then be effectively used to increase the localization speed of such a technique.

## Acknowledgment

The authors would like to thank the people at Innomedic for providing the robotic manipulator.

## References

- [1] Lufkin R, Teresi L, Chui L, Hanafee W. A technique for MR-guided needle placement. *Am J Roentgenol* 1988;151:193–6.
- [2] Dumoulin CL, Souza SP, Darrow RD. Real-time position monitoring of invasive devices using magnetic resonance. *Magn Reson Med* 1993;29:411–5.
- [3] Silverman SG, Collick BD, Figueira MR, Khorasani R, Adams DF, Newman RW, et al. Interactive MR-guided biopsy in an open-configuration MR imaging system. *Radiology* 1995;197:175–81.
- [4] Coutts GA, Gilderdale DJ, Chui M, Kasuboski L, DeSouza NM. Integrated and interactive position tracking and imaging of interventional tools and internal devices using small fiducial receiver coils. *Magn Reson Med* 1998;40:908–13.
- [5] Flask C, Elgort D, Wong E, Shankaranarayanan A, Lewin J, Wendt M, et al. A method for fast 3D tracking using tuned fiducial markers and a limited projection reconstruction FISP (LPR-FISP) sequence. *J Magn Reson Imaging* 2001;14:617–27.
- [6] de Oliveira A, Rauschenberg J, Beyersdorff D, Semmler W, Bock M. Automatic passive tracking of an endorectal prostate biopsy device using phase-only cross-correlation. *Magn Reson Med* 2008;59:1043–50.
- [7] Patil S, Bieri O, Jhooti P, Scheffler K. Automatic slice positioning (ASP) for passive real-time tracking of interventional devices using projection-reconstruction imaging with echo-dephasing (PRIDE). *Magn Reson Med* 2009;62:935–42.
- [8] Plathow C, Zimmermann H, Fink C, Umatham R, Schöbinger M, Huber P, et al. Influence of different breathing maneuvers on internal and external organ motion: use of fiducial markers in dynamic MRI. *Int J Radiat Oncol Biol Phys* 2005;62:238–45.
- [9] Qin L, Schmidt EJ, Hoge WS, Santos J, Tempany-Afdhal C, Butts-Pauly K, et al. Improved prostate-cancer staging with an integrated Endorectal/tracking coil assembly. *Proc. of 8th IMRI Symposium*, Leipzig, Germany; 2010. p. 193.
- [10] Schmidt EJ, Yoneyama R, Dumoulin CL, Darrow RD, Klein E, Kiruluta AJ, et al. 3D coronary motion tracking in swine models with MR tracking catheters. *J Magn Reson Imaging* 2009;29:86–98.
- [11] Ooi MB, Krueger S, Thomas WJ, Swaminathan SV, Brown TR. Prospective real-time correction for arbitrary head motion using active markers. *Magn Reson Med* 2009;62:943–54.
- [12] Bock M, Volz S, Zühlsdorff S, Umatham R, Fink C, Hallscheidt P, et al. MR-guided intravascular procedures: real-time parameter control and automated slice positioning with active tracking coils. *J Magn Reson Imaging* 2004;19:580–9.
- [13] Wacker FK, Elgort D, Hillenbrand CM, Duerk JL, Lewin JS. The catheter-driven MRI scanner: a new approach to intravascular catheter tracking and imaging-parameter adjustment for interventional MRI. *Am J Roentgenol* 2004;183:391–5.
- [14] deSouza NM, Kormos DW, Krausz T, Coutts GA, Hall AS, Burl M, et al. MR-guided biopsy of the breast after lumpectomy and radiation therapy using two methods of immobilization in the lateral decubitus position. *J Magn Reson Imaging* 1995;5:525–8.
- [15] Konings MK, Bartels LW, Smits HF, Bakker CJ. Heating around intravascular guidewires by resonating RF waves. *J Magn Reson Imaging* 2000;12:79–85.
- [16] Burl M, Coutts GA, Young IR. Tuned fiducial markers to identify body locations with minimal perturbation of tissue magnetization. *Magn Reson Med* 1996;36:491–3.
- [17] Chen QS, Defrise M, Deconinck F. Symmetric phase-only matched filtering of Fourier–Mellin transforms for image registration and

- recognition. *IEEE Trans Pattern Anal Machine Intell* 1994;16: 1156–68.
- [18] Kozak J, Nesper M, Fischer M, Lutze T, Göggelmann A, Hassfeld S, et al. Semiautomated registration using new markers for assessing accuracy of a navigation system. *Comput Aided Surg* 2002;7:11–24.
- [19] Rachinger J, von Keller B, Ganslandt O, Fahlbusch R, Nimsky C. Application accuracy of automatic registration in frameless stereotaxy. *Stereotact Funct Neurosurg* 2006;84:109–19.
- [20] Krishnan R, Hermann E, Wolff R, Zimmermann M, Seifert V, Raabe A. Automated fiducial marker detection for patient registration in image-guided neurosurgery. *Comput Aided Surg* 2003;8: 17–23.
- [21] Busse H, Garnov N, Thörmer G, Zajonz D, Gründer W, Kahn T, et al. Flexible add-on solution for MR image-guided interventions in a closed-bore scanner environment. *Magn Reson Med* 2010;64:922–8.
- [22] Moche M, Zajonz D, Kahn T, Busse H. MRI-guided procedures in various regions of the body using a robotic assistance system in a closed-bore scanner: preliminary clinical experience and limitations. *J Magn Reson Imaging* 2010;31:964–74.
- [23] Krafft AJ, Jenne JW, Maier F, Stafford RJ, Huber PE, Semmler W, et al. A long arm for ultrasound: a combined robotic focused ultrasound setup for magnetic resonance-guided focused ultrasound surgery. *Med Phys* 2010;37:2380–93.
- [24] Busse H, Trampel R, Gründer W, Moche M, Kahn T. Method for automatic localization of MR-visible markers using morphological image processing and conventional pulse sequences: feasibility for image-guided procedures. *J Magn Reson Imaging* 2007;26:1087–96.
- [25] Rea M, McRobbie D, Elhawary H, Tse ZT, Lampert M, Young I. Sub-pixel localisation of passive micro-coil fiducial markers in interventional MRI. *MAGMA* 2009;22:71–6.
- [26] Quick HH, Zenge MO, Kuehl H, Kaiser G, Aker S, Massing S, et al. Interventional magnetic resonance angiography with no strings attached: wireless active catheter visualization. *Magn Reson Med* 2005;53:446–55.
- [27] Minard KR, Wind RA. Solenoidal microcoil design: Part I. Optimizing RF homogeneity and coil dimensions. *Concepts Magn Reson* 2001;13: 128–42.
- [28] Melzer A, Gutmann B, Remmele T, Wolf R, Lukoscheck A, Bock M, et al. INNOMOTION for percutaneous image-guided interventions. *IEEE* 2008;27:66–73.
- [29] Busch M, Vollmann W, Bertsch T, Wetzler R, Bornstedt A, Schnackenburg B, et al. On the heating of inductively coupled resonators (stents) during MRI examinations. *Magn Reson Med* 2005;54:775–82.
- [30] Kuehne T, Weiss S, Brinkert F, Weil J, Yilmaz S, Schmitt B, et al. Catheter visualization with resonant markers at MR imaging-guided deployment of endovascular stents in swine. *Radiology* 2004;233: 774–80.
- [31] Garnov N, Thörmer G, Trampel R, Gründer W, Kahn T, Moche M, et al. Suitability of miniature inductively coupled RF coils as MR-visible markers for clinical purposes. *Med Phys* 2011;38:6327–35.
- [32] Wang D, Strugnell W, Cowin G, Doddrell DM, Slaughter R. Geometric distortion in clinical MRI systems. Part I. Evaluation using a 3D phantom. *Magn Reson Imaging* 2004;22:1211–21.
- [33] Wang D, Strugnell W, Cowin G, Doddrell DM, Slaughter R. Geometric distortion in clinical MRI systems. Part II. Correction using a 3D phantom. *Magn Reson Imaging* 2004;22:1223–32.
- [34] Mascott CR. Comparison of magnetic tracking and optical tracking by simultaneous use of two independent frameless stereotactic systems. *Neurosurgery* 2005;57:295–301.

## Arbeit 6 – Studie zur Anwenderabhängigkeit einer Echtzeit-Navigation

Eine komplexe medizinische Assistenztechnik ist generell schwierig zu bewerten. Klinische Ergebnisse sind zwar von hoher Relevanz, oft jedoch durch niedrige Fallzahlen, heterogene Fälle sowie die Ausführung durch erfahrene Anwender gekennzeichnet. Experimentelle Ergebnisse hingegen können nicht uneingeschränkt auf die klinische Situation übertragen werden, erlauben dafür aber größere Untersuchungszahlen, standardisierte Messbedingungen und gezielte Vergleiche zwischen verschiedenen Anwendergruppen.

In der nächsten Arbeit [86] wurden daher 240 experimentelle Biopsien unter Echtzeit-Navigation durchgeführt und hinsichtlich Trefferquote, Zeitbedarf und Anwenderfreundlichkeit ausgewertet. Jeder der 24 medizinischen Anwender punktierte dabei zehn Zielobjekte (Durchmesser um 8,5 mm) in einem Gewebephantom. Um den Einfluss mancher Faktoren zu verringern, wurden die Zielobjekte mit Hilfe einer Schablone einheitlich räumlich angeordnet und mussten in derselben Reihenfolge punktiert werden. Ferner erhielten alle Studienteilnehmer eine 6-minütige Video-Einweisung in die Technik und das Vorgehen. Durch Rekrutierung von jeweils acht Medizinstudenten, Assistenzärzten und Fachärzten konnten Abhängigkeiten vom Erfahrungsgrad untersucht werden.

Im Ergebnis zeigte die Kombination aus *flexibler* MR-Referenzierung und optischem Tracking trotz fehlender Bildkontrolle eine hohe Trefferquote, z. B. 92,5% im Mittel für Fachärzte. Während die Trefferquoten sich zwischen den Gruppen *nicht* signifikant unterschieden, wurden die Biopsiezeiten mit abnehmender Erfahrung *signifikant* länger. Insgesamt zeigte das System bei allen experimentellen Biopsien eine hohe Genauigkeit und gute Anwenderfreundlichkeit. Die Ergebnisse dieser kontrollierten Untersuchung belegen den potenziellen Wert einer Echtzeit-Navigation für die Interventionsführung.

Die Punktion an einem unbewegten Phantom stellt natürlich eine Vereinfachung gegenüber dem realen Einsatz dar. Die klinische Genauigkeit wird maßgeblich durch die Beweglichkeit der betreffenden Körperregion beeinflusst. Diese Limitation gilt jedoch prinzipiell für jede stereotaktische Zielhilfe. Beim klinischen Einsatz des Navigationssystems sollte die finale Nadellage jedoch praktisch immer durch eine Kontrollaufnahme bestätigt werden. So könnte eine mögliche Abweichung einfach detektiert und korrigiert werden. Der dazugehörige Datensatz ließe sich außerdem als aktualisierte Referenz verwenden.

RESEARCH ARTICLE

# Targeting Accuracy, Procedure Times and User Experience of 240 Experimental MRI Biopsies Guided by a Clinical Add-On Navigation System

Harald Busse\*, Tim Riedel, Nikita Garnov, Gregor Thörmer, Thomas Kahn, Michael Moche

Department of Diagnostic and Interventional Radiology, Leipzig University Hospital, Leipzig, Germany

\* E-mail: [harald.busse@medizin.uni-leipzig.de](mailto:harald.busse@medizin.uni-leipzig.de)



## Abstract

### Objectives

MRI is of great clinical utility for the guidance of special diagnostic and therapeutic interventions. The majority of such procedures are performed iteratively ("in-and-out") in standard, closed-bore MRI systems with control imaging inside the bore and needle adjustments outside the bore. The fundamental limitations of such an approach have led to the development of various assistance techniques, from simple guidance tools to advanced navigation systems. The purpose of this work was to thoroughly assess the targeting accuracy, workflow and usability of a clinical add-on navigation solution on 240 simulated biopsies by different medical operators.

### Methods

Navigation relied on a virtual 3D MRI scene with real-time overlay of the optically tracked biopsy needle. Smart reference markers on a freely adjustable arm ensured proper registration. Twenty-four operators – attending (AR) and resident radiologists (RR) as well as medical students (MS) – performed well-controlled biopsies of 10 embedded model targets (mean diameter: 8.5 mm, insertion depths: 17-76 mm). Targeting accuracy, procedure times and 13 Likert scores on system performance were determined (strong agreement: 5.0).

### Results

Differences in diagnostic success rates (AR: 93%, RR: 88%, MS: 81%) were not significant. In contrast, between-group differences in biopsy times (AR: 4:15, RR: 4:40, MS: 5:06 min: sec) differed significantly ( $p < 0.01$ ). Mean overall rating was 4.2. The average operator would use the system again (4.8) and stated that the outcome justifies the extra effort (4.4). Lowest agreement was reported for the robustness against external perturbations (2.8).

### OPEN ACCESS

**Citation:** Busse H, Riedel T, Garnov N, Thörmer G, Kahn T, Moche M (2015) Targeting Accuracy, Procedure Times and User Experience of 240 Experimental MRI Biopsies Guided by a Clinical Add-On Navigation System. PLoS ONE 10(7): e0134370. doi:10.1371/journal.pone.0134370

**Editor:** Heye Zhang, Shenzhen institutes of advanced technology, CHINA

**Received:** February 12, 2015

**Accepted:** July 9, 2015

**Published:** July 29, 2015

**Copyright:** © 2015 Busse et al. This is an open access article distributed under the terms of the [Creative Commons Attribution License](https://creativecommons.org/licenses/by/4.0/), which permits unrestricted use, distribution, and reproduction in any medium, provided the original author and source are credited.

**Data Availability Statement:** All dataset files are available from the figshare database (<http://dx.doi.org/10.6084/m9.figshare.1425092>).

**Funding:** The authors acknowledge support from the German Research Foundation (DFG) and Universität Leipzig within the program of Open Access Publishing.

**Competing Interests:** The authors have declared that no competing interests exist.

## Conclusions

The described combination of optical tracking technology with an automatic MRI registration appears to be sufficiently accurate for instrument guidance in a standard (closed-bore) MRI environment. High targeting accuracy and usability was demonstrated on a relatively large number of procedures and operators. Between groups with different expertise there were significant differences in experimental procedure times but not in the number of successful biopsies.

## Introduction

Minimally invasive diagnostic and therapeutic procedures are typically performed under image guidance. Established imaging techniques like ultrasound (US) and computed tomography (CT) are widely available and allow for fast or even real-time control of the procedure. In special cases, however, MRI becomes the method of choice, most often when targets or critical anatomical structures along the access path are only visible by MRI [1]. The last two decades have seen a number of dedicated MRI systems, in particular open units that provide good access to the patient and have been successfully used for image-guided procedures [2–5]. The ongoing development of faster pulse sequences has largely contributed to make instrument navigation more intuitive [6,7]. At the same time, traditional 60-cm bore MRI systems have increasingly been replaced by wide-bore models that offer some more space for operation [8–12].

Some interventions, often in well-defined regions of the body, can actually be performed inside the magnet, whereas the most common practice with cylindrical MRI systems is to slide the patient in and out of the magnet for successive imaging and intervention steps, respectively [11,13,14]. This gives the operator unobstructed access to the patient but is generally time-consuming and prone to positioning errors. Guidance can be improved by providing the operator with an overlay of the instrument position on continuously reformatted MRI data. In one implementation [15], this was achieved by a navigation system with optical real-time instrument tracking. The system is characterized by a floating reference structure that enables navigation for procedures in practically all parts of the body. It has already been applied clinically for various percutaneous interventions, mainly biopsies, in different target regions, for example, the shoulder, breast, liver, paravertebral region, pelvis or the femur. Corresponding information for some of these cases can be found in the literature [8,15,16]. In comparison with other techniques, continuous registration is ensured by a fast, one-time 3D localization of three smart MR markers that can be reliably detected over a wide variety of imaging conditions. The setup is invariant against both motion of the patient table as well as that of the rolling 3D digitizer. Any multislice or 3D data can be loaded for planning purposes and control images can be automatically prescribed along any optically measured instrument pose [15].

Detailed evaluation of the usability and workflow of a new enabling technology is generally difficult. Clinical studies obviously provide more meaningful parameters but are often limited by small case numbers, an uncontrolled procedural complexity and results from properly trained physicians only. Experimental results, on the other hand, need to be interpreted more carefully but also provide the unique opportunity to improve statistical power, minimize unwanted variation by standardized operating conditions, and deliberately determine the impact of user expertise, in our case, on targeting accuracy and procedure times.

The goal of this work was therefore a comprehensive experimental assessment of the overall targeting accuracy, usability and workflow of such a navigational tool by analyzing a large number of phantom biopsies performed by medical operators with different levels of expertise.

## Materials and Methods

### Hardware Components and Setup

[Fig 1](#) gives an overview of the hardware components and setup of the navigation system for MRI-guided interventions. In short, the position, orientation, and motion of a medical instrument, e. g., biopsy gun or coaxial needle, can be followed in a multiplanar virtual MRI scene that is displayed on a nearby screen. A compact reference device with a set of three reflective markers needs to be attached to the instrument. An optical 3D digitizer (Polaris Spectra, NDI, Waterloo, ON, Canada) then tracks this instrument relative to a second reference set on a board that remains fixed to the patient table. This board also features a set of MR markers [\[17\]](#) that are used for registration of the navigation scene. A special guiding device (front-end module) is used to hold, adjust and lock the coaxial needle in the intended biopsy position. Further details about the navigation principle can be found in a previous work [\[15\]](#).

### Biopsy Phantom

A standardized biopsy phantom was used for all trials ([Fig 2](#)). It consisted of plain, opaque glaze inside a large acrylic glass cylinder (10 cm high and 20 cm in diameter). Ten soft green peas were used as biopsy targets. The average diameter was determined with a caliper on 100 randomly selected peas. A geometric template disc was used to reproducibly arrange the peas in 3D for all trials. Artificial vascular structures were embedded in the phantom so that the interventionalist would have to navigate around these structures while performing the biopsies. The level of targeting complexity varied with the insertion depth of the targets and with the potential presence of vessel structures along the shortest access path perpendicular to the phantom surface ([Fig 2](#)).

### Operators

Biopsies were performed by 24 operators with different interventional expertise: 8 attending (AR) and 8 resident radiologists (RR) from the Diagnostic and Interventional Radiology Department as well as 8 medical students (MS) from the local School of Medicine. A 6-minute instruction video was presented to each operator immediately before the biopsies. One resident radiologist had clinical experience with this navigation system; all other operators had never used it before. Our clinical study evaluating the safety and workflow of the used system was approved by the IRB committee of the Leipzig University Faculty of Medicine. The present phantom study does not involve any healthcare interventions on a person. All operators participated voluntarily in this study and were informed that they could opt out without penalty.

### MR Imaging

The biopsies were performed with a 60-cm closed-bore 1.5-T MRI system (Magnetom Symphony, Siemens Healthcare, Erlangen, Germany). Prior to the biopsies, the phantom setup was registered to MRI coordinates by a one-time acquisition of MR-marker images and a subsequent, fully automatic 3D localization (15–17) of the marker signals. A balanced steady-state free precession (SSFP) sequence with large volume coverage in three orthogonal views (axial, coronal, sagittal) was used for marker imaging (TR/TE = 6.8/2.8 ms, single slice with thickness = 300 mm, field of view FOV = 300 mm × 300 mm, acquisition matrix = 512 × 512, flip

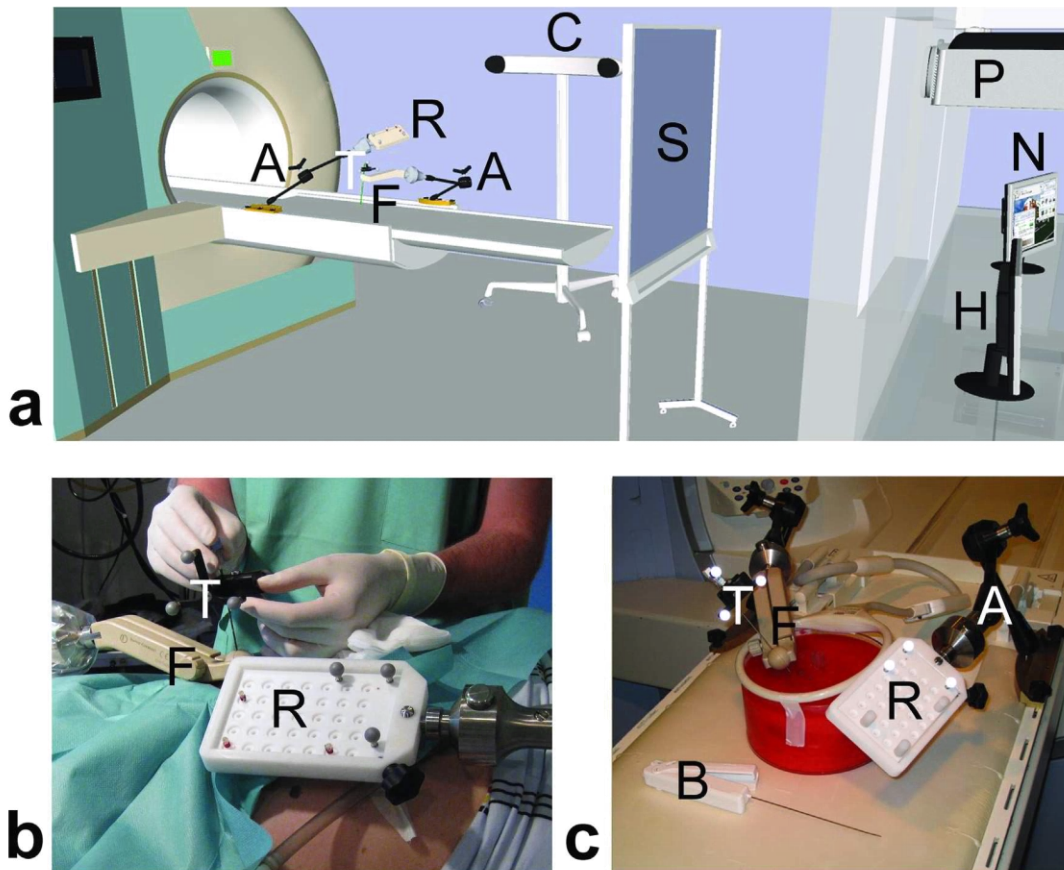


**Fig 1. Add-on navigation solution for MRI-guided interventions.** (a) Schematic drawing of the overall setup illustrating the components at the MRI table ("A" articulating arm, "R" reference board, "F" front-end module for alignment; "T" tracker for instrument), in the MR room ("C" optical 3D tracking camera, "S" projection screen) and in the control room ("P" LCD projector, "N" navigation workstation, "H" MR host computer). (b) Clinical setup of an MRI-navigated biopsy in the kidney. (c) Experimental setup used for the assessment of targeting accuracy, procedure times and usability ("B" biopsy gun).

doi:10.1371/journal.pone.0134370.g001

angle = 0.8°, receiver bandwidth = 222 Hz/pixel, total acquisition time = 10.5 s, and manufacturer's distortion correction enabled). Data from a T1-weighted volume-interpolated breath-hold examination (VIBE) were used for anatomic imaging (TR/TE = 3.8/1.7 ms, 60 slices with thickness = 2.0 mm, FOV = 210 mm × 210 mm, acquisition matrix = 256 × 167, flip angle = 15°, total acquisition time = 23 s).

### Navigation PC

MRI data from the MR console were manually sent to the navigation PC. Automatic marker localization [18] was handled by a stand-alone application written under IDL (Exelis Visual Information Solutions, Boulder, CO, USA). The navigation software [15] featured modules for graphical access planning and navigation (Fig 3). Phantom registration was only needed once per session and simply involved the measured MR-marker coordinates as well as the fixed 3D geometries of tracker and markers to automatically compute the transformation matrix between tracked instrument and MR coordinates.

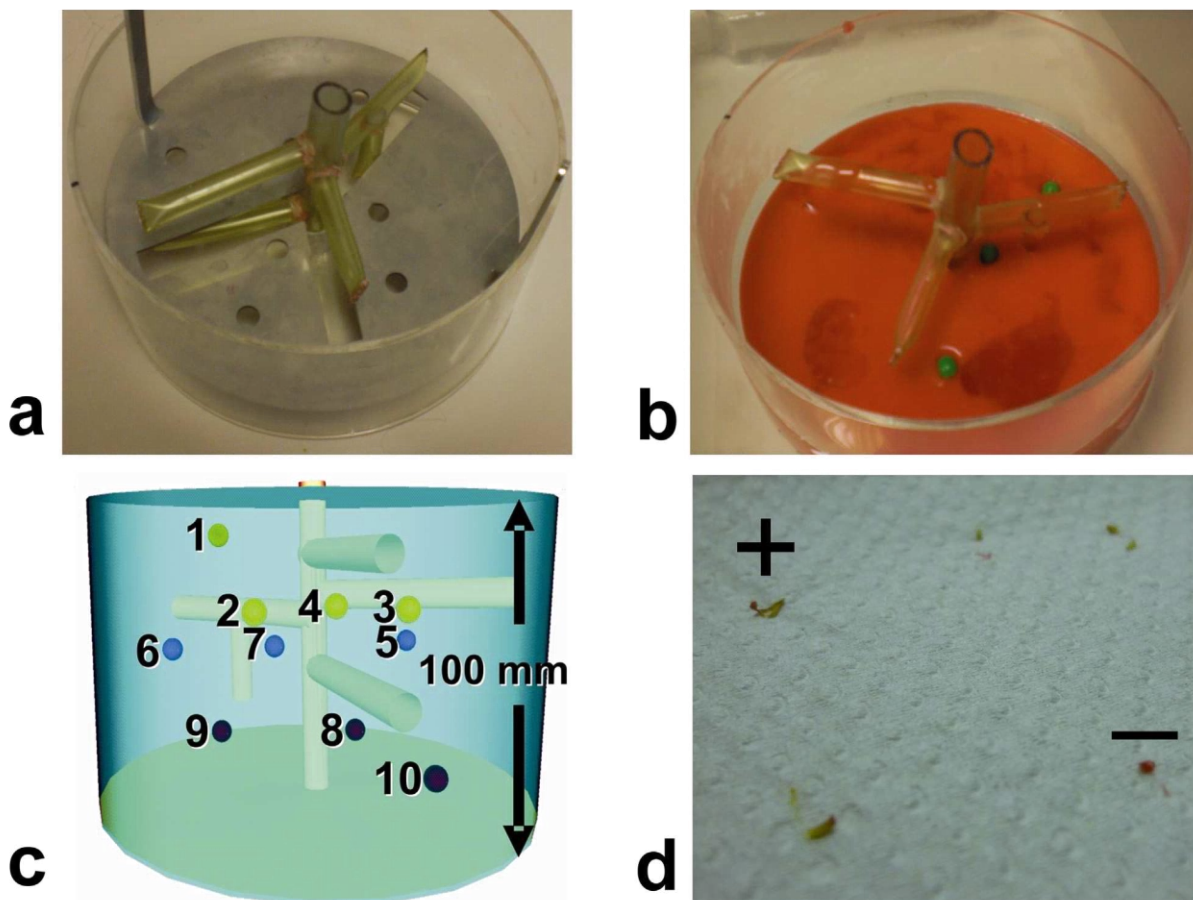


**Fig 2. Standardized biopsy phantom.** (a) Acrylic glass cylinder (10 cm high and 20 cm in diameter) with model vasculature and target positioning template. A three-dimensional structure of silicone tubes served as model vasculature that needed to be avoided. Custom-drilled holes inside a stainless steel disc ensured that experimental targets were placed in the same 3D positions for all trials. (b) The tissue phantom was made out of ordinary red cake glaze in double concentration (160 g powder per 400 ml of water). Ten ordinary green peas were embedded as biopsy targets. The surface of the hardened glaze was later impregnated with a virucidal hand disinfectant (Sterilium Viruguard) and the phantom was stored in a refrigerator. (c) Target difficulty varied with insertion depth (four distinct levels between 17–76 mm from the phantom surface) and placement with respect to the vasculature. Three targets (# 4, 7 and 9) were located under a vessel or another target and could only be accessed by an oblique path. (d) Photograph of tissue samples taken with the fully automatic biopsy gun. Biopsy was counted as success when sample contained green material from the pea (+ sign). Samples of base material (cake glaze) appeared red (-sign).

doi:10.1371/journal.pone.0134370.g002

### Biopsy Cycle

Each operator performed 10 successive biopsy cycles in the same order (Fig 2). A biopsy cycle consisted of five individual steps. During access planning (i), the operator moved the coaxial needle (16G, 135 mm long, Invivo Germany, Schwerin) with the attached tracker over the phantom and followed the corresponding navigation scene on the in-room projection screen to identify the next target and define a corresponding access path. Arm adjustment (ii) involved the rough positioning along that access path and locking of the articulating arm above the phantom. The navigation step (iii) comprised insertion of the coaxial needle into the front-end module, alignment of the virtual needle tip with the center of the MR-visible pea on the navigation screen (Fig 3) and accurate fixation of the instrument. In the sampling step (iv), the biopsy gun (18G, 175 mm long, Invivo Germany) was cocked, inserted into the coaxial needle and released for sample collection. For control imaging (v), the biopsy instrument remained in



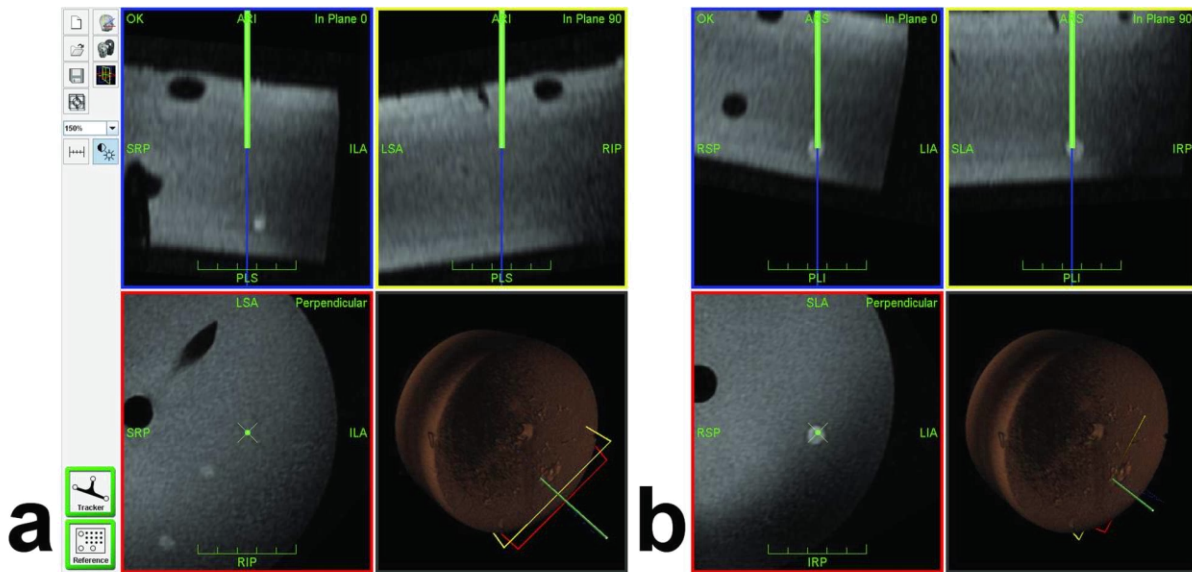


**Fig 3. Navigation Interface During Target Approach.** The navigation interface continuously displays three orthogonal planes reconstructed from the planning MRI dataset along (in-plane 0° and in-plane 90°, blue and yellow frames) and perpendicular (red frame) to the tracked needle. The virtual needle and its extension are displayed as green and blue lines, respectively (virtual tip at the end of the green line). The fourth view indicates the 3D position of the needle and all viewing planes with respect to the volume-rendered MRI dataset. Phantom vessels (tubes) and targets (peas) appear as hypointense and hyperintense structures, respectively. (a) Sample screenshot of a partially inserted needle with the virtual extension slightly off target (#10, in plane 0°). Two other targets (#6 and #7) happen to appear in the perpendicular view. (b) Later screenshot after corresponding adjustment showing the virtual needle tip inside the target (in all views).

doi:10.1371/journal.pone.0134370.g003

place. The MR table was moved into the scanner, the phantom was imaged with the control sequence (see above) and the table was moved back out for the next biopsy cycle. A biopsy was regarded as diagnostic success if the sample clearly contained green material from the pea (Fig 2). For each simulated biopsy, we recorded the partial times for (i) access planning, (ii)

**Table 1. Mean Likert item scores on usability and workflow of navigation tool by 24 operators from three groups.**

Question	All	Rank	AR *	RR *	MS *
Q01—I have understood how the navigation system works.	4.89	1	4.75	4.88	4.75
Q12—I would use the system again.	4.75	2	4.75	4.88	4.63
Q09—The system provides additional safety.	4.67	3	4.63	4.88	4.50
Q05—I had the impression that biopsies became easier with the number of targets.	4.67	4	4.50	4.75	4.75
Q11—Biopsies would <i>not</i> be simpler without the navigation scene on the screen. †	4.67	4	4.75	4.50	4.75
Q08—The time required to perform a biopsy with that system is <i>not</i> too long. †	4.58	6	4.50	4.63	4.63
Q10—The extra technical efforts needed are justified in view of the benefit.	4.42	7	4.50	4.38	4.38
Q13—I have confidence in this technique.	4.21	8	4.25	4.13	4.25
Q02—I can easily orient myself and guide the needle by looking at the navigation screen.	4.13	9	4.13	4.38	3.88
Q03—It is easy to mentally transfer the images on the navigation screen to the real world.	3.92	10	3.88	4.38	3.50
Q04—Operation of the navigation system is self-explaining.	3.88	11	3.88	3.75	4.00
Q06—The articulating module enables easy adjustment and fixation of the biopsy needle.	3.67	12	3.13	4.00	3.88
Q07—The navigation system is <i>not</i> susceptible to external perturbations. †	2.79	13	2.88	3.25	2.25
Mean over all items	4.24		4.19	4.37	4.16

\* AR: attending radiologists, RR: resident radiologists, and MS: medical students

† opposite item with reverse score, original item was negatively keyed

doi:10.1371/journal.pone.0134370.t001

arm adjustment, (iii) navigation, (iv) sampling, and (v) control. Each operator was asked to rate 13 items (Table 1) related to the usability and workflow of the system on a Likert scale from strong (5) and basic (4) agreement via indifference (3) to basic (2) and strong (1) disagreement. These questions are summarized in Table 1 along with the results.

## Statistical Analysis

Sampling success rates were analyzed with a one-way ANOVA with factor group. Partial times for individual working steps as well as total biopsy-cycle times were analyzed with a one-way, repeated measures ANOVA with factor (operator) group (RR, AR, MS) using the average time of all group members for a given target. Total biopsy times were also analyzed with a one-way, repeated measures ANOVA across all operators with factor target (#1 - #10). User ratings were analyzed with the same test using the score average for all group members for a given item. Negatively-keyed items were scored reversely. If the main effect was significant, post-hoc Bonferroni results were considered. The assumption of sphericity was validated with Mauchly's test. All tests were performed with SPSS Version 20.0 (IBM Corp., Armonk, NY).

## Results

### Biopsy Phantom

The viscoelastic properties of the phantom material were subjectively considered to be similar to those of biological tissues. The red glaze alone was so opaque that peas were invisible for the operator. They had an average diameter of  $8.5 \pm 0.5$  mm (mean  $\pm$  SD) with individual values in the 7.0–9.5 mm range. The green pea material collected with the biopsy gun was clearly discernible from the red base material (Fig 2). A single phantom was used by up to six operators because it could be preserved for several weeks. A new phantom was built whenever previous needle insertions left clear traces or voids in the material or when the entire phantom started to decay.

### Success Rates and Biopsy Times for Different Groups

The distribution of the number of hits was  $6 \times 9$  and  $2 \times 10$  for attending radiologists (AR),  $1 \times 7$ ,  $2 \times 8$ ,  $3 \times 9$  and  $2 \times 10$  for resident radiologists (RR), and  $1 \times 6$ ,  $2 \times 7$ ,  $2 \times 8$ ,  $1 \times 9$  and  $2 \times 10$  for medical students. This corresponds to mean success rates (95% confidence intervals) of 92.5% (88.6–96.4%) for AR, 87.5% (78.8–96.2%) for RR, 81.3% (69.1–93.4%) for MS (Fig 4), and 87.1% (82.3–91.8%) for all 24 operators with no significant differences between them ( $p = 0.132$ ). In contrast, the mean times for a complete biopsy cycle in minutes and seconds (AR: 04:15, RR: 04:40, MS: 05:06) were significantly ( $p < 0.01$ ) different (Fig 5). The breakdown of the total times into individual steps for each operator group is shown in Fig 6. The largest absolute time differences between groups were observed for the navigation step (AR: 01:16, RR: 01:25, MS: 01:48,  $p < 0.01$ ). Differences in the mean sampling times were also significant ( $p < 0.05$ ) with a maximum of about 4 s between AR and MS. All other time differences were insignificant (planning:  $p = 0.289$ , adjustment:  $p = 0.512$ , control:  $p = 0.327$ ).

### Biopsy Times for Different Targets

The plot of the total biopsy times over all 24 operators against target number is shown in Fig 7. The corresponding mean values range between 4:15 and 5:07 ( $\Delta t_{\max} = 0:52$ ) and this chronological series features two prominent (differential) increases for targets #4 and #9 (+77% and +73% of  $\Delta t_{\max}$ ). The repeated-measure ANOVA of these biopsy time differences revealed a  $p$ -value of 0.065.

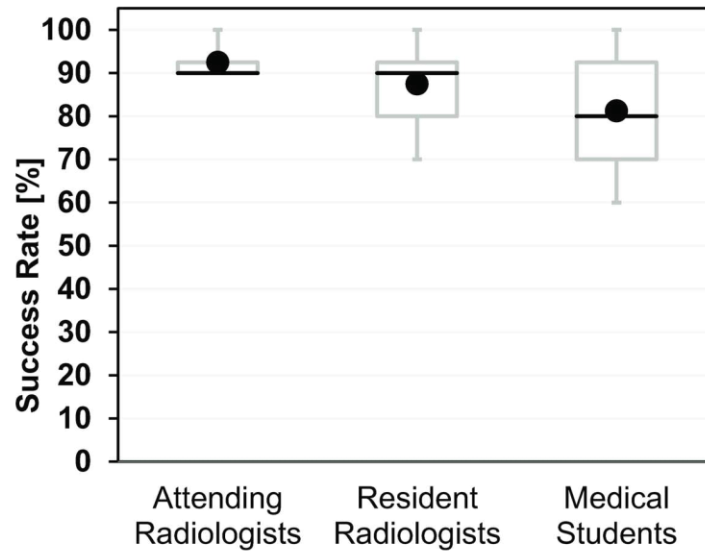


**Fig 4. Success rates of experimental biopsies performed by 24 operators from three different groups (AR, RR, MS).** Each operator performed 10 trials and the individual success rate was simply the number of successful biopsies multiplied by 10%. Each box with whiskers represents the summary for 8 operators in each group. The gray box stretches from the first (25%, Q1) to the third (75%, Q3) quartile and the black line indicates the second (50%, Q2) quartile (median). Owing to the low number of operators per group ( $n = 8$ ), the whiskers correspond to the minimum and maximum success rates observed for a single operator. The black circles indicate the mean success rates. Please note that minimum, Q1, and Q2 of the success rate coincide at 90% for the group of attending radiologists. Between-group differences in the mean success rate were statistically not significant ( $p = 0.132$ ).

doi:10.1371/journal.pone.0134370.g004

### Item Scores

There was no significant between-group difference of the mean item scores ( $p = 0.093$ ). The rounded Likert scores (*LS*) over all items were 4.37 (AR), 4.19 (RR), 4.16 (MS), and 4.24 (all, Table 1). The majority (9/13) of mean item scores averaged over all groups showed normal to strong agreement (4.13–4.79), in particular, whether the operators would use the system again ( $LS = 4.75$ , Q12), felt that the outcome justifies the extra effort (4.42, Q10), and trusted the system (4.21, Q13). While average scores were slightly lower with respect to whether the system was self-explaining (3.88, Q04) and regarding the handling of the guiding device (3.67, lowest score of 3.13 by AR, Q06), operators were indifferent about the system's stability against external perturbations (2.79, lowest score of 2.25 by MS, Q07).

### Discussion

The original presentation of the navigation system included a brief assessment of its technical accuracy and a clinical case [15]. The goal of the present work was a clear-cut analysis of the overall diagnostic accuracy, usability and workflow of such an assistance device on a relevant number of experimental biopsies by various medical experts and trainees. Equipment and devices were the same as those used clinically and the range of experimental target depths (17 to 76 mm) was chosen to include some typical insertion lengths for clinical application, for example, the reported 70 mm for liver interventions [11,19]. A key factor for the validity of such a user-dependent assessment was the carefully controlled, standardized fabrication of the phantom.

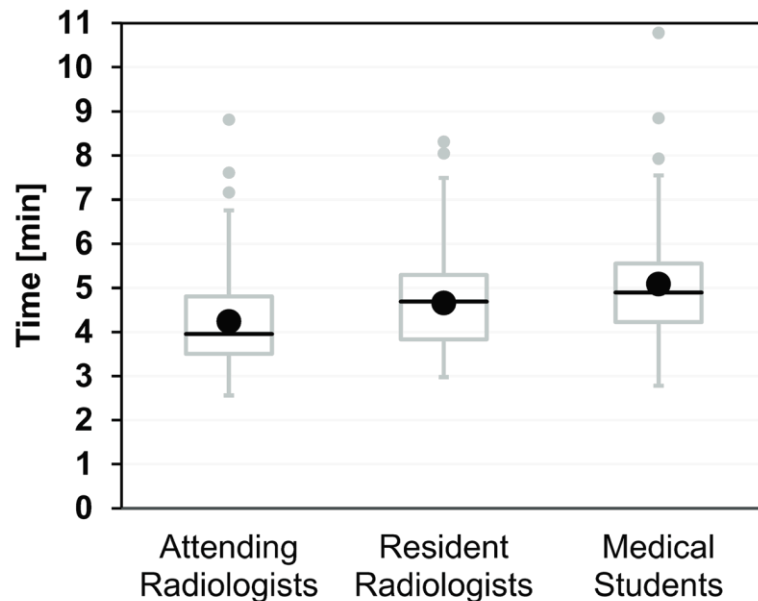


**Fig 5. Experimental total biopsy times for 24 operators from three different groups (AR, RR, MS).** Each operator performed 10 biopsy cycles in the same order. Each box with whiskers represents the summary of 80 biopsy times from 8 operators. The gray box and black line indicate Q1–Q3. Whiskers were plotted according to the definition by J. W. Tukey and either indicate the last values a maximum of  $1.5 \times \text{IQR}$  (interquartile range =  $Q3 - Q1$ ) away from Q1 and Q3, respectively, or the minimum and maximum, whichever comes first. Each group had 2–3 upper outliers (gray circles) with times greater than  $Q3 + 1.5 \times \text{IQR}$ . The black circles indicate the mean biopsy times, which were significantly different between groups ( $p < 0.01$ ). Post-hoc Bonferroni testing revealed significant differences between AR and RR as well as AR and MS.

doi:10.1371/journal.pone.0134370.g005

In the clinical case, correct positioning of the biopsy device is usually evaluated by the MR-visible needle artifact [2,3,10–12,14,19,20]. Its position, size and shape, however, depends on the type of pulse sequence, magnetic field strength and needle orientation with respect to the main field, which is generally seen as a limitation [3,5,8,10,20,21]. A potential offset between MR artifact and true needle position as well as artifact diameters of a few millimeters can be tolerated for the majority of lesions which tend to be larger than that. In a previous work on MR-guided biopsies of 50 liver lesions, however, an average diameter of 15 mm was already considered to be relatively small [3]. Our experimental targets, in comparison, were even smaller (8.5 mm) coming close to the needle artifact size observed here (4–6 mm) and making the usual assessment of positioning accuracy rather difficult. We have therefore decided to judge diagnostic success by the simple presence of green pea material in the otherwise red biopsy sample. This yields an upper limit of the 2D positional accuracy of approximately 4 mm (half the pea diameter) instead of an exact figure. A previous technical assessment has found the average 2D target accuracy to be 2.2 mm and 3.9 mm depending on how far away the reference markers were located from the isocenter [15].

Diagnostic success rates were generally high for all operator groups. The apparent increase seen from medical students via resident to attending radiologists would be in line with the simple picture of better performance by more experienced operators. Statistically, however, there was no significant difference between these groups.

Procedure time is often regarded as a critical factor for MR-guided biopsies [3,11,19,22] and was therefore studied in more detail. The mean times for complete biopsy cycles differed significantly between groups with longer times for less experienced, as expected [7], and the largest

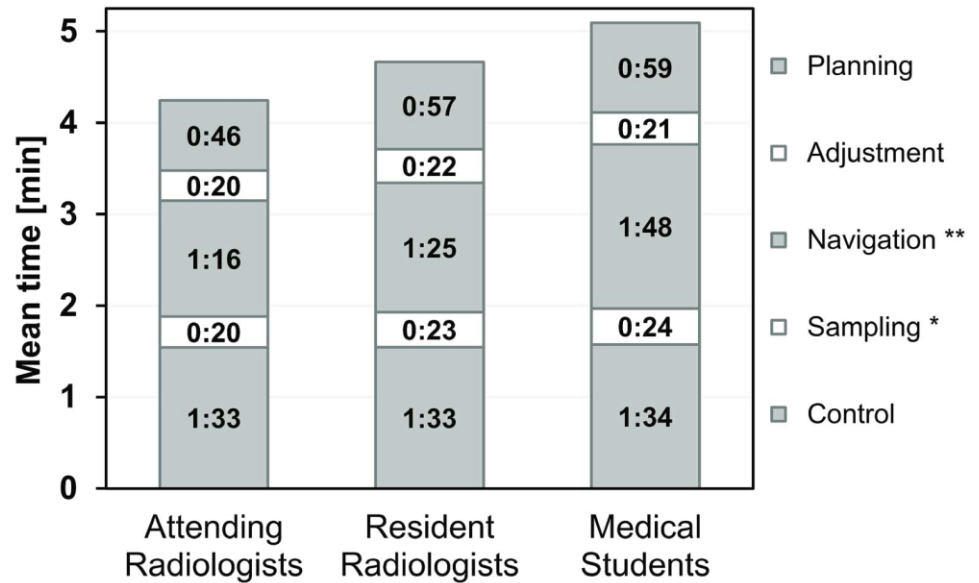


**Fig 6. Contribution of five working steps (planning, adjustment, navigation, sampling and control) to the mean experimental biopsy time for each operator group (AR, RR, MS).** The times stated are averages of 80 individual measurements from 8 operators on 10 targets each. Navigation times ranged between 01:16 (AR) and 01:48 (MS) and differences between operator groups were significant (ANOVA  $p < 0.01$ , \*\*). Sampling times ranged between 00:20 (AR) and 00:24 (MS) and between-group differences were significant ( $p < 0.05$ , \*). All other working step times were not significantly different (see text for details).

doi:10.1371/journal.pone.0134370.g006

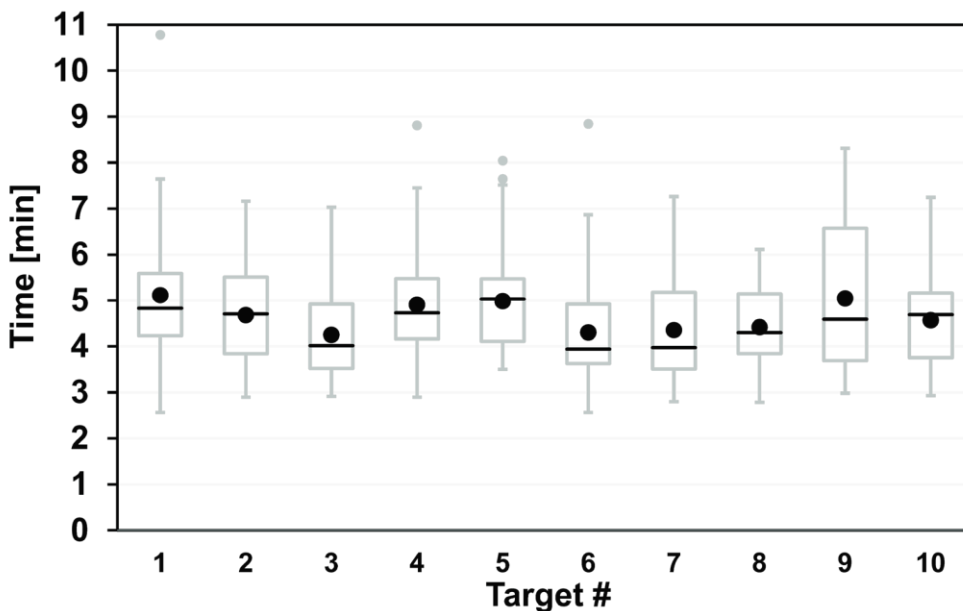


**Fig 7. Experimental total biopsy times for 24 operators as a function of target number with variable target depth and ease of access.** Each operator approached the targets #1 - #10 in the same order (see Fig 2 for details). Each box with whiskers represents the summary of 24 approaches of a single target by all operators (see Fig 5 for plot details). Four targets had 1–2 upper outliers (gray circles) with times greater than  $Q3 + 1.5 \times IQR$ . The statistical differences in the biopsy time per target (black circles indicate mean) were not significant ( $p = 0.065$ ).

doi:10.1371/journal.pone.0134370.g007

between-group differences for the navigation step. The absolute time differences for the puncture step ( $<3.5$  s) were considered negligible but reached significance. The average biopsy cycle times for all professionals (AR and RR) and all operators are considered to be acceptable (4:28 and 4:41 min) with a minimum of only 2:34 min for target #8.

The needle-placement step took around 1.5 min here, which is on the order of those reported for other experimental settings. Meyer et al. [6], for example, have determined puncture times and target errors using a prototype navigation system and real-time MRI in a short, wide-bore 1.5-T system. In a phantom, they achieved a similar mean targeting error (4.0 mm) in about half the time (0:37 min) for experienced operators and 20 trials. In five pigs, the error doubled and the average placement time increased to 5:14 min. Despite low statistical power, these quantitative figures for both settings serve as rough estimators of the loss in accuracy and time introduced by the in vivo setting. Despite some fundamental differences in these approaches (virtual versus real-time images, outside versus inside the bore), a few extra minutes and millimeters are likely to apply for our in-vivo application as well.

A phantom study by Hata et al. [23] has shown that the use of a robotic manipulator significantly reduced the time for needle alignment (from 2:49 to 0:36 min, accuracy 3.0 mm), again with figures being on a similar order of magnitude. Much faster needle placements were experimentally achieved with an augmented reality system outside the bore of a 1.5-T system ranging between 4.2 s ( $n = 70$ ) in a phantom to 30 s in three pigs ( $n = 10$ ) [24]. Similarly, the mean needle-to-target distance increased from 2.6 mm to about 10 mm for the animal work. The extent to which high-tech solutions will be developed and clinically deployed still remains to be seen.

The dependence of the average biopsy time with target number or course of time shows no clear trend. The longest biopsy time was observed for the first target although it was the easiest one (short and direct access, not obstructed by vessels). This could be explained by a simple learning effect [11,12,20] which would be in line with the corresponding subjective evaluation (Q05). The two prominent (differential) increases at targets #4 and #9 might be attributed to the increased complexity of the corresponding target approaches (location under vessels) although the overall time differences were not statistically significant ( $p = 0.065$ ).

The good performance of the navigation system is also supported by the operators' subjective evaluation. Predominantly high user scores suggest good usability and acceptance of the technique. Regardless of the level of experience, operators considered the solution to be easily understandable and provide additional safety and would also use it again. Replies by medical students to practical items like procedure duration or extra efforts, however, should be interpreted with some caution because of a generally limited experience in that area.

While the average operator rated the system to be marginally self-explaining (3.88, Q04), most users easily understood the working principle (4.79, Q01). We believe that the video instruction has largely contributed to this user rating, in particular because early attempts with simple text instructions were found to be insufficient. A slight agreement was reported for the handling of the articulating arm (3.67, Q06). A later inspection of one of the originally used arms revealed a light corrosion in the fixation mechanism that was probably the result of an early test inside a water bath. In addition, the manufacturer has commented that these elements are now made of stainless steel.

A minimal disagreement was observed with respect to the system's susceptibility against external perturbations (2.79, Q07). Stereotactic guidance systems with reference elements for image registration are generally susceptible to such errors. Displacements of the target region or the patient's body are inherent limitations of any system and may be addressed by additional patient markers or measures of immobilization [23,24]. The rigidity of the reference, however, depends on the specific organ region and type of procedure. In our case, the flexibility of a reference element for practically the whole body was obtained at the cost of stability. One MRI-

specific limitation is the geometric image distortion at the edges of the FOV (closer to the wall of the bore). That issue has already been extensively discussed in the literature and specific figures can be found in [17]. On the other hand, any stereotactic error will be seen in the control images and can be immediately corrected for by a simple update of the navigational road map. A clear advantage of such a floating reference is that navigation is neither affected by repositioning of the 3D digitizer nor by movements of the MR table.

## Conclusions

This study demonstrates high targeting accuracy, usability, and workflow of an "in-and-out" navigation solution for closed-bore scanners in an experimental setting. It must be stressed that during our clinical application, biopsies will never be taken without inspection of the control images. Therefore, the diagnostic accuracies observed here should be regarded as conservative estimates while the total biopsy times are rather lower limits. We believe that this approach is a feasible option for dedicated procedures when following some guidelines. While the clinical performance can only be assessed on real patients, this work provides some valuable findings for a large number of procedures and many different operators that may be relevant for other enabling technologies as well.

## Acknowledgments

The authors would like to thank all operators for participating in this study.

## Author Contributions

Conceived and designed the experiments: HB TR NG MM. Performed the experiments: HB TR NG GT. Analyzed the data: HB TR. Contributed reagents/materials/analysis tools: HB TR NG GT TK MM. Wrote the paper: HB TR NG GT TK MM.

## References

1. Tatli S, Morrison PR, Tuncali K, Silverman SG. Interventional MRI for oncologic applications. *Tech Vasc Interv Radiol*. 2007; 10: 159–170. PMID: [18070694](#)
2. König CW, Trübenbach J, Fritz J, Lauer UM, Claussen CD, Pereira PL. Contrast enhanced MR-guided biopsy of hepatocellular carcinoma. *Abdom Imaging*. 2004; 29: 71–76. PMID: [15160756](#)
3. Fischbach F, Bunke J, Thormann M, Gaffke G, Jungnickel K, Smink J, et al. MR-guided freehand biopsy of liver lesions with fast continuous imaging using a 1.0-T open MRI scanner: experience in 50 patients. *Cardiovasc Intervent Radiol*. 2011; 34: 188–192. doi: [10.1007/s00270-010-9836-8](#) PMID: [20358370](#)
4. Ricke J, Thormann M, Ludewig M, Jungnickel K, Gresser O, Wybranski C, et al. MR-guided liver tumor ablation employing open high-field 1.0T MRI for image-guided brachytherapy. *Eur Radiol*. 2010; 20: 1985–1993. doi: [10.1007/s00330-010-1751-5](#) PMID: [20306080](#)
5. Streitparth F, Walter T, Wonneberger U, Chopra S, Wichlas F, Wagner M, et al. Image-guided spinal injection procedures in open high-field MRI with vertical field orientation: feasibility and technical features. *Eur Radiol*. 2010; 20: 395–403. doi: [10.1007/s00330-009-1567-3](#) PMID: [19727752](#)
6. Meyer BC, Brost A, Kraitchman DL, Gilson WD, Strobel N, Hornegger J, et al. Percutaneous punctures with MR imaging guidance: comparison between MR imaging-enhanced fluoroscopic guidance and real-time MR imaging guidance. *Radiology*. 2013; 266: 912–919. doi: [10.1148/radiol.12120117](#) PMID: [23297324](#)
7. Rothgang E, Gilson WD, Wacker F, Hornegger J, Lorenz CH, Weiss CR. Rapid freehand MR-guided percutaneous needle interventions: an image-based approach to improve workflow and feasibility. *J Magn Reson Imaging JMRI*. 2013; 37: 1202–1212. doi: [10.1002/jmri.23894](#) PMID: [23334924](#)
8. Moche M, Trampel R, Kahn T, Busse H. Navigation concepts for MR image-guided interventions. *J Magn Reson Imaging JMRI*. 2008; 27: 276–291. doi: [10.1002/jmri.21262](#) PMID: [18219682](#)

9. Stataus J, Maderwald S, Forsting M, Barkhausen J, Ladd ME. MR-guided core biopsy with MR fluoroscopy using a short, wide-bore 1.5-Tesla scanner: feasibility and initial results. *J Magn Reson Imaging JMRI*. 2008; 27: 1181–1187. doi: [10.1002/jmri.21075](https://doi.org/10.1002/jmri.21075) PMID: [18425833](https://pubmed.ncbi.nlm.nih.gov/18425833/)
10. Kühn J-P, Langner S, Hegenscheid K, Evert M, Kickhefel A, Hosten N, et al. Magnetic resonance-guided upper abdominal biopsies in a high-field wide-bore 3-T MRI system: feasibility, handling, and needle artefacts. *Eur Radiol*. 2010; 20: 2414–2421. doi: [10.1007/s00330-010-1809-4](https://doi.org/10.1007/s00330-010-1809-4) PMID: [20503050](https://pubmed.ncbi.nlm.nih.gov/20503050/)
11. Hoffmann R, Thomas C, Rempp H, Schmidt D, Pereira PL, Claussen CD, et al. Performing MR-guided biopsies in clinical routine: factors that influence accuracy and procedure time. *Eur Radiol*. 2012; 22: 663–671. doi: [10.1007/s00330-011-2297-x](https://doi.org/10.1007/s00330-011-2297-x) PMID: [21960160](https://pubmed.ncbi.nlm.nih.gov/21960160/)
12. Fritz J, Henes JC, Thomas C, Clasen S, Fenchel M, Claussen CD, et al. Diagnostic and interventional MRI of the sacroiliac joints using a 1.5-T open-bore magnet: a one-stop-shopping approach. *AJR Am J Roentgenol*. 2008; 191: 1717–1724. doi: [10.2214/AJR.08.1075](https://doi.org/10.2214/AJR.08.1075) PMID: [19020241](https://pubmed.ncbi.nlm.nih.gov/19020241/)
13. Salomonowitz E. MR imaging-guided biopsy and therapeutic intervention in a closed-configuration magnet: single-center series of 361 punctures. *AJR Am J Roentgenol*. 2001; 177: 159–163. PMID: [11418418](https://pubmed.ncbi.nlm.nih.gov/11418418/)
14. Das CJ, Goenka AH, Srivastava DN. MR-guided abdominal biopsy using a 1.5-Tesla closed system: a feasibility study. *Abdom Imaging*. 2010; 35: 218–223. doi: [10.1007/s00261-009-9504-0](https://doi.org/10.1007/s00261-009-9504-0) PMID: [19259724](https://pubmed.ncbi.nlm.nih.gov/19259724/)
15. Busse H, Garnov N, Thörmer G, Zajonz D, Gründer W, Kahn T, et al. Flexible add-on solution for MR image-guided interventions in a closed-bore scanner environment. *Magn Reson Med*. 2010; 64: 922–928. doi: [10.1002/mrm.22464](https://doi.org/10.1002/mrm.22464) PMID: [20806383](https://pubmed.ncbi.nlm.nih.gov/20806383/)
16. Busse H, Kahn T, Moche M. Navigation concepts for magnetic resonance imaging-guided musculoskeletal interventions. *Top Magn Reson Imaging TMRI*. 2011; 22: 179–188. PMID: [23514925](https://pubmed.ncbi.nlm.nih.gov/23514925/)
17. Garnov N, Thörmer G, Trampel R, Gründer W, Kahn T, Moche M, et al. Suitability of miniature inductively coupled RF coils as MR-visible markers for clinical purposes. *Med Phys*. 2011; 38: 6327. doi: [10.1118/1.3655027](https://doi.org/10.1118/1.3655027) PMID: [22047397](https://pubmed.ncbi.nlm.nih.gov/22047397/)
18. Busse H, Trampel R, Gründer W, Moche M, Kahn T. Method for automatic localization of MR-visible markers using morphological image processing and conventional pulse sequences: feasibility for image-guided procedures. *J Magn Reson Imaging JMRI*. 2007; 26: 1087–1096. PMID: [17896386](https://pubmed.ncbi.nlm.nih.gov/17896386/)
19. Moche M, Zajonz D, Kahn T, Busse H. MRI-guided procedures in various regions of the body using a robotic assistance system in a closed-bore scanner: preliminary clinical experience and limitations. *J Magn Reson Imaging JMRI*. 2010; 31: 964–974. doi: [10.1002/jmri.21990](https://doi.org/10.1002/jmri.21990) PMID: [20373442](https://pubmed.ncbi.nlm.nih.gov/20373442/)
20. Zangos S, Melzer A, Eichler K, Sadighi C, Thalhammer A, Bodelle B, et al. MR-compatible assistance system for biopsy in a high-field-strength system: initial results in patients with suspicious prostate lesions. *Radiology*. 2011; 259: 903–910. doi: [10.1148/radiol.11101559](https://doi.org/10.1148/radiol.11101559) PMID: [21364080](https://pubmed.ncbi.nlm.nih.gov/21364080/)
21. Lewin JS, Duerk JL, Jain VR, Petersilge CA, Chao CP, Haaga JR. Needle localization in MR-guided biopsy and aspiration: effects of field strength, sequence design, and magnetic field orientation. *AJR Am J Roentgenol*. 1996; 166: 1337–1345. PMID: [8633445](https://pubmed.ncbi.nlm.nih.gov/8633445/)
22. Noroozian M, Gombos EC, Chikarmane S, Georgian-Smith D, Raza S, Denison CM, et al. Factors That Impact the Duration of MRI-Guided Core Needle Biopsy. *Am J Roentgenol*. 2010; 194: W150–W157.
23. Hata N, Tokuda J, Hurwitz S, Morikawa S. MRI-compatible manipulator with remote-center-of-motion control. *J Magn Reson Imaging*. 2008; 27: 1130–1138. doi: [10.1002/jmri.21314](https://doi.org/10.1002/jmri.21314) PMID: [18407542](https://pubmed.ncbi.nlm.nih.gov/18407542/)
24. Wacker FK, Vogt S, Khamene A, Jesberger JA, Nour SG, Elgort DR, et al. An augmented reality system for MR image-guided needle biopsy: initial results in a swine model. *Radiology*. 2006; 238: 497–504. PMID: [16436814](https://pubmed.ncbi.nlm.nih.gov/16436814/)



## Arbeit 7 – Vergleich verschiedener Navigationsverfahren unter praktischen Aspekten

Nach der anwenderspezifischen Genauigkeit und Bedienbarkeit des Systems stehen in der abschließenden Arbeit [75] praktische Erwägungen im Vordergrund. Aus Sicht der interventionellen Anforderungen, hier aus dem muskuloskelettalen Bereich, wird das System anderen prototypischen und kommerziellen Navigationsverfahren gegenüber gestellt. Diese lassen sich wie folgt kategorisieren:

- Rahmenbasierte Stereotaxie mit direkter Kontrolle in einem *offenen* MRT [87]
- Echtzeit-Navigation in einem *offenen* MRT [29, 88–90]
- Freihand-Navigation innerhalb und außerhalb eines kurzen *wide-bore* MRT-Systems [91]
- Echtzeit-Navigation an einem *geschlossenen* MRT (eigenes System)
- *Augmented-reality*-Navigation an einem geschlossenen MRT [92]
- Robotisch assistierte Navigation an einem geschlossenen MRT [85] (eigenes System)

Trotz der grundlegenden Vielfalt an Assistenzmöglichkeiten hängt der zukünftige Ausbau derartiger Techniken auch von der tatsächlichen Verbreitung sowie der klinischen Akzeptanz ab. Dabei zeichnen sich die offenen MRT-Systeme durch eine fluoroskopische Option (navigiert oder Freihand) aus, die mit Bildwiederholzeiten von etwa 1 s (d. h. 1 fps) auch ein kontrolliertes Arbeiten in bewegten Organbereichen erlauben. Die interventionelle Nutzung offener Systeme scheint jedoch in den letzten Jahren eher rückläufig zu sein. Zu den Hauptgründen dürften technische und wirtschaftliche Faktoren zählen, z. B. geringere Feldstärken (1,0 bzw. 1,2 T gegenüber 1,5 bis 3 T), eingeschränkte diagnostische Möglichkeiten, hohe Gesamtkosten sowie eine unklare Vergütung.

Demgegenüber finden sich stereotaktische Elemente in vielen Anwendungsbeispielen – effektiv beruhen auch die letzten beiden Systeme (*augmented reality* und robotische Assistenz) auf diesem Prinzip. Das Fehlen einer echten bildgebenden Kontrolle könnten Navigationssysteme durch flexible Bereitstellung, erweiterte Planungsmöglichkeiten und standardisierte Arbeitsabläufe teilweise kompensieren, so wie es das hier vorgestellte Konzept nahelegt. So lange geschlossene MRT-Systeme den diagnostischen Standard darstellen, scheinen stereotaktische Assistenzsysteme weiterhin bedeutend zu sein.

Das robotische System zeigt zudem einen Weg auf, eine bildgebende Führung an geschlossenen MRT-Systemen zu ermöglichen. Die Manipulation könnte passiv (Manipulator) oder aktiv (robotisch) von außerhalb gesteuert werden, fände aber unter fortlaufender Bildkontrolle im Magneten statt. Die automatische Festlegung der entsprechenden MRT-Ansichten könnte dann ebenfalls mit der hier beschriebenen, Tracking-Technologie auf der Basis drahtloser, semiaktiver MRT-Marker erfolgen.

# Navigation Concepts for Magnetic Resonance Imaging–Guided Musculoskeletal Interventions

Harald Busse, PhD, Thomas Kahn, MD, and Michael Moche, MD

**Abstract:** Image-guided musculoskeletal (MSK) interventions are a widely used alternative to open surgical procedures for various pathological findings in different body regions. They traditionally involve one of the established x-ray imaging techniques (radiography, fluoroscopy, computed tomography) or ultrasound scanning. Over the last decades, magnetic resonance imaging (MRI) has evolved into one of the most powerful diagnostic tools for nearly the whole body and has therefore been increasingly considered for interventional guidance as well.

The strength of MRI for MSK applications is a combination of well-known general advantages, such as multiplanar and functional imaging capabilities, wide choice of tissue contrasts, and absence of ionizing radiation, as well as a number of MSK-specific factors, for example, the excellent depiction of soft-tissue tumors, nonosteolytic bone changes, and bone marrow lesions. On the downside, the magnetic resonance–compatible equipment needed, restricted space in the magnet, longer imaging times, and the more complex workflow have so far limited the number of MSK procedures under MRI guidance.

Navigation solutions are generally a natural extension of any interventional imaging system, in particular, because powerful hardware and software for image processing have become routinely available. They help to identify proper access paths, provide accurate feedback on the instrument positions, facilitate the workflow in an MRI environment, and ultimately contribute to procedural safety and success.

The purposes of this work were to describe some basic concepts and devices for MRI guidance of MSK procedures and to discuss technical and clinical achievements and challenges for some selected implementations.

**Key Words:** interventional MRI, musculoskeletal system, soft tissue, bone, minimally invasive, percutaneous, needle-based procedures, tumor, biopsies, ablation, stereotactic guidance, navigation, targeting accuracy, clinical workflow

(*Top Magn Reson Imaging* 2011;22: 179–188)

Image-guided musculoskeletal (MSK) interventions comprise a number of diagnostic and therapeutic procedures involving bones, joints, muscles, and other soft-tissue structures that surround and support the organs of the MSK system. Many of these procedures can be performed in a percutaneous manner. Projection radiography and x-ray fluoroscopy were among the first imaging modalities to be used for such minimally invasive treatments. Later, ultrasound (US) and computed tomography (CT) imaging provided improved anatomical orientation because of the absence of superposition. The introduction and wide distribution of magnetic resonance imaging (MRI) systems

with powerful diagnostic capabilities have then propelled the use of MRI for image guidance.

Whereas CT remains the standard modality for depicting osteolytic and calcified lesions, MRI is the method of choice for nonosteolytic bone changes, lesions in the bone marrow, and soft-tissue tumors. Magnetic resonance imaging is also superior when critical structures along the needle path are not visible by other modalities and for cases where US and CT have clear limitations (US: limited penetration depth, bone and air-tissue interfaces; CT: children, pregnant women). An overview of indications for and examples of MSK interventions under MRI guidance can be found in the literature.<sup>1,2</sup>

Magnetic resonance imaging–guided MSK interventions fall into four main categories: biopsies, preoperative markings, drainages, and focal therapies. Most common MRI-guided therapies are spine injections for pain management (selective nerve blocks, among others) and thermal ablations (using focused US, radiofrequency, laser and cryo devices) of osseous lesions. Still, the majority of MSK procedures are performed under US and CT<sup>3</sup> rather than under MRI guidance because of some inherent advantages such as wider availability, lower costs of operation, less technical skills required, shorter procedure times, and less procedural issues with interventional access or special equipment.

One way to make MRI-guided procedures more convenient is to consider standard diagnostic MRI systems as interventional platforms, which means uncompromised imaging performance, wide availability, and lower costs compared with dedicated platforms such as open MRI systems. In settings with standard or wide-bore cylindrical magnets, however, access to the patient is generally limited, and procedural workflow is typically slow, making it difficult to accurately guide and place instruments. This could be one of the reasons for a growing demand of proper technical concepts such as innovative navigation solutions.

## FUNDAMENTAL CONCEPTS AND DEVICES

### Basic Guidance

Medical navigation is the process of locating and controlling the movement of medical instruments both inside and outside the patient's body. Magnetic resonance imaging–guided procedures are often performed in a percutaneous manner and use a coaxial technique to introduce medical instruments such as biopsy or ablation devices.<sup>4</sup> Navigation typically involves extra hardware and software, which need to be operated by trained persons. Some of these techniques mean a deviation from traditional approaches with established workflows and may then require extra work steps and time. For the most common type of magnet design, a cylindrical closed-bore system, procedures are often carried out with the MRI table and patient moved out of the bore. One relatively simple but effective way to then find a good entry point is to place a magnetic resonance (MR)–visible marker on the skin and to image and adjust it in relation to the specific MSK anatomy.

From the Department of Diagnostic and Interventional Radiology, Leipzig University Hospital, Leipzig, Germany.

Reprints: Harald Busse, PhD, Department of Diagnostic and Interventional Radiology, Leipzig University Hospital, Liebigstr. 20, 04103 Leipzig, Germany (e-mail: harald.busse@medizin.uni-leipzig.de).

The authors declare no conflict of interest.

Copyright © 2013 by Lippincott Williams & Wilkins

### Stereotactic Guidance

Stereotactic approaches outside the bore typically rely on special frames and devices to align the instrument (frame-based) or use a system for instrument tracking (frameless) to map the measured instrument position with the MRI coordinates. Instrument and device positions outside the bore need to be accurately registered with the MRI coordinates. Care must be taken to have the treated part of the body in the same position as that when the underlying reference MR images were acquired. The extremities are particularly prone to motion and need to be further immobilized, for example, by placing a vacuum mattress or splint filled with polystyrene balls around them. Commercial devices come in different sizes and generally help to stabilize traumatic injuries. Some of them can be safely used in the magnet. Unlike interventions in other regions of the body, MSK procedures are usually less affected by respiratory or other types of inherent organ motion, which reduces the number of potential error sources for stereotactic approaches. Analgesia and optional sedation are used to ensure proper patient comfort but may also add to the safety and accuracy of the navigation procedure.

### MR Fluoroscopic Guidance

Magnetic resonance fluoroscopy provides a snapshot of the true needle position with respect to the anatomy. This eliminates the need for time-consuming control scans but is limited to cases where the needle can be manipulated in the gap between entry point at the patient and magnet cover and therefore special wide-bore or open magnet configurations. Signal intensities and image contrast of the dynamic sequences may be different from those of dedicated diagnostic acquisitions because these sequences were optimized with respect to acquisition time rather than image quality or detail and may, for example, require a larger slice thickness. Under fluoroscopic imaging, a simple finger-pointing technique can be used to define the entry point. The interventionalist moves his/her finger along the skin of the patient and follows the continuously provided control images to ultimately define a fixed scan plane that includes both entry and target points. A subsequent freehand needle insertion can then be controlled by the displayed MR-fluoroscopic images along that control plane. By default, the geometry of the scan plane and other parameters cannot be changed during continuous scanning.

### System Interfaces

Over the last years, some MRI manufacturers have developed special user interfaces for interactive scan control that are typically operated from a workstation in the control room and display images on an in-room monitor next to the patient. Examples include the Interactive Front End by Siemens, iSuite by Philips, and iDriveProPlus by General Electric. These tools allow the operator during scanning to graphically adjust the scan planes relative to the needle position and also provide complementary information from multiple orthogonal image views. So far, these interfaces have predominantly been used for cardiac and abdominal cases but can easily be applied to a number of MSK procedures as well. They are generally reported to be time-efficient, reliable, and safe but may require good communication between the interventionalist and the technical operator at the scanner console.<sup>5</sup>

## EXAMPLES OF NAVIGATION FOR MSK PROCEDURES

The following examples provide a brief overview and discussion of specific navigation techniques used for MSK interventions.

### Frame-Assisted Navigation Inside an Open MRI

The drilling of osteochondral lesions can be performed under arthroscopic or x-ray guidance. Magnetic resonance imaging is indicated (i) for complex anatomies where the lesion is difficult to locate or that involve nearby critical structures, (ii) for long access paths, and (iii) for early stages that cannot be visualized by other imaging modalities. X-ray guidance, however, uses ionizing radiation and may require the interventionalist to repeatedly switch between two orthogonal imaging planes. Magnetic resonance imaging, in contrast, is inherently multiplanar and provides a fluoroscopic navigation option, although oblique imaging is usually restricted to the plane of intervention. In addition, this requires a magnet design where procedures can be performed inside the magnet.

A purely passive navigation concept for MSK procedures in a high-field (1.0-T) open scanner has, for example, been described by Bail and coworkers.<sup>6</sup> It relies on a rigid C-shaped navigation device with a working gap of up to 15 cm that can be adjusted to different anatomical regions (Fig. 1). A tubular MR-visible marker and a working capsule for the drill with a cylindrical marker are inserted at opposite ends of the device and fixed with two locking bolts. Test drills were performed in fresh human cadaver ankle joints using a 4.5-mm diameter cylindrical plug in the medial talar dome as target defect. Images were acquired with a 21-cm-diameter surface ring coil.

A dedicated user interface on the scanner console was used to interactively define an imaging plane that contained access (lateral process of the talus) and target points. The navigation device was then moved around the ankle such that both markers became visible within the prescribed scan plane and adjusted to bring the virtual axis, defined by the markers, into line with the prescribed drilling direction. In the cadaver study ( $n = 9$ ), drilling was performed with an MR-compatible drilling device (Invivo, Schwerin, Germany) and a 3.4-mm titanium spiral drill bit. An interactive proton density-weighted, fast-spin-echo sequence with a display rate of 1 image every 1.6 seconds (slice thickness, 3.5 mm) was used for guidance.

Interactive sequences with T1- and T2-weighted image contrast were also available on this platform. Deviations between target and actual drill positions were measured by MRI and with a caliper at the excised talus and determined to be 1.6 and 2.5 mm on average in two orthogonal planes (maximum, 3.5 mm). Average procedure time was less than 8 minutes, with approximately 3.5 minutes for image-plane definition and device adjustment each, and slightly over 1 minute for MR-fluoroscopic drilling. Displacements of the navigation guide or deviations of the actual drill position from the prescribed path could be easily and instantly corrected for by hand.

The same navigation device has also been applied for the retrograde drilling of 12 experimental lesions ( $4.5 \times 10$ -mm cylindrical plug) in the medial and lateral femoral condyles of 6 cadaver knees. The rationale for such MSK procedures is to provide a percutaneous alternative to the surgical treatment of joint disorders such as osteochondritis dissecans, which, despite a generally low incidence, is well known to cause joint pain and later osteoarthritis in physically active children and adolescents. For the experiments, the knee specimens were placed in lateral position and 90-degree flexion near the isocenter of a 1.0-T open magnet. Procedure and imaging protocol were similar to the talar drilling described above.

Lesions in the medial and lateral condyles were approached from the corresponding epicondyles forming angles of 60 to 80 degrees between drilling direction and orientation of the static magnetic field, which is vertical for this particular magnet design.

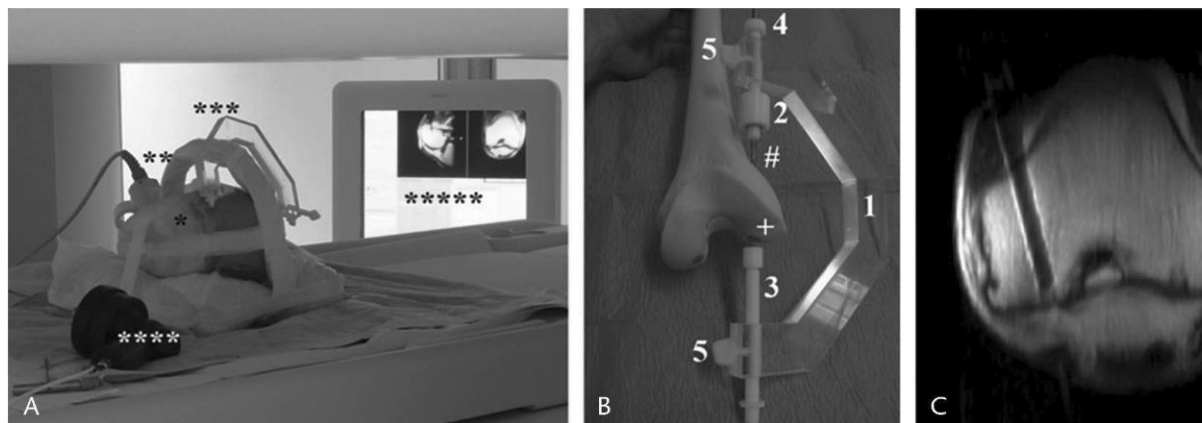


**FIGURE 1.** Navigation concept for MRI-guided procedures in the 45-cm large gap of an open, biplanar 1.0-T magnet with a pole diameter of 160 cm. A, Experimental setup for the drilling of orthopedic lesions shows cadaver knee (\*) in 90-degree flexion, large surface coil for imaging (\*\*), passive navigation device (\*\*\*), MR-compatible drilling device (Invivo, \*\*\*\*), and in-room monitor (\*\*\*\*\*) for interactive guidance. The scanner design provides enough space for the interventional radiologist to partly climb into the bore and operate the instruments from the side of the patient (not shown here). B, Illustration of navigated drilling of a virtual lesion (+) in the condyle of a model femur. C-shaped handle (1) with cylinder (2) and tube markers (3) as well as titanium drill (#) inserted into drilling capsule (4). After alignment, device is locked with 2 bolts (5) on both sides. C, Sample proton density-weighted, fast-spin-echo image (repetition time, 400 milliseconds; echo time, 8 milliseconds; slice thickness, 3.5 mm; in-plane resolution,  $0.6 \times 1.0$  mm) illustrating image quality and contrast during interactive navigation. Reproduced from Seebauer et al.<sup>24</sup> With kind permission from Springer Science and Business Media.

Average deviations between target and actual drill positions ( $n = 12$ ) were determined to be 1.9 and 1.4 mm in two orthogonal planes (maximum, 3.7 mm) with no significant differences between medial and lateral lesions. Average procedure time was 14 minutes, with less than 4 minutes for image-plane definition, slightly over 6 minutes for device adjustment, and slightly over 4 minutes for MR-fluoroscopic drilling. This suggests that procedures in the knee are more complex than those in the ankle, whereas the experimental drilling accuracy is comparable for both regions.

### Tracked Navigation Inside an Open MRI

Frameless external referencing techniques have been relatively common for interventional procedures in early open MRI systems operating at low-field and mid-field strengths. The simple rationale is to use the measured instrument coordinates to continuously define the scan plane of the MR-fluoroscopic sequence and thus avoid imaging with time-consuming manual adjustments of the instrument and the control plane.

The instrument position can be recorded with optical 3-dimensional (3D) digitizers (stereoscopic cameras) via active elements such as infrared light-emitting diodes on special handpieces or via passive elements such as coated spheres reflecting the light from a source built into the position sensor. Optical instrument tracking has also been used for MSK biopsies, spinal biopsies, and arthrographic injections, and examples include 3D optical digitizers (passive) in 0.2-T<sup>7,8</sup> or 0.23-T<sup>9</sup> C-shaped open magnets with a horizontal gap as well as a built-in active tracking option<sup>10</sup> in a mid-field 0.5-T magnet with a 58-cm-wide vertical gap.

The main drawbacks of these low- and mid-field MRI systems are their limited image quality and limited choice of imaging options. Whereas that performance is considered to be sufficient for purposes such as interventional guidance or basic examinations, it is not adequate for routine diagnostics. Although the majority of these early open MRI models have been discontinued, some vendors have developed high-field (1.0- to 1.2-T) open MRI systems that provide a satisfactory

compromise between imaging performance, patient comfort, and interventional access. Except for the need of specific interfaces to the scanner hardware and pulse sequences, frameless optical tracking systems can be easily migrated to other or newer MRI models.

In addition to freehand, frame-based, and frameless optical navigation options in such scanners, one clinical site with a 1.0-T open magnet has also presented a commercial prototype for needle tracking and automatic scan plane selection that relies on active MR markers integrated into the handpiece.<sup>11</sup> Although these open MRIs enable MSK diagnostics in special patient positions, for example, the so-called apprehension position for shoulder examinations (90-degree abduction and maximum tolerable external rotation), the number of reported navigated MSK procedures in these systems is still relatively low. For interventional procedures, there seems to be an effective shift in scanner preference from open to wide-bore scanners.

### Freehand Navigation Inside and Outside a Wide-Bore MRI

Over the last years, wide-bore scanners at different field strengths (1.5 and 3.0 T) have become available from all major scanner manufacturers, primarily to improve patient comfort, reduce claustrophobic reactions, and to examine obese patients. At the same time, the wide bore provides some extra space between the patient and the magnet tunnel to better accommodate imaging, monitoring, and interventional equipment, such as coils, guiding devices, needles, and probes. A wider bore also allows for nearly any patient entry into the magnet, including supine and lateral positions, which may be preferred or required for specific MSK procedures. In selected cases and when the operator can reach the entry site while the patient is inside the magnet, needles and tools may actually be manipulated and inserted under MR fluoroscopy.

An example of an interventional environment involving a wide-bore scanner is shown in Figure 2A. This particular 1.5-T model features a cover-to-cover length of only 125 cm, which

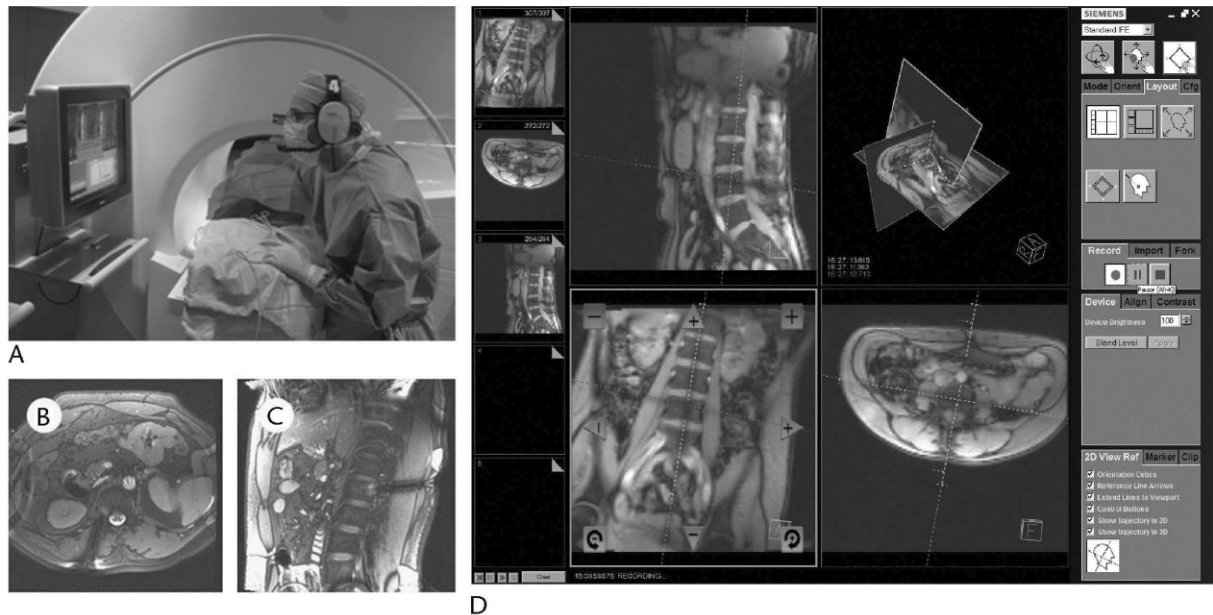


**FIGURE 2.** Navigation concept for MRI-guided procedures in the cylindrical tunnel of a 70-cm wide-bore 1.5-T magnet, here with a cover length of 125 cm. Clinical example illustrates instrument navigation for laser ablation of a bone metastasis in the first lumbar vertebral body of a 43-year-old man with a history of melanoma. A, The operator reaches into the gap between patient and magnet, adjusts and advances the instrument under real-time MRI control while following the continuously displayed images on an in-room monitor. Magnetic resonance-compatible microphone and headset are used to communicate specific acquisition parameters and scan plane settings with the technician in the control room. Oblique axial (B) and oblique sagittal views (C) of the coaxial needle used to accurately place the laser applicator. D, Example of an integrated user interface for graphical scan control (Interactive Front End; Siemens Corporate Research, Baltimore, MD) during real-time MRI. Images are displayed in 2D views with annotated lines for intersecting planes as well as 3D views. Buttons and graphical manipulators allow the user to shift, tilt, or rotate the scan planes in real time. Screenshot shows 3 independent real-time gradient-echo images of the lumbar spine displayed at an update rate of 0.9 seconds. A to C were reproduced from Ahrar and Stafford<sup>12</sup> with permission from Elsevier. D is for illustrative purposes only; MR images are not related to the clinical case described here.

makes it a potential choice for direct manipulation in the magnet. The needle can be advanced to the target lesion in two ways. In the intermittent mode, the needle is advanced incrementally outside the bore with intermittent imaging to control the position, here using 1 to 3 planes of a trueFISP (true fast imaging with steady state precession) sequence with acquisition time of less than 1 second per slice, a thickness of 4 mm, and an in-plane resolution around 1 mm. In real-time mode, the interventional radiologist reaches into the magnet and controls his action by looking at the continuously displayed MR images on a movable in-room monitor. The acquisition parameters of the real-time sequence (segmented trueFISP) differ somewhat from those of typical trueFISP.<sup>11</sup> In the clinical example shown, MRI and MR thermometry were used to guide and control the laser ablation of a bone metastasis in the first lumbar vertebral body of a 43-year-old man with a history of melanoma (Figs. 2B, C). This procedure has been performed after successful animal tests in the lumbar spine of dogs and first laser ablation trials under thermometry in regions such as the vertebral body and iliac bone.

Scanner manufacturers, third-party vendors, and research institutions have also developed appropriate user interfaces that assist the radiologist with the key tasks: definition of entry site, trajectory planning, monitoring of needle insertion, and safe navigation to the target region. The scan planes are usually adjusted by a technician in the control room, which requires an effective communication between the radiologist and the technician. One example of such a user interface is shown in Figure 2D. The software runs on a separate computer, continuously receives the reconstructed images from the real-time

sequence, and displays them in 2D and 3D views. The user has a choice of image contrast, gradient echo versus fully balanced pulse sequence, and a variety of scan options, such as type of k-space sampling, magnetization preparation, fat suppression, and parallel imaging. More advanced solutions involve input devices such as keys, switches, and track balls for the operator or make use of different kinds of tracking sensors to automatically define the corresponding scan planes.

### Tracked (Virtual) Navigation Outside a Closed-Bore MRI

One drawback of traditional stereotactic approaches, the lack of instant visual feedback on the needle position, can be addressed by tracking the needle outside the bore and computing a set of multiplanar reconstructions as a function of tip position and needle direction. Such a virtual real-time navigation then requires patient and MRI coordinates to be properly registered and the actual needle position to be verified. One of these approaches, the so-called iMRI Navigator (Localite, Sankt Augustin, Germany), uses a sterile, attachable needle tracker with optical markers and a stereoscopic infrared camera for tracking. Patient registration is enabled by a table-mounted reference board that can be freely adjusted and locked and involves a simple and fast (<30 s) localization of 3 to 5 custom MR markers only.<sup>13</sup> The navigation system is operated from a stand-alone PC in the control room whose display is projected onto a large screen in the MR room. Owing to the flexible mounting of the reference board to slits at the sides of the

patient table and the robust marker localization in practically any position, this system is not limited to a specific body region and has already been used for clinical cases in the liver, kidney, thoracic wall, pelvis, and extremities, among others.

Figure 3 gives an example for an MRI-guided MSK intervention in a 43-year-old male patient with a suggestive lesion in the shoulder area and a history of melanoma. This patient was scheduled for a navigated presurgical hook-wire insertion under MR control, because the lesion was thought to be difficult to identify in situ. Setup of the add-on components (in-room camera and display screen, table-mounted guiding arm, and reference board) and positioning of patient and imaging coils required 5 and 10 minutes, respectively. The patient was moved into the magnet to acquire both marker and reference 3D data.

The navigation software reported an average 3D deviation of 1.4 mm for marker localization, which is regarded as low. Further patient preparation and access planning involved the following steps: skin disinfection, sterile draping, insertion of coaxial needle and optical tracker into articulating guiding arm, virtual navigation to define the needle path, locking of the guidance mechanism, and local anesthesia (15 minutes).

After partial, double-oblique insertion of the coaxial needle (about halfway, 45 mm) under navigational guidance, the needle direction was verified and slightly adjusted. In the following transverse control image, the needle tip was located right at the edge of the lesion. An oblique VIBE (volume-interpolated breath-hold examination) image along the needle path then confirmed the final placement to be correct (total time, 13 minutes). After

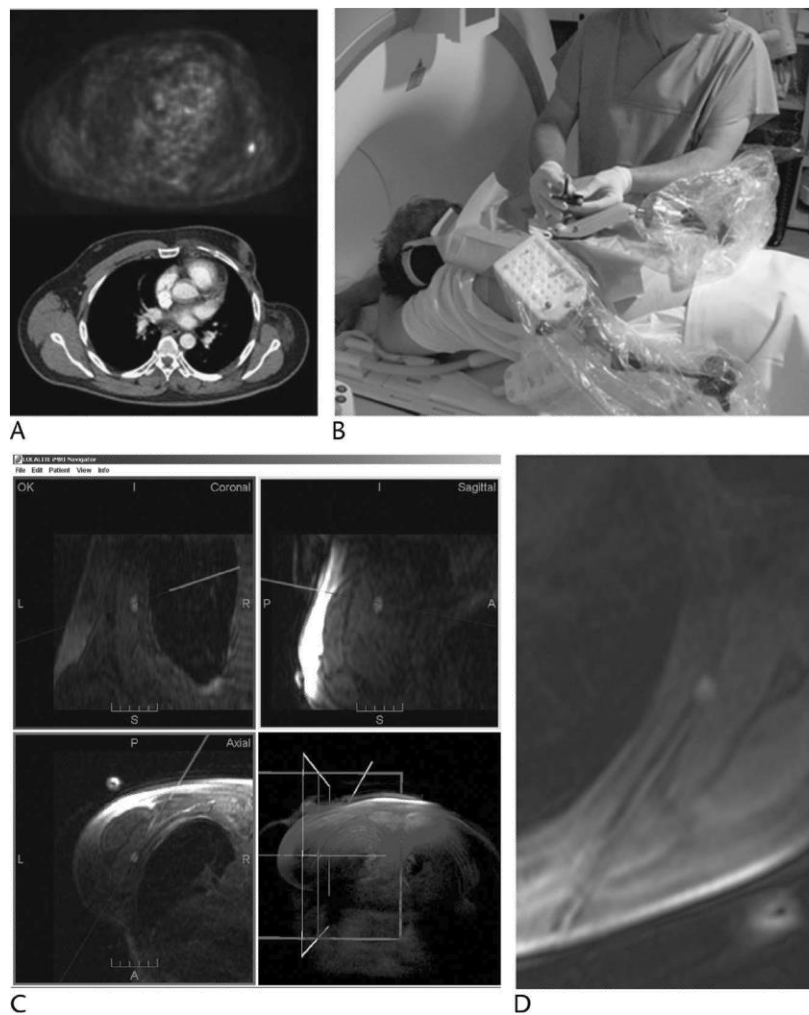


**FIGURE 3.** Navigation concept for MRI-guided MSK procedures outside a conventional, 60-cm-diameter, closed-bore 1.5-T magnet. Clinical application for preoperative marking of a suggestive lesion in a 43-year-old male patient with malignant melanoma in a complex location between left scapula and rib cage. A, Early positron emission tomographic image (top) shows high fluorodeoxyglucose uptake in a region that could be loosely correlated with an irregular but isointense region in CT images (bottom). B, Clinical setting during MRI-guided navigation of coaxial needle at the patient (in prone position) using optical tracker and special 6-DOF guiding device (interventional front-end module; Invivo). Table-mounted marker board ensures accurate patient registration outside the bore. C, Screenshot of navigation software with overlay of virtual needle direction on continuously reformatted MRI views, here along standard radiological planes. Unlike CT imaging, unenhanced T1-weighted MR images already reveal lesion as well-defined hyperintense region. D, Oblique intraoperative VIBE image (slice thickness, 5 mm) along final needle trajectory (double oblique between scapula and rib cage; insertion depth, 95 mm).

insertion of the hook wire, the tumor could be easily located in the subsequent surgical procedure and completely removed. Histopathology confirmed R0 resection of the metastasis of a malignant melanoma.

The same system has also been used for a navigated biopsy of a paravertebral lesion suggestive of a metastasis from breast cancer in a 67-year-old woman (Fig. 4). The patient underwent CT-guided biopsy in which 50 mL of yellowish fluid were aspirated. Microbiological analysis of the sample showed no result, and the patient was scheduled for biopsy under MR guidance. Unenhanced T2-weighted MRI showed distinct substructure of the lesion with fluid and solid components. Needle was navigated under virtual real-time guidance into the solid part of the lesion. Histopathologic analysis of the sample could rule out metastatic breast cancer and revealed a leiomyogenic tumor instead.

### Augmented Navigation Outside a Closed-Bore MRI

An augmented-reality guidance concept for MSK interventions in a standard closed-bore MRI environment has recently been described.<sup>14</sup> It also requires proper patient immobilization throughout the procedure and accurate registration of MRI to system coordinates. The intervention is then performed conveniently outside the magnet, but without immediate MRI control. The needle is navigated with a real view of the patient augmented by accurately overlaid MR images of the anatomy. Figure 5 shows the system setup and an example of a spinal injection procedure in a phantom.

The planning and control software was developed under an open-source package for biomedical image analysis and visualization (3D Slicer, [www.slicer.org](http://www.slicer.org)) and can run on different platforms and hardware, for example, on laptop computers.

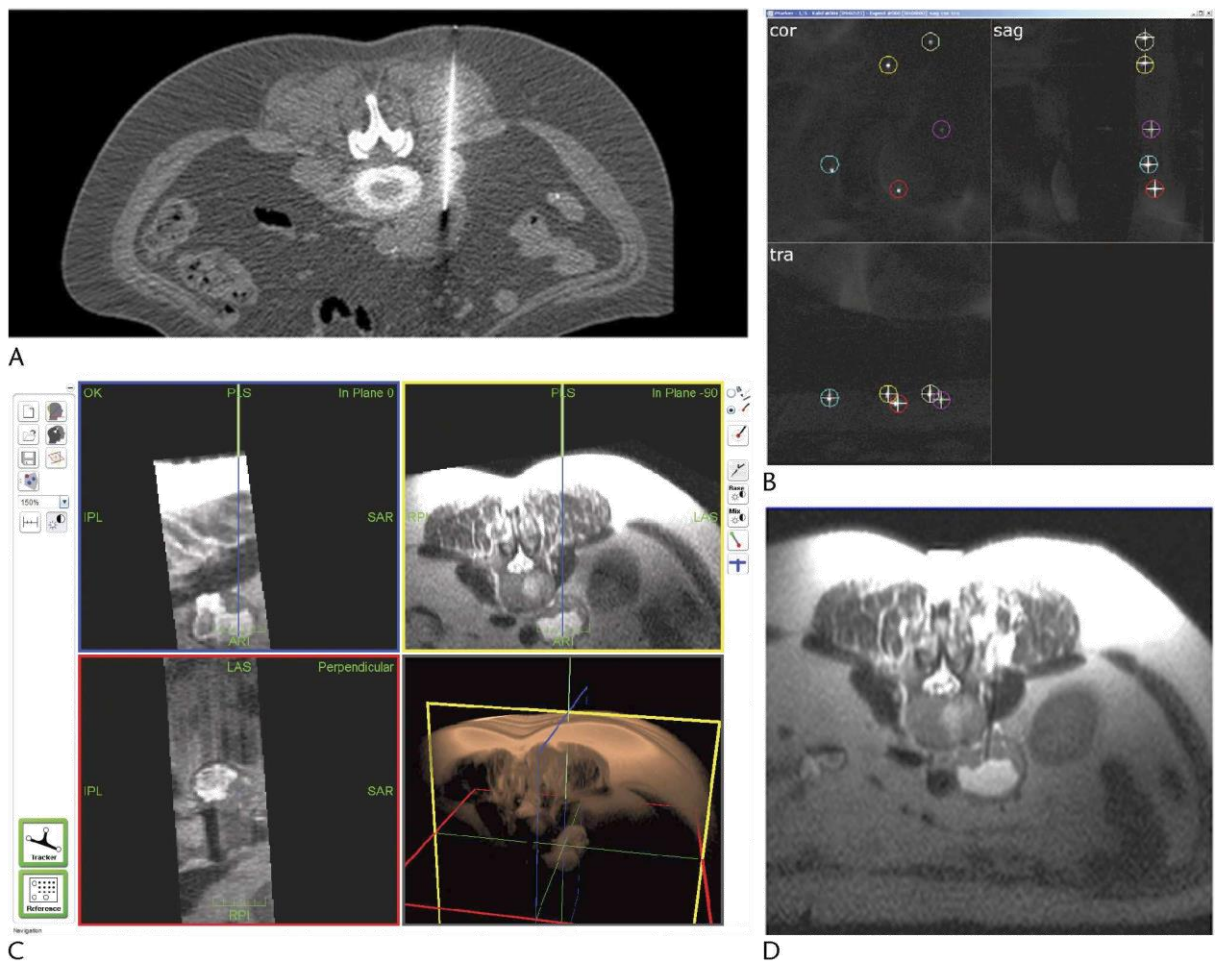


**FIGURE 4.** Biopsy of a para-aortal, infrarenal lymph node swelling in a 67-year-old female patient with breast cancer. A, Initial CT-guided biopsy. Whereas axial control slice shows the needle tip in the area of interest, the biopsy revealed fluid only. B, Navigated MRI-guided biopsy. Tool for automatic detection of MR reference markers, here 5, in 3 orthogonal planes providing the basis for accurate patient registration outside the bore.<sup>13</sup> C, Procedure was planned on unenhanced half-Fourier single-shot turbo-spin-echo (HASTE) image data (repetition time, 1,100 milliseconds; echo time, 122 milliseconds; slice thickness, 3.0 mm; in-plane resolution,  $0.9 \times 0.9$  mm; 2 signal averages; 30 slices) that was transferred to the navigation workstation. Screenshot of navigation software (iMRI Navigator; Localite) indicates virtual needle direction and extension into the body (green and blue lines). T2-weighted MRI with fluid (hyperintense) and less intense solid tissue components. The MR signals were detected with a single, 19-cm diameter loop coil placed on the back. D, Axial control slice showing needle tip in the target area. Biopsy was successful, and histology revealed a leiomyogenic tumor with no histological evidence for breast cancer.



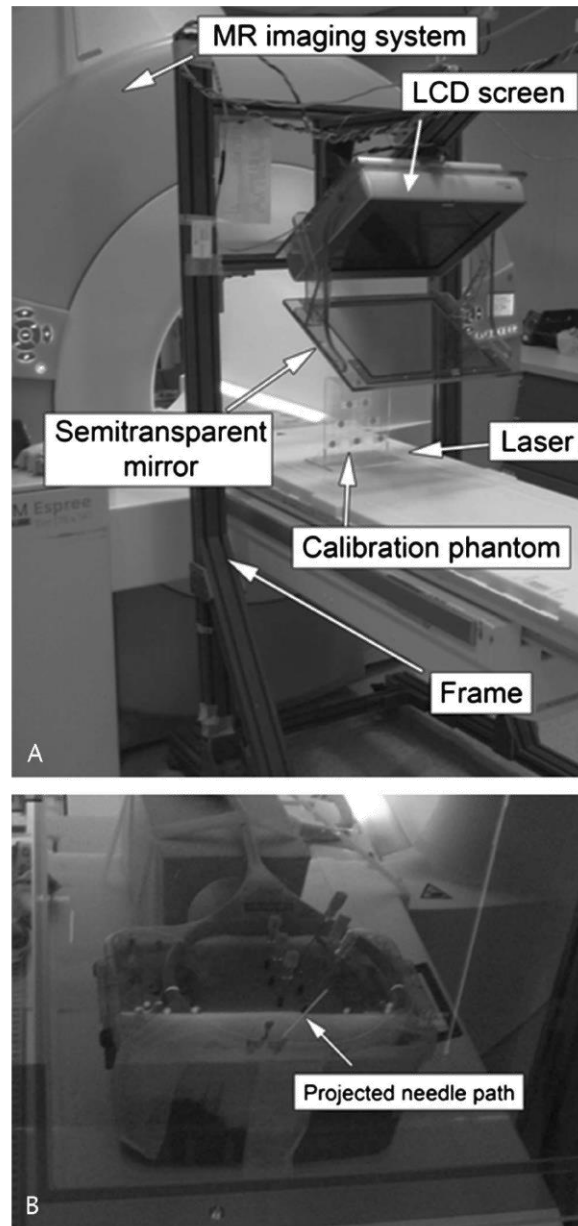


**FIGURE 5.** Augmented-reality guidance concept for MSK interventions in a 1.5-T cylindrical closed-bore MRI. A, Photograph showing stationary mechanical framework near the magnet opening with properly mounted, MR-compatible LCD screen and semitransparent mirror under which the patient will be positioned. B, Once the frame has been accurately aligned with the scanner axes, patient-to-image registration involves just 1 degree of freedom, the well-defined vertical translation of the patient table. Registered axial MR images of the patient anatomy are then projected from the LCD screen onto the mirror and augment the physician's real view of the interventional region. In addition, the intersection of the projected image with the object is marked by a laser line. Photographs courtesy of Jan Fritz and John Carrino, Russell H. Morgan Department of Radiology and Radiological Science, The Johns Hopkins University School of Medicine, Baltimore, Md).

Targeting accuracy of this system has been evaluated in a total of 60 trials in a lumbar spine phantom involving facet joints, disks, and spinal canals.<sup>15</sup> Planning and actual insertion of a single needle required an average of about 1 and 1.5 minutes only. The authors of that work see a potential for simplifying the current practice of MRI-guided lumbar spinal injections. An independent analysis of needle-placement trials on a total of 40

volunteers suggests that learners procedurally trained by such a system may perform better than untrained ones.<sup>16</sup>

In a human cadaver study, 176 (94.1%) of 187 lumbosacral spinal targets could be reached with the needle. Injections were successful for all accessible targets, took a median procedure time of 10.2 minutes (5–19 minutes), and required 47 (26.7%) needle adjustments in 176 cases.<sup>17</sup> The application spectrum of

this concept has been extended to MRI-guided arthrography in the shoulder and hip joints.<sup>18</sup> Two operators performed a total of 23 shoulder and 22 hip injections in 12 human cadavers. All 45 procedures were fully completed (intra-articular injection rate, 100%), required 6 (13%) needle adjustments, took an average of 14 minutes (6–27 minutes), and had a mean target error of 3.1 mm with an SD of 1.2 mm, suggesting accurate and efficient MR guidance for shoulder and hip arthrography in human cadavers.

Another augmented form of navigation can be realized by complementing the morphological image data with information from functional MRI studies or even other imaging modalities. The independent, reference-based navigation systems described above are suitable platforms for such extensions. The successful implementation of multimodal navigation, however, requires powerful and reliable algorithms for image registration unless the underlying image data are already given in a common coordinate system.

Reports about MRI-guided MSK procedures under multimodal guidance are generally rare. There are, however, a number of indications where image fusion may provide a potential clinical benefit, such as the overlay of metabolic information from nuclear medicine examinations, such as positron emission tomography (PET). Visual distinction between vital and necrotic tumor areas allows for improved targeting and less sampling errors. In some cases, the overlay of CT information may compensate for poor MR visualization. Fused CT images of fine bone structures of the midface, for example, have been used for the navigation of transnasal biopsies near the skull base that were performed in an open 0.5-T MRI with vertical magnet gap.<sup>19</sup> A more recent example involving CT data reports on the usefulness of overlaid PET on CT images for the sampling of a PET-only visible lymph node deep in the pelvis.<sup>20</sup>

Given that PET scanners are increasingly combined and distributed in the form of integrated (hybrid) PET/CT and PET/MRI units, MSK navigation may increasingly rely on multimodal



**FIGURE 6.** Magnetic resonance-compatible robotic manipulator for percutaneous procedures in a closed-bore cylindrical magnet. A, Clinical example I: soft-tissue biopsy of iliac lymph node in a 38-year-old woman with known cervical cancer. Clinical setup with robotic C-arm locked on MR table and application module (AMO) already moved into initial position. A sterile cover is placed over AMO and robotic arm. B, Screenshot of user interface on standalone control PC divided into areas for MR image selection, graphical trajectory planning, and numerical coordinate information and with general control buttons. Planned needle position and direction are then accurately realized by pneumatic actuators and optical sensors. C, Detail of B indicating planned needle path with entry point (circle), target point (X), and insertion depth. After MRI verification of the direction, needle is inserted manually outside the bore. D, Control MR image showing coaxial needle in final position for biopsy. E, Clinical example II: bone biopsy in the distal right femur of a 37-year-old woman with persistent pain when walking. Suspicious lesion was detected in bone scintigraphy but could neither be seen with conventional x-ray nor with CT.<sup>22</sup> Detail of clinical setup on MR table with right leg immobilized by vacuum mattress. A 19-cm-wide loop coil is used for MR signal reception. D, Bone biopsy set (Invivo) used for penetration of the cortical bone. Stylet and trocar are inserted through a guiding sleeve that attaches to the AMO of the robotic arm.

information as well once the technical platforms and algorithms have become routinely available.

### Robotic Navigation Outside a Closed-Bore MRI

Robotic manipulators may be considered as a further stage in the development from basic assistance concepts toward dedicated navigation solutions. These manipulators generally enable or facilitate the accurate alignment of instruments along a predefined path. They also serve as smart instrument holders that maintain a specific pose. This may, for example, be important to keep a loosely inserted needle in position for adequate control imaging. On the downside, all components, in particular, actuators and sensors, need to be MR-compatible. Depending on the specific purpose and range of applications, the geometric design may also be challenging, because the manipulator needs to fit into the gap between patient and magnet.

Unlike industrial robots, legal and ethical concerns prevent medical robots from actually performing the intervention. The number of robotic manipulators for MRI-guided interventions is generally limited, and many systems were developed for specific organs, most commonly the prostate or breast. One of the devices, the Innomotion System (Innomedic, Philippsburg, Germany), was deliberately designed for nearly any body region, underwent European conformity (CE) certification, and has been applied for a number of clinical cases at different institutions.<sup>21–23</sup> The wide range of motion also makes this device a good choice for MSK procedures, and corresponding cases include paraspinal injections, soft-tissue biopsies in the pelvis, and bone biopsies in the extremities, among others.

The central part of the Innomotion System is a 5-DOF robotic arm with an application module (AMO) at the end. The arm can be fixed in discrete positions along an arch that tightly fits into a 60-cm-wide magnet tunnel. The AMO features a plugging mechanism for different types of sterile instrument adaptors and a set of four passive marker spheres filled with MR contrast solution that are used for registration of the device with the patient. System components and two examples of clinical MSK cases are shown in Figure 6. Although this particular system is currently not commercially available, this example is meant to allow one to better identify opportunities and challenges of robotic guidance concepts for MSK procedures in general.

### SUMMARY AND CONCLUSIONS

The last two decades have seen the development of a variety of techniques and devices that successfully assist with interventions in an MRI environment in practically all regions of the body. Much of this technology can be easily applied to guide MSK interventions as well. Navigation systems range from simple stereotactic aids or sophisticated needle-tracking devices to user interfaces for MR-fluoroscopic guidance. Open magnet designs allow for imaging in special patient positions and also provide the largest range of guidance options, from freehand or frame-assisted approaches to real-time monitoring following the instrument itself. On the downside, open MRI systems come in a number of different field strengths (currently 1.0 and 1.2 T) than standard ones (1.5 and 3.0 T) and are also not widely available, partly because of performance and economic considerations, which makes continuous development and broader distribution of navigation techniques more difficult.

Cylindrical magnets are open to a variety of stereotactic solutions outside the bore that are controlled intermittently. Current developments are aiming to improve the accuracy and workflow of MRI-guided procedures. Wide-bore (70-cm) systems

are likely to become the next standard platform for MRI diagnostics, at least at 1.5 T. In these units, fluoroscopic interventional guidance is feasible only when the treated region can be reached from the magnet opening, for example, in very short units. On the other hand, this limitation may also be addressed by further considering manual or robotic manipulators. Besides the accuracy and safety of these navigation concepts, the key challenges for a wider use lie in their seamless integration, ease of use, cost-effectiveness, and proper clinical validation.

### REFERENCES

1. Smith KA, Carrino J. MRI-guided interventions of the musculoskeletal system. *J Magn Reson Imaging*. 2008;27:339–346.
2. Blanco Sequeiros R, Carrino JA. Musculoskeletal interventional MR imaging. *Magn Reson Imaging Clin N Am*. 2005;13:519–532.
3. Gogna A, Peh WCG, Munk PL. Image-guided musculoskeletal biopsy. *Radiol Clin North Am*. 2008;46:455–473, v.
4. Moche M, Trampel R, Kahn T, et al. Navigation concepts for MR image-guided interventions. *J Magn Reson Imaging*. 2008;27:276–291.
5. Fischbach F, Bunke J, Thormann M, et al. MR-guided freehand biopsy of liver lesions with fast continuous imaging using a 1.0-T open MRI scanner: experience in 50 patients. *Cardiovasc Intervent Radiol*. 2011;34:188–192.
6. Bail HJ, Teichgräber UKM, Wichlas F, et al. Passive navigation principle for orthopedic interventions with MR fluoroscopy. *Arch Orthop Trauma Surg*. 2010;130:803–809.
7. Petersilge CA, Lewin JS, Duerk JL, et al. MR arthrography of the shoulder: rethinking traditional imaging procedures to meet the technical requirements of MR imaging guidance. *AJR Am J Roentgenol*. 1997;169:1453–1457.
8. Lewin JS, Petersilge CA, Hatem SF, et al. Interactive MR imaging-guided biopsy and aspiration with a modified clinical C-arm system. *AJR Am J Roentgenol*. 1998;170:1593–1601.
9. Sequeiros RB, Niinimäki J, Ojala R, et al. Magnetic resonance imaging-guided diskography and diagnostic lumbar 0.23T MRI: an assessment study. *Acta Radiol*. 2006;47:272–280.
10. Genant JW, Vandevenne JE, Bergman AG, et al. Interventional musculoskeletal procedures performed by using MR imaging guidance with a vertically open MR unit: assessment of techniques and applicability. *Radiology*. 2002;223:127–136.
11. Wonneberger U, Krüger S, Wirtz D, et al. Clinically usable tool for dynamic scan-plane tracking for real-time MRI-guided needle interventions in a high-field-open MRI system In: Proceedings of the 19th Annual Meeting of the ISMRM; Montreal, QC; 2011. Abstract 202.
12. Ahrar K, Stafford RJ. Magnetic resonance imaging-guided laser ablation of bone tumors. *Tech Vasc Interv Radiol*. 2011;14:177–182.
13. Busse H, Garnov N, Thörner G, et al. Flexible add-on solution for MR image-guided interventions in a closed-bore scanner environment. *Magn Reson Med*. 2010;64:922–928.
14. U-Thainual P, Fritz J, Moonjaita C, et al. MR image overlay guidance: system evaluation for preclinical use [published online ahead of print August 25, 2012]. *Int J Comput Assist Radiol Surg*. 2012.
15. Fritz J, U-Thainual P, Ungi T, et al. Augmented reality visualization with image overlay for MRI-guided intervention: accuracy for lumbar spinal procedures with a 1.5-T MRI system. *AJR Am J Roentgenol*. 2012;198:W266–W273.
16. Yeo CT, Ungi T, U-Thainual P, et al. The effect of augmented reality training on percutaneous needle placement in spinal facet joint injections. *IEEE Trans Biomed Eng*. 2011;58:2031–2037.
17. Fritz J, U-Thainual P, Ungi T, et al. Augmented reality visualisation using an image overlay system for MR-guided interventions: technical

- performance of spine injection procedures in human cadavers at 1.5 Tesla. *Eur Radiol*. 2013;23:235–245.
18. Fritz J, U-Thainual P, Ungi T, et al. Augmented reality visualization with use of image overlay technology for MR imaging-guided interventions: assessment of performance in cadaveric shoulder and hip arthrography at 1.5 T. *Radiology*. 2012;265:254–259.
  19. Moche M, Schmitgen A, Schneider JP, et al. First clinical experience with extended planning and navigation in an interventional MRI unit [in German]. *Rofo*. 2004;176:1013–1020.
  20. Abi-Jaoudeh N, Kruecker J, Kadoury S, et al. Multimodality image fusion-guided procedures: technique, accuracy, and applications. *Cardiovasc Intervent Radiol*. 2012;35:986–998.
  21. Melzer A, Gutmann B, Remmele T, et al. Innomotion for percutaneous image-guided interventions: principles and evaluation of this MR- and CT-compatible robotic system. *IEEE Eng Med Biol Mag*. 2008;27:66–73.
  22. Moche M, Zajonz D, Kahn T, et al. MRI-guided procedures in various regions of the body using a robotic assistance system in a closed-bore scanner: preliminary clinical experience and limitations. *J Magn Reson Imaging*. 2010;31:964–974.
  23. Zangos S, Melzer A, Eichler K, et al. MR-compatible assistance system for biopsy in a high-field-strength system: initial results in patients with suspicious prostate lesions. *Radiology*. 2011;259:903–910.
  24. Seebauer CJ, Bail HJ, Rump JC, et al. Advancements in orthopedic intervention: retrograde drilling and bone grafting of osteochondral lesions of the knee using magnetic resonance imaging guidance. *Cardiovasc Intervent Radiol*. 2010;33:1230–1234.

## 4. Ausblick

---

Über die letzten Jahre sind zahlreiche Komponenten, Systeme und Techniken entwickelt worden, die erfolgreich für unterschiedliche MRT-geführte Interventionen eingesetzt wurden. Die Assistenzsysteme reichen von einfachen stereotaktischen Elementen über Systeme zur räumlichen Nadelverfolgung (*Tracking*) bis zu umfangreichen Schnittstellen zur MR-fluoroskopischen Steuerung.

Eine offene Magnetkonfiguration bietet neben erhöhtem Patientenkomfort verschiedene interventionelle Optionen, von Freihand- und rahmengestützten Verfahren bis zu einer bildgebenden Steuerung, die dem Instrument in nahezu Echtzeit folgt. Im Hinblick auf Feldstärke (1,0-1,2 T versus 1,5-3T), Bildgebungsoptionen und betriebswirtschaftliche Aspekte sind offene Systeme jedoch den röhrenförmigen Standardsystemen unterlegen. Die interventionelle Nutzung offener Systeme könnte sich daher perspektivisch auf spezielle Zentren beschränken, was die weitere Erprobung und Integration entsprechender Assistenztechniken erschweren würde.

Für die geschlossene Bauform bieten sich stereotaktische Techniken an, die außerhalb der Röhre durchgeführt und intermittierend kontrolliert werden und sich bereits seit vielen Jahren in konventionellen OP-Umgebungen (ohne Magnetfeld) etabliert haben. Das hier vorgestellte Verfahren wurde sowohl an einem offenen als auch an einem Standard-MRT implementiert und klinisch erprobt. Praktisch sollten die Ergebnisse jedoch vor allem für die überwiegend geschlossenen Systeme von Bedeutung sein [93]. Insgesamt konnte gezeigt werden, dass die mit kommerziellen Partnern entwickelten Komponenten sicher einsetzbar sind, weder Bildgebung noch Patientenkomfort beeinträchtigen und zuverlässig funktionieren. Eine erste größere klinische Auswertung von über 50 mit dem System navigierten Leberbiopsien zeigte vielversprechende Ergebnisse [18].

*Wide-bore* (70-cm) MRT-Systeme scheinen sich gegenwärtig als Standardplattform für die moderne MRT-Diagnostik zu etablieren, zumindest bei 1,5 T. Dies kommt den stereotaktischen Lösungen entgegen, da einerseits mehr Platz für Intervention und Zubehör zur Verfügung steht und andererseits Robustheit und Genauigkeit der Referenzierung erhöht werden können. An sehr kurzen Magneten lassen sich Eingriffe von der Magnetöffnung aus

auch fluoroskopisch kontrollieren. Die Zukunft der sehr kurzen *wide-bore* Systeme darf als ungewiss eingeschätzt werden, da diese einen deutlichen Mehraufwand erfordern, um die technischen Spezifikationen längerer Systeme zu erreichen. Mittelfristig könnten daher auch Assistenzsysteme bedeutsam werden, die mit Hilfe eines Telemanipulators bzw. einer robotischen Hilfe unabhängig von der Magnetlänge eingesetzt werden [94–97]. Für bestimmte Anwendungsbereiche, so z. B. bei neurologischen Eingriffen [98] oder Prostatainterventionen [99] gibt es hierzu bereits kommerzielle Produkte.

Zu den speziellen technischen Limitationen des hier beschriebenen stereotaktischen Systems zählt die Anfälligkeit einer frei positionierbaren Referenzplatte gegenüber einer versehentlichen Verschiebung. Ein damit einhergehender Registrierungsfehler ließe sich mit der hier vorgestellten Lösung dennoch relativ leicht und schnell dadurch beheben, dass die Marker nochmals aufgenommen und lokalisiert werden (etwa 1 Minute). Wären hingegen die Zugangswege einer Anwendung regional begrenzt, z. B. bei transperineal oder transrektal geführten Prostatainterventionen, so könnte die Referenzanordnung fest mit dem Patiententisch verbunden werden, was sich positiv auf die Robustheit auswirken sollte.

Eine weitere technische Besonderheit ist die hier kompakt gewählte optische Markerkonfiguration, die naturgemäß mit einer geringeren Genauigkeit der Referenzierung einhergeht. In einem *wide-bore*-System oder bei Anwendungen in einer peripheren Körperregion, die mehr Platz böte, ließe sich durch Verwendung einer ausgedehnten Markeranordnung die Genauigkeit verbessern. Ferner finden sich in einer methodischen Evaluation des optischen Trackingsystems konkrete Angaben, wonach die Messfehler der longitudinalen Koordinate ( $z$ ) merklich größer als die der lateralen ( $x$ - $y$ ) sind [32]. Daher sollte sich bei möglichst senkrechter Ausrichtung zwischen Markerebene und optischer Achse eine höhere stereoskopische Genauigkeit ergeben, was hier – aufgrund der räumlichen Enge – nur eingeschränkt realisierbar war.

Eine spezielle Fehlerquelle der MR-Referenz ist die inhärente Gradientenverzerrung, die sich mit zunehmendem Abstand vom Isozentrum auf die Markerlokalisierung auswirkt und letztlich zu systematischen Abweichungen der Zielposition führen kann. Dieser Effekt tritt bei sämtlichen bildbasierten Messungen auf und betrifft auch einfache, kontrastmittel-gefüllte Marker. Als grobe Korrektur kann die mathematische Anpassung des jeweiligen Herstellers

(hier: *großes FOV*) genutzt werden. Ferner wäre eine experimentelle Erfassung mit anschließender Kalibrierung denkbar [100], die jedoch aufwändig und gerätespezifisch wäre. Alternativ könnte eine symmetrische bzw. über das Messfeld verteilte Markieranordnung dazu beitragen, die Summe der systematischen Abweichungen zu reduzieren.

Die hier vorgestellte Markertechnik – die Kombination eines elementaren MR-Effekts mit einer leistungsstarken, numerischen Bildanalyse [81, 101] – hätte zudem weitere Anwendungsmöglichkeiten, insbesondere bei der dynamischen Einstellung oder Verfolgung interventioneller Werkzeuge im MRT. Aufgrund der umfassenden technisch-methodischen Vorarbeiten wäre eine entsprechende Produktentwicklung naheliegend. Die Vermarktung einer Spezialtechnik mit anfänglich geringen Stückzahlen scheint jedoch nicht so einfach zu sein, wie auch der weiterhin hohe Anteil an Forschungslösungen für vergleichbare interventionelle Entwicklungen zeigt. In diesem Bereich wäre eine gezielte industrielle Unterstützung sicherlich hilfreich.

Wahrscheinlich wird die zukünftige Entwicklung von Assistenzsystemen nicht allein darauf abzielen, deren Zuverlässigkeit, Sicherheit und Genauigkeit zu erhöhen. Wesentliche Aspekte, auch für die Akzeptanz von weniger erfahrenen Anwendern, könnten die einfache Integration in eine diagnostische Umgebung (Verfügbarkeit), die Optimierung der Arbeitsabläufe (Ergonomie) sowie die optionale Anpassung an ausgewählte Anwendungsbereiche (Modularität) sein.

## Literaturverzeichnis

---

1. Jaffe TA, Nelson RC (2016) Image-guided percutaneous drainage: a review. *Abdom Radiol* 41:629–636.
2. Mueller PR, Stark DD, Simeone JF, et al (1986) MR-guided aspiration biopsy: needle design and clinical trials. *Radiology* 161:605–609.
3. Lewin JS, Nour SG, Duerk JL (2000) Magnetic resonance image-guided biopsy and aspiration. *Top Magn Reson Imaging* 11:173–183.
4. Gupta S, Madoff DC (2007) Image-guided percutaneous needle biopsy in cancer diagnosis and staging. *Tech Vasc Interv Radiol* 10:88–101.
5. Lipnik AJ, Brown DB (2015) Image-guided percutaneous abdominal mass biopsy: technical and clinical considerations. *Radiol Clin North Am* 53:1049–1059.
6. Weiss CR, Nour SG, Lewin JS (2008) MR-guided biopsy: a review of current techniques and applications. *J Magn Reson Imaging* 27:311–325.
7. Gough-Palmer AL, Gedroyc WMW (2008) Laser ablation of hepatocellular carcinoma--a review. *World J Gastroenterol* 14:7170–7174.
8. Ahmed M, Solbiati L, Brace CL, et al (2014) Image-guided tumor ablation: standardization of terminology and reporting criteria--a 10-year update. *J Vasc Interv Radiol* 25:1691–1705.e4.
9. Beland MD, Sternick LA, Baird GL, et al (2016) Optimizing modality selection for image-guided procedures: an analysis of the challenges to ultrasound guidance. *Abdom Radiol* 41:590–599.
10. Charalel RA, McGinty G, Brant-Zawadzki M, et al (2015) Interventional radiology delivers high-value health care and is an Imaging 3.0 vanguard. *J Am Coll Radiol* 12:501–506.
11. Ng S, Tan KA, Anil G (2015) The role of interventional radiology in complications associated with liver transplantation. *Clin Radiol* 70:1323–1335.
12. Fiedler VU, Schwarzmaier HJ, Eickmeyer F, et al (2001) Laser-induced interstitial thermotherapy of liver metastases in an interventional 0.5 Tesla MRI system: technique and first clinical experiences. *J Magn Reson Imaging* 13:729–737.
13. Puccini S, Bär N-K, Bublat M, et al (2003) Simulations of thermal tissue coagulation and their value for the planning and monitoring of laser-induced interstitial thermotherapy (LITT). *Magn Reson Med* 49:351–362.
14. Rieke V (2011) MR Thermometry. In: Kahn T, Busse H (eds) *Interventional Magnetic Resonance Imaging*. Springer: Berlin, Heidelberg, pp 271–288.
15. Kahn T, Busse H (2012) *Interventional Magnetic Resonance Imaging*. Springer: Berlin, Heidelberg.
16. Salomonowitz E (2001) MR imaging-guided biopsy and therapeutic intervention in a closed-configuration magnet: single-center series of 361 punctures. *Am J Roentgenol* 177:159–163.



17. Kaiser WA, Pfeleiderer SOR, Baltzer PAT (2008) MRI-guided interventions of the breast. *J Magn Reson Imaging* 27:347–355.
18. Moche M, Heinig S, Garnov N, et al (2015) Navigated MRI-guided liver biopsies in a closed-bore scanner: experience in 52 patients. *Eur Radiol*. doi: 10.1007/s00330-015-4097-1
19. Rothgang E, Gilson WD, Wacker F, et al (2013) Rapid freehand MR-guided percutaneous needle interventions: an image-based approach to improve workflow and feasibility. *J Magn Reson Imaging* 37:1202–1212.
20. Noroozian M, Gombos EC, Chikarmane S, et al (2010) Factors that impact the duration of MRI-guided core needle biopsy. *Am J Roentgenol* 194:W150-157.
21. Lufkin R, Duckwiler G, Spickler E, et al (1988) MR body stereotaxis: an aid for MR-guided biopsies. *J Comput Assist Tomogr* 12:1088–1089.
22. Busse H, Kahn T, Moche M (2012) Navigation techniques for MRI-guided interventions. In: Kahn T, Busse H (eds) *Interventional Magnetic Resonance Imaging*. Springer: Berlin, Heidelberg, pp 53–75.
23. Arnolli MM, Hanumara NC, Franken M, et al (2015) An overview of systems for CT- and MRI-guided percutaneous needle placement in the thorax and abdomen. *Int J Med Robot Comput Assist Surg* 11:458–475.
24. Lufkin R, Teresi L, Chiu L, Hanafee W (1988) A technique for MR-guided needle placement. *Am J Roentgenol* 151:193–196.
25. Floery D, Helbich TH (2006) MRI-Guided percutaneous biopsy of breast lesions: materials, techniques, success rates, and management in patients with suspected radiologic-pathologic mismatch. *Magn Reson Imaging Clin N Am* 14:411–425, viii.
26. Beyersdorff D, Winkel A, Hamm B, et al (2005) MR imaging-guided prostate biopsy with a closed MR unit at 1.5 T: initial results. *Radiology* 234:576–581.
27. Mueller PR, Stark DD, Simeone JF, et al (1989) Clinical use of a nonferromagnetic needle for magnetic resonance-guided biopsy. *Gastrointest Radiol* 14:61–64.
28. Kugel H (2012) Safety Considerations in Interventional MRI. In: Kahn T, Busse H (eds) *Interventional Magnetic Resonance Imaging*. Springer: Berlin, Heidelberg, pp 77–88.
29. Lewin JS, Petersilge CA, Hatem SF, et al (1998) Interactive MR imaging-guided biopsy and aspiration with a modified clinical C-arm system. *Am J Roentgenol* 170:1593–1601.
30. Sequeiros RB, Klemola R, Ojala R, et al (2003) Percutaneous MR-guided discography in a low-field system using optical instrument tracking: a feasibility study. *J Magn Reson Imaging* 17:214–219.
31. Wood BJ, Zhang H, Durrani A, et al (2005) Navigation with electromagnetic tracking for interventional radiology procedures: a feasibility study. *J Vasc Interv Radiol* 16:493–505.
32. Khadem R, Yeh CC, Sadeghi-Tehrani M, et al (2000) Comparative tracking error analysis of five different optical tracking systems. *Comput Aided Surg* 5:98–107.

33. Li Q, Zamorano L, Jiang Z, et al (1999) Effect of optical digitizer selection on the application accuracy of a surgical localization system—a quantitative comparison between the OPTOTRAK and flashpoint tracking systems. *Comput Aided Surg* 4:314–321.
34. Moche M, Trampel R, Kahn T, Busse H (2008) Navigation concepts for MR image-guided interventions. *J Magn Reson Imaging* 27:276–291.
35. Soh E, Bearcroft PWP, Graves MJ, et al (2008) MR-guided direct arthrography of the glenohumeral joint. *Clin Radiol* 63:1336–1341–1343.
36. Fischbach F, Bunke J, Thormann M, et al (2011) MR-guided freehand biopsy of liver lesions with fast continuous imaging using a 1.0-T open MRI scanner: experience in 50 patients. *Cardiovasc Intervent Radiol* 34:188–192.
37. Stattaus J, Maderwald S, Forsting M, et al (2008) MR-guided core biopsy with MR fluoroscopy using a short, wide-bore 1.5-Tesla scanner: feasibility and initial results. *J Magn Reson Imaging* 27:1181–1187.
38. Stattaus J, Maderwald S, Baba HA, et al (2008) MR-guided liver biopsy within a short, wide-bore 1.5 Tesla MR system. *Eur Radiol* 18:2865–2873.
39. Wonneberger U, Schnackenburg B, Streitparth F, et al (2010) Evaluation of magnetic resonance imaging-compatible needles and interactive sequences for musculoskeletal interventions using an open high-field magnetic resonance imaging scanner. *Cardiovasc Intervent Radiol* 33:346–351.
40. Meyer BC, Brost A, Kraitchman DL, et al (2013) Percutaneous punctures with MR imaging guidance: comparison between MR imaging-enhanced fluoroscopic guidance and real-time MR Imaging guidance. *Radiology* 266:912–919.
41. Yutzy SR, Duerk JL (2008) Pulse sequences and system interfaces for interventional and real-time MRI. *J Magn Reson Imaging* 27:267–275.
42. Graves MJ, Wakely S, Bearcroft PW, et al (2008) MR-guided direct arthrography of the hip. *J Magn Reson Imaging* 28:462–465.
43. Wonneberger U, Krüger S, Wirtz D, et al (2011) Clinically usable tool for dynamic scan-plane tracking for real-time MRI-guided needle interventions in a high-field-open MRI system. *Proc Int Soc Magn Reson Med Sci Meet Exhib, Montreal, Ontario, Canada*, p 202.
44. Ahrar K, Ahrar JU, Javadi S, et al (2013) Real-time magnetic resonance imaging-guided cryoablation of small renal tumors at 1.5 T. *Invest Radiol* 48:437–444.
45. Schneider JP, Schulz T, Schmidt F, et al (2001) Gross-total surgery of supratentorial low-grade gliomas under intraoperative MR guidance. *Am J Neuroradiol* 22:89–98.
46. Boss A, Rempp H, Martirosian P, et al (2008) Wide-bore 1.5 Tesla MR imagers for guidance and monitoring of radiofrequency ablation of renal cell carcinoma: initial experience on feasibility. *Eur Radiol* 18:1449–1455.
47. Garnon J, Ramamurthy N, Caudrelier J J, et al (2016) MRI-guided percutaneous biopsy of mediastinal masses using a large bore magnet: technical feasibility. *Cardiovasc Intervent Radiol* 39:761–767.

48. Kitchen ND, Lemieux L, Thomas DG (1993) Accuracy in frame-based and frameless stereotaxy. *Stereotact Funct Neurosurg* 61:195–206.
49. Ishii M, Gallia GL (2010) Application of technology for minimally invasive neurosurgery. *Neurosurg Clin N Am* 21:585–594, v.
50. Luther N, Iorgulescu JB, Geannette C, et al (2015) Comparison of navigated versus non-navigated pedicle screw placement in 260 patients and 1434 screws: screw accuracy, screw size, and the complexity of surgery. *J Spinal Disord Tech* 28:E298–303.
51. D’Amico RS, Kennedy BC, Bruce JN (2014) Neurosurgical oncology: advances in operative technologies and adjuncts. *J Neurooncol* 119:451–463.
52. Tokuda J, Tuncali K, Iordachita I, et al (2012) In-bore setup and software for 3T MRI-guided transperineal prostate biopsy. *Phys Med Biol* 57:5823–5840.
53. Kugel H, Bremer C, Püschel M, et al (2003) Hazardous situation in the MR bore: induction in ECG leads causes fire. *Eur Radiol* 13:690–694.
54. Ooi MB, Krueger S, Thomas WJ, et al (2009) Prospective real-time correction for arbitrary head motion using active markers. *Magn Reson Med* 62:943–954.
55. Rachinger J, von Keller B, Ganslandt O, et al (2006) Application accuracy of automatic registration in frameless stereotaxy. *Stereotact Funct Neurosurg* 84:109–117.
56. Das CJ, Goenka AH, Srivastava DN (2010) MR-guided abdominal biopsy using a 1.5-Tesla closed system: a feasibility study. *Abdom Imaging* 35:218–223.
57. Langen H-J, Kugel H, Landwehr P (2002) MR-guided core biopsies using a closed 1.0 T imager. First clinical results. *Eur J Radiol* 41:19–25.
58. Streitparth F, Walter T, Wonneberger U, et al (2010) Image-guided spinal injection procedures in open high-field MRI with vertical field orientation: feasibility and technical features. *Eur Radiol* 20:395–403.
59. Chopra SS, Rump J, Schmidt SC, et al (2009) Imaging sequences for intraoperative MR-guided laparoscopic liver resection in 1.0-T high field open MRI. *Eur Radiol* 19:2191–2196.
60. Fischbach F, Porsch M, Krenzien F, et al (2011) MR imaging guided percutaneous nephrostomy using a 1.0 Tesla open MR scanner. *Cardiovasc Intervent Radiol* 34:857–863.
61. Zangos S, Eichler K, Wetter A, et al (2006) MR-guided biopsies of lesions in the retroperitoneal space: technique and results. *Eur Radiol* 16:307–312.
62. Busse H, Thomas M, Seiwerts M, et al (2008) In vivo glenohumeral analysis using 3D MRI models and a flexible software tool: feasibility and precision. *J Magn Reson Imaging* 27:162–170.
63. Tasaki A, Nimura A, Nozaki T, et al (2015) Quantitative and qualitative analyses of subacromial impingement by kinematic open MRI. *Knee Surg Sports Traumatol Arthrosc* 23:1489–1497.
64. Enders J, Zimmermann E, Rief M, et al (2011) Reduction of claustrophobia with short-bore versus open magnetic resonance imaging: a randomized controlled trial. *PLoS One* 6:e23494.

65. Enders J, Zimmermann E, Rief M, et al (2011) Reduction of claustrophobia during magnetic resonance imaging: methods and design of the “CLAUSTRO” randomized controlled trial. *BMC Med Imaging* 11:4.
66. Black PM, Moriarty T, Alexander E, et al (1997) Development and implementation of intraoperative magnetic resonance imaging and its neurosurgical applications. *Neurosurgery* 41:831-842-845.
67. Schenck JF, Jolesz FA, Roemer PB, et al (1995) Superconducting open-configuration MR imaging system for image-guided therapy. *Radiology* 195:805–814.
68. Seifert V, Zimmermann M, Trantakis C, et al (1999) Open MRI-guided neurosurgery. *Acta Neurochir (Wien)* 141:455–464.
69. Verheyden P, Katscher S, Schulz T, et al (1999) Open MR imaging in spine surgery: experimental investigations and first clinical experiences. *Eur Spine J* 8:346–353.
70. Schulz T, Schneider JP, Bootz F, et al (2001) Transnasal and transsphenoidal MRI-guided biopsies of petroclival tumors. *J Magn Reson Imaging* 13:3–11.
71. Bootz F, Keiner S, Schulz T, et al (2001) Magnetic resonance imaging--guided biopsies of the petrous apex and petroclival region. *Otol Neurotol* 22:383–388.
72. Bootz F, Schulz T, Weber A, et al (2001) The use of open MRI in otorhinolaryngology: initial experience. *Comput Aided Surg* 6:297–304.
73. Schneider JP, Schulz T, Horn LC, et al (2002) MR-guided percutaneous core biopsy of small breast lesions: first experience with a vertically open 0.5T scanner. *J Magn Reson Imaging* 15:374–385.
74. Moche M, Trampel R, Kahn T, Busse H (2008) Navigation concepts for MR image-guided interventions. *J Magn Reson Imaging* 27:276–291.
75. Busse H, Kahn T, Moche M (2011) Navigation concepts for magnetic resonance imaging-guided musculoskeletal interventions. *Top Magn Reson Imaging* 22:179–188.
76. Burl M, Coutts GA, Young IR (1996) Tuned fiducial markers to identify body locations with minimal perturbation of tissue magnetization. *Magn Reson Med* 36:491–493.
77. Flask C, Elgort D, Wong E, et al (2001) A method for fast 3D tracking using tuned fiducial markers and a limited projection reconstruction FISP (LPR-FISP) sequence. *J Magn Reson Imaging* 14:617–627.
78. Busse H, Garnov N, Thörmer G, et al (2010) Flexible add-on solution for MR image-guided interventions in a closed-bore scanner environment. *Magn Reson Med* 64:922–928.
79. Busse H, Schmitgen A, Trantakis C, et al (2006) Advanced approach for intraoperative MRI guidance and potential benefit for neurosurgical applications. *J Magn Reson Imaging* 24:140–151.
80. Moche M, Schmitgen A, Schneider JP, et al (2004) [First clinical experience with extended planning and navigation in an interventional MRI unit]. *RöFo Fortschritte Auf Dem Geb Röntgenstrahlen Nukl* 176:1013–1020.

81. Busse H, Trampel R, Gründer W, et al (2007) Method for automatic localization of MR-visible markers using morphological image processing and conventional pulse sequences: feasibility for image-guided procedures. *J Magn Reson Imaging* 26:1087–1096.
82. Garnov N, Thörmer G, Trampel R, et al (2011) Suitability of miniature inductively coupled RF coils as MR-visible markers for clinical purposes. *Med Phys* 38:6327.
83. Thörmer G, Garnov N, Moche M, et al (2012) Simultaneous 3D localization of multiple MR-visible markers in fully reconstructed MR images: proof-of-concept for subsecond position tracking. *Magn Reson Imaging* 30:371–381.
84. Melzer A, Gutmann B, Remmele T, et al (2008) INNOMOTION for percutaneous image-guided interventions: principles and evaluation of this MR- and CT-compatible robotic system. *IEEE Eng Med Biol Mag* 27:66–73.
85. Moche M, Zajonz D, Kahn T, Busse H (2010) MRI-guided procedures in various regions of the body using a robotic assistance system in a closed-bore scanner: preliminary clinical experience and limitations. *J Magn Reson Imaging* 31:964–974.
86. Busse H, Riedel T, Garnov N, et al (2015) Targeting accuracy, procedure times and user experience of 240 experimental MRI biopsies guided by a clinical add-on navigation system. *PloS One* 10:e0134370.
87. Seebauer CJ, Bail HJ, Rump JC, et al (2010) Advancements in orthopedic intervention: retrograde drilling and bone grafting of osteochondral lesions of the knee using magnetic resonance imaging guidance. *Cardiovasc Intervent Radiol* 33:1230–1234.
88. Petersilge CA, Lewin JS, Duerk JL, Hatem SF (1997) MR arthrography of the shoulder: rethinking traditional imaging procedures to meet the technical requirements of MR imaging guidance. *Am J Roentgenol* 169:1453–1457.
89. Sequeiros RB, Niinimäki J, Ojala R, et al (2006) Magnetic resonance imaging-guided diskography and diagnostic lumbar 0.23T MRI: an assessment study. *Acta Radiol* 1987 47:272–280.
90. Genant JW, Vandevenne JE, Bergman AG, et al (2002) Interventional musculoskeletal procedures performed by using MR imaging guidance with a vertically open MR unit: assessment of techniques and applicability. *Radiology* 223:127–136.
91. Ahrar K, Stafford RJ (2011) Magnetic resonance imaging-guided laser ablation of bone tumors. *Tech Vasc Interv Radiol* 14:177–182.
92. Wacker FK, Vogt S, Khamene A, et al (2006) An augmented reality system for MR image-guided needle biopsy: initial results in a swine model. *Radiology* 238:497–504.
93. Kaye EA, Granlund KL, Morris EA, et al (2015) Closed-Bore Interventional MRI: Percutaneous Biopsies and Ablations. *AJR Am J Roentgenol* 205:W400-410.
94. Kettenbach J, Kronreif G (2015) Robotic systems for percutaneous needle-guided interventions. *Minim Invasive Ther Allied Technol* 24:45–53.
95. Hata N, Song S-E, Olubiyi O, et al (2016) Body-mounted robotic instrument guide for image-guided cryotherapy of renal cancer. *Med Phys* 43:843–853.

96. Cleary K, Melzer A, Watson V, et al (2006) Interventional robotic systems: applications and technology state-of-the-art. *Minim Invasive Ther Allied Technol* 15:101–113.
97. Tavallaei MA, Johnson PM, Liu J, Drangova M (2016) Design and evaluation of an MRI-compatible linear motion stage. *Med Phys* 43:62.
98. Chittiboina P, Heiss JD, Lonser RR (2015) Accuracy of direct magnetic resonance imaging-guided placement of drug infusion cannulae. *J Neurosurg* 122:1173–1179.
99. Yakar D, Schouten MG, Bosboom DGH, et al (2011) Feasibility of a pneumatically actuated MR-compatible robot for transrectal prostate biopsy guidance. *Radiology* 260:241–247.
100. Wang D, Yang Z (2008) A detailed study on the use of polynomial functions for modeling geometric distortion in magnetic resonance imaging. *Med Phys* 35:908–916.
101. Rea M, McRobbie D, Elhawary H, et al (2009) Sub-pixel localisation of passive micro-coil fiducial markers in interventional MRI. *Magn Reson Mat Phys Med Biol* 22:71–76.

## Danksagung

---

Mein Dank gilt vor allem Prof. Dr. Thomas Kahn, Direktor der Klinik und Poliklinik für Diagnostische und Interventionelle Radiologie des Universitätsklinikums Leipzig, der mir die Forschung auf dem Gebiet der Interventionellen MRT erst ermöglicht und durch sein fachliches und persönliches Engagement stets vorangebracht hat.

Besonders bedanken möchte ich mich bei Dr. habil. Michael Moche, Leiter des Arbeitsbereichs Interventionelle Radiologie, der mir mit seiner interventionellen Expertise und seinem unermüdlichen Einsatz immer wieder entscheidend zur Seite stand.

Zu großem Dank verpflichtet bin ich den wissenschaftlichen Mitarbeiterinnen und Mitarbeitern, die mir bei den Messungen, Auswertungen und Diskussionen sowie den kleinen und großen Entwicklungen geholfen haben, ganz besonders bei Dr.-Ing. Nikita Garnov, Dr. Gregor Thörmer, Dr. Robert Trampel und Prof. Dr. Wilfried Gründer.

Gleichzeitig möchte ich mich bei allen ärztlichen Kolleginnen und Kollegen bedanken, die durch ihr interventionelles Interesse und ihren Einsatz zum Fortschritt beigetragen haben, unter anderem bei Jochen Fuchs, Tim-Ole Petersen und Dr. Matthias Seiwerts. Für die geleistete Arbeit möchte ich mich auch bei den ehemaligen Doktoranden bedanken, speziell bei Dr. Tim Riedel und Dr. Dirk Zajonz.

Für die fachlich-technische Unterstützung möchte ich den Mitarbeitern unserer kommerziellen Partner danken, insbesondere Dipl.-Ing. Axel Winkel (Invivo) sowie Dipl.-Inf. Arno Schmitgen und Dipl.-Phys. Martin Bublat (Localite GmbH).

Ein abschließendes Dankeschön gilt den vielen Kolleginnen und Kollegen, mit denen ich über die letzten Jahre, auch in anderen Projekten, zusammenarbeiten durfte und die mich auf vielfältige Weise unterstützt und motiviert haben.

## Erklärung

---

Hiermit erkläre ich, die vorliegende Habilitationsschrift selbständig und ohne unerlaubte fremde Hilfe angefertigt zu haben. Ich habe keine anderen als die im Literaturverzeichnis angeführten Quellen benutzt und sämtliche Textstellen, die wörtlich oder sinngemäß aus veröffentlichten oder unveröffentlichten Schriften entnommen wurden, als solche kenntlich gemacht. Ebenfalls sind alle von anderen Personen bereitgestellten Materialien oder erbrachten Dienstleistungen als solche gekennzeichnet.

Leipzig, den 18.08.2016

Dr. rer. nat. Harald Busse